Her Dark Materials:
exploration of magnetic phenomena
in quantum materials using neutron scattering

Siobhan Maeve Tobin
Somerville College

University of Oxford
A thesis presented for the degree of
Doctor of Philosophy

Hilary 2024

Abstract

In this thesis I present experimental investigations of four different quantum materials, each of which showcases the strongly correlated magnetism of 3*d* transition metal ions.

The topological semimetal candidate $YbMnSb_2$ has a high magnetic ordering temperature of $T_N \approx 345\,K$. I performed unpolarised and polarised neutron diffraction, as well as triple-axis spectroscopy on $YbMnSb_2$. From these results, I refined the magnetic and crystal structure of $YbMnSb_2$. Similar to other square net antimonides $YbMnSb_2$ displays C-type antiferromagnetism with the moments oriented along the *c* axis. I interpreted the spin wave spectrum using linear spin wave theory, where the predominant exchange interactions are in-plane; however, the out-of-plane exchange along the *c* axis is surprisingly large. This interaction acts through the Sb square net and so may influence the charge transport properties of the material. Our magnetic model of $YbMnSb_2$ is consistent with this compound being a gapped Dirac semimetal.

The topological insulator $MnSb_4Te_7$ is closely related to the much-studied van der Waals crystal $MnBi_2Te_4$. $MnSb_4Te_7$ had been identified as a possible axion insulator candidate. However, the ground state magnetic structure in the bulk had not been determined. I utilised single crystal neutron diffraction for this task and found that there is a strong degree of site-mixing between Mn and Sb sites. This leads to a magnetic structure where Mn^{2+} moments are coupled ferrimagnetically within the site-mixed magnetic layers but antiferromagnetically between magnetic layers with propagation vector $\mathbf{q} = (0, 0, 1/2)$. The application of an external magnetic field of 0.2 T drives a spin-flip transition, removing the interlayer antiferromagnetic coupling. The magnetism in $MnSb_4Te_7$ is increasingly 2D at low temperatures.

The charge-doped antiferromagnetic Mott insulator $La_{2-x}Ba_xCoO_4$ is a structural analogue of the high temperature cuprate superconductors, which have properties that are also sensitive to dopant concentration x. The cuprates show a signature hour-glass shaped spin wave spectrum, which has also been observed in other similar insulators and explained using a disordered charge stripe model. I studied this material through magnetometry, time-of-flight neutron spectroscopy and single crystal diffraction. I discovered that the magnetic order in $La_{2-x}Ba_xCoO_4$ is very short range with a correlation length of ≈ 15 Å and is described by the incommensurate propagation vector $\mathbf{q} = (0.5 \pm 0.23, 0.5 \pm 0.23)$ in the (h, h) plane for x = 0.5. The spin wave spectrum has the characteristic hour-glass shape of the cuprates. These results are in contrast to the equivalent Sr-doped compound $La_{1.5}Sr_{0.5}CoO_4$, which has long-range collinear magnetic order and does not feature the hour-glass.

Finally, the rare earth iron garnets are of prime interest for spintronic applications due to their very coherent, spin-polarised magnons. I present a study of the novel cobalt-doped rare earth iron garnet $Lu_3Co_{0.5}Si_{0.5}Fe_4O_{12}$, which utilised magnetometry and two different inelastic neutron scattering techniques. This material orders ferrimagnetically at $T_C \approx 480\,K$. Introducing cobalt generates a high degree of magnetocrystalline anisotropy in the system at low temperatures, comparable with the magnetic rare earths. However, at room temperature, $Lu_3Co_{0.5}Si_{0.5}Fe_4O_{12}$ is a soft magnet, similar to YIG and LuIG. This is an indication that the Co^{2+} moments are disordered by 300 K. The spin wave spectrum is gapped at low temperatures. The gap between the first acoustic and optical magnon modes is temperature-dependent and comparable with thermal energies at 300 K.

Popular science prologue

During the course of my PhD, I have studied the material properties of several crystals. What do they have in common? All of them are magnetic (in some way or another), and all of them are shiny black or grey in colour: some more silvery, some more smoky. But that's about it for shared interests; from a physics perspective, they are quite distinct in their electronic and magnetic properties. I refer to them as my dark materials, and this thesis is titled *Her Dark Materials*, a spin on Philip Pullman's *His Dark Materials* novels, which are set in Oxford too.

In *His Dark Materials*, Pullman's characters inhabit and travel to numerous parallel worlds. The physics of the worlds is universal, but not all characters can see this to begin with. In the books, the fate of the universe actually depends on a certain property of amber being discovered by a physicist. While I will not claim the fate of our universe depends on my dark materials and the physics in this thesis, I have nevertheless learned a lot about what's going on between the atoms of these crystals. I haven't built a device that does something (like *The Amber Spyglass*) but I have mapped the magnetism of these crystals in the 'parallel world' of reciprocal space using *The Subtle Knife* of neutron scattering. Understanding the electronic and magnetic interactions at this level can inform the design of quantum materials for applications in information storage and energy-efficient electronics.

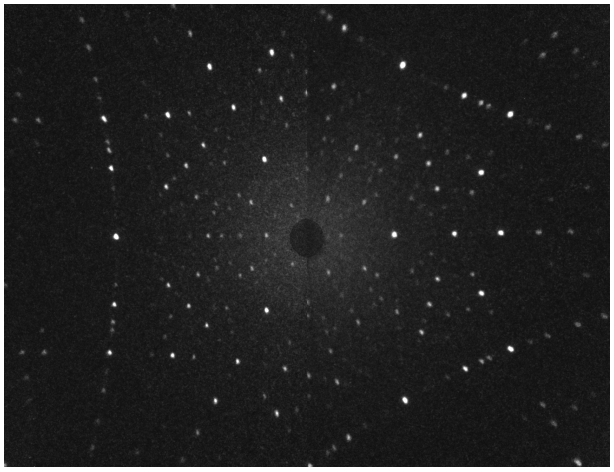

A pattern of sparkles from a crystal scattering neutron particles

Acknowledgements

First of all, I would like to thank my supervisor Andrew Boothroyd. I have learned a lot of physics from Andrew, who is also a champion tea drinker. Nothing really phases Andrew; his favourite animal is the sloth. When I reflect on Andrew's supervision style, this quote (which is actually about training horses) comes to mind:

> *Ask often, be content of little, reward always*
> – NUNO OLIVEIRA.

Thanks Andrew for your kind guidance and your eternal enthusiasm for experimental physics, especially neutrons and quirky quantum materials. It has been a privilege to be your student.

By doing condensed matter physics across university laboratories and central facilities, I have worked with a large number of great people. Thankyou to:

- Dharmalingam Prabhakaran, Guo Yan-Feng, and Su Hao, who synthesised with the fabulous samples I studied;
- everyone in the He supply chain, whether for neutron detectors or cryostats;
- Helen Walker, Christian Balz, Ross Stewart, Duc Le, from ISIS;
- Anne Stunault, Bachir Ouladdiaf, Andrea Piovano, Ketty Beauvois, Frédéric Boudarot, Jose Alberto Rodríguez-Velamazán, Martin Böhm, Ursula Bengaard Hansen and Navid Qureshi (MAG2POL is a game-changer!) from the Institute Laue Langevin;
- Kirrily Rule, and Richard Mole from ANSTO. Also a shoutout to all my former colleagues at ANSTO, especially the radionuclide metrology, nuclear analysis and sample environment gangs, for turning me into an actual scientist from a very green ANU graduate!

I would particularly like to thank the excellent and patient post-docs for whom no question was too big or small, and no beam-time too exhausting: Vivi Peçanha-Antonio, Jian-Rui Soh, Marein Rahn, Henrik Jacobsen, Rebecca Scatena, Quanzheng Tao and Anuradha Vibhakar. Vivi especially, your mix of spin-wave skills, spectroscopy smarts, sarcasm, snack supply and Southern Hemisphere

superiority kept me sane and laughing. Your warmth radiated from Day 1 – unlike the radiators in our office[1]!

I am so grateful to Mohammed Cheddi and Jon Denton and the Clarendon Workshop team for outstanding technical support and good humour.

I want to highlight some amazing women who have been role models for me. Having done physics for more than ten years post-secondary school, the adage "if you can see it, you can be it" has never rung truer. It's definitely a thing that there are pockets of physics with a stronger history of participation and progress made by women. Condensed matter physics, particularly the scattering community, is one such area. So I want to write down for the record some heroines of mine: Dorothy Crowfoot-Hodgkin (a Somerville alumna), Kathleen Lonsdale, P. Jane Brown, Mildred Dresselhaus and Margeret Elcombe. Closer to home, the friendship and encouragement I have received from Jodie Bradby, Helen Maynard-Casely, Vivi Peçanha-Antonio and Leonie Woodland inspires me to walk a little taller (and to grumble, laugh and try again!). At the moment, physics is still mostly done by straight cisgender men from the OECD. Here's to a more inclusive future! A supportive culture enables more people to overcome obstacles and challenges [1], and we are all a part of that.

At this point in my education, it is impossible to look back without being filled with an attitude of gratitude. Thankyou to my physics teacher at high school, John Daniel, and to the wonderful people – especially Alix and Matt Verdon – I met through the (crazy) Physics Olympiad program, which steered me through my last year of school, through undergrad and beyond. My colleagues in the teaching laboratories have reminded me of how complicated and fun experiments can be: thanks for keeping me grounded, Jenny Barnes, Rich Gardner, Richard George, Liana Warren, and Jonathan Rogers!

The Rhodes Scholarship has been a big part of my time here in Oxford, and I would not have been able to come here without it. Some of the soul-stirring and thought-provoking conversations I had at Rhodes House will stay with me forever, as will the camaraderie of 'physics friends' Hamza Waseem and Saru Bhattacharyya. The Oxford Gliding Club has been an even bigger part of my time in Oxford and not in my wildest dreams did I imagine I would finish my DPhil as a *licensed glider pilot*. Being a part of that awesome community has expanded my horizons in so many ways. Lastly I would not have gotten through the tough times in Oxford without Chris Ebbs, Paris Jaggers, Femke Vulto, and Rupert Stuart-Smith.

[1] That was Room 107 in the Clarendon Laboratory, for the record.

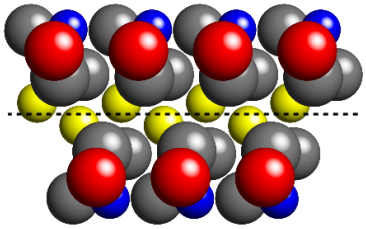

Glide plane (symmetry)

Glider plane (aircraft)

Figure 1: Glide plane (symmetry) = reflection combined with translation of a crystal motif. Source: [2]. Glider plane (aircraft) = a fixed-wing aircraft in free flight without an engine. Pilot: me. Photo credit: Adam Poultney.

Australian friends and family, I have missed you so much. My sisters Isla and Aithne and parents Deborah and Stephen most of all; your love from afar keeps me going. Especially my mum, who really set up the scaffolding for this whole Oxford adventure! This one's for you.

Finally thankyou to Matt Berrington for moving to the UK, for cooking a lot of tasty food, for being a sounding board for physics explanations, for providing numerous Python and experiment hacks, for being by my side during adventures in all weathers, and pushing me out of bed in the morning.

References

[1] G. Nehmeh and A. Kelly. "Women physicists and sociocognitive considerations in career choice and persistence". *Journal of Women and Minorities in Science and Engineering* 24.2 (2018). DOI: 10.1615/JWomenMinorScienEng.2017019867 (cited on page vi).

[2] J. K. Cockcroft, M. Attfield, P. Barnes, and H. Driessen. *Glide Symmetry*. URL: http://pd.chem.ucl.ac.uk/pdnn/symm1/glide1.htm (visited on 2023) (cited on page vii).

Table of Contents

Abstract **iii**

Popular science prologue **iv**

Acknowledgements **v**

List of Figures **xii**

List of Tables **xvii**

Symbols **xx**

List of Abbreviations **xxii**

1 Introduction **1**

1.1 Motivated by magnetism 1

1.2 More magnetism 4

1.2.1 Magnetic interactions 4

1.2.2 Which ions? 8

1.2.3 Phase transitions 8

1.3 Topological materials 9

1.3.1 Magnetic topological insulators 10

1.3.2 Topological semimetals 12

1.3.3 Magnetic topological materials 14

1.4 Thesis Outline 14

2 Experimental methods **17**

2.1 An introduction to scattering methods 17

2.1.1 Welcome to reciprocal space 17

2.1.2 Elastic scattering 18

2.1.3 Inelastic scattering . . . 19
2.1.4 The accounting of scattering probability: scattering cross-sections . . . 19
2.1.5 What to scatter? . . . 20
2.2 X-ray diffraction . . . 23
2.2.1 What: Thomson scattering . . . 24
2.2.2 How? . . . 25
2.3 Neutron diffraction . . . 27
2.3.1 What: nuclear diffraction . . . 28
2.3.2 What: magnetic diffraction . . . 29
2.3.3 How: single crystal diffraction . . . 31
2.3.4 What: polarised neutron diffraction . . . 33
2.3.5 How: polarised neutron diffraction . . . 34
2.4 Inelastic neutron scattering . . . 35
2.4.1 What: spin-wave spectroscopy . . . 35
2.4.2 How: triple-axis spectroscopy . . . 37
2.4.3 How: time-of-flight spectroscopy . . . 37
2.5 Samples . . . 39
2.6 Transport and magnetometry . . . 41
2.6.1 Magnetometry . . . 41
2.6.2 AC susceptibility . . . 43
2.6.3 Resistivity . . . 43
2.7 Other techniques . . . 44
2.7.1 Angle-resolved photoemission spectroscopy . . . 44
2.7.2 Quantum oscillations . . . 45
2.7.3 Scanning tunneling microscopy . . . 45
2.7.4 Muon spin relaxation . . . 45
2.8 Time scales of different experimental probes . . . 46

3 The magnetism of the topological semimetal $YbMnSb_2$ 49
3.1 Introduction . . . 49
3.1.1 The $AMnX_2$ family of quantum materials . . . 50
3.1.2 $YbMnSb_2$ . . . 53
3.2 $YbMnSb_2$ sample and initial characterisation . . . 55
3.2.1 X-ray diffraction . . . 56

3.2.2 Magnetometry . . . 57
3.2.3 Resistivity . . . 58
3.3 Single crystal neutron diffraction of $YbMnSb_2$ . . . 58
3.3.1 Method . . . 58
3.3.2 Description of data analysis . . . 59
3.3.3 Refinement results . . . 61
3.3.4 Magnetic space group . . . 63
3.3.5 Temperature dependence of reflections . . . 63
3.4 Half-polarised neutron diffraction of $YbMnSb_2$ . . . 65
3.4.1 Method . . . 65
3.4.2 Results . . . 66
3.5 Discussion of magnetic structure of $YbMnSb_2$ . . . 69
3.6 Inelastic neutron scattering of $YbMnSb_2$ . . . 72
3.6.1 Method . . . 72
3.6.2 Data analysis . . . 73
3.6.3 Results . . . 75
3.6.4 Discussion . . . 77
3.7 Conclusions regarding the magnetism of $YbMnSb_2$ . . . 82

4 The magnetic order of the topological semimetal $MnSb_4Te_7$ 93
4.1 Introduction . . . 93
4.1.1 Potential applications of $(MnX_2Y_4)(X_2Y_3)_m$ . . . 94
4.2 Quantum materials of interest . . . 94
4.2.1 $MnBi_2Te_4$ . . . 95
4.2.2 Sb-doped $MnBi_2Te_4$ / Bi-doped $MnSb_4Te_7$ . . . 100
4.2.3 $MnSb_2Se_4$ . . . 101
4.2.4 $MnSb_2Te_4$ . . . 102
4.2.5 $MnSb_4Te_7$ . . . 105
4.3 $MnSb_4Te_7$ samples and initial characterisation . . . 106
4.4 Single crystal neutron diffraction of $MnSb_4Te_7$ at ILL D10 . . . 108
4.4.1 Zero-field diffraction . . . 108
4.4.2 Magnetic structure analysis and results . . . 109
4.4.3 Temperature dependence of a magnetic peak . . . 114
4.4.4 Diffraction in a magnetic field . . . 114

4.4.5 Discussion . . . 115
4.5 Conclusion . . . 116

5 The spin disorder and hourglass excitation spectrum of the charge-doped cobalt oxide $La_{2-x}Ba_xCoO_4$ 121
5.1 Introduction . . . 121
5.1.1 Manifestations of charge and spin order . . . 122
5.1.2 The $La_{2-x}A_xMO_4$ family of materials . . . 125
5.1.3 $La_{2-x}Ba_xCoO_4$ . . . 131
5.2 A review of different models for magnetic excitations seen in cobalt oxides . . . 132
5.2.1 No hourglass: Heisenberg exchange and crystal field anisotropy model for x = 0 and x = 1/2 . . . 133
5.2.2 Emergence of the hourglass at intermediate doping (x = 1/3) . . . 137
5.2.3 Intermediate doping concentrations: a slightly stripy spin glass and a real-space modelling approach . . . 139
5.2.4 An alternative model for intermediate doping concentrations: nanoscale phase separation of undoped and checkerboard regions . . . 141
5.2.5 Summary of different magnetic excitation models . . . 142
5.3 $La_{2-x}Ba_xCoO_4$ samples and initial characterisation . . . 145
5.3.1 X-ray diffraction . . . 145
5.3.2 Magnetometry . . . 146
5.4 Single crystal neutron diffraction of $La_{2-x}Ba_xCoO_4$ on ILL D10 . . . 148
5.4.1 Method . . . 148
5.4.2 Analysis and results . . . 148
5.4.3 Discussion . . . 149
5.5 Single crystal time-of-flight spectroscopy of $La_{2-x}Ba_xCoO_4$ on ISIS MERLIN . . . 150
5.5.1 Analysis and results of MERLIN elastic line data . . . 153
5.5.2 Discussion of elastic scattering from MERLIN . . . 157
5.5.3 Analysis and results of inelastic scattering measurement . . . 158
5.5.4 Discussion of inelastic scattering from MERLIN . . . 158
5.6 Conclusions regarding the spin and charge order of $La_{2-x}Ba_xCoO_4$ . . . 161

6 The anisotropic magnetism of the cobalt-doped rare earth iron garnet $Lu_3Co_{0.5}Si_{0.5}Fe_4O_{12}$ 169
6.1 Introduction . . . 169
6.1.1 Rare earth iron garnets . . . 170

6.1.2 Doping of rare earth iron garnets . . . 171
6.1.3 Spin waves of rare earth iron garnets . . . 174
6.2 $Lu_3Fe_4Co_{0.5}Si_{0.5}O_{12}$ sample and initial characterisation . . . 178
6.2.1 Magnetisation measurements . . . 182
6.3 Inelastic neutron scattering of $Lu_3Fe_4Co_{0.5}Si_{0.5}O_{12}$ . . . 189
6.3.1 Method . . . 189
6.3.2 Data analysis . . . 191
6.3.3 Results . . . 191
6.3.4 Discussion . . . 201
6.4 Conclusion . . . 203

Conclusion **209**

List of Figures

1 Glide(r) planes vii

1.1 Electrons have intrinsic spin represented by the red arrow, meaning a single electron acts like a tiny magnetic dipole 1
1.2 Long-tailed tits in different 'magnetic' ground states. 2
1.3 Band structure of different topological materials. 10
1.4 The classical Hall effect 11
1.5 Topological insulators 13

2.1 The crystal structure: basis + lattice 18
2.2 Scattering triangle for elastic scattering. 19
2.3 The differential cross section 20
2.4 Sample mounted on a microloop. Grease holds it in place. 25
2.5 4-circle κ x-ray diffractometer 26
2.6 X-ray Laue backscattering camera 26
2.7 Laue backscattering. 27
2.8 Two experimental set-ups on the D10 instrument at the ILL. 32
2.9 D10 data visualisation 32
2.10 Set-up on D3 for half-polarised neutron diffraction 34
2.11 A triple-axis spectrometer 38
2.12 Time-of-flight spectroscopy 39
2.13 Flux growth method 40
2.14 Optical floating zone method 40
2.15 Magnetometry measurement 42
2.16 Resistivity measurement 44
2.17 The energy (time) and length scales of different physical phenomena 46
2.18 The energy (time) and length scales covered by different experimental methods . . . 47

3.1 Unit cell of $YbMnSb_2$ . . . 50
3.2 Sample of $YbMnSb_2$ crystals and x-ray Laue diffraction . . . 56
3.3 $YbMnSb_2$ XRD precession images . . . 57
3.4 Bulk magnetisation and resistivity for $YbMnSb_2$ . . . 58
3.5 Bulk field-dependent magnetisation for $YbMnSb_2$ with applied $\mu_0 H \parallel b$ axis. . . . 59
3.6 Plots showing calculated vs observed intensities of reflections from $YbMnSb_2$ D10 experiment . . . 62
3.7 Temperature dependence of structurally forbidden (100) reflection of $YbMnSb_2$ . . . 64
3.8 Description of D10 experiment for $YbMnSb_2$ and temperature dependence of (001) and (002) reflections . . . 65
3.9 D3 experiment on $YbMnSb_2$ . . . 67
3.10 Magnetic structure factors of $YbMnSb_2$ calculated from measured flipping ratios. . . 68
3.11 Magnetic structure factors of $YbMnSb_2$ calculated from measured flipping ratios as a function of Q . . . 69
3.12 Magnetisation density distribution in the unit cell of $YbMnSb_2$ . . . 70
3.13 magnetisation density contour map of $YbMnSb_2$ reconstructed from ILL D3 data. . . 70
3.14 *Ab initio* electronic dispersion of $YbMnSb_2$ along in-plane high symmetry directions 72
3.15 Delaunay triangulation plot for 18 meV $h0l$ plane data . . . 74
3.16 One dimensional cuts along $\mathbf{Q} = (10l)$, $\parallel (h00)$, and $\parallel (hh0)$ for varying ΔE from $YbMnSb_2$ IN8 experiment . . . 76
3.17 Spin-wave scattering and model for $h0l$ plane of $YbMnSb_2$. . . . 78
3.18 Spin wave data and model for hhl plane of $YbMnSb_2$. . . . 79
3.19 Spin-wave dispersion of $YbMnSb_2$. . . . 80
3.20 Magnetic unit cell and exchange paths of $YbMnSb_2$. . . . 80

4.1 Quintuple and septuple layers, $(MnBi_2Te_4)(Bi_2Te_3)_m$ structure . . . 96
4.2 Six septuple layer $MnBi_2Te_4$ demonstrates characteristics of the axion insulator state at zero magnetic field, and the Chern insulator state at high magnetic field. . . . 97
4.3 $n \rightarrow p$ carrier transition and topological phase diagram of $Mn(Sb_xBi_{(1-x)})_2Te_4$ . . . 101
4.4 Layer-number dependent magnetism in $MnSb_2Te_4$ . . . 104
4.5 $MnSb_4Te_7$ x-ray diffraction, magnetometry and resistivity . . . 107
4.6 $MnSb_4Te_7$ magnetoresistance . . . 108
4.7 $MnSb_4Te_7$ neutron Laue . . . 109
4.8 Possible magnetic structures of $MnSb_4Te_7$ . . . 110

4.9 $MnSb_4Te_7$ magnetic structure refinement results . . . 113
4.10 $MnSb_4Te_7$ reflection intensity vs. temperature for a non-nuclear reflection (1 0 0.5). . 114
4.11 $MnSb_4Te_7$ reflection intensities vs. magnetic field for two different temperatures . . 115

5.1 An example of the crystal structure of the transition metal oxides such as cuprates, nickelates and cobaltates belonging to tetragonal space group $I4/mmm$ . . . 123
5.2 Charge order (CO) and spin order (SO) on a square lattice *ab* plane layer for materials such as the cobalt oxides with dopant concentration x . . . 124
5.3 Possible spin states of different Co ions in an octahedral crystal field. . . . 127
5.4 Phase diagram of Sr-doped cobaltates . . . 131
5.5 Three different approaches to modelling the excitation spectrum of $La_{2-x}Sr_xCoO_4$ . . 133
5.6 The magnetic structure and exchange interactions of La_2CoO_4 . . . 134
5.7 $La_{2-x}Sr_xCoO_4$, x = 1/2 magnetisation and inelastic neutron scattering data, charge/spin stripe and crystal field model . . . 136
5.8 Constant energy slices of the $La_{2-x}Sr_xCoO_4$, x = 1/3 excitation spectrum. . . . 138
5.9 Simulation of magnetic excitations of disordered stripes in $La_{2-x}Sr_xCoO_4$, x =1/3. . . 141
5.10 Influence of the exchange interaction parameter ratio J/J' . . . 141
5.11 Cartoon showing key features of magnetic excitation spectra for different models and doping concentrations of $La_{2-x}Sr_xCoO_4$ . . . 144
5.12 X-ray Laue diffraction pattern from $La_{2-x}Ba_xCoO_4$, x = 1/2 . . . 145
5.13 Magnetisation data for $La_{2-x}Ba_xCoO_4$ . . . 147
5.14 The unit cells of the structures proposed for $La_{2-x}Ba_xCoO_4$ . . . 149
5.15 Plots showing calculated vs observed intensities of reflections from D10 experiment on $La_{2-x}Ba_xCoO_4$, x = 1/3 and x = 1/2. . . . 150
5.16 Equivalent views of the structures proposed for $La_{2-x}Ba_xCoO_4$ . . . 151
5.17 Single crystal diffraction of $La_{2-x}Ba_xCoO_4$, x = 1/3, measured on D10 at the ILL. . . . 152
5.18 $La_{2-x}Ba_xCoO_4$, x = 1/2 MERLIN elastic line data with cuts showing magnetic order peaks . . . 154
5.19 $La_{2-x}Ba_xCoO_4$, x = 1/3 MERLIN elastic line data with cuts showing magnetic order peaks . . . 155
5.20 $La_{2-x}Ba_xCoO_4$, x = 1/2 and x = 1/3 MERLIN elastic line data with cuts showing charge order peaks . . . 156
5.21 Example constant energy slice of the $(h, k, 0)$ plane from inelastic neutron scattering of $La_{2-x}Ba_xCoO_4$, $x = 1/2$, with example $\mathbf{Q}$ cuts shown . . . 159

5.22 The (fuzzy) hourglass shape of the magnetic excitations of $La_{2-x}Ba_xCoO_4$, $x = 1/2$. 160
5.23 Key features of $La_{2-x}Ba_xCoO_4$, x = 1/2 excitations seen in constant energy slices . . . 161
5.24 Constant energy slices of $La_{2-x}Ba_xCoO_4$, x = 1/2 and x = 1/3 MERLIN data for low ΔE, together with LSWT fits . . . 162
5.25 $La_{2-x}Ba_xCoO_4$, x = 1/2, energy slices all the way up to $\Delta E = 60$ meV, with $E_i = 70.80$ meV . . . 164

6.1 Crystal structure of the rare earth iron garnets . . . 171
6.2 Exchange interactions in the rare earth iron garnets . . . 175
6.3 Different exchange path symmetries for nearest-octahedral-site neighbour interaction in rare earth iron garnet. . . . 176
6.4 Spin waves of YIG measured with inelastic neutron scattering . . . 177
6.5 Spin polarised magnons in ferrimagnetic rare earth iron garnet. . . . 178
6.6 The single crystal sample of LuCoSiIG used for inelastic neutron scattering measurements. . . . 179
6.7 LuCoSiIG XRD precession images . . . 180
6.8 Laue diffraction of LuCoSiIG . . . 181
6.9 Temperature dependence of magnetisation of $Lu_3Fe_4Co_{0.5}Si_{0.5}O_{12}$ from 15 K to 600 K 183
6.10 Temperature dependence of magnetisation of $Lu_3Fe_4Co_{0.5}Si_{0.5}O_{12}$ for different field strengths and directions . . . 184
6.11 Modified Curie-Weiss law fit of $Lu_3Fe_4Co_{0.5}Si_{0.5}O_{12}$ magnetisation data . . . 185
6.12 Field-dependent magnetisation of $Lu_3Fe_4Co_{0.5}Si_{0.5}O_{12}$ . . . 186
6.13 The real part of the AC susceptibility of $Lu_3Fe_4Co_{0.5}Si_{0.5}O_{12}$ . . . 189
6.14 The imaginary part of the AC susceptibility of $Lu_3Fe_4Co_{0.5}Si_{0.5}O_{12}$ . . . 190
6.15 Elastic line data from inelastic neutron scattering of LuCoSiIG at 1.9 K on ANSTO PELICAN, $h\,h\,l$ plane with $E_i = 14.9$ meV . . . 192
6.16 Elastic line data from inelastic neutron scattering of LuCoSiIG at 1.9 K on ANSTO PELICAN, $h\,h\,l$ plane with $E_i = 3.7$ meV . . . 192
6.17 PELICAN data showing spin wave dispersion of LuCoSiIG at a temperature of 1.9 K along $(h\,h\,0)$ . . . 193
6.18 TAIPAN constant energy, **Q** cut data showing spin wave dispersion of LuCoSiIG at a temperature of 6 K . . . 194
6.19 'Averaged spin' magnetic structure used for spin wave modelling of LuCoSiIG . . . 195
6.20 Spin wave dispersion for LuCoSiIG 'averaged spin' model along (hhh) and $(hh0)$. . 195

6.21 Cubic and rhombohedral unit cells 196
6.22 'Averaged spin' model in the cubic and rhombohedral unit cells 196
6.23 Low energy spin wave dispersion of LuCoSiIG 197
6.24 'Randomised' structure used for spin wave modelling of LuCoSiIG 197
6.25 Elastic line data from inelastic neutron scattering of LuCoSiIG at 250 K on ANSTO PELICAN, $h\,h\,l$ plane with E_i = 3.7 meV 198
6.26 PELICAN data showing spin wave dispersion of LuCoSiIG at a temperature of 250 K along $(h\,h\,0)$ direction with $E_i = 3.7$ meV. 199
6.27 TAIPAN data showing the decrease in the energy between the first acoustic and optical magnons of LuCoSiIG with temperature. 200
6.28 Temperature dependence of the energy gap between the first acoustic and optical magnons for LuCoSiIG, TbIG and YIG 203

List of Tables

2.1 Different neutron beams, their approximate energies, and moderator materials. . . . 22

3.1 Possible basis vectors given by MAG2POL for $\mathbf{q} = (0, 0, 0)$. . . . 60
3.2 Structural refinement parameters for $YbMnSb_2$ in the paramagnetic phase 61
3.3 Magnetic, structural and extinction parameters for $YbMnSb_2$ at 2 K 61
3.4 Magnetic space groups derived from space group $P4/nmm$ 64
3.5 Experimentally determined parameters for $A\mathrm{Mn}X_2$ 81
3.6 $A\mathrm{Mn}X_2$ materials overview 88

4.1 Exchange parameters for $MnBi_2Te_4$ and $MnSb_2Te_4$ 98
4.2 Structure parameters for $MnSb_2Te_4$ 102
4.3 Structure parameters for $MnSb_4Te_7$ 107
4.4 Possible basis vectors for irreps describing $MnSb_4Te_7$ magnetic structure given by MAG2POL 111
4.5 Structure refinement of $MnSb_4Te_7$ 113

5.1 Some examples of cobalt oxides and their properties 129
5.2 Fitted parameters of a modified Curie-Weiss law (Equation 5.6) for $La_{2-x}Ba_xCoO_4$ magnetisation data. . . . 147
5.3 Structure refinement for $La_{2-x}Ba_xCoO_4$, x =1/2 151
5.4 Structure refinement for $La_{2-x}Ba_xCoO_4$, x =1/3 152
5.5 Comparison of peaks seen in elastic line data for x = 1/2 and x = 1/3 $La_{2-x}Ba_xCoO_4$ crystals. . . . 157
5.6 Correlation lengths for $La_{2-x}A_xCoO_4$ 158
5.7 Spin wave model parameters for $La_{2-x}Sr_xCoO_4$ 162

6.1 Fitted parameters of a modified Curie-Weiss law (Equation 6.2) for $Lu_3Fe_4Co_{0.5}Si_{0.5}O_{12}$ magnetisation data. . . . 184
6.2 Magnetic hysteresis parameters for some REIG 187

6.3 Experimentally determined exchange parameters for some REIG. 202

Symbols

$\mathbf{l}$	lattice vectors
$\mathbf{a}_i$	primitive lattice vectors
λ	wavelength
$\mathbf{Q}$	scattering vector
$\mathbf{G}$	reciprocal lattice vectors
v_0	volume of primitive unit cell
v_m	volume of primitive magnetic unit cell
$\mathbf{k}_i$	initial momentum
$\mathbf{k}_f$	final momentum
$\phi = 2\theta$	scattering angle
μ_N	nuclear magneton
b	neutron scattering length
E	energy
p	momentum
$\frac{d\sigma}{d\Omega}$	differential scattering cross section
r_0	classical radius of the electron
f_A	atomic form factor
f_M	magnetic form factor
F_N	nuclear structure factor
$\mathbf{F}_M$	magnetic structure factor
$\mathbf{M}(\mathbf{r})$	magnetisation of the magnetic unit cell
$\rho(\mathbf{r})$	electron cloud density
$\underset{\sim}{\varepsilon}$	initial x-ray polarisation
$\underset{\sim}{\varepsilon}'$	final x-ray polarisation
N	number of unit cells in the crystal
N_m	number of magnetic unit cells in the crystal

γ_n	gyromagnetic factor of the neutron
μ_B	Bohr magneton
T_C	Curie temperature
T_N	Néel temperature
J_{ij}	Heisenberg exchange parameter
D	easy axis/plane anisotropy
S	spin spin
$\mathbf{q}$	magnetic structure propagation vector
χ	(DC) magnetic susceptibility
χ'	AC magnetic susceptibility, real component
χ''	AC magnetic susceptibility, imaginary component
M	magnetisation
M_S	saturated magnetisation
M_R	remanent magnetisation
H_C	coercive field/coercivity

List of Abbreviations

AFM ..... antiferromagnet(ic/ism)

ARPES ..... angle-resolved photoemission spectroscopy

CDW ..... charge density wave

CF/CEF ..... crystal field/crystal electric field

DSM ..... Dirac semimetal

EDX ..... energy-dispersive x-ray spectroscopy

FM ..... ferromagnet(ic/ism)

INS ..... inelastic neutron scattering

MFF ..... magnetic form factor

MPMS ..... magnetic properties measurement system

MSF ..... magnetic structure factor

nn ..... nearest neighbour

nnn ..... next-nearest neighbour

NSF ..... nuclear structure factor

PPMS ..... physical properties measurement system

QAHE ..... quantum anomalous Hall effect

REIG ..... rare earth iron garnet

REXS ..... resonant elastic x-ray scattering

SDW ..... spin density wave

SQUID ..... superconducting quantum interference device

STEM ..... scanning transmission electron microscope

STM ..... scanning tunneling microscope

TAS ..... triple axis spectroscopy/spectrometer

TI ..... topological insulator

TOF ..... time-of-flight

WSM ..... Weyl semimetal

XRD ..... x-ray diffraction

1

Introduction

1.1 Motivated by magnetism

All materials studied in this thesis are magnetic, yet I wouldn't describe them as 'magnets'. None of them would be suitable for use in everyday applications of Big Magnetism: fridge magnets, cassette tapes, compass needles, transformers. In the case of the compass needle, it is easy to see there is a macroscopic magnetic moment – a combined north pole /south pole (dipole) that aligns opposite to the north pole/south pole of the Earth. This originates from the electrons in the material. An electron e^- has a negative charge $e \approx 1.602 \times 10^{-19}$ C and an intrinsic angular momentum called *spin*, which means the electron can be considered as a tiny magnetic dipole (Figure 1.1). The electron can 'spin' in either direction, and we usually represent the spin direction with an arrow pointing up for 'anti-clockwise' and down for 'clockwise'.

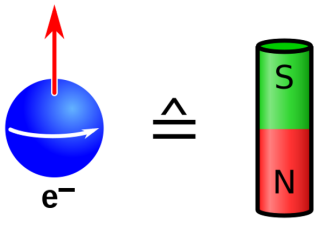

Figure 1.1: Electrons have intrinsic spin, meaning a single electron acts like a tiny magnetic dipole. In this diagram, the spin is represented by the red arrow. Figure from reference [1] under CC BY-SA 4.0.

Other subatomic particles can also have an intrinsic spin and a magnetic moment (e.g. atomic nuclei can be magnetic) but in this work I only consider magnetism originating from the electrons in the context of solid materials. There are an uncountable number of electrons in the world but

in solids, it is only the unpaired electrons that contribute to the magnetism. This is because the Pauli exclusion principle permits two electrons with opposing spins to pair up in the same energy state, effectively neutralising their contribution to the overall magnetic moment of the atom, so only the unpaired electrons count. Across a crystal made up of many atoms, the odd electrons can arrange themselves and their spins into a pattern – this is the *magnetic structure* of a material. The case where there is no pattern among the unpaired electron spins (random directions) is known as *paramagnetism*. The compass needle is made of a *ferromagnetic* material, with all unpaired electron spins pointing in the same direction, adding up to a large magnetic moment overall. In an *antiferromagnetic* material, the unpaired spin directions alternate in some regular way (we describe the repeating pattern in terms of a *magnetic unit cell*), meaning that the aggregate magnetic moment is zero. Hence you wouldn't refer to a block of antiferromagnetic material as a "magnet". A variation on antiferromagnetism is *ferrimagnetism*, where there isn't a balanced split between spins pointing one way and the other, so there is still an overall magnetic moment. In a diagram, these kinds of magnetic structures (and there are many more) are typically represented by patterns of arrows, but I've gone with birds instead in Figure 1.2.

a) ferromagnetic ↑↑↑↑↑↑↑↑ b) antiferromagnetic ↑↓↑↓ c) another antiferromagnetic order with a different unit cell ↑↑↑↑↓↓↓↓

Figure 1.2: Long-tailed tits in different 'magnetic' ground states. Picture credits: a) John Walters [2], b) reference [3] under CC BY-SA 4.0, c) Matthew Binns [4].

In this thesis, I will focus on four different materials that are all (a little bit) antiferromagnetic. The scientist who discovered antiferromagnetism, Louis Néel, famously said that antiferromagnetic materials are interesting but practically good for nothing (or words to that effect). In the fifty years since Néel was awarded his Nobel Prize (for discovering antiferromagnetism with neutron scattering), antiferromagnetic materials have displayed a wide array of physical phenomena and generated technological developments, far exceeding his expectations. Much of modern condensed matter physics investigates *emergent* or *collective* properties, which cannot be understood by considering one electron at a time and then adding them together (as I did to explain, roughly,

the magnetism of the compass). Furthermore, quantum mechanics[1] is essential to the 'many-body' physics of these strongly correlated electron systems, and so they have been given the moniker *quantum materials*. Material properties are influenced not just by which atoms/ions are included, but also the crystal structure and symmetry, the direction within the crystal (physicists' favourite word for direction-dependent anything is *anisotropy*), and temperature[2]. Several experiments in this thesis also consider the magnetic dynamics of these materials, i.e. how the spins are set in motion or 'excited' at different energies. The magnetic energy modes or *excitations* at low temperature in a well-ordered crystal are not random but are quantised in one way or another!

The materials I have studied are:

- **$YbMnSb_2$: a topological semimetal.** This material has very direction dependent electronic conduction properties, which are influenced by its magnetic structure.
- **$MnSb_4Te_7$: a topological insulator.** This material is part of a family of materials with very weak bonds between crystal planes (the *van der Waals materials*). The surface can have very different electronic properties to the bulk material, but you can't have a surface without the bulk! Similarly, electronic and magnetic phenomena are often two sides of the same coin.
- **$La_{2-x}Ba_xCoO_4$: a charge-doped antiferromagnetic Mott insulator**. It has magnetic energy modes that are similar to those seen in some superconductors, but is more disordered than most!
- **$Lu_3Co_{0.5}Si_{0.5}Fe_4O_{12}$: an anisotropic ferrimagnetic iron garnet**. The rare earth iron garnets have very coherent magnetic excitations, but here the Co^{2+} changes the degree of ferrimagnetism and anisotropy.

The remainder of this introduction will touch on some key concepts in the field of strongly correlated electron systems in slightly more technical parlance. § 1.2 discusses aspects of magnetism in more detail, while § 1.3 introduces topological materials. A lengthier material-specific introduction is found at the start of each relevant chapter.

[1] The very very short version of quantum mechanics is: firstly, particles can act like waves and vice versa, secondly, only certain combinations of energy and momentum are allowed (quantisation). For electrons in atoms in crystals, we talk of *quantum numbers*, which can only be integers e.g. $n = 1, 2, 3, \ldots$ for energy, l for angular momentum, and in special cases, half-integers. The spin of a single electron is $s = 1/2$.

[2] Without delving deeply into thermodynamics, temperature T plays the role of a natural energy scale $E = k_B T$, where k_B is the *Boltzmann constant* $\approx 1.381 \times 10^{-23}\,\mathrm{J\,K^{-1}}$. 'Room temperature' $\approx 300\,\mathrm{K}$. Quantum mechanical effects including magnetism, are stronger at low temperatures. To give a more classical example, iron is ferromagnetic, but heat it up to 770°C (= 1043 K) and it is no longer magnetic but still a solid.

1.2 More magnetism

The fact of the matter is, everything is a little bit magnetic, even this hapless frog (link to levitating diamagnetic frog video [5]). For a good overview of different kinds of magnetism and how these can play out in real materials, see reference [6].

1.2.1 Magnetic interactions

The four fundamental forces of nature are: the gravitational force, the electromagnetic force, the strong and weak nuclear forces. The range of the electromagnetic force is infinite and so an exact model of magnetism requires all electromagnetic particles to be considered. It is totally impractical to build up a model of magnetism in condensed matter from the electromagnetic force up. Hence we describe *effective interactions* between magnetic moments to generate useful models of magnetic materials. These interactions stem from the electromagnetic force but are strongly influenced by the symmetries[3] present in the electronic / crystal environment and quantum mechanical constraints such as the Pauli exclusion principle. In this way, magnetic models are frequently coupled to the electronic and orbital structure in a the material. Here I present the cast of magnetic interactions discussed in this thesis in a succinct, mostly non-mathematical way.

Exchange interaction

The *exchange interaction* describes how magnetic moments prefer to align (ferromagnetic exchange) or anti-align (antiferromagnetic exchange) with their neighbours. The exchange interaction is really the main character in this thesis. The name comes from the fundamental symmetry governing the exchange (swapping places) of electrons in a material[4]. Roughly speaking, electrons with the same spin ($\uparrow\uparrow$) occupy different energy states (by the Pauli exclusion principle) in one atom and are indistinguishable when exchanged. Since the electrons with the same spin are in different energy states (and so different places), then their energy due to the electrostatic force (Coulomb interaction) is lower. The converse is that electrons with different spins ($\downarrow\uparrow$) can be in the same energy state/place, but would experience stronger Coulomb repulsion. Hence the exchange interaction favours ferromagnetism (alignment of spins), but this competes with the difference in energy levels in the atom.

Taking a bigger picture, the exchange interaction also manifests between magnetic moments on

[3] The physics of crystalline solid materials involves a LOT of symmetries! In fact, every crystal belongs to one of the 230 *space groups*, each with its own list of mathematical operators that constrain structural symmetries. For an introduction, see reference [7, 8].

[4] Exchange interactions apply to all fermions and bosons but I only think about (some) electrons.

different atomic sites. There is no one general explanation for what happens, as the situation is pretty much unique for each material and made much more complicated by the changes in electronic band structure: are the unpaired electrons from two neighbouring ions independent? In an ionic bond? Hopping around? In an anti-bonding orbital? The end result can favour antiferromagnetism in many different forms, or ferromagnetism.

The Heisenberg model of exchange is defined by the following Hamiltonian term (Equation 1.1):

$$\mathcal{H}_{\text{exchange}} = \sum_{\langle ij \rangle} J_{ij}\, \mathbf{S}_i \cdot \mathbf{S}_j \tag{1.1}$$

where the sum is over pairs of spins $\mathbf{S}_i$ and $\mathbf{S}_j$, denoted $\langle ij \rangle$. The Heisenberg model is useful when the ions have a defined number of electrons and are spaced apart such that there isn't strong overlap between their orbitals. Generally, a specified number of 'neighbouring' spins are considered: nearest neighbours, next-nearest neighbours, and so on, each pair with their own J_{ij}. The J_{ij} can also be anisotropic (i.e. different in x, y, z), for example Equation 1.2:

$$\mathcal{H}_{\text{exchange}} = \sum_{\langle ij \rangle} J_{ij}^{x}\, S_i^x\, S_j^x + J_{ij}^{y}\, S_i^y\, S_j^y + J_{ij}^{z}\, S_i^z\, S_j^z\,. \tag{1.2}$$

The model can be extended qualitatively to consider interactions such as *superexchange*, where there is a non-magnetic ion acting as an exchange intermediary between two magnetic ions, and the Ruderman, Kittel, Kasuya and Yoshida *RKKY interaction*, where the exchange intermediaries are the conduction electrons in a metal.

Ising-like interaction

The *Ising model* looks like a simplified Heisenberg model. Instead of the spins having any angle between them, in the Ising model (Equation 1.3), all spins are along one axis and are represented by σ_i and $\sigma_j = \pm 1$ (rather than the spins being vectors $\mathbf{S}_i$ and $\mathbf{S}_j$ and calculating the dot product).

$$\mathcal{H}_{\text{Ising}} = \sum_{\langle ij \rangle} J_{ij}\, \sigma_i \sigma_j \tag{1.3}$$

For the Ising model to apply, there is usually a strong anisotropy or reduction of dimensionality in the system: magnetic moments may be practically confined to chains (1D) or planes (2D).

Anisotropy

The interactions above may have an "anisotropic" parameter as far as J_x, J_y, J_z go, but the interactions govern the degree of collinearity of neighbouring spins, rather than the absolute direction the spins prefer to point. This preferred spin orientation (and direction of the bulk magnetisation in ferromagnets and ferrimagnets) is governed by the magnetic anisotropy. Magnetic anisotropy can have a number of origins. For example, in ferromagnets, the shape of the sample can introduce anisotropy due to the demagnetisation effect strongly influencing the domain structure. Similarly, a material surface may have different anisotropy to the bulk material. However, in my work, the main anisotropy to consider comes from coupling of the crystal structure with the magnetism: *magnetocrystalline anisotropy*. Magnetic anisotropy is responsible for hysteresis in ferromagnets, and intertwined with phenomena such as magnetostriction, magnetoresistance and magnetoelasticity. Magnetocrystalline anisotropy, also called *single-ion anisotropy*, can stem from several different quantum interactions, several of which are discussed next.

In the context of a Hamiltonian, the energy associated with single-ion magnetic anisotropy is usually parametrised

$$\mathcal{H}_{\text{aniso}} = \sum_i (D\, S_i^z)^2 \tag{1.4}$$

where a negative D in Equation 1.4 denotes an easy-axis anisotropy along z (in coordinates where $\mathbf{D}$ is diagonal) and a positive D, easy-plane anisotropy (moments lie in the plane perpendicular to D). An effective magnetic field along the local z direction would have the same form as Equation 1.4. Since Equation 1.4 only involves one spin, it is not a spin-spin interaction, hence the moniker 'single-ion anisotropy' (also it comes about from picturing the crystal field environment of just a single ion).

Crystal field

The magnetic moment of an ion with unpaired electron(s) is made up of a contribution from the total spin quantum number S and also the total orbital angular momentum quantum number L, giving the total angular momentum quantum number $J = L + S$, and effective magnetic moment

$$\mu_{\text{eff}} = g_J \sqrt{J(J+1)}\, \mu_{\text{B}}, \tag{1.5}$$

where g_J is the *g factor*[5]. In the case where $L = 0$ and μ_{eff} is the *spin only moment*, this simplifies to $g = 2$. $S = 1/2 \times$ (number of unpaired electrons) is intuitive enough, but what about L? The *crystal field* (CF, or crystal electric field [CEF], also known as the *ligand field*) refers to the electric field surrounding the magnetic ion and can have a big effect on L. For some ions, e.g. high spin transition metal ions, the crystal field completely *quenches* the orbital angular momentum (meaning an electron cannot swap to another orbital of the same energy) and $L = 0$.

A little bit more about the crystal field... The range of the electromagnetic force is infinite so every ion in the crystal contributes somehow, but it is the contribution of the ions in local environment (i.e. ions that neighbour the magnetic ion) that is meant by the term crystal field. Simply put, the bonds and interactions responsible for the crystal structure will affect the shape of the orbitals with unpaired electrons in them, introducing splitting of otherwise degenerate L states and anisotropy. The electric field cannot really be modelled as a sum of point charges either, as the orbitals take up quite a bit of space on the length scale of the local ionic environment. The orbital ordering and energy gaps between different L_z states changes with temperature, which can drive temperature-dependent magnetic phenomena. At high temperatures, there is sufficient energy available for the unpaired electrons to bypass the crystal field constraints and realise their full orbital angular momentum potential! In this thesis, I don't present any crystal field calculations, but I do discuss the effects of the crystal field. One way of presenting the crystal field mathematically is via Stevens operators $O_q^{(k)}$, which are basically glorified total angular momentum operators[6], and associated coefficients B_q^k which depend on every single quantum number out there:

$$\mathcal{H}_{\text{CF}} = \sum_{k=0,2,4,6} \sum_{q=-k}^{k} B_q^k O_q^{(k)} \tag{1.6}$$

Spin-orbit coupling

The last interaction I will introduce here is the *spin-orbit interaction*, which ties in nicely with the crystal field discussion above. The spin-orbit interaction does what it says on the tin and couples L and S. One spin-orbit coupling (SOC) Hamiltonian term is

$$\mathcal{H}_{\text{SOC}} = \lambda \mathbf{L} \cdot \mathbf{S}. \tag{1.7}$$

[5]The g factor relates the intrinsic angular momentum of a particle to its magnetic moment. This is explained in more detail in the next chapter.

[6]You too, would be glorified, if you were an operator derived from tesseral harmonic functions.

When spin-orbit coupling is strong, L and S are not good quantum numbers and everything is spoken about in terms of J. There is a trend that SOC increases $\sim Z^4$, where Z is the atomic number.

1.2.2 Which ions?

The relative energy scales of the above interactions is determined by the magnetic ion and its crystal environment, which is always temperature-dependent. In this thesis, the magnetic ions in my materials are Mn^{2+}, Co^{2+} and Fe^{3+}. All of these are *transition metal ions* with incomplete $3d$ electron shells. Common features of these ions are that [9]:

- they have low or no orbital angular momentum ($L = 0$, e.g. Fe^{3+});
- magnetic ordering temperatures are high because unpaired electrons are split into different energy levels by the exchange interaction;
- there can be a high degree of overlap between $3d$ orbitals;
- in metallic materials, the unpaired electrons can be itinerant as the $3d$ shells are outermost.

In contrast, magnetic rare earth ions have incomplete $4f$ shells and

- large L and large SOC;
- smaller crystal field effects, because the $4f$ shells are well inside the ionic radius and so shielded from the crystal field by shells further out;
- lower ordering temperatures;
- large magnetic moments, which are strongly localised.

These are some general trends and naturally, there are exceptions (but not really in this particular thesis).

1.2.3 Phase transitions

This section does not aim to (re)introduce statistical mechanics or thermodynamics but simply highlight the fact that condensed matter physicists get excited about phase transitions when a solid material turns into another (magnetic) version of the same solid material! A *magnetic ordering transition* in a crystalline solid can be described by Landau's theory of continuous (i.e. no latent heat involved) phase transitions [7]. The key takeaways are:

- some sort of symmetry is broken during the phase transition as the temperature reduces;
- the new lower symmetry must be a subgroup of the old higher symmetry;

- there is an *order parameter*, some sort of physically measurable quantity, that grows from zero to non-zero at the ordering temperature;
- the order parameter continues to increase as the temperature decreases in a manner described by a *critical exponent*;
- the order parameter of the new phase must transform as an irreducible representation ("irrep") of the parent phase.

Given all of these constraints (and because symmetry of the crystal is involved, that's a LOT of constraints), magnetism enthusiasts look out for:

- Breaking of time-reversal symmetry due to ordering of the magnetic moments[7];
- An increase in magnetisation M for a ferromagnet;
  - This is shown to follow $M \propto |T - T_C|^{2\beta}$ for Curie temperature T_C and critical exponent β
- Or an increase in intensity of a Bragg peak forbidden by the non-magnetic structure for an antiferromagnet (more on this in the chapters ahead);
- Some kind of physically plausible magnetic structure that also agrees with the symmetry constraints imposed by the irreps of the parent crystal structure.

Examples of characterising magnetic order are given in this thesis. Additional examples appear in reference [10] and the group theory symmetry considerations are given a full treatment in references [7, 8]. A magnetic ordering transition may be accompanied by other changes in physical properties, such as a structural transition or in an electronic or thermal property. For example, a phase transition between a metallic state and an insulating state would show up in measurements of electrical resistivity.

Mentioning electronic properties of materials is a neat segue into the next section.

1.3 Topological materials

As the name suggests, a topological material has an electronic band structure that is topologically non-trivial[8]. Two kinds of topological materials are shown in Figure 1.3: topological semimetals

[7] Going back to the idea of spin = intrinsic angular momentum: if you run time backwards, your electrons "rotate" the other way and the direction of spin changes! This means time-reversal symmetry is broken for all magnetic structures except the paramagnetic case. Obviously this is not an experiment we get to do in real life, but you get the idea.

[8] Topology is a branch of mathematics concerned with loops, knots and braids. That is to say electronic energy levels in a topological material have crossings in reciprocal space that cannot be removed by sliding the levels around each

and topological insulators. At first glance, the band structure of the topological insulator seems much the same as its trivial counterpart. However, the key feature lies in the fact that the former phase cannot be transformed into the latter without merging and separating the electronic bands in a topologically-significant way. Topological materials have excellent transport qualities due to the linear dispersion about the Fermi energy. For example, a topological insulator can transport charge on its surface, but not through its bulk (picture a chocolate bar wrapped in metal foil). Tuning the Fermi level as well as the band structure topology is a key driver of experimental work.

The study of topological materials has the potential to shed light on exotic transport phenomena, and to advance quantum computing. Experimental work to uncover new examples of topological materials is a booming area of physics. A key property of topological materials is that the states are topologically protected, i.e. it is difficult to transform a topological insulator into an ordinary insulator as this requires going through a topological phase transition (e.g. following the diagram in Figure 1.3 from right to left), in effect changing the "knots" in the electronic band structure. For this reason, topological materials may be a robust platform for quantum computation as they are relatively immune to background perturbations. Topological quasiparticles are the basis for the topological quantum computing architecture favoured by Microsoft.

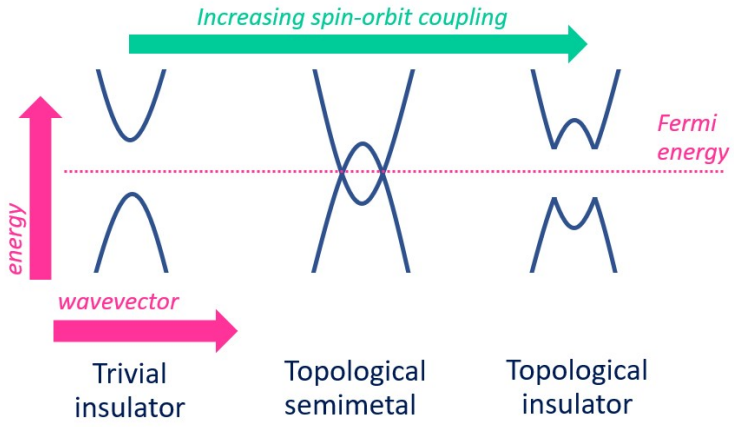

Figure 1.3: Band structure of different topological materials.

1.3.1 Magnetic topological insulators

Magnetic topological insulators combine atypical transport phenomena such as the Quantum Anomalous Hall Effect (QAHE) with magnetic order.

other in reciprocal space.

Quantum anomalous Hall effect

First of all, what is a Hall effect? All Hall effects work along the lines (pardon the pun) of: put a physical quantity along $\hat{\mathbf{x}}$, put another physical quantity along $\hat{\mathbf{z}}$ and then a third physical quantity is measured along or across the $\hat{\mathbf{y}}$ direction, where $\hat{\mathbf{x}}$, $\hat{\mathbf{y}}$ and $\hat{\mathbf{z}}$ are orthogonal axes. The original classical Hall effect has a current I_x flowing through a material along $\hat{\mathbf{x}}$ and a magnetic field $\mathbf{B}$ threading through the material along $\hat{\mathbf{z}}$. The resultant quantity in the $\hat{\mathbf{y}}$ direction is the Hall voltage V_{H}. This is depicted in Figure 1.4. The effect is most apparent in thin materials, where the material is approximately 2D in the xy plane.

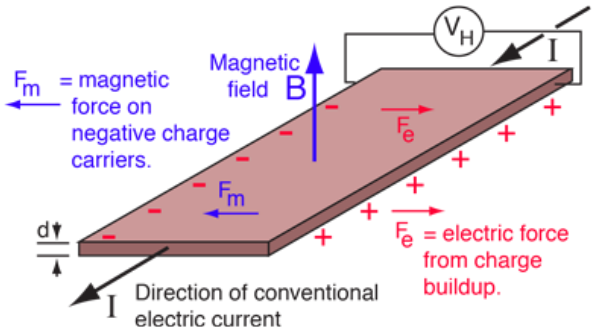

Figure 1.4: The classical Hall effect. Figure from reference [11], reproduced with permission of the author. Copyright Carl Rodney Nave.

The Hall voltage is given by

$$V_{\mathrm{H}} = \frac{I_x B}{n e d} \tag{1.8}$$

where n is the *charge carrier density* and d the thickness of the material as per Figure 1.4. 2D electronic systems, either as thin films or surfaces, also exhibit the *quantum Hall effect*, which is the quantisation of the Hall resistance (or its inverse, the Hall conductance σ_{xy}) in very high magnetic fields ($\sim 1\,\mathrm{T} - 10\,\mathrm{T}$) [12, 13]:

$$\begin{aligned} R_{xy} &= \frac{1}{\sigma_{xy}} = \frac{V_{\mathrm{H}}}{I_x} = \frac{h}{\nu e^2}, \\ \nu &= 1,\ 2,\ 3,\ 4,\ \ldots \quad \text{for the } \textit{integer} \text{ quantum Hall effect} \\ \nu &= \frac{1}{3}, \frac{2}{5}, \frac{3}{7}, \frac{2}{3}, \ldots \quad \text{for the } \textit{fractional} \text{ quantum Hall effect.} \end{aligned} \tag{1.9}$$

Furthermore, in the quantum Hall effect, the longitudinal resistance $R_x = V_x / I_x$ also vanishes! Note that unlike Equation 1.8, Equation 1.9 does not explicitly depend on any physical properties of the sample (the only degree of freedom is ν). This remarkable phenomenon was used in the redefinition of SI units in 2016 [14]. For more details of what physics ν reveals, see references [12, 13]. Now this brings us to the *quantum anomalous Hall effect* (QAHE). This is when the quantum Hall

effect is present, despite the lack of external magnetic field (very anomalous) [15]! Several seminal papers [16, 17] presented theoretical descriptions of the effect in terms of topological parameters such as Berry curvature and Chern number ($\mathbf{Z_2}$ topological invariant, some kind of "topological charge" that is quantised).

The phase diagram for these materials depends on such topological quantities. For example, reversing the magnetisation in a material displaying the QAHE changes σ_{xy} from $-e^2/h$ to e^2/h and the Chern number by two [15].

Chern insulators

Indeed, the quantum Hall effect occurs in *Chern insulators*, where chiral edge modes are responsible for the zero longitudinal resistance and finite Hall resistance. This is shown in the diagram in Figure 1.5. Here there is a cross-over between particle physics and condensed matter physics, as the relativistic Dirac equations describes quasiparticles associated with the chiral edge modes in topological insulator systems – a concept first proposed by Conyers Herring in 1937. A comprehensive review of the mathematical physics and experimental progress in realising the QAHE is given in reference [15], while a more pedagogical treatment of the theory behind many topological forms of matter is offered in reference [18].

Axion insulators

A variation on the topological insulator theme is the *axion insulator*. A Chern insulator under an external magnetic field H_C will reverse its magnetisation, swap the sign of its Hall conductance σ_{xy} and change its Chern number by two in one fell swoop. On the other hand, an axion insulator will undergo the same change in two steps, i.e. first change its Chern number by one and show a zero Hall conductance plateau. The "axion" name is borrowed from theoretical particle physics, where the electrodynamic description is the same as in these insulators, and the purported existence of axions may solve the strong charge parity problem. An axion insulator simultaneously breaks both time reversal and spatial inversion symmetries in the bulk, and there are magnetic structures that satisfy these requirements. For more details, see references [15, 18].

1.3.2 Topological semimetals

As with topological insulators, topological semimetals are defined by the topology of their Fermi surface / band structure. There are three main classifications of topological semimetal: Dirac, Weyl and nodal-line [20]. High energy particle physicists have been waiting a 'Weyl' to observe these

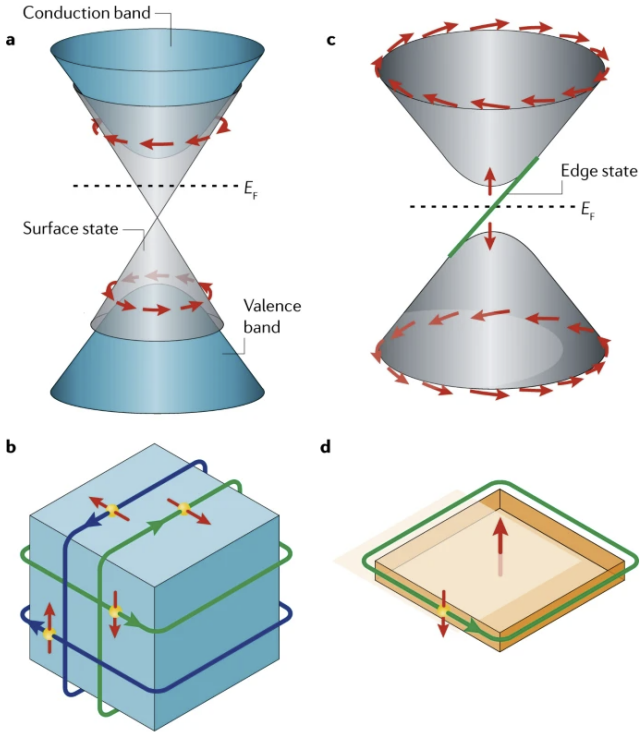

Figure 1.5: Topological insulators. Caption from [19]: "The massless Dirac-like dispersion of the surface state with spin–momentum locking in a topological insulator. The surface state band connects the bulk valence and the bulk conduction bands. b) Real-space picture of the surface state in a topological insulator. Electrons with spins pointing up and down (red arrows) move in opposite directions. c) The gapped Dirac-like dispersion of the surface state in a magnetic topological insulator. d) The chiral edge mode that appears in a magnetic topological insulator when the Fermi level, E_F, is located in the mass gap induced by the magnetic exchange interaction. The edge electrons conduct electricity without dissipation in one direction along the edge of the sample." Figure from reference [19], reproduced with permission from Springer Nature.

quasiparticle fermions – no Weyl fermion candidate has emerged from high energy particle physics experiments – so topological semimetals are also a promising testing ground for fundamental physics. Topological semimetals, unlike topological insulators, are gapless at the Fermi energy, meaning the quasiparticle charge carriers are massless.

Dirac semimetals

The hallmark of a Dirac semimetal is an intersection of four electronic bands at a point close to the Fermi energy, combined with linear dispersion close to this point [21]. This Dirac point is a robust, topologically significant feature on the Fermi surface. It also obeys the Dirac equation, hence the name of the associated quasiparticle is the *Dirac fermion*. If there is an energy gap between the Dirac cones, the semimetal is said to be *gapped* and will have a larger quasiparticle mass, tending towards being a topological insulator instead. Dirac nodes are protected by the 3D nature of the material, alongside time-reversal and inversion symmetries.

Weyl semimetals

Breaking one of these symmetries results in a Weyl semimetal [22]. A Weyl semimetal is distinguished by pairs of nodes where two electronic bands touch; partnered Weyl nodes have opposite chirality and are sources/sinks of Berry curvature [21]. The Fermi surface enclosing a Weyl point has a well-defined Chern number. *Weyl fermions* (quasiparticles corresponding to Weyl nodes) must occur in pairs in order to conserve this topological charge. Weyl semimetals established by broken time-reversal symmetry, i.e. magnetic order, are relatively uncommon in the literature [23]. Weyl semimetals exhibit Fermi arc surface states on their Fermi surface, which have been observed via angle-resolved photoemission spectroscopy (ARPES).

Weyl semimetals can be further divided into two types. Type I Weyl semimetals have dispersion cones that are locally symmetric in reciprocal space and do not intersect the Fermi level except at the nodes. In a Type II Weyl semimetal, the dispersion cones are tilted, breaking Lorentz invariance [24]. This is due to the intersection of electron and hole pockets in the Fermi surface, hence the cones intersect the Fermi level as well as the nodes.

Nodal line semimetals

A nodal line semimetal has doubly-degenerate bands intersecting along a 1D line in reciprocal space rather than at discrete points [22].

1.3.3 Magnetic topological materials

In summary, the influence of magnetism on topological states is yet to be fully understood, and the catalogue of magnetic topological semimetals and topological insulators is ever expanding. Magnetic topological materials also demonstrate *spin-momentum locking* (see Figure 1.5), which will be key in developing spintronic technologies relying on spin-polarised currents of electrons.

1.4 Thesis Outline

The remainder of this thesis is organised as follows:

Chapter 2 — introduces some basic tenets of crystallography and the experimental methods used in the work

Chapter 3 — presents a study of the magnetism of the topological semimetal $YbMnSb_2$

Chapter 4 — describes the magnetic structure of the topological semimetal $MnSb_4Te_7$

Chapter 5 — investigates the magnetic and charge order of $La_{2-x}Ba_xCoO_4$

Chapter 6 — showcases the spin waves and anisotropic magnetism of the doped rare earth iron garnet $Lu_3Co_{0.5}Si_{0.5}Fe_4O_{12}$

Chapter 7 — conclusion.

References

[1] MikeRun. *Electron spin classical model (symbols)*. URL: https://commons.wikimedia.org/wiki/File:Electron-spin-classical-model-symbols-simplified.svg (cited on page 1).

[2] J. Walters. *12 long-tailed tits*. URL: https://x.com/JWentomologist/status/937784216405803010 (cited on page 2).

[3] TSRL. *Long-tailed tits resting, mid-afternoon in energy saving anti-parallel paired formation in a willow*. URL: https://en.wikipedia.org/wiki/Long-tailed_tit#/media/File:Antipaired_LTTs.jpg (cited on page 2).

[4] M. Binns. *Even bigger assemblage of long tailed tits*. URL: https://tophilllow.blogspot.com/2011_06_01_archive.html (cited on page 2).

[5] G. McLeod. *levitating frog*. URL: https://www.youtube.com/watch?v=A1vyB-O5i6E (cited on page 4).

[6] R. Skomski. "Models of magnetic anisotropy". *Simple Models of Magnetism*. Ed. by R. Skomski. Oxford University Press, 2008. DOI: 10.1093/acprof:oso/9780198570752.003.0003 (cited on page 4).

[7] M. S. Dresselhaus, D. Dresselhaus, and A. Jorio. *Group Theory: Application to the Physics of Condensed Matter*. Springer-Verlag Berlin, 2007 (cited on pages 4, 8, 9).

[8] G. Burns and M. Glazer. *Space Groups for Solid State Scientists*. 3rd edition. Academic Press, 2013 (cited on pages 4, 9).

[9] A. T. Boothroyd. *Principles of Neutron Scattering from Condensed Matter*. Oxford University Press, 2020 (cited on page 8).

[10] F. Fernandez-Alonso and D. L. Price. *Neutron Scattering – Magnetic and Quantum Phenomena*. Vol. 48. Experimental Methods in the Physical Sciences. Academic Press, 2015 (cited on page 9).

[11] C. R. Nave. *Hall Effect*. URL: http://hyperphysics.phy-astr.gsu.edu/hbase/magnetic/Hall.html (cited on page 11).

[12] K. v. Klitzing. "Physics and Applications of the Quantum Hall Effect". *Physics and Applications of Quantum Wells and Superlattices*. Ed. by E. E. Mendez and K. von Klitzing. Boston, MA: Springer US, 1987. DOI: 10.1007/978-1-4684-5478-9_10 (cited on page 11).

[13] R. E. Prange and S. M. Girvin. *The Quantum Hall Effect*. Graduate Texts in Contemporary Physics. Springer, 1990 (cited on page 11).

[14] *26th meeting of the CGPM*. URL: https://www.bipm.org/en/committees/cg/cgpm/26-2018 (cited on page 11).

[15] C.-Z. Chang, C.-X. Liu, and A. H. MacDonald. "Colloquium: Quantum anomalous Hall effect". *Reviews of Modern Physics* 95.1 (2023). DOI: 10.1103/RevModPhys.95.011002 (cited on page 12).

[16] D. J. Thouless, M. Kohmoto, M. P. Nightingale, and M. den Nijs. "Quantized Hall Conductance in a Two-Dimensional Periodic Potential". *Physical Review Letters* 49.6 (1982). DOI: 10.1103/PhysRevLett.49.405 (cited on page 12).

[17] F. D. M. Haldane. "Model for a Quantum Hall Effect without Landau Levels: Condensed-Matter Realization of the "Parity Anomaly"". *Physical Review Letters* 61.18 (1988). DOI: 10.1103/PhysRevLett.61.2015 (cited on page 12).

[18] R. Moessner and J. E. Moore. *Topological Phases of Matter*. Cambridge University Press, 2021 (cited on page 12).

[19] Y. Tokura, K. Yasuda, and A. Tsukazaki. "Magnetic topological insulators". *Nature Reviews Physics* 1.2 (2019). DOI: 10.1038/s42254-018-0011-5 (cited on page 13).

[20] D. J. Fisher. *Topological Semimetals*. Materials Research Forum LLC, 2019 (cited on page 12).

[21] A. A. Burkov. "Topological semimetals". *Nature Materials* 15.11 (2016). DOI: 10.1038/nmat4788 (cited on pages 13, 14).

[22] N. P. Armitage, E. J. Mele, and A. Vishwanath. "Weyl and Dirac semimetals in three-dimensional solids". *Re-*

views of Modern Physics 90.1 (2018). DOI: 10.1103/RevModPhys.90.015001 (cited on page 14).

[23] J.-R. Soh, P. Manuel, N. M. B. Schröter, C. J. Yi, F. Orlandi, Y. G. Shi, D. Prabhakaran, and A. T. Boothroyd. "Magnetic and electronic structure of Dirac semimetal candidate $EuMnSb_2$". *Physical Review B* 100.17 (2019). DOI: 10.1103/PhysRevB.100.174406 (cited on page 14).

[24] A. A. Soluyanov, D. Gresch, Z. Wang, Q. Wu, M. Troyer, X. Dai, and B. A. Bernevig. "Type-II Weyl semimetals". *Nature* 527.7579 (2015). DOI: 10.1038/nature15768 (cited on page 14).

2

Experimental methods

Here I outline the experimental techniques I used to get the results presented in this thesis. I also give a nod to some other complementary methods that I personally did not use but appear in background literature. In the spirit of not letting maths get in the way of exciting physics experiments, I did not include all the equations, only the ones that help tell the story. Like many generations of grad students before me, I started by reading *Neutron Scattering: a primer*, by Roger Pynn [1]. For a more theoretically comprehensive, mathematically thorough – and thoroughly enjoyable – treatment of neutron scattering please read my supervisor's book [2] [1]. For a pleasantly paced introduction to scattering of both x-rays and neutrons, see [3].

2.1 An introduction to scattering methods

2.1.1 Welcome to reciprocal space

A crystalline solid consists of a repeating pattern of atoms extending in three dimensional *real space*. The *basis* defines which atoms make up the building block of the pattern, and the *lattice* defines how copies of this building block are repeated to create the crystal. The lattice is the array of points generated by

$$\mathbf{l} = n_1\mathbf{a}_1 + n_2\mathbf{a}_2 + n_3\mathbf{a}_3 \tag{2.1}$$

where n_1, n_2, n_3 are integers and $\mathbf{a}_1$, $\mathbf{a}_2$, $\mathbf{a}_3$ are the *primitive lattice vectors* needed to define a single unit cell.

An efficient way to define this periodicity mathematically is to consider a Fourier transform of the lattice in real space into *reciprocal space*: the *reciprocal lattice*. This is the array of points defined by

[1] I was not paid for this product placement.

the *reciprocal lattice vectors*

$$\mathbf{G} = m_1\mathbf{a}_1^* + m_2\mathbf{a}_2^* + m_3\mathbf{a}_3^* \tag{2.2}$$

$$\text{where } \mathbf{a}_1^* = \frac{2\pi}{v_0}\mathbf{a}_2 \times \mathbf{a}_3, \quad \mathbf{a}_2^* = \frac{2\pi}{v_0}\mathbf{a}_3 \times \mathbf{a}_1, \quad \mathbf{a}_3^* = \frac{2\pi}{v_0}\mathbf{a}_1 \times \mathbf{a}_2,$$

$$\text{and } v_0 = \text{ volume of primitive unit cell in real space } = \mathbf{a}_1 \cdot \mathbf{a}_2 \times \mathbf{a}_3.$$

With the right particle probe, a known initial momentum $\mathbf{k}_i$ and a detected final momentum $\mathbf{k}_f$, a scattering experiment will do the Fourier transform for you for free[2] (this is explained later in § 2.2.1).

2.1.2 Elastic scattering

The cornerstone of *elastic scattering* or *diffraction* (where the energy of the scattered particle is unchanged) is Bragg's law [3]:

$$n\lambda = 2d\sin\theta \tag{2.3}$$

where d is the spacing between lattice planes, n is an integer, and θ is the angle between the incident beam and the crystal plane. Bragg's law is powerful; however, it is a special case of a more general description of diffraction [2]. To stay versatile at this early stage, I will quickly introduce the famous scattering triangle defined by

$$\mathbf{Q} = \mathbf{k}_i - \mathbf{k}_f \tag{2.4}$$

where $\mathbf{Q}$ is the *scattering vector*, $\mathbf{k}_i$ is the initial momentum divided by the reduced Planck constant $\hbar$[4], and $\mathbf{k}_f$ is the final momentum divided by $\hbar$. This vector sum is shown in Figure 2.2. We note

[2] Terms and conditions apply, phase information not always included.

[3] The Bragg father-son team can be credited with kick-starting crystallography. Bragg Junior was an Australian with British heritage, like me.

[4] Hot tip: momentum $\mathbf{p}$ is $|\mathbf{p}| = 2\pi\hbar/\lambda$. This is de Broglie's equation, which is at the heart of wave-particle duality and quantum mechanics

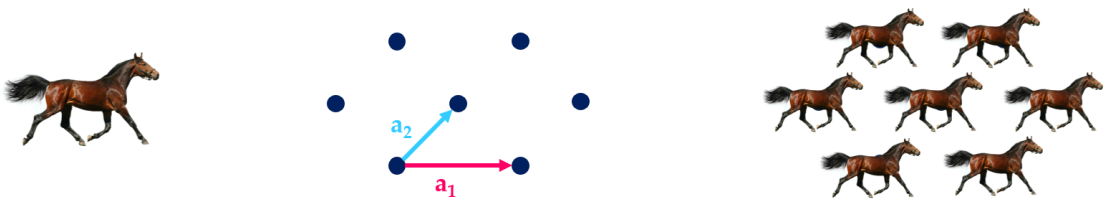

basis *lattice* *crystal structure*

Figure 2.1: Together, the basis and the lattice make up the crystal structure.

that for elastic scattering $k_i = k_f = k$ and

$$Q = |\mathbf{Q}| = 2k \sin\theta = \frac{4\pi \sin\theta}{\lambda}. \tag{2.5}$$

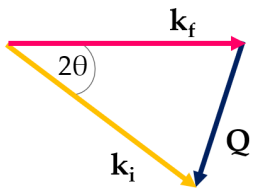

Figure 2.2: Scattering triangle for elastic scattering.

If the scattering vector $\mathbf{Q}$ equals a reciprocal lattice vector $\mathbf{G}$, and the condition of elastic scattering is imposed, Bragg's law is equivalent to Equation 2.4.

2.1.3 Inelastic scattering

A material may have some dynamics involving different atoms or larger particles, and scattered radiation can exchange energy with these processes too. This means we can also measure the energy distribution of a material in reciprocal space and link that to the crystal dynamics. This is discussed later in §2.4, but for now, note that *inelastic scattering* refers to energy loss or gain by the scattered radiation or particle. In general, inelastic scattering processes are much weaker than elastic scattering.

2.1.4 The accounting of scattering probability: scattering cross-sections

In order to keep track of everything being scattered, it is useful to define scattering cross-sections. The *total scattering cross-section* is the fraction of particles scattered by the target sample given an incident particle flux Φ_0 (of particles per unit area per second):

$$\sigma_s = \frac{\text{total number of particles scattered per second}}{\Phi_0}. \tag{2.6}$$

Of course, the particles may be scattered by the target in any direction. In fact, the distribution of scattered particles is very direction dependent! So defining a *differential cross-section* (Figure 2.3) is key to accounting for scattered particles:

$$\frac{d\sigma}{d\Omega} = \frac{\begin{array}{c}\text{number of particles scattered per second} \\ \text{into solid angle } d\Omega \text{ about a given direction}\end{array}}{\Phi_0 \times d\Omega}. \tag{2.7}$$

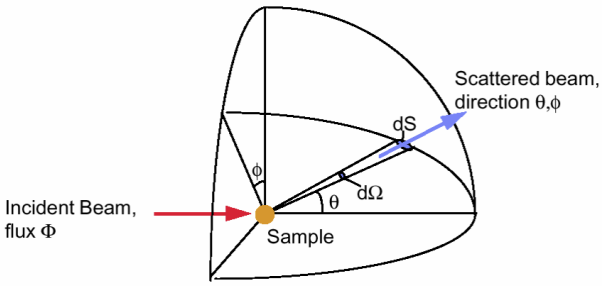

Figure 2.3: The differential cross section. Figure from source [4].

As mentioned above, it is possible that the energy, as well as the momentum, of a particle may change through the scattering process. Hence we use the *double differential scattering cross-section* to define both the energy and directional dependence of scattered particles:

$$\frac{d^2\sigma}{d\Omega\, dE_f} = \frac{\begin{array}{c}\text{number of particles scattered per second} \\ \text{into solid angle } d\Omega \text{ about a given direction} \\ \text{with final energy between } E_f \text{ and } E_f + dE_f\end{array}}{\Phi_0 \times d\Omega \times dE_f}\,. \tag{2.8}$$

The full equations relevant to specific types of radiation and this thesis are presented later.

2.1.5 What to scatter?

Many things can be scattered, but the most suitable choices for condensed matter experiments are often neutrons and x-rays. In this thesis, I will only analyse *coherent* scattering (where the scattering is **Q**-dependent due to correlation among all atoms in the solid, i.e. the structure of the sample and the average over all lattice points) rather than *incoherent* scattering (uniform in **Q** and a measure of self-correlation of atoms, i.e. the random variations in scattering amplitude on equivalent sites). This is discussed more in the next part on neutrons.

Neutrons

Neutrons are an excellent probe of "where atoms are" (§ 2.3) and "what atoms do "[5] (§ 2.4). The mass of a neutron places it in the sweet spot of being able to tune its momentum and energy to the range relevant to many particle processes in condensed matter systems. This thesis focuses entirely on inorganic crystalline solids, their magnetism and magnetic excitations, but neutrons can also probe liquids, thin films, and biological 'soft' condensed matter such as lipid bilayers.

[5]This is a quote from the press release for the 1994 Nobel Prize in Physics [5], awarded to Clifford G. Shull and Bertram N. Brockhouse for pioneering neutron scattering techniques.

Thanks to their lack of electric charge, neutrons primarily interact with atomic nuclei via the strong nuclear force. Given that the nucleus is very small ($\sim 10^{-15}$ m) compared to the overall size of an atom (~ 1 Å $= 10^{-10}$ m), and the strong nuclear force has a tiny length scale of influence ($\sim 10^{-15}$ m), most neutrons will in fact not interact with the first atom in their path – or even the first million atoms in their path. Instead neutrons are weak scatters that penetrate deeply ($\sim$cm) into 'most' solid materials and rarely interact with more than one nucleus. The weakness of neutron scattering signals necessitates large samples: on the order of 100 mg for diffraction and >1 g (being strategic, as large as possible) for inelastic scattering[6].

I say 'most' solid materials, because neutron scattering does depend on which specific nuclei are doing the scattering – or non-scattering and absorbing of the neutrons instead! Neutron scattering lengths b vary haphazardly across the periodic table (taking a weighted average neutron scattering length based on those for the isotopes for each element) and may be positive or negative. This variation in neutron scattering lengths can be a real advantage, because there can be a large contrast in scattering lengths between elements that are close in atomic number and size. Of course, some elements in their naturally-occurring isotopes are very strongly absorbing and therefore not ideal for a neutron scattering experiment (looking at you, gadolinium).

A neutron, being a spin-1/2 particle, has a small magnetic moment of $-1.91304273(45)\ \mu_N$ [6] [7]. This means neutrons can probe magnetism and the magnetic excitations (spin waves) of materials. Although neutrons can magnetically interact with nuclei, the spin-ordering of nuclei only happens at extremely low temperatures ($\sim$ mK). Instead, the main contribution to purely magnetic scattering comes from the neutron's spin interacting with the unpaired electrons that make ions magnetic. Hence, neutrons are a probe of the magnetic structure and dynamics of materials. This is discussed in detail in §2.3.2 and §2.4. Spin polarisation of neutron beams and its application to neutron diffraction is discussed in §2.3.4.

It is impossible to govern (unless dealing with isotopically pure elements[8]) which isotopes will end up where in a typical crystal synthesis. This leads to some natural randomness among lattice sites, which drives incoherent neutron scattering. The nuclear spin points in a random direction at practical temperatures, and its value is also isotope-dependent. Therefore, depending on the material, there may be a significant incoherent background in a neutron scattering experiment from both isotopic and nuclear spin effects. The good news is that this background is independent of **Q**

[6] Size is relative and some crystallographers manage to do great science with microscopic crumbs!

[7] $\mu_N = \dfrac{e\hbar}{2m_p}$, the nuclear magneton

[8] Expensive.

Table 2.1: Different neutron beams, their approximate energies, and moderator materials.

Neutron beam	Energy (meV)	Wavelength (Å)	Moderator	Temperature (K)
Cold	2	6.4	liquid H	25
Thermal	25	1.8	liquid water	300
Hot	200	0.6	graphite	2400

and so appears flat in scattering data, though it may compromise signal-to-noise.

Neutrons, left all alone, decay in about 10 minutes. You can't buy them off the shelf. So neutron scattering experiments must take place on site at a *neutron source* – either a nuclear research reactor (e.g. to be found at the Institut Laue Langevin [ILL] or the Australian Nuclear Science and Technology Organisation [ANSTO]) or a spallation source (such as ISIS). Nuclear research reactors produce continuous beams of neutrons via controlled nuclear fission of ^{235}U. At a spallation source, the production of neutrons starts with protons accelerated in a linear accelerator and then a synchrotron. This beam of protons is then pulsed (at ISIS, 50 Hz) and sent onto a heavy metal target, which undergoes spallation, generating a pulse of neutrons around 100 μs long. There is a distinct energy distribution for each method of neutron production: neutrons originating from the fission of ^{235}U have an average kinetic energy of 2 MeV, whereas spalled neutrons have an average kinetic energy of 20–30 MeV. These energies are too high for condensed matter scattering experiments[9]. Hence, neutrons thermalise in *moderators* (see Table 2.1 for a description of different neutron beams) before travelling through neutron guides to the various instruments. After moderation, the neutrons have an energy distribution à la Maxwell at the temperature of the moderator, so further energy selection of neutrons takes place at each instrument. At a research reactor, this is done with monochromator crystals. At a spallation source, the time for neutrons to thermalise is much shorter than the gap between individual pulses. Hence, a system of choppers is needed to alter the pulse shape and reduce harmonics etc.

X-rays

X-rays for use in condensed matter studies tend to have an energy in the range of 10–100 keV, and a corresponding wavelength of 0.1–1 Å. Again, this wavelength range is comparable to atomic spacings in solid materials, so x-ray diffraction is a useful structural probe. X-rays strongly interact with the electron cloud of an atom. The more electrons, the more scattering, so x-ray scattering amplitudes increase with atomic number, lacking the contrast between neighbouring elements that

[9] And for the research reactor case, too high to sustain the fission chain reaction.

you see in neutron scattering. However, the strong scattering means that much smaller sample sizes can be accommodated for an x-ray experiment. The optics for x-ray beams are also much more advanced and high resolution than for neutrons, meaning the x-ray beam can be focused on an area of $\sim$ 100 μm^2 rather than $\sim$ 1 cm^2! X-rays can be sensitive to different ionic species and orbital order, which neutrons can only probe indirectly via magnetic or structural distortion. X-rays are quickly attenuated in a solid material. The attenuation depends on angle of incidence, the material and the energy of the x-rays. A typical x-ray diffraction experiment might probe the material to a depth of only 10–100 μm. Hence a pristine surface is required if the results are also to give an indication of the properties of the bulk.

Unlike neutrons, x-rays are massless: the relationship between energy and momentum is linear ($E = pc$) rather than quadratic ($E = p^2/(2m)$) as for massive (non-relativistic!) particles. A small change in x-ray momentum leads to a tiny change in energy, and so inelastic x-ray scattering techniques cover a smaller range of energies than inelastic neutron scattering techniques.

Scattering from x-rays is generally considered to be coherent, as the electron clouds rarely vary from one lattice site to the next and x-ray scattering from the nuclei is negligible.

Lab-based instruments use x-rays generated from the collisions of accelerated electrons with a metal anode. This leads to large peaks in the x-ray spectrum at energies associated with specific transitions from the target metal, on a background of *bremsstrahlung*. The x-rays produced also depend on the voltage the electrons are accelerated through.

Synchrotron x-rays (not used for work in this thesis) produce x-rays by accelerating electrons to near the speed of light in a ring. The electrons then emit x-rays at a tangent to the ring as they experience an acceleration perpendicular to their path (bremsstrahlung). Polarisation analysis is also possible on synchrotron beamlines.

2.2 X-ray diffraction

Lab-based x-ray diffraction is useful for sample characterisation: to ascertain the crystalline quality of the sample, to check for twinning and other surprises. For further experiments on single crystals, it is important to know the directions of the crystal axes so the crystal can be aligned accordingly. X-ray diffraction can provide complementary structural information to a neutron diffraction experiment and may be the only practical option if the sample is small or strongly absorbs neutrons. It's also pretty fast these days, with Bragg peaks being measured in seconds, rather than minutes as for neutron diffraction.

2.2.1 What: Thomson scattering

The differential cross section for elastic x-ray scattering by a single fixed atom (Thomson scattering) is

$$\frac{d\sigma}{d\Omega} = r_0^2 \left| f_A(\mathbf{Q}) \right|^2 (\underset{\sim}{\varepsilon}'^* \cdot \underset{\sim}{\varepsilon})^2 \tag{2.9}$$

where $\underset{\sim}{\varepsilon}$ and $\underset{\sim}{\varepsilon}'$ are the initial and final polarisations of the x-ray beam, $r_0 = \mu_0 e^2/(4\pi m_\mathrm{e}) = 2.818 \times 10^{-15}$ m is the *classical radius of the electron*, and

$$f_A(\mathbf{Q}) = \int \exp(i\mathbf{Q} \cdot \mathbf{r})\, \rho(\mathbf{r})\, d\mathbf{r} \tag{2.10}$$

is the *atomic form factor*, which is the Fourier transform of the electron density of the electron cloud for that atom $\rho(\mathbf{r})$. For a lattice of points $\mathbf{l}$ decorated with a basis of atoms m, the differential cross-section for elastic x-ray scattering is:

$$\frac{d\sigma}{d\Omega} = r_0^2 \underbrace{\left| \sum_{\mathbf{l}} \exp(i\mathbf{Q} \cdot \mathbf{l}) \right|^2}_{\text{FT of lattice}} \underbrace{\left| \sum_{d} f_{A_d}(\mathbf{Q}) \exp(i\mathbf{Q} \cdot \mathbf{d}) \right|^2}_{\text{FT of basis}} (\underset{\sim}{\varepsilon}'^* \cdot \underset{\sim}{\varepsilon})^2. \tag{2.11}$$

where each atom in the basis has position $\mathbf{d}$ and atomic form factor F_{A_d}. This expression is essentially the amplitude squared of the product of two Fourier transforms, one for the lattice and one for the basis. This makes sense given that the crystal structure is the convolution of the lattice points with the basis of atoms (which is itself a convolution of the atomic positions of that basis and the electron clouds of those atoms). This is what I meant when I said scattering experiments do the Fourier transform for you, although I haven't exactly proven it. Note that this expression does only depend on the amplitudes of the Fourier components – the phase information has been lost. This is the *phase problem* of crystallography, which means (generally) we can only refine our best guesses of crystal structures rather than obtaining them directly by Fourier transforming the data. Depending on the arrangement of atoms within the basis given by vectors $\mathbf{d}$, the phase factor may lead to destructive interference and systematic absences of intensity at certain reflections. Combined with the reflection conditions associated with the lattice, this can enable the *space group* symmetry of the crystal to be determined.

In the case where the incident x-ray beam is unpolarised and the detector of the scattered beam is insensitive to polarisation, the term involving the incident polarisation $\underset{\sim}{\varepsilon}$ and the scattered

polarisation $\underset{\sim}{\varepsilon}'$ simply averages to the Thomson scattering expression

$$(\underset{\sim}{\varepsilon}'^{*} \cdot \underset{\sim}{\varepsilon})^2 = (1 + \cos^2\theta)/2. \tag{2.12}$$

2.2.2 How?

Here I briefly describe the two instruments I used for x-ray diffraction in the Clarendon Laboratory. The Agilent Supernova is a single crystal diffractometer with a molybdenum anode source (Mo $K_\alpha = 0.71$ Å) [7]. The crystal is lassooed with a microloop (Figure 2.4), which is then mounted on a four-circle κ geometry goniometer (Figure 2.5). The detector arm is on one circle of the goniometer, with the sample's orientation controlled by the other three circles. CrysAlisPro software controlled the goniometer and acquisition of images from the CCD area detector, ensuring full coverage of reciprocal space. The software can also do a fast refinement of the crystal structure based on the automatically identified peaks.

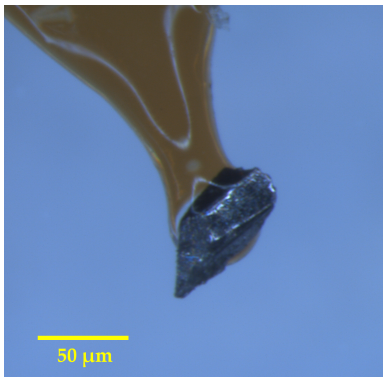

Figure 2.4: Sample mounted on a microloop. Grease holds it in place.

The x-ray Laue backscattering camera (Photonic Science) uses a 'white'[10] beam of x-rays (from a tungsten anode [11]) to access lots of reflections while keeping the detector fixed in backscattering geometry (Figure 2.6). Because so many peaks are seen in just one exposure, this is an ideal instrument for aligning larger samples: the aim is to see the symmetry first-hand. I think the raw images are stunning (see Figure 2.7 for some examples).

[10] Many wavelengths, akin to white light.

[11] As a heavy element, tungsten has a broad and high intensity spectrum of *bremsstrahlung* = "braking radiation" from the electrons slowing down

[12] No this material does not feature anywhere else in this thesis, but I spent a good two weeks of my life aligning these crystals, so these images deserve to be shown off.

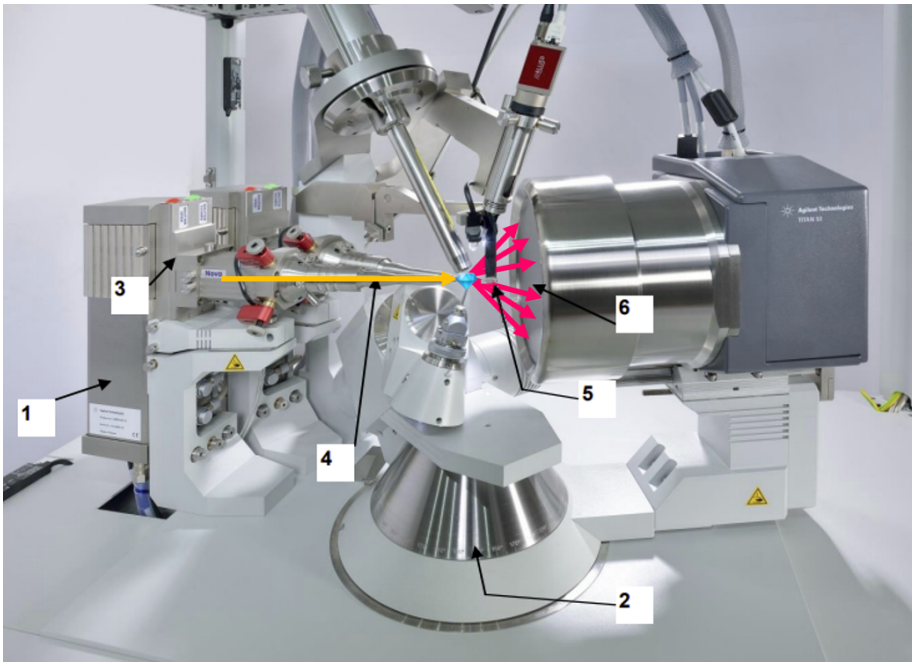

Figure 2.5: Agilent Supernova 4-circle κ x-ray diffractometer: incident x-rays represented by the orange arrow, scattered x-rays represented by the pink arrows, sample represented by the diamond emoji. Key parts of the diffractometer are labelled: 1) x-ray tube, 2) 4-circle κ goniometer [the κ just refers to the geometry], 3) x-ray shutter, 4) collimator, 5) beamstop, 6) beryllium window. The grey box on the right is the CCD detector. Figure adapted from source [7].

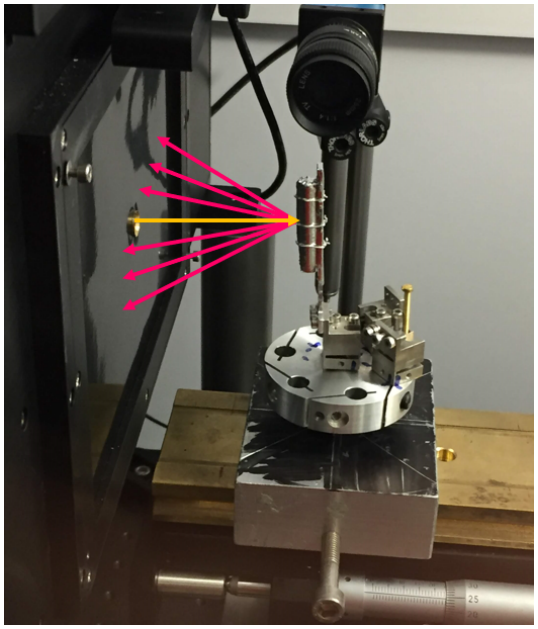

Figure 2.6: The x-ray Laue backscattering camera: incident x-rays represented by the orange arrow, backscattered x-rays represented by the pink arrows. The sample is wrapped in aluminium foil (a window was cut in the foil to so the x-rays could access the surface of the crystal).

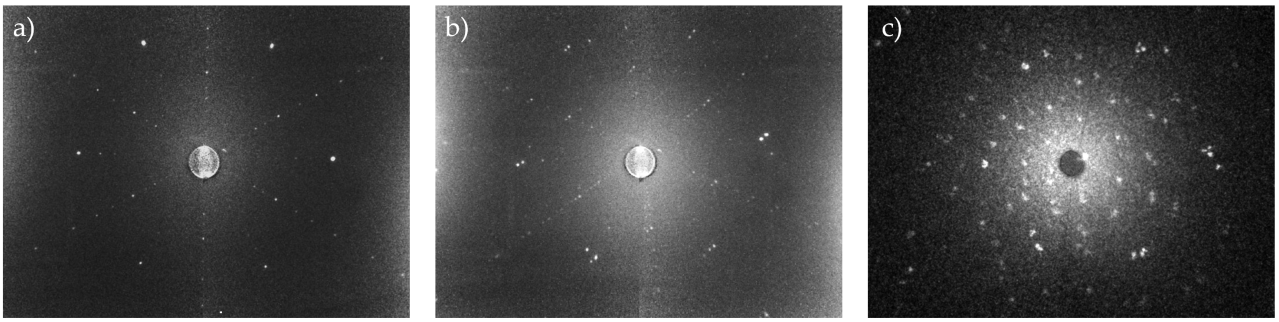

Figure 2.7: Laue backscattering of EuCuAs[12]. Behold the six-fold symmetry! a) A single exposure of a single crystal on the x-ray Laue backscattering camera. b) a composite image from the x-ray Laue backscattering camera of coaligned crystals on a single mount. Because the x-ray beam is so narrow (<1 mm), multiple exposures were taken, translating the mount between each so that the beam pointed at a different crystal. c) Neutron Laue backscattering image from ILL's OrientExpress instrument [8] of the same coaligned crystals. As the neutron beam is much wider (∼cm), the entire ensemble of crystals is exposed simultaneously. With b) and c), some 'mosaicity' of the ensemble is seen.

2.3 Neutron diffraction

Neutron diffraction features in some shape or form in every subsequent chapter of this thesis, so pay attention to this introduction to a fantastic experimental technique! Take the *interaction potential* $\tilde{V}(\mathbf{r})$ to describe all interactions the neutrons have with the sample in real space. It turns out that what we are really interested in is this potential in the case where the neutrons have incident and final momenta $\mathbf{k}_i$ and $\mathbf{k}_f$ respectively:

$$\begin{aligned} \langle \mathbf{k}_f | \, \tilde{V}(\mathbf{r}) \, | \mathbf{k}_i \rangle &= \int \exp(-i\mathbf{k}_f \cdot \mathbf{r}) \tilde{V}(\mathbf{r}) \exp(i\mathbf{k}_i \cdot \mathbf{r}) d^3\mathbf{r} \\ &= \int \exp(i\mathbf{Q} \cdot \mathbf{r}) \tilde{V}(\mathbf{r}) d^3\mathbf{r} \\ &= \mathcal{F}\left(\tilde{V}(\mathbf{r})\right)(\mathbf{Q}) \\ &= V(\mathbf{Q}), \end{aligned} \tag{2.13}$$

i.e. the interaction potential – in reciprocal space – as a function of $\mathbf{Q}$, the scattering vector. The interaction potential consists of a nuclear term $V_N(\mathbf{Q})$ and a magnetic term $V_M(\mathbf{Q})$ (and several other terms to do with electric fields, but these are miniscule):

$$V(\mathbf{Q}) = V_N(\mathbf{Q}) + V_M(\mathbf{Q}). \tag{2.14}$$

2.3.1 What: nuclear diffraction

Unlike x-ray scattering which depends on electron density rho(r), neutron scattering depends on the nuclear potential, which we treat as a delta function characterised by the neutron scattering length. The neutron scattering length is a measure of the strength and sign of the nuclear interaction potential experienced by scattered neutrons: positive indicates a repulsive pseudopotential[13]; negative, an attractive pseudopotential. To begin with, let us consider the elastic scattering of neutrons off a single nucleus. Typically, the number of protons, but not the number of neutrons (if there are different isotopes), for the nucleus is known, so the *average neutron scattering length* $\bar{b}$ for that element is assigned to the nucleus.

$$\begin{aligned} \tilde{V}_N(\mathbf{r}) &= \frac{2\pi\hbar^2}{m_n}\bar{b}\delta(\mathbf{r}) \\ V_N(\mathbf{Q}) &= \frac{2\pi\hbar^2}{m_n}\bar{b}\exp\left(i\mathbf{Q}\cdot\mathbf{r}\right) \end{aligned} \tag{2.15}$$

Of course, the actual nuclear interaction is not so simple, but in the far-field context of neutron diffraction, it will do fine. The total scattering cross-section and differential cross-section for elastic scattering off this lone nucleus are given by

$$\sigma_s = 4\pi\bar{b}^2, \quad \frac{d\sigma}{d\Omega} = \bar{b}^2. \tag{2.16}$$

Arrange many nuclei in a regular crystalline structure and the differential cross-section for coherent elastic scattering becomes:

$$\left(\frac{d\sigma}{d\Omega}\right)_{\text{coh}} = \Bigg|\underbrace{\sum_{\mathbf{l}}\exp\left(i\mathbf{Q}\cdot\mathbf{l}\right)}_{\text{FT of lattice}}\Bigg|^2 \left|F_N(\mathbf{Q})\right|^2. \tag{2.17}$$

$F_N(\mathbf{Q})$ is the *nuclear structure factor*, which is basically a Fourier transform of the scattering length density of the unit cell, multiplied by an exponential factor.

$$F_N(\mathbf{Q}) = \underbrace{\sum_{\mathbf{d}}\bar{b}_d\exp\left(i\mathbf{Q}\cdot\mathbf{d}\right)}_{\substack{\text{FT of basis of atoms } d \\ \text{weighted by } \bar{b}_d}} \underbrace{\exp\left(-W_d\right)}_{\substack{\text{Debye-Waller} \\ \text{factor}}} \tag{2.18}$$

The *Debye-Waller factor* is included to account for the fact that we are scattering off real, not perfectly rigid, crystals. There will be some random motion of individual nuclei that increases with

[13] Actually the nuclear potential is always attractive.

temperature, which means that neutrons scatter off a slightly diffuse object rather than a perfect point. The Debye-Waller factor depends on temperature, Q and the specific nucleus at site d, but for most occasions (low-ish temperature and low Q), $\exp(-W_d) \approx 1$.

The lattice vector sum below (left hand side of Equation 2.19) gives a total of N unit cells, and Bragg peaks whenever the Laue condition $\mathbf{Q} = \mathbf{G}$ is fulfilled:

$$\left| \sum_{\mathbf{l}} \exp(i\mathbf{Q} \cdot \mathbf{l}) \right|^2 = N \frac{(2\pi)^3}{v_0} \sum_{\mathbf{G}} \delta(\mathbf{Q} - \mathbf{G}). \tag{2.19}$$

Then the differential cross-section for coherent elastic neutron scattering off nuclei is

$$\left(\frac{d\sigma}{d\Omega} \right)_{\text{coh}} = N \frac{(2\pi)^3}{v_0} \sum_{\mathbf{G}} \left| F_N(\mathbf{G}) \right|^2 \delta(\mathbf{Q} - \mathbf{G}). \tag{2.20}$$

This result is similar to that for x-ray diffraction in that it depends on the squared amplitudes of Fourier transforms of both the lattice and the basis. Note that different systematic absences will exist for neutron and x-ray diffraction on the same material with the same wavelength due to the differences between the atomic form factor and the neutron scattering length.

2.3.2 What: magnetic diffraction

Magnetic neutron scattering is generally weaker than nuclear neutron scattering, due to the very small magnetic moment of the neutron. What makes magnetic neutron scattering at all feasible experimentally is that the range of the electromagnetic force partially compensates for the tiny magnetic moment of the neutron. The range of the electromagnetic force is much, much larger than that of the strong nuclear force! For polarised neutron scattering, there can be interference terms between nuclear and magnetic scattering, but for now, we consider the case of unpolarised neutrons where such cross terms are zero.

Neutron scattering is only sensitive to the components of the magnetisation $\mathbf{M}(\mathbf{r})$ that are perpendicular to $\mathbf{Q}$. It doesn't really matter as to the origin of the magnetisation, all that matters (for now) is that neutrons do not 'see' magnetisation parallel to the scattering vector. I will bash my way through this as quickly as possible. Let's consider the *magnetisation of the magnetic unit cell* $\mathbf{M}(\mathbf{r})$ as having a transverse (divergence-free) component $\mathbf{M}_\perp(\mathbf{r})$ and a longitudinal (curl-free[14]) component $\mathbf{M}_\parallel(\mathbf{r})$:

$$\mathbf{M}(\mathbf{r}) = \mathbf{M}_\perp(\mathbf{r}) + \mathbf{M}_\parallel(\mathbf{r}), \tag{2.21}$$

[14]Reminder: $\mathbf{B} = \mu_0(\mathbf{H} + \mathbf{M})$ and $\nabla \cdot \mathbf{B} = 0$, so $\nabla \cdot \mathbf{M} = -\nabla \cdot \mathbf{H}$ don't hate me

$$\nabla \cdot \mathbf{M}_{\perp}(\mathbf{r}) = 0, \quad \nabla \times \mathbf{M}_{\parallel}(\mathbf{r}) = 0. \tag{2.22}$$

If we consider one of Maxwell's equations

$$\nabla \cdot \mathbf{B} = 0, \tag{2.23}$$

the vector potential $\mathbf{A}$

$$\mathbf{B} = \nabla \times \mathbf{A}, \tag{2.24}$$

and the gauge transformation

$$\mathbf{A} \mapsto \mathbf{A} + \nabla f, \tag{2.25}$$

it is apparent that $\mathbf{M}_{\parallel}(\mathbf{r})$ corresponds to a gauge freedom ∇f and will not change $\mathbf{B}$. Hence, the magnetic field $\mathbf{B}$ that scatters the neutrons is only dependent on the transverse magnetisation $\mathbf{M}_{\perp}(\mathbf{r})$. In real space:

$$\mathbf{B}(\mathbf{r}) = \mu_0 \mathbf{M}_{\perp}(\mathbf{r}). \tag{2.26}$$

Now if we Fourier transform the magnetisation of the unit cell $\mathbf{M}(\mathbf{r})$ into reciprocal space (and multiply the result by $\gamma r_0/(2\mu_{\mathrm{B}})$, where $\gamma = |\mu_n/\mu_N| = 1.913$ is the *ratio of the neutron magnetic moment to the nuclear magneton*[15]), we get the *magnetic structure factor* (MSF) $\mathbf{F}_M(\mathbf{Q})$.

$$\mathcal{F}\left(\mathbf{M}(\mathbf{r})\right)(\mathbf{Q}) = \frac{2\mu_{\mathrm{B}}}{\gamma r_0}\mathbf{F}_M(\mathbf{Q}) \tag{2.27}$$

$$\mathbf{F}_M(\mathbf{Q}) = \mathbf{F}_{M_{\perp}}(\mathbf{Q}) + \mathbf{F}_{M_{\parallel}}(\mathbf{Q}) \tag{2.28}$$

The divergence of the transverse magnetisation still has to equal zero after being Fourier transformed as $\mathcal{F}\left(\nabla \cdot \mathbf{B}\right) = 0$:

$$\mathcal{F}\left(\nabla \cdot \mathbf{M}_{\perp}(\mathbf{r})\right)(\mathbf{Q}) = -i\frac{2\mu_{\mathrm{B}}}{\gamma r_0}\mathbf{Q} \cdot \mathbf{F}_{M_{\perp}}(\mathbf{Q}) = 0, \tag{2.29}$$

So $\mathbf{F}_{M_{\perp}}(\mathbf{Q})$ is perpendicular to $\mathbf{Q}$, and $\mathbf{F}_{M_{\parallel}}(\mathbf{Q})$ is parallel to $\mathbf{Q}$. By extension back to real space (stay with me!), $\mathbf{M}_{\perp}(\mathbf{r})$ must also be perpendicular to $\mathbf{Q}$. Combining Eqn. 2.29 with Eqns. 2.22, 2.23, and 2.25, we arrive at the keystone of magnetic diffraction: neutrons only probe the component of the magnetisation that is perpendicular to the scattering vector, $\mathbf{M}_{\perp}(\mathbf{r})$. It is also possible to arrive

[15] $\mu_n/\mu_N = -1.91304273(45)$ [6]. γ is not to be confused with the *gyromagnetic ratio* $\equiv$ magnetic moment/intrinsic (or 'spin') angular momentum, $\gamma_n = \frac{\mu_n}{I} = g_n\frac{\mu_N}{\hbar} = 1.832471 \times 10^8\,\mathrm{s^{-1}\,T^{-1}}$ [6]. $I = \frac{\hbar}{2}$ for a neutron. The *g-factor* of the neutron is the relevant dimensionless quantity $g_n = -3.82608545(90)$ [6] (so $g_n = -2\gamma$). Also, while we're here: $\mu_N = \frac{m_e}{m_p}\mu_{\mathrm{B}}$.

at this result from the bottom up, based on the contributions of an individual electron's spin and orbital magnetisation to the magnetic interaction potential.

The differential cross-section for magnetic elastic scattering is

$$\left(\frac{d\sigma}{d\Omega}\right)_{\text{mag.coh}} = N_m \frac{(2\pi)^3}{v_m} \sum_{\mathbf{G}_m} \left|\mathbf{F}_{M_\perp}(\mathbf{Q})\right|^2 \delta(\mathbf{Q} - \mathbf{G}_m) \tag{2.30}$$

where N_m is the number of magnetic unit cells, v_m is the volume of the magnetic unit cell, and $\mathbf{G}_m$ are the reciprocal magnetic lattice vectors. The equation for the MSF is

$$\mathbf{F}_M(\mathbf{Q}) = \frac{\gamma r_0}{2\mu_\text{B}} \sum_j f_{Mj}(\mathbf{Q})\, \boldsymbol{\mu}_j\, e^{i\mathbf{Q}\cdot\mathbf{r}_j}\, e^{-W_j(\mathbf{Q})} \tag{2.31}$$

$$\mathbf{F}_{M_\perp}(\mathbf{Q}) = \hat{\mathbf{Q}} \times \left(\mathbf{F}_M(\mathbf{Q}) \times \hat{\mathbf{Q}}\right) = \mathbf{F}_M - \left(\mathbf{F}_M \cdot \hat{\mathbf{Q}}\right) \hat{\mathbf{Q}} \tag{2.32}$$

for magnetic sites j located at $\mathbf{r}_j$ with moments $\boldsymbol{\mu}_j$. Here $f_{Mj}(\mathbf{Q})$ is the *magnetic form factor*. This is a Fourier transform of the spatial distribution of the unpaired electron responsible for the magnetism of site j. Since these electrons are usually outermost, the form factor is largest at low Q and tails off at high Q in a Gaussian-like way for an isotropic orbital. The term $e^{-W_j(\mathbf{Q})}$ is the Debye-Waller factor: given low temperatures (often needed to be in the magnetically ordered phase) and low Q (where magnetic scattering is largest), it is generally ok to take $e^{-W_j(\mathbf{Q})} \approx 1$.

2.3.3 How: single crystal diffraction

Here I will introduce some instruments (all at the ILL) that I utilised during my thesis for unpolarised neutron diffraction. Firstly, D10: a four-circle diffractometer that views monochromated thermal neutrons with an area detector (64 pixels × 64 pixels, 8 cm × 8 cm) [9]. It can be used in four-circle mode with the sample in a bottom-loading, constant-flow He cryostat on an Eulerian cradle and the detector on the fourth circle, or in two-circle mode with a larger sample environment such as a cryomagnet (Figure 2.8). A 3D peak in reciprocal space is built up taking 2D frames from the detector at regular intervals as the sample is rotated through an angle, see Figure 2.9. Each peak is modelled as an ellipsoid in reciprocal space, and then integration is performed over that ellipsoid to find the total peak intensity. The integrated intensity is also corrected for instrument geometry relative to the scattering angle (Lorentz correction). This is done using the ILL program RACER. The area detector is also useful for measuring diffuse or weak peaks that are not structural in origin.

ILL also has Laue diffractometers, which see a white neutron beam. The two I met were OrientEx-

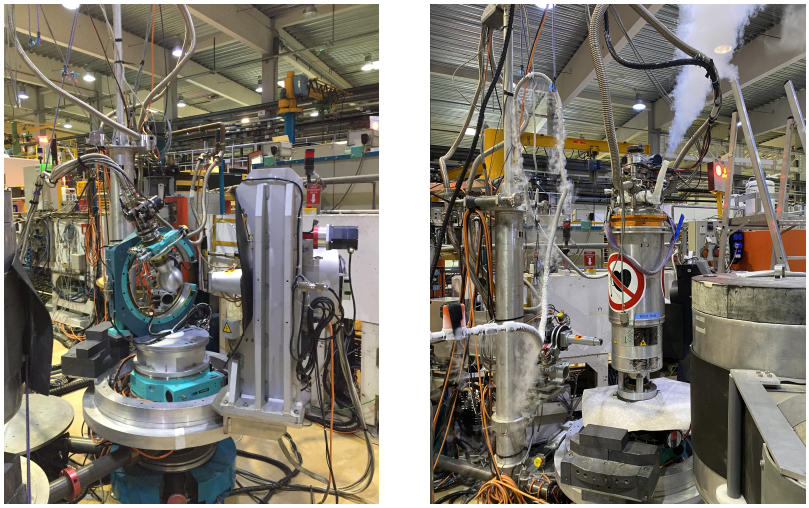

(a) Eulerian cradle **(b)** Vertical cryomagnet

Figure 2.8: Two experimental set-ups on the D10 instrument at the ILL.

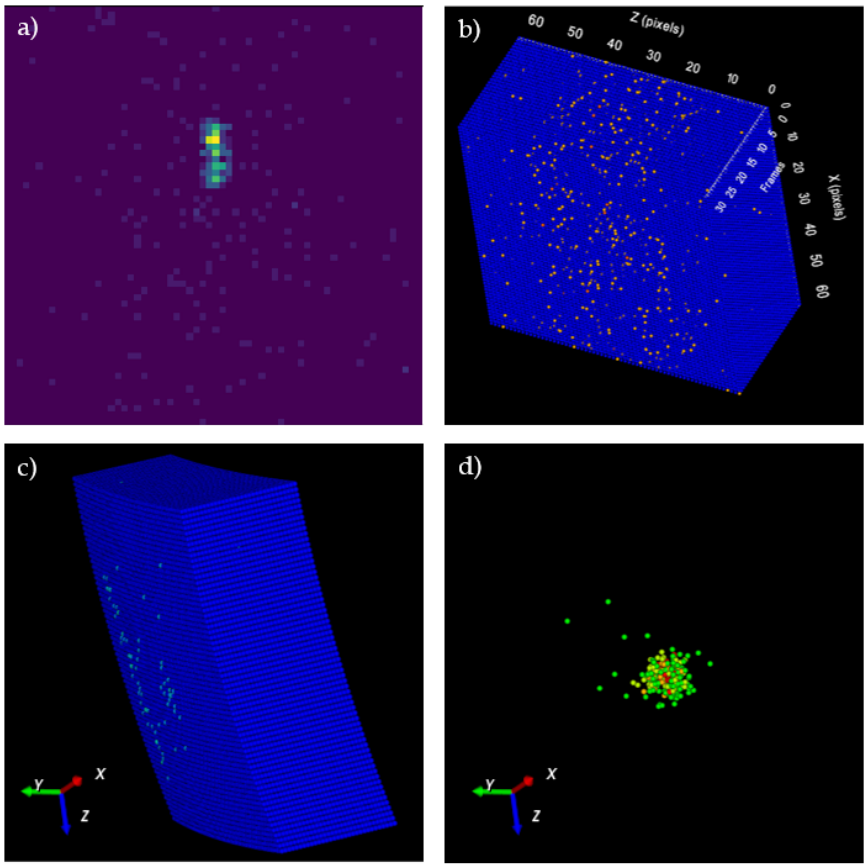

Figure 2.9: D10 data visualisation: a) a frame from the area detector at a specific sample orientation; b) one angle of the sample orientation is adjusted incrementally, building up a volume consisting of a stack of frames (here x and z are the axes of the detector and y is the sample orientation angle changed for each frame; c) the volume is transformed into reciprocal space co-ordinates; d) applying a noise threshold to the data in c) enables the peak to be visualised. This is what is modelled as an ellipsoid and integrated by RACER. 3D visualisation done using Int3D [10].

press and CYCLOPS. OrientExpress has a similar set-up to the x-ray Laue backscattering camera shown in Figure 2.6, but the detector is able to rotate through the scattering angle 2θ so it can be used in transmission geometry as well [8]. An example of raw data from OrientExpress is pictured in Figure 2.7 c). CYCLOPS has an array of very large area detectors arranged in an octagonal configuration around the sample to view a large range of 2θ at once [11].

2.3.4 What: polarised neutron diffraction

So far, all the neutrons we have met have been unpolarised, i.e. spins all akimbo, pointing in random directions. Now I introduce (spin-)polarised neutrons! Some scattering processes can flip the spin of a neutron: for example, magnetic moments perpendicular to the neutron spin result in spin-flipped scattering, but magnetic moments parallel to the neutron spin result in non-spin-flipped scattering. Also, interference terms between magnetic and nuclear scattering are non-zero when they occur at the same $\mathbf{Q}$ for polarised neutrons. In short, the information about the spin state of the neutron before and after scattering is very valuable and can even solve the phase problem. For more information about the benefits of polarising your neutrons[16], see reference [2]. The trade-off is that there is a substantial reduction in neutron flux for these experiments, which occurs through the polarisation process. For example, spin polarisation can be done with spin-polarised ^{3}He as a spin filter[17], and/or with a polarising crystal as a monochromator[18].

It is possible to analyse all components of polarisation before and after scattering, but this is complicated. Instead, longitudinal polarisation analysis considers polarisation $\mathbf{P}$ only along one axis. Here that is the z axis, the vertical axis in real space. For the half-polarised technique, the incident beam is polarised along z perpendicular to the propagation direction of the neutrons, but there is no polarisation analysis of the scattered neutrons. The ratio of scattered intensities at a Bragg peak from 'spin up' and 'spin down' incident beams is known as the *flipping ratio*, R. The general equation for R (see reference [2]) can be simplified under the following conditions:

- the magnetisation of the sample is parallel to the z axis such that $\mathbf{F}_M \parallel \hat{\mathbf{z}} \,\forall\, \mathbf{G}$ (you might have to make this happen with an applied magnetic field);
- and the crystal is centrosymmetric;

[16] I guess if you are having an MRI, your neutrons are a bit polarised!

[17] ^{3}He preferentially absorbs neutrons with spin antiparallel to the spin of the ^{3}He nucleus. If using polarised ^{3}He, a good achievement would be 80% polarised neutrons.

[18] With $\mathbf{M}_{\text{monochromator}} \perp \mathbf{Q}$, and $|F_N(\mathbf{Q})| = |F_M(\mathbf{Q})|$, the reflected neutrons will be polarised; the sign of the polarisation depends on the signs of the form factors. The polarised fraction is $P_f = \dfrac{2F_M(\mathbf{Q})F_N(\mathbf{Q})}{F_N(\mathbf{Q})^2 + F_M(\mathbf{Q})^2}$. Typical polarisation fractions for ILL's D3 are in the range ~80%–97% depending on filters used[12]

- and the beam is perfectly polarised along z

then [2]

$$
\begin{aligned}
R &= \frac{1 + (\beta^2 + 2\beta)\sin^2\alpha}{1 + (\beta^2 - 2\beta)\sin^2\alpha}, \\
\beta &= F_M / F_N, \\
\alpha &= \angle(\hat{\mathbf{z}}, \mathbf{G}).
\end{aligned}
\tag{2.33}
$$

In the case where scattering is only in the horizontal plane ($\mathbf{P} \perp \mathbf{G}$), and magnetic scattering is much weaker than nuclear scattering ($\beta \ll 1$), then further simplification gives $R \approx 1 + 4\beta$.

2.3.5 How: polarised neutron diffraction

The instrument I used for polarised neutron diffraction was D3 at ILL. D3 has high flux and is located on a neutron guide that views the 'hot' source (graphite moderator) [12]. The main distinguishing features of D3 from an unpolarised neutron diffractometer are that D3 uses a polarising monochromator, guide magnetic fields to keep the spins pointing a certain way, and 'cryoflippers' to reverse the spin direction. A schematic diagram of D3 in the half-polarised set-up is shown in Figure 2.10.

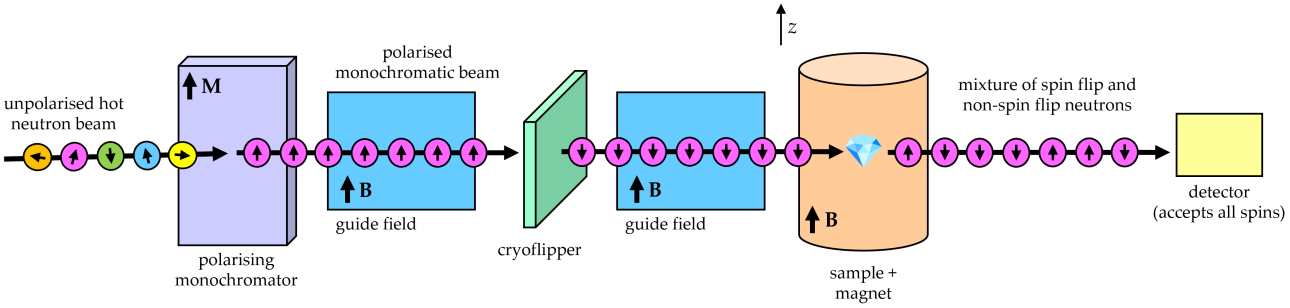

Figure 2.10: Set-up on D3 for half-polarised neutron diffraction. By activating the cryoflipper, the polarisation of the incident beam can be made spin up or spin down. Here, it's spin down. In order to calculate the flipping ratio, a spin up measurement also needs to be done for the same $\mathbf{Q}$.

If full longitudinal polarisation analysis is done, then there is a ^{3}He spin filter between the sample and the detector, so the detector only measures either spin up or spin down neutrons. For spherical polarimetry, it's even more sophisticated but I didn't do that, and won't go there now!

2.4 Inelastic neutron scattering

For inelastic scattering, $k_i \neq k_f$, so the scattering triangle is no longer isosceles; hence the expression for Q becomes

$$Q^2 = k_i^2 + k_f^2 - 2k_i k_f \cos(2\theta). \tag{2.34}$$

There are many processes that result in inelastic scattering and an *energy transfer* ($\Delta E = \hbar\omega$) from the neutrons to the sample (with initial state $|\lambda_i\rangle$ and final state $|\lambda_f\rangle$). We consider neutrons which start in the state $(\mathbf{k}_i, \sigma_i)$ and are scattered into the state $(\mathbf{k}_f, \sigma_f)$, where σ_i and σ_f are the initial and final spin polarisations respectively. The initial state $|\lambda_i\rangle$ of the sample will not be fixed but vary according to some (likely thermal) distribution, so we consider all possible transitions λ_i to λ_f, each with probability p_{λ_i}. The master equation for the double differential cross-section is:

$$\frac{d^2\sigma}{d\Omega\, dE_f} = \underbrace{\frac{k_f}{k_i}\left(\frac{m_n}{2\pi\hbar^2}\right)^2}_{\substack{\text{density of states} \\ \text{from FGR}/\Phi_0}} \underbrace{\sum_{\lambda_i} p_{\lambda_i}}_{\substack{\text{sum over} \\ \text{all } \lambda_i \\ \text{possible}}} \underbrace{\sum_{\lambda_f} \left| \langle\, \sigma_f \lambda_f \,|\, V(\mathbf{Q}) \,|\, \sigma_i \lambda_i \,\rangle \right|^2}_{\text{Fermi's Golden Rule (FGR)}} \underbrace{\delta(E_{\lambda_f} - E_{\lambda_i} - \hbar\omega)}_{\text{conservation of energy}}. \tag{2.35}$$

This contains all inelastic (and elastic) processes. Unless you are doing polarised inelastic neutron scattering, your data will contain signals from all of these, both nuclear and magnetic. Magnetic excitations can be isolated from the many scattering features by judiciously ignoring the elastic line and any signals that get stronger with increasing Q and increasing temperature (almost certainly these are phonons[19]). If these magnetic excitations are collective and quantised, they are also known as *spin waves* or *magnons*.

2.4.1 What: spin-wave spectroscopy

The double differential cross-section for magnetic neutron scattering is

$$\frac{d^2\sigma}{d\Omega\, dE_f} = \frac{k_f}{k_i}\left(\frac{\gamma r_0}{2\mu_B}\right)^2 S(\mathbf{Q}, \omega) \tag{2.36}$$

where $S(\mathbf{Q}, \omega)$ is the *scattering response function*, which is the component of the dynamic magnetic structure factor perpendicular to $\mathbf{Q}$. The interesting parts of Eqn. 2.35 are now all in $S(\mathbf{Q}, \omega)$. The scattering response function is, in turn, made up of the reduced partial response functions

[19] A phonon is a quantised, collective vibration of atoms in a material. In neutron scattering, this involves only the nuclear term in $V_N(\mathbf{Q})$.

$S_{\alpha\beta}(\mathbf{Q},\omega)$ (plus the magnetic form, and Debye-Waller factors that we have already met):

$$S(\mathbf{Q},\omega) = f_M^2(Q)\exp(-2W)\sum_{\alpha\beta}(\delta_{\alpha\beta} - \hat{Q}_\alpha\hat{Q}_\beta)\, S_{\alpha\beta}(\mathbf{Q},\omega). \tag{2.37}$$

The indices α and β refer to the three Cartesian axes, and $\hat{Q}_\alpha$ is the magnitude of the α component of the scattering unit vector. The $S_{\alpha\beta}(\mathbf{Q},\omega)$ are also known as the Fourier transform of *spin-spin correlation functions*, because the full expression entails breaking down the Fermi Golden Rule term of Equation 2.35 into the product of the creation of spin along the α direction from state λ_f to state λ_i and the annihilation of spin along the β direction from state λ_i to state λ_f. This kind of makes sense as a mathematical description of spins wobbling around and scattering neutrons from sample state $|\lambda_i\rangle$ to $|\lambda_f\rangle$ with an associated energy transfer ΔE. With z as the axis of quantisation (i.e. the direction along which the magnetic moments point in the ground state; the direction of the ordered spins) and a Holstein-Primakoff transformation mapping the raising and lowering operators to bosonic-like excitations (that's the spin-waves, more on this in [2]), the nine components of the spin-spin correlation can be determined:

- S_{zz} is elastic scattering, since S^z cannot change the $|\lambda\rangle$ of the sample (equivalently, it can't change the number of magnons).
- S_{xz}, S_{zx}, S_{yz} and S_{zy} are zero, because S^z does not change the number of magnons but S^x and S^y do, since they are composed of raising and lowering operators (again, see [2]);
- however, this also means S_{xx}, S_{yy}, S_{xy} and S_{yx} can all be non-zero for inelastic scattering.
- Together, $S_{xx} + S_{yy} + S_{xy} + S_{yx} = S_\perp(\mathbf{Q},\omega)$ in the case of spins aligned along the z axis in the ground state magnetic structure.

The full expression for the spin-spin correlation for magnons also enforces conservation of energy ($\Delta E = \pm\hbar\omega_{\mathbf{q}}$, for magnon dispersion $\hbar\omega_{\mathbf{q}}$, see the appendix for an example of magnon dispersion derived via linear spin wave theory) and conservation of momentum ($\mathbf{Q} = \mathbf{G} + \mathbf{q}$). Arriving at a full analytic expression for $S(\mathbf{Q},\omega)$ is longwinded in all contexts and impossible in some, but suffice to say, $S(\mathbf{Q},\omega)$ is essentially the dynamic magnetic structure factor. Convolve $S(\mathbf{Q},\omega)$ with the spin wave dispersion $\hbar\omega_{\mathbf{q}}$ (and the instrument resolution function), square the result, and you have the spin wave intensities measured by inelastic neutron scattering.

2.4.2 How: triple-axis spectroscopy

Triple-axis spectroscopy is the original neutron spectroscopy technique developed by Bertram Brockhouse in the 1950s. A triple-axis spectrometer is so named because it possesses three "axes":

1. the monochromator,
2. the sample, and
3. the analyser.

Bragg reflection of the white neutron beam from the monochromator crystal defines the incident momentum $\mathbf{k}_i$. Bragg reflection of the neutrons scattered from the sample from the analyser crystal defines the final momentum $\mathbf{k}_f$. The latter reflection also sends the neutrons with $\mathbf{k}_f$ into the detector. Spectrometer components rotate around the three axes, and in the case of the sample and analyser-detector, also translate. This allows the scattered intensities at a range of ΔE and $\mathbf{Q}$ to be sampled. A schematic diagram of a TAS is shown in Figure 2.11a). The scattering angle at the analyser crystal $2\theta_A$ is usually fixed, so that k_f is held constant, while k_i is varied. An example of a classic thermal TAS used in this thesis is TAIPAN at ANSTO [13]. Another TAS used in this thesis is IN8 at the ILL, which features the FLATCONE analyser-detector array [14]. The 31 analyser-detector pairs span 75° and effectively sample many nearby points in $\mathbf{Q}$ in parallel (see Figure 2.11). TAS instruments are found at reactor sources to make use of high constant flux near the reactor. Some advantages of this method are high $\mathbf{Q}$ and ΔE resolution, as well as the ability to collect data solely at interesting regions of $\mathbf{Q}$ space, meaning TAS instruments are ideal for parametric studies. The disadvantages are that it takes many long measurements to build up a big picture of reciprocal space, and inevitably, some regions of $\mathbf{Q}$ and ΔE are inaccessible due to the restrictions of the instrument geometry.

2.4.3 How: time-of-flight spectroscopy

Instead of using crystals to monochromate the white beam of neutrons, time-of-flight (TOF) spectrometers utilise a system of choppers, carefully timed, to block neutrons with unwanted energies. This is shown in Figure 2.12 a) and b). A direct geometry TOF spectrometer thus has neutrons with k_i incident on the sample. The sample sits in the middle of a cylindrical array of detectors, usually spanning over 180° in the horizontal plane and somewhat less in the vertical plane – an example is shown in Figure 2.12 c). The ΔE is measured by timing the neutrons with selected k_i from the final chopper to the detector. Not all scattering angles can be measured simultaneously. Some detectors may be masked by the sample environment, and there will be gaps between the

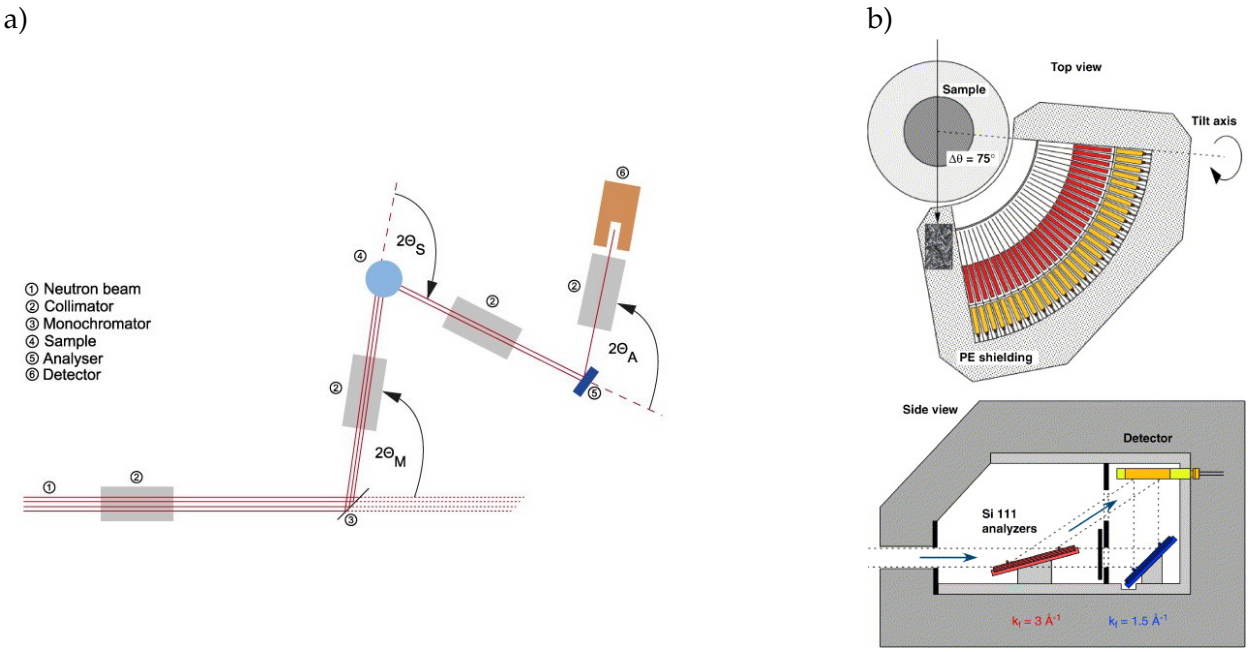

Figure 2.11: a) A schematic diagram of a triple-axis spectrometer, b) The FLATCONE array, consisting of 31 analyser-detector pairs spanning 75°, with two options for k_f across the whole array. Subfigure a) source [15]. Subfigure b) reprinted from reference [14], reproduced with permission from Elsevier.

detectors; however, rotating the sample about the cylindrical axis of the detector bank within the sample environment compensates for this. TOF instruments tend to have superior coverage of **Q** but inferior resolution of **Q** compared to TAS instruments. TOF data analysis inevitably involves integrating over a range of energies and momenta, but the ΔE resolution can be very fine, with narrow pulse widths and timing channels possible with many layers of precise choppers. Owing to the subtleties of chopper timing, TOF instruments usually operate at specific, discrete k_i, and are typically installed at spallation sources, where the neutron beam is already pulsed. However, there is a slight disadvantage for cold neutrons at a spallation source as the fast neutrons from the following pulse can make it through the open choppers as well - this necessitates more choppers, and a corresponding loss of flux. Two TOF spectrometers utilised in this thesis are PELICAN at ANSTO (cold neutrons, reactor source) [16], and MERLIN at ISIS (thermal neutrons, spallation source) [17]. The latter can operate in repetition-rate multiplication mode, which admits several k_i onto the sample at once [18]. The pulse rate of ISIS, combined with the sample-detector geometry, means that data can be distinguished according to k_i.

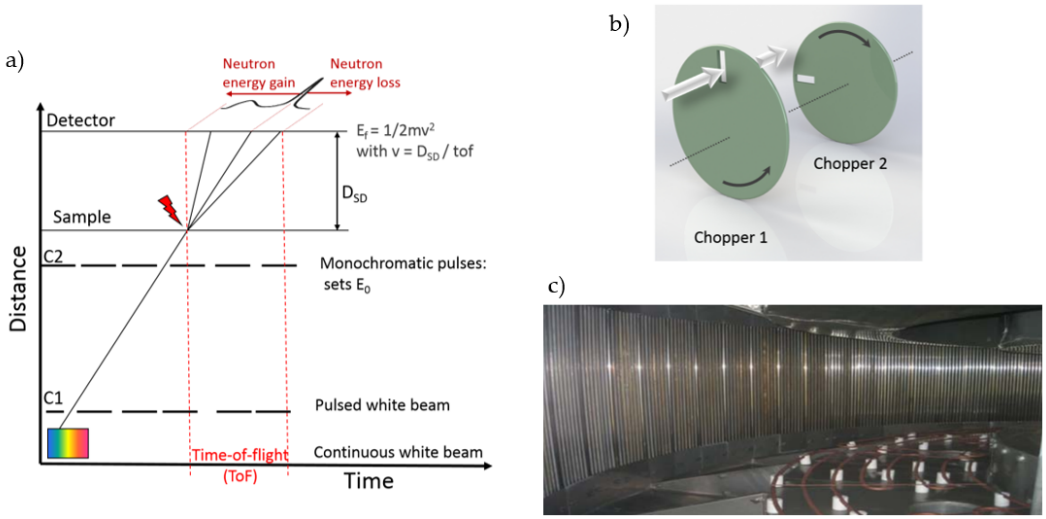

Figure 2.12: a) Basic distance-time diagram for a time-of-flight instrument. In reality there are more choppers between C1 and C2, especially at a spallation source. b) Schematic diagram of chopper system. c) PELICAN detector bank consisting of 200 position-sensitive ^{3}He tubes aligned vertically. This detector bank covers 0.8 sr. Subfigures a) and b) from reference [19], reproduced under CC BY 4.0. Subfigure c) from reference [16], reproduced with permission from the Physical Society of Japan.

2.5 Samples

The primary consideration for any hard condensed matter experiment is the quality of the samples. I was fortunate enough to collaborate with several crystal growing wizards during the course of my DPhil, and their samples underpin my results – a big thanks to Dharmalingam Prabhakaran of the Clarendon Laboratory, University of Oxford, and Hao Su and Yanfeng Guo of Shanghai Tech University.

The samples studied in this thesis were grown by one of two methods, the flux growth method and the optical floating zone method. The former entails mixing powdered elements or parent compounds and a chosen flux material together in a crucible. The crucible is then heated and cooled very slowly to allow crystals to form in the flux. Centrifuging gets rid of the still-molten flux and reveals small crystals, usually in the form of platelets. This process is depicted in Figure 2.13. Crystals produced in this way tend to be small and may have impurities of other compounds remaining on the surface, but their platelet shape often features natural facets, making them easy to align.

The optical floating zone method, shown in Figure 2.14, begins with a polycrystalline seed rod[20]. The furnace has a very localised hot spot due to intense focussing of the light from the halogen or

[20]This can be produced in different ways, variations of shake 'n' bake etc.

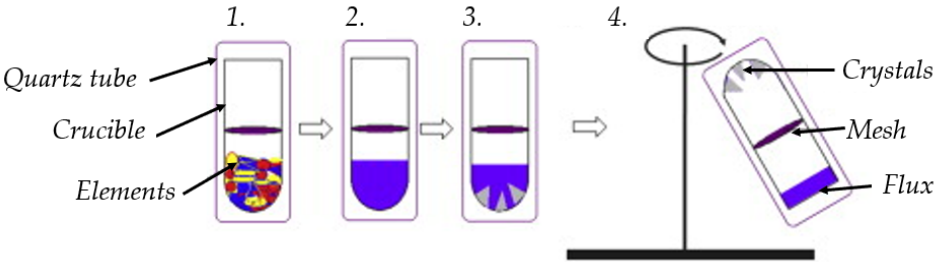

Figure 2.13: The flux growth method: 1) mix ingredients and flux together, 2) melt, 3) cool down slowly, allowing crystals to grow, 4) while still above the melting point of the flux, centrifuge to get rid of remaining flux. Figure adapted from [20], copyright Elsevier (2015).

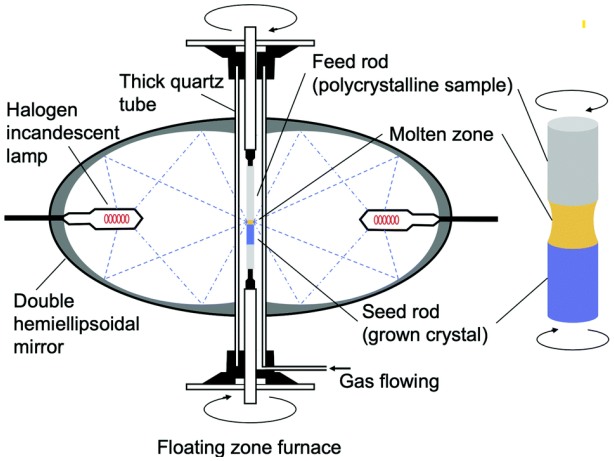

Figure 2.14: The optical floating zone growth method. Figure from reference [21], reproduced under CC BY-NC 3.0.

xenon lamp by the ellipsoidal mirrors. By moving the seed rod slowly through this floating zone while it is continuously rotated, each part of the seed rod is melted and cooled in turn. A new, single crystal will form. It is possible to grow very large crystals using this technique, although the diameter is limited by the surface tension of the melt in the floating zone. Crystals produced are cylindrical and lack natural facets, but it is likely that any impurities that preferred to stay in the melt ended up at one end of the crystal (rather than being present throughout the sample). However, the presence of impurities is unlikely as there is no crucible or extra material present while the crystal grows, aside from inert gas that flows through the quartz tube.

Single crystals offer additional richness in the form of defined crystal orientations, whereas powdered samples offer an average over all crystal orientations. A full structural refinement might be impossible without the additional information given by knowing the crystal orientation. It is important to gauge the quality of the single crystal. Broad Bragg peaks indicate short-range rather than long-range order. Several peaks instead of one single peak indicates twinning or multiple crystal grains. However, there might be times when only a powdered sample is feasible due to the

size of crystallites produced or heavy twinning, mosaicity etc. In some cases, a powdered sample may even be preferable: a powder can be packed into sample cans of different geometry (annular, flat etc.), which can be advantageous if the sample is strongly absorbing. A powdered sample can also be mixed with other powders, e.g. with a material that acts as a calibrant in the case of high pressure experiments. Happily for me, fantastic single crystals were synthesised for all materials highlighted by this thesis!

2.6 Transport and magnetometry

2.6.1 Magnetometry

Measuring bulk material properties of samples was done using a Quantum Design physical properties measurement system (PPMS). This versatile instrument consists of a superconducting cryomagnet, cooled by liquid helium (LHe) and liquid nitrogen (LN), and a probe that can be configured for different measurements of magnetic and transport properties. The temperature dependence of properties such as resistivity and magnetisation can be used to track phase changes in a material, as well as indicating the energy scales associated with the interactions behind these phases (energy $\sim k_{\mathrm{B}}T$).

The PPMS can be used as a vibrating sample magnetometer to measure the magnetic moment P to within 10^{-6} emu: for an explanation of what an emu (electromagnetic unit) is, see Figure 2.15 a). In this mode, the sample is oscillated vertically ($\hat{\mathbf{z}}$ axis) over a distance of A ($\sim$ mm) at a frequency ω ($\sim$ 40 Hz) while in a magnetic field applied by the PPMS. The pickup coil assembly is shown in Figure 2.15 b). The two coils are wound in opposite directions from the same wire to create a first-order gradiometer. The total magnetic moment of the moving sample generates a time-varying magnetic flux ϕ_B, which results in a voltage V in the pick-up coils (Eqn. 2.38).

$$\begin{aligned} V &= -\frac{d\phi_B}{dt} = -\frac{d\phi_B}{dz}\frac{dz}{dt} \\ &\propto P\omega A\sin(\omega t) \end{aligned} \tag{2.38}$$

A more sensitive magnetometry technique involves the superconducting quantum interference device (SQUID), packaged as a Quantum Design magnetic properties measurement system (MPMS). This can measure the magnetic moment to within 10^{-8} emu. The sample is secured in the middle of a drinking straw, which is then moved through the coils. Some sample mounting considerations are detailed in [22]. Four superconducting coils are wound to create a second-order gradiometer.

The actual SQUID component then converts the induced current into a voltage.

For both instruments, measurements are taken at many temperatures and/or applied fields, and sometimes with different sample orientations relative to the applied field. All measurements take place under vacuum. In the end, all the analysis is done assuming the sample has a dipolar moment induced by the applied field. The bulk magnetisation M (magnetic moment per unit

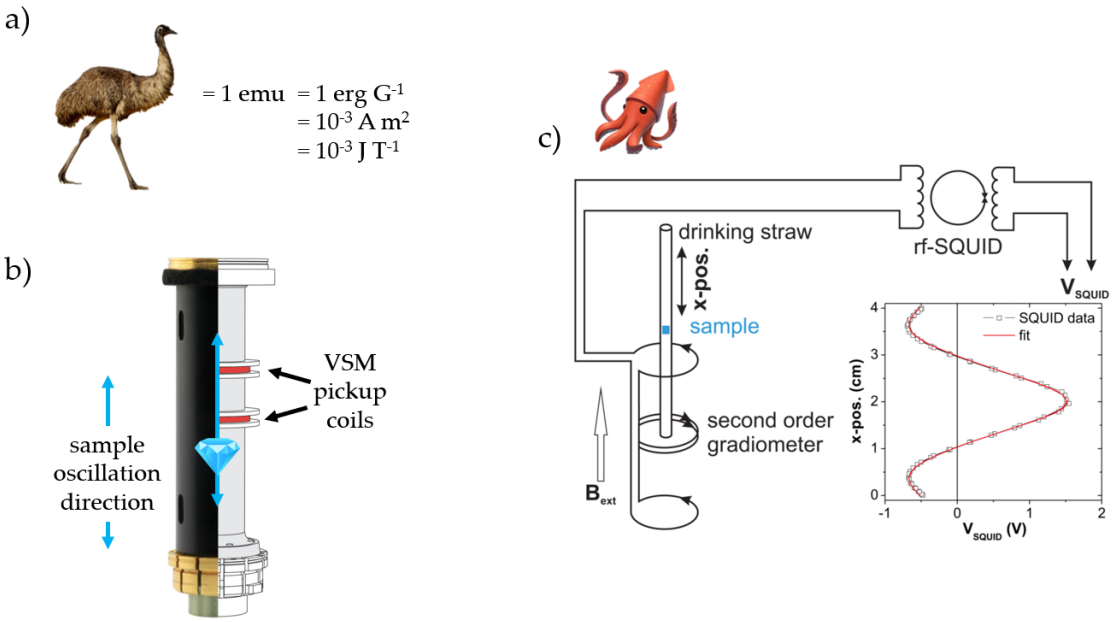

Figure 2.15: Magnetometry basics: a) the emu, b) the vibrating sample magnetometer (VSM), c) the SQUID. Subfigure b) adapted from source [23]. Subfigure c) adapted from reference [24], reproduced under CC BY 4.0.

volume) is related to the susceptibility χ by $M = \chi H$. χ is dimensionless in SI units. However it is more common to present the magnetisation (and then also the susceptibility) as another intensive quantity: per mol, per g or per formula unit (f.u.)[21]. Warning: there is another definition of emu out there (such that it has dimensions cm^3) and also people tend to leave out Oe from units because it doesn't affect the number if working in [cgs]... The measured quantity, which is total magnetic moment P[emu], is extensive. An intensive quantity is the molar magnetisation M[emu mol^{-1}] and this is the starting point for all calculated quantities going forward:

$$M[\text{emu mol}^{-1}] = \frac{P[\text{emu}]\, m_r[\text{g mol}^{-1}]}{m[\text{g}]}, \tag{2.39}$$

where m is the sample mass and m_r is the mass per mol of the material. Fitting the Curie-Weiss law (Eqn. 2.40) to the inverse susceptibility versus temperature data reveals two parameters: the

[21] I cannot take this unit seriously

Curie-Weiss temperature θ_{CW}, which is usually negative for an antiferromagnet ($\theta_{CW} \approx -T_N$) and positive for a ferromagnet ($\theta_{CW} \approx T_C$); and the Curie constant C, which is an indicator of the effective moment per ion [25].

$$\begin{aligned} \chi^{-1} &= \frac{T - \theta_{CW}}{C} \quad [\text{emu}^{-1}\,\text{mol}\,\text{Oe}] \\ C &= \frac{N_A \mu_{\text{eff}}^2}{30 k_B} \quad [\text{emu}\,\text{mol}^{-1}\,\text{Oe}^{-1}\,\text{K}] \\ \mu_{\text{eff}} &= \sqrt{8C} \quad [\mu_B \text{ per magnetic ion}] \end{aligned} \tag{2.40}$$

2.6.2 AC susceptibility

A useful variation on magnetisation measurements is to measure the AC susceptibility defined as $\chi_{AC} = M_{AC}/H_{AC}$. The sample is subject to a small ($\sim 5\,\text{Oe}$) sinusoidally-varying magnetic field $H_{AC}\cos(2\pi\nu t)$, superimposed on a constant (usually) coaxial field H_{DC}. The oscillation frequency ν typically ranges from 10^{-1}–10^4 Hz [26]. When $1/\nu$ is on the timescale of magnetisation dynamics of the sample, the response is complex: $\chi_{AC} = \chi' + i\chi''$. These measurements are susceptible (pardon the pun) to low-frequency phenomena such as domain wall dynamics and order-through-disorder such as spin glasses and frustrated magnets. Relaxation and dissipation phenomena manifest in the out-of-phase imaginary component.

2.6.3 Resistivity

The PPMS can also be used to measure resistivity at different temperatures and magnetic fields. A four-point probe measurement offers the highest accuracy for samples of uniform thickness t, measuring both I_x and V_x. A fifth point is added to measure transverse resistivity V_y, needed for Hall effect measurements. The geometry for such a five-point measurement is displayed in Figure 2.16 a) (for a four-point measurement, get rid of the contact labelled V_{b+}). The sample is mounted on a standard puck, shown in Figure 2.16 b), with thin gold wires attached using silver paste for low contact resistance ($\sim 2\,\Omega$).

The longitudinal resistivity ρ_{xx} and the transverse or Hall resistivity ρ_{xy} are defined as follows:

$$\begin{aligned} \rho_{xx} &= \frac{V_x A}{I_x l} \\ \rho_{xy} &= \frac{V_y t}{I_x}. \end{aligned} \tag{2.41}$$

As the sample and contact placement will not have the ideal symmetry shown in Figure 2.16 a), the

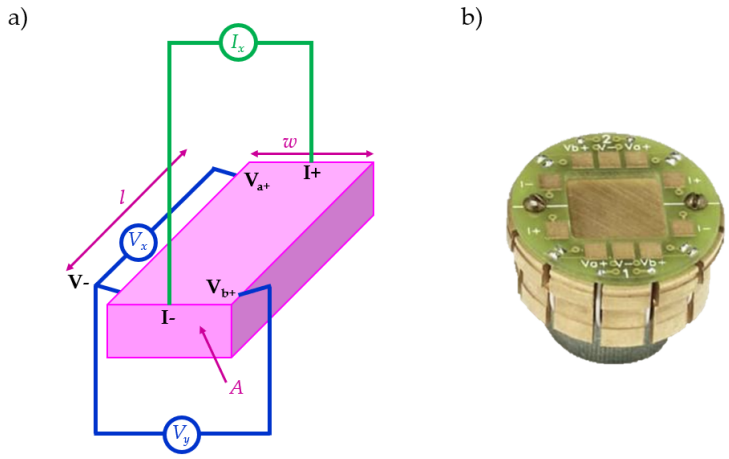

Figure 2.16: a) Resistivity measurement geometry for a sample where the distance between contacts V- and V_{a+} is l, the distance between contacts V- and V_{b+} is w, and the cross-sectional area is $A = wt$; b) example resistivity puck. Subfigure b) adapted from source [23].

measured quantities will actually be sampling both components of the resistivity. So it is necessary to symmetrise the signals V_x' and V_y' by averaging the signals taken in antiparallel magnetic fields:

$$V_x = \frac{1}{2}\left(V_x'(B) - V_x'(-B)\right) \tag{2.42}$$

and similarly for V_y.

2.7 Other techniques

Here I wish to provide a succinct outline of complementary techniques that are mentioned in references, but that were not utilised directly in the work presented in this thesis.

2.7.1 Angle-resolved photoemission spectroscopy

Angle-resolved photoemission spectroscopy (ARPES) harnesses the photoelectric effect to probe the electronic band structure of materials. Given sufficient energy, photons incident on a surface can cause the emission of electrons from a metal. During photoemission, the momentum in the plane of the surface is conserved. A position-sensitive spectrometer allows the momentum and energy of the electrons to be measured, and rotating the crystalline sample allows different wavevector cuts to be taken. In this way, reciprocal space maps can be built up at different energies, charting the Fermi surface.

2.7.2 Quantum oscillations

This is another method used to map the Fermi surface. When subject to an external magnetic field, electrons in motion have their energy levels quantised into Landau levels. Therefore, the density of states varies dramatically with energy. Given that the gap between Landau levels is porportional to the size of the magnetic field, different Landau levels can be made to intersect the Fermi surface. Metallic materials owe many of their properties to the density of states at the chemical potential[22]; hence the variation of the density of states with field leads to modulations in electrical quantities. This is the basis of quantum oscillations techniques, as well as the quantum Hall effect. Low temperature, field-dependent measurements of quantities such as magnetic susceptibility (de Haas – van Alphen effect) and resistivity (Shubnikov – de Haas) at different sample orientations can provide information to reconstruct the Fermi surface.

2.7.3 Scanning tunneling microscopy

This technique can image materials at the atomic level by performing a raster scan of a very pristine surface with a very fine tip of scanning tunneling microscope (STM). The tunneling voltage from the tip through the material is measured. The information in STM is gathered in real space, rather than reciprocal space as for the scattering techniques discussed earlier. In constant current mode, the STM is sensitive to the bumps in the surface caused by the individual atoms as well as local charge density. In voltage sweep mode, the STM probes the density of states at one fixed location on the surface. Because electrons can only tunnel so far, this method is only suitable for atomically-thin films of metallic materials.

2.7.4 Muon spin relaxation

A muon is a heavy electron (the muon's mass is $\sim 200\, m_e$), which (unlike an electron) decays. Like an electron, it also has an intrinsic spin $S = 1/2$ and will precess in a magnetic field. The properties of the decay products are influenced by where in a material the muon spent its final moments, so measuring these decay products can provide information about 'local' magnetism. A positive muon (mean lifetime $\sim 2\,\mu$s) will decay into a positron and two neutrinos. The anisotropic distribution of emitted positrons is correlated with the distribution of muon spin directions upon the decay of the muons. Muons are beamed at a sample and then the emitted positron distribution is measured as a function of time ($\sim \mu$s). This is a form of spectroscopy known as muon spin relaxation (μSR). In this way, μSR provides information about the local magnetic field and dynamics at the muon stopping

[22]The Fermi energy is defined as the chemical potential at zero temperature.

sites. μSR is not a 'scattering' experiment and does not provide information about structures in reciprocal space, but instead probes an ensemble average of stopping sites, which is determined computationally.

2.8 Time scales of different experimental probes

As a concluding remark for this chapter, I present two diagrams showing the energy (time) and length scales covered by different physical phenomena (Figure 2.17) and experimental methods (Figure 2.18). As you can see, there's many more than those I have discussed here. Also note that inelastic neutron scattering is quite far-reaching!

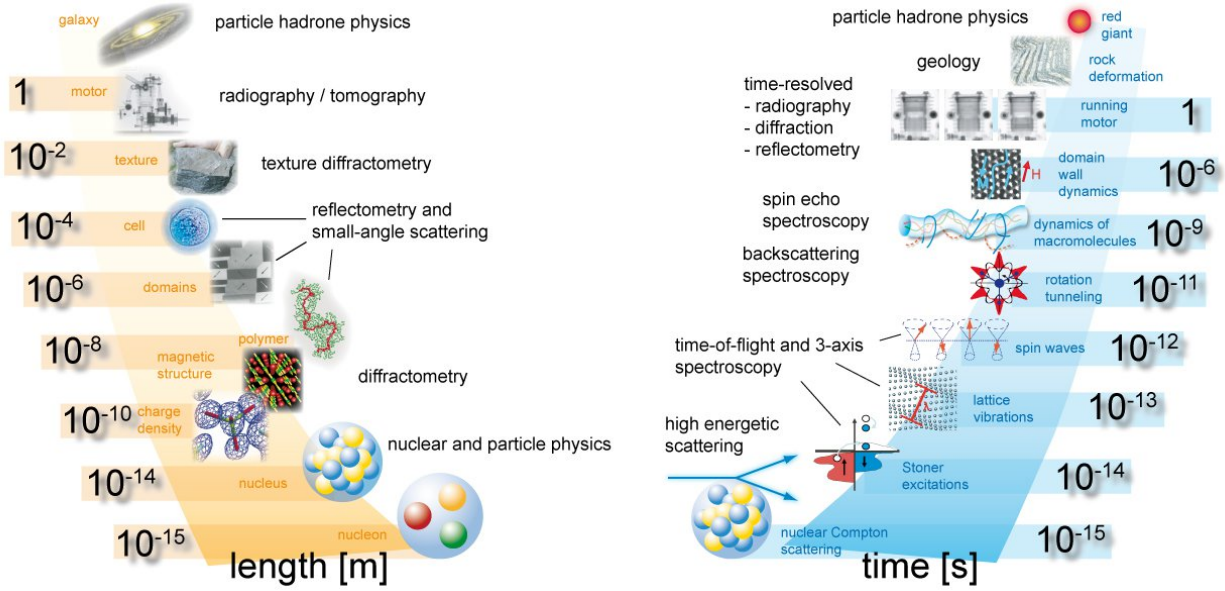

Figure 2.17: The energy (time) and length scales of different physical phenomena. Source: [27].

References

[1] R. Pynn. *Neutron scattering: a primer*. 1990. URL: https://www.ncnr.nist.gov/summerschool/ss16/pdf/NeutronScatteringPrimer.pdf (cited on page 17).

[2] A. T. Boothroyd. *Principles of Neutron Scattering from Condensed Matter*. Oxford University Press, 2020 (cited on pages 17, 18, 33, 34, 36).

[3] D. S. Sivia. *Elementary Scattering Theory*. Oxford University Press, 2011 (cited on page 17).

[4] M. Wolff. *Neutron scattering*. URL: https://www.teknik.uu.se/digitalAssets/386/c_386360-l_3-k_neutron_scattering_reduced.pdf (cited on page 20).

[5] *1994 Nobel Prize in Physics Press Release*. 1994. URL: https://www.nobelprize.org/prizes/physics/1994/press-release/ (cited on page 20).

[6] *CODATA Value: neutron magnetic moment to nuclear magneton ratio*. URL: https://physics.nist.gov/cgi-bin/cuu/Value?munsmun (visited on 2023) (cited on pages 21, 30).

[7] *Agilent SuperNova User Manual*. URL: https://www.agilent.com/Library/usermanuals/Public/

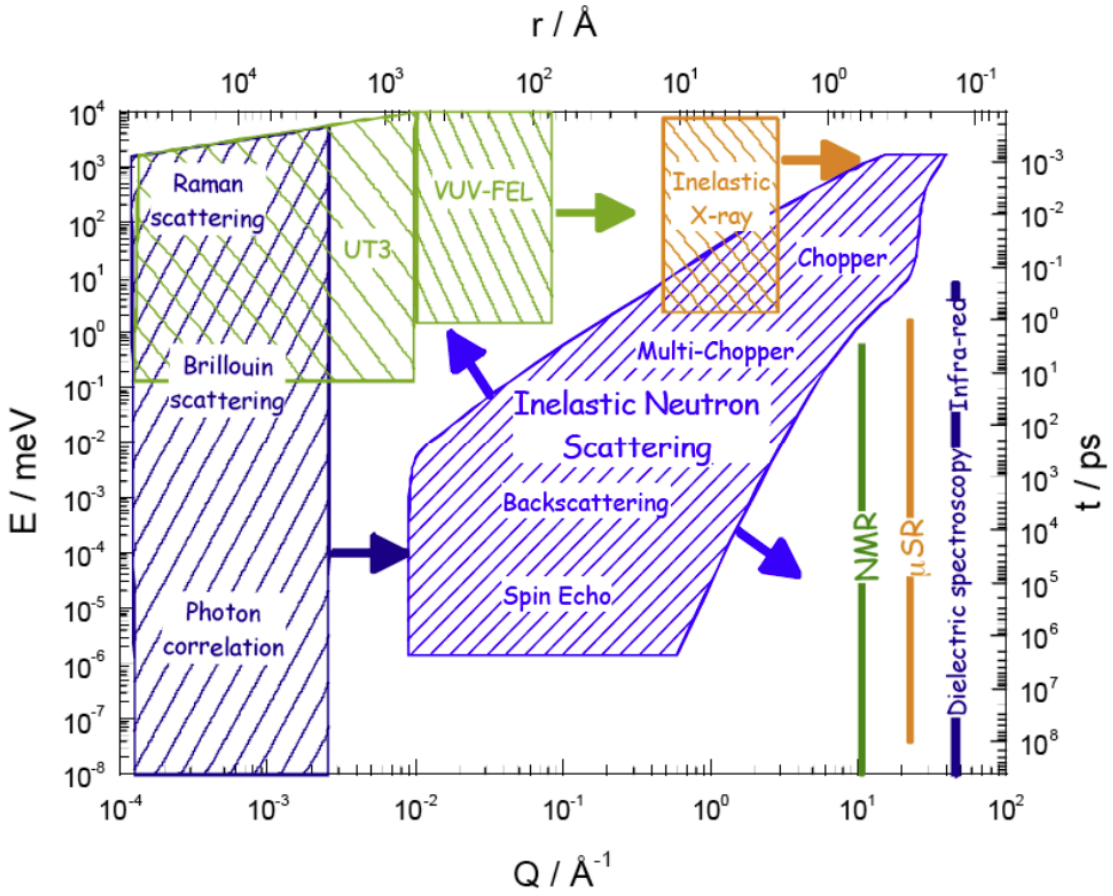

Figure 2.18: The energy (time) and length scales covered by different experimental methods. Source: [28].

SuperNova_User_Manual.pdf (cited on pages 25, 26).

[8] B. Ouladdiaf, J. Archer, G. J. McIntyre, A. W. Hewat, D. Brau, and S. York. "OrientExpress: A new system for Laue neutron diffraction". *Physica B: Condensed Matter* 385-386 (2006). DOI: 10.1016/j.physb.2006.05.337 (cited on pages 27, 33).

[9] *D10: four-circle diffractometer with three-axis energy analysis*. URL: https://www.ill.eu/users/instruments/instruments-list/d10/description/instrument-layout (cited on page 31).

[10] N. A. Katcho, L. Cañadillas-Delgado, O. Fabelo, M. T. Fernández-Díaz, and J. Rodríguez-Carvajal. "Int3D: A Data Reduction Software for Single Crystal Neutron Diffraction". *Crystals* 11.8 (2021). DOI: 10.3390/cryst11080897 (cited on page 32).

[11] B. Ouladdiaf, J. Archer, J. R. Allibon, P. Decarpentrie, M.-H. Lemée-Cailleau, J. Rodríguez-Carvajal, A. W. Hewat, S. York, D. Brau, and G. J. McIntyre. "CYCLOPS – a reciprocal-space explorer based on CCD neutron detectors". *Journal of Applied Crystallography* 44.2 (2011). DOI: 10.1107/S0021889811006765 (cited on page 33).

[12] *D3: The Spin Polarised Hot Neutron Beam Facility*. URL: https://www.ill.eu/users/instruments/instruments-list/d3/description/instrument-layout (cited on pages 33, 34).

[13] S. A. Danilkin, G. Horton, R. Moore, G. Braoudakis, and M. Hagen. "The TAIPAN thermal triple-axis spectrometer at the OPAL reactor". *Journal of Neutron Research* 15.1 (2007). DOI: 10.1080/10238160601045755 (cited on page 37).

[14] M. Kempa, B. Janousova, J. Saroun, P. Flores, M. Boehm, F. Demmel, and J. Kulda. "The FlatCone multianalyzer setup for ILL's three-axis spectrometers". *Physica B: Condensed Matter* 385-386 (2006). DOI: 10.1016/j.physb.2006.05.371 (cited on pages 37, 38).

[15] *Three-axis spectroscopy - Dynamics - Techniques for ... - Neutron research - The NMI3 information portal*. URL:

https://nmi3.eu/neutron-research/techniques-for-/dynamics/three-axis-spectroscopy.html (visited on 2023) (cited on page 38).

[16] D. Yu, R. Mole, T. Noakes, S. Kennedy, and R. Robinson. "Pelican - a Time of Flight Cold Neutron Polarization Analysis Spectrometer at OPAL". *Journal of the Physical Society of Japan* 82.Suppl.A (2013). DOI: 10.7566/JPSJS.82SA.SA027 (cited on pages 38, 39).

[17] R. I. Bewley, R. S. Eccleston, K. A. McEwen, S. M. Hayden, M. T. Dove, S. M. Bennington, J. R. Treadgold, and R. L. S. Coleman. "MERLIN, a new high count rate spectrometer at ISIS". *Physica B: Condensed Matter* 385-386 (2006). DOI: 10.1016/j.physb.2006.05.328 (cited on page 38).

[18] M. Russina and F. Mezei. "First implementation of Repetition Rate Multiplication in neutron spectroscopy". *Nuclear Instruments and Methods in Physics Research Section A: Accelerators, Spectrometers, Detectors and Associated Equipment* 604.3 (2009). DOI: 10.1016/j.nima.2009.03.010 (cited on page 38).

[19] Q. Berrod, K. Lagrené, J. Ollivier, and J.-M. Zanotti. "Inelastic and quasi-elastic neutron scattering. Application to soft-matter". *EPJ Web of Conferences* 188 (2018). DOI: 10.1051/epjconf/201818805001 (cited on page 39).

[20] T. Nishinaga. *Handbook of Crystal Growth*. 2nd. Elsevier, 2015. DOI: 10.1016/C2011-0-04376-4 (cited on page 40).

[21] N. Kase, N. Kimizuka, and N. Miyakawa. "Recent progress of the single crystal growth of homologous $(InGaO_3)_m(ZnO)_n$". *CrystEngComm* 24.25 (2022). DOI: 10.1039/D2CE00439A (cited on page 40).

[22] M. A. Garcia, E. Fernandez Pinel, J. de la Venta, A. Quesada, V. Bouzas, J. F. Fernández, J. J. Romero, M. S. Martín González, and J. L. Costa-Krämer. "Sources of experimental errors in the observation of nanoscale magnetism". *Journal of Applied Physics* 105.1 (2009). DOI: 10.1063/1.3060808 (cited on page 41).

[23] *Physical Properties Measurement System*. URL: https://www.qdusa.com/products/ppms.html (cited on pages 42, 44).

[24] M. Buchner, K. Höfler, B. Henne, V. Ney, and A. Ney. "Tutorial: Basic principles, limits of detection, and pitfalls of highly sensitive SQUID magnetometry for nanomagnetism and spintronics". *Journal of Applied Physics* 124.16 (2018). DOI: 10.1063/1.5045299 (cited on page 42).

[25] S. Mugiraneza and A. M. Hallas. "Tutorial: a beginner's guide to interpreting magnetic susceptibility data with the Curie-Weiss law". *Communications Physics* 5.1 (2022). DOI: 10.1038/s42005-022-00853-y (cited on page 43).

[26] C. V. Topping and S. J. Blundell. "A.C. susceptibility as a probe of low-frequency magnetic dynamics". *Journal of Physics: Condensed Matter* 31.1 (2018). DOI: 10.1088/1361-648X/aaed96 (cited on page 43).

[27] *Neutron methods and techniques for research*. URL: https://nmi3.eu/neutron-research/techniques-for-.html (cited on page 46).

[28] V. G. Sakai. *Quasi-elastic neutron scattering*. URL: https://www.oxfordneutronschool.org/2017/Lectures/OSNS17-VGarciaSakai-QENS.pdf (cited on page 47).

3

The magnetism of the topological semimetal $YbMnSb_2$

3.1 Introduction

Topological semimetals have excellent transport qualities due to the linear dispersion about the Fermi energy and resulting quasiparticle excitations. The influence of magnetism on topological states is dramatic but far from fully explored, and the catalogue of magnetic topological semimetals is ever expanding. Several examples of magnetic topological semimetals have been found in the family $AMnX_2$ (A = Ca, Sr, Ba, Yb, Eu; X = Bi, Sb). Dirac or Weyl fermions are harboured by the Bi or Sb 'square' net, which lies between magnetic Mn layers in the ab plane. Although materials in the $AMnX_2$ have fairly similar crystal structures, the Mn (and in some cases Eu) ions produce a variety of magnetic structures, which is further expanded by the influence of an external magnetic field. The magnetic structure has simultaneous ramifications for the band structure topology and magnetic excitations of these materials. Here I will focus on $YbMnSb_2$, which has been the subject of much experimental and theoretical work to pinpoint its topological semimetal nature and magnetic order. How and whether the electrons involved in the topological quasiparticle phenomena are coupled with those responsible for magnetism and spin waves are key research questions.

In this chapter I will present my experimental work on $YbMnSb_2$. This includes:

- sample characterisation with X-ray diffraction, bulk magnetisation and resistivity measurements (§ 3.2);
- determination of the crystal structure and magnetic order based on single crystal neutron

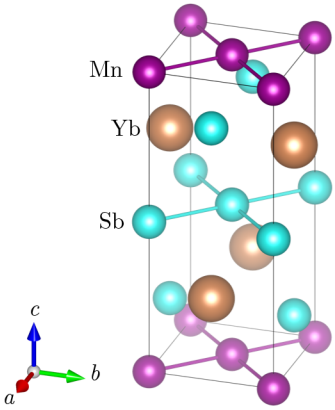

Figure 3.1: Unit cell of $YbMnSb_2$. This figure was originally published in reference [1]. Copyright American Physical Society (2023).

diffraction data (§ 3.3);

- a magnetisation density map of the unit cell (§ 3.4);
- spin wave dispersion mapped using inelastic scattering data (§ 3.6);
- a linear spin wave theory model of the magnetic excitations of $YbMnSb_2$.

The main findings are that $YbMnSb_2$ exhibits a C-type AFM structure, with magnetic moments along the c axis, and strong coupling between Mn layers along the c axis relative to other materials in the $AMnX_2$ family.

Firstly I will introduce the $AMnX_2$ family of topological semimetals (§ 3.1.1) and then focus on $YbMnSb_2$ in particular (§ 3.1.2).

3.1.1 The $AMnX_2$ family of quantum materials

The family of quantum materials $AMnX_2$ (A = Ca, Sr, Ba, Yb, Eu; X = Bi, Sb) has demonstrated characteristics of the topological semimetals, with Weyl or Dirac fermions being hosted on the quasi-2D plane formed by the Sb or Bi 'square' [2–4]. To explain the significance of the square net, the review by Klemenz [5] compares the structure to graphene, the ubiquitous Dirac semimetal consisting of 2D planes. In graphene, half-filled p_z orbitals arising from bonds in plane results in linear dispersion about the Fermi level. Whilst the linear part of the electronic spectrum of graphene extends 10 meV either side of the Fermi level, the range is much smaller (less than 1 meV) in the square net materials $AMnX_2$. Nevertheless the origin of the semimetallicity in the $AMnX_2$ family is a combination of structure (both in-plane inter-atomic distance and distance to nearest

ion of different species, as measured perpendicular to the plane), and in-plane electron count of six valence electrons. If the square net cannot be stabilised by the (usually d) bands of the nearest neighbours along the c direction, then a Peierls distortion or Mott insulator state is favoured instead. Based on the structural parameters and oxidation states of constituent ions, $YbMnSb_2$ is one of many $AMnX_2$ materials that fulfils these topological semimetal criteria, as described in [6].

With Mn^{2+} present, the X ion adopts the -1 oxidation state in the square net plane and the -3 oxidation state in the 'rock salt' plane where the interatomic spacing is much larger between X ions [5]. This leaves the A ions in a $+2$ oxidation state. The square net valence electron count is then six (s^2p^4), with two lone pairs in s and p_z, and just two electrons participating in a total of four p_x and p_y bonds [5]. It is this delocalised bonding which lends these materials their semimetal character [6].

Some examples of $AMnX_2$ compounds are given in Table 3.6. There are some broad trends to consider in the materials presented in Table 3.6:

1. The magnetic ions.
   (a) For most examples in Table 3.6, the only magnetic species is Mn^{2+}.
   (b) Divalent Eu is also magnetic; however in $EuMnSb_2$ and $EuMnBi_2$, the Eu moments undergo a transition to AFM order at a much lower temperature $\sim$20 K than the Mn moments. Studies have reached differing conclusions regarding the orientation of Eu moments: canted A-type AFM [7, 8], or in the ab plane and $\perp$ to Mn moments [9], or along the c axis [10].
   (c) The spin orientation of the Eu moments may provide a tuning parameter for an energy gap between nested Dirac cones of different spin in $EuMnBi_2$ [11–13].
   (d) Divalent Yb is non-magnetic.
2. The space group symmetry of the material.
   (a) Space groups include $P4/nmm$, $Pnma$, $Imm2$ and $I4/mmm$. $P4/nmm$ is primitive tetragonal, and $I4/mmm$ is body-centred tetragonal, while $Pnma$ and $Imm2$ are orthorhombic.
   (b) Some materials such as $EuMnSb_2$ and $YbMnSb_2$ have been attributed to both the $Pnma$ [8, 14] and $P4/nmm$ [7, 15] space groups.
   (c) For tetragonal space groups, the 'square net' lives up to its name; however, $P4/nmm$ has a glide in the plane of the 'square net', whereas $I4/mmm$ has a mirror plane.

(d) For the orthorhombic space groups, there is a slight distortion of the 'square net' with some X atoms being displaced along the c axis. Given the 'square net' of X ions hosts the purported topological quasiparticles in the ab plane, this is an important distinction. $Pnma$ or $Imm2$ reduces the symmetry and hence eliminates the degeneracy of the Dirac bands. For example, the polarity of the $Imm2$ space group leads to spin valley splitting of the Dirac bands in $BaMnBi_2$ [11]. Reduced structural symmetry is also associated with a greater energy gap between Dirac points [16, 17].

(e) The anisotropy of the Dirac/Weyl dispersion tends to increase as the symmetry of the space group decreases [18].

(f) For topological materials adopting orthorhombic symmetry, the Dirac dispersion is located on the $\Gamma - Y$ high symmetry line, rather than the $\Gamma - M$ high symmetry line [19].

(g) For this family of materials, the unit cells with the $I4/mmm$, $Pnma$ or $Imm2$ symmetry have (respectively) the c, a or b axis approximately twice the length of the c axis of the unit cell with $P4/nmm$ symmetry.

(h) The three compounds displaying G-type AFM order of the Mn moments ($EuMnBi_2$, $BaMnSb_2$ and $SrMnBi_2$) all belong to the $I4/mmm$ space group [2, 10]. C-type AFM is pervasive for $Pnma$ and $P4/nmm$ compounds. No magnetic structures with non-zero propagation vectors $\mathbf{q}$ have been reported.

3. The size of the alkali earth / rare earth ion, i.e. Ca (smallest) to Ba (largest).

   (a) The mean distance between Mn layers increases slightly with increasing ionic radius.

   (b) $P4/nmm$ is more commonly reported as the symmetry for small A atoms, compared to $I4/mmm$ etc. for large A.

4. The size of the element X that makes up the square net, i.e. Bi (large) vs. Sb (small).

   (a) The corresponding strength of spin orbit coupling (SOC) is larger with Bi than Sb. Increasing SOC increases the energy gap in the Dirac dispersion; hence, the mass of the Dirac fermion quasiparticles also increases.

   (b) For the A = Ca, Sr, Ba compounds, the T_N is comparable whether X = Bi or Sb; however for A = Eu, Yb, the T_N is higher for X = Sb than X = Bi. T_N ranges from 246 K for $CaMnBi_2$ to $\sim$ 345 K for $YbMnSb_2$ and $EuMnSb_2$.

5. Deficiencies and other defects in the composition of these materials – more likely with larger

ions, this has symmetry implications as well as potential disruption of magnetic order.

(a) Temperature-dependent Eu spin canting was found in $Eu_{(1-x)}Sr_xMnSb_2$ [9]. For $x \geq 0.5$, Eu spin canting and intra- (inter-) layer conductivity (decreased) increased with x [9].

(b) In $CaMn_{1-x}Cu_xBi_2$, Cu doping suppresses AFM order ($T_N \approx 85\,K$), while likely introducing Mn spin canting [20]. A similar effect was observed empirically in $EuMn_{1-x}Zn_xSb_2$ [21], and with deficiencies of Sr and Mn in $Sr_{1-y}Mn_{1-z}Sb_2$ [22].

6. Topology of the electronic band structure.

(a) A good summary of the Fermiology of $AMnX_2$ compounds based on ARPES data is given in [23].

(b) Most of these materials are reported as Dirac semimetals, based on *ab initio* calculations as well as experimental techniques such as ARPES, and SdH oscillations. There are few exceptions. Whether $EuMnSb_2$ and $SrMnSb_2$ are Dirac semimetals or not any kind of topological semimetal is debated [8, 9, 16, 24].

(c) The structure of $BaMnX_2$, assigned to polar space group $Imm2$, breaks inversion symmetry [11, 25]. Thus, the Dirac cones of the electronic dispersion are split into Weyl points, irrespective of the magnetic order of the Mn spins.

(d) Intriguingly, $YbMnX_2$ materials are the only suggested 'purely magnetic' Weyl semimetal candidates in works including [4, 10, 26–29]; however, this is debated and hinges on there being canting of the Mn spins. I discuss this further below.

3.1.2 $YbMnSb_2$

The magnetic topological semimetal $YbMnSb_2$ has been intensely studied via via quantum oscillations, magnetometry, optical spectroscopy, *ab initio* band structure calculations, ARPES, and single-crystal neutron diffraction [4, 15, 30, 31]. The structural symmetries of $YbMnSb_2$ are described by the $P4/nmm$ space group with lattice parameters $a = b = 4.31(2)$ Å, $c = 10.85(1)$ Å [15], but it can also be refined in the $Pnma$ space group [14]. $YbMnSb_2$ is of particular note due to its superior thermoelectric properties among topological semimetals [32] as a result of anomalous transport in the Sb plane. This includes a high ab-plane Seebeck coefficient of 185 μV K^{-1} at a temperature of 380 K, and a high power factor of 0.9 mW m^{-1} K^{-2} [33]. $YbMnSb_2$ is stable until 1100 K [33], providing an ample temperature buffer for thermoelectric applications.

The Mn^{2+} moments of $YbMnSb_2$ order antiferromagnetically below $T_N \approx 345\,K$. This is notable for

being the highest magnetic ordering temperature reported of the $A\mathrm{Mn}X_2$ semimetals to date. The Yb ions are in the divalent +2 oxidation state and are non-magnetic [30]. Magnetism, thermoelectric properties and topological band structure are all linked, with strong Berry curvature around Weyl points linked to possible enhancement of the (anomalous) Nernst effect[1] in another material Co_2MnGa [35]. The isostructural $YbMnBi_2$ was found to exhibit a large anomalous Nernst effect, which was unexpected given the AFM nature of the magnetism [29]. There is evidence for this kind of synergy between the magnetic and thermoelectric properties of $YbMnSb_2$ in [36]: Shubnikov-de Haas type oscillations were observed in the magnetic field dependence of the *ab* plane Seebeck coefficient, as well as a large Nernst coefficient of 40 μV K^{-1} resulting from the small effective mass of the charge carriers and band crossing close to the Fermi energy. No anomalous Nernst effect was seen in $YbMnSb_2$ as for $YbMnBi_2$. The temperature dependence of the resistivity, Seebeck and Nernst coefficients hinted at a Lifshitz transition at around 60 K [36]. As yet, there are no temperature-dependent ARPES results published to confirm this.

Around four magnetic structures – and correspondingly different semimetal topologies – have been proposed for $YbMnSb_2$:

- C-type antiferromagnetic (AFM) order of the Mn spins in the *ab* plane [30]. This was the most energetically favourable magnetic structure found through *ab initio* calculations. ARPES measurements showed good agreement with the predicted Fermi surface from DFT, and so $YbMnSb_2$ was categorised as a Dirac semimetal.

- G-type AFM magnetic structure within the *ab* plane [31]. This optical spectroscopy study informed calculations suggesting $YbMnSb_2$ is a nodal line semimetal.

- C-type AFM along the *c* axis with spin canting leading to a ferromagnetic (FM) component in the *ab* plane, and a Weyl semimetal state [27]. Reference [4] reported magnetic hysteresis consistent with a weak FM component due to spin canting, with the implication being that $YbMnSb_2$ is a Weyl semimetal. The work [29] drew a similar conclusion for $YbMnBi_2$, although the spin canting away from the *c* axis was estimated at just 0.018° based on magnetometry measurements, which would be too small to generate Weyl nodes.

- C-type AFM along the *c* axis with no spin canting [14, 15], informing calculations that point to $YbMnSb_2$ being a gapped Dirac semimetal. This is the conclusion reached through neutron diffraction work described in this chapter (also published as [15]).

Of these works, *ab initio* calculations suggested these different magnetic orders were energetically

[1] For background on the Nernst effect in metals, see [34].

favourable in [4, 30, 31] based on experimental evidence that indirectly probed the magnetic structure, whereas our results from unpolarised and half-polarised neutron diffraction experiments unequivocally determine the magnetic structure [15]. This is discussed in detail in § 3.3 and § 3.4. The half-polarised diffraction data also enable us to ascertain the localisation of the magnetic moments within the unit cell.

The interactions between Mn^{2+} spins that determine the magnetic ground state for $YbMnSb_2$ had not been elucidated prior to the inelastic neutron scattering work shown in § 3.6, subsequently published in [1]. Given the range of magnetic structures and accompanying topological characters that have been proposed for $YbMnSb_2$ in the literature, determining which interactions are responsible for stabilising the magnetic ground state is important. Of prime interest are the interactions and spin waves along the *c* axis which couple Mn electrons in different *ab* plane layers. These may be mediated by topological Sb electrons. Inelastic neutron scattering acts as a direct probe of such interactions; hence we study $YbMnSb_2$ using this technique and present the results in § 3.6 together with a model Hamiltonian determined by linear spin wave theory. Topological semimetals are heralded as a novel class of materials for spintronic applications. They demonstrate spin-momentum locking, which will be key in developing spintronic technologies relying on spin-polarised currents of electrons. Hence, mapping the magnon spectrum of $YbMnSb_2$ may pave the way for applications utilising magnons and topological fermions in tandem.

We find that the spin waves are well described by a Heisenberg exchange Hamiltonian with easy-axis anisotropy, and this work was the subject of the publication [1]. While the exchange interactions between nearest and next-nearest Mn neighbours in the *ab* plane are comparable to those measured for other $AMnX_2$ compounds, the ferromagnetic exchange along the *c* axis is surprisingly strong. The unusually strong exchange coupling along the *c* axis for $YbMnSb_2$ may have implications for the topological quasiparticles sandwiched between ferromagnetically coupled Mn ions [37]. The results in this chapter highlight $YbMnSb_2$ as a standout magnetic Dirac semimetal among the $AMnX_2$ class of quantum materials and invite further magnon missions for the magnetic topological semimetals.

3.2 $YbMnSb_2$ sample and initial characterisation

Single crystals in the form of platelets of typical dimensions $4 \times 4 \times 0.2$ mm^3 were grown by a flux method (Sb flux), by Hao Su and Yanfeng Guo of ShanghaiTech University. The details of the growth are reported in [4, 31]. The platelet crystals were individually examined (by me) via Laue

x-ray diffraction (Oxford Diffraction). For all neutron diffraction, magnetometry and transport measurements, the same single crystal of mass 107.4 mg was used. For inelastic neutron scattering, I coaligned 20 crystals with a total mass of 0.84 g on a 0.5 mm thick aluminium plate with the c axis perpendicular to the large face of the plate. Crystals were affixed to the plate with hydrogen-free CYTOP^{TM} fluoropolymer [38]. The overall coalignment of the crystals was checked using a x-ray Laue diffractometer (Photonic Science). To estimate the mosaicity of the ensemble of 20 crystals combined, I stacked Laue images of individual crystals taken with the aluminium plate in a fixed orientation. The combined Laue image shows the patterns are translated slightly with respect to each other both horizontally and vertically, but the patterns hardly show any relative rotation. This implies the crystals are slightly misaligned in the ac and bc planes, most likely from the glue not drying completely flat. The estimated mosaicity of the ensemble of crystals was $\sim 3°$ (full width at half maximum). The assembly of $YbMnSb_2$ crystals for inelastic neutron scattering on IN8 is shown in Figure 3.2 together with the combined Laue figure.

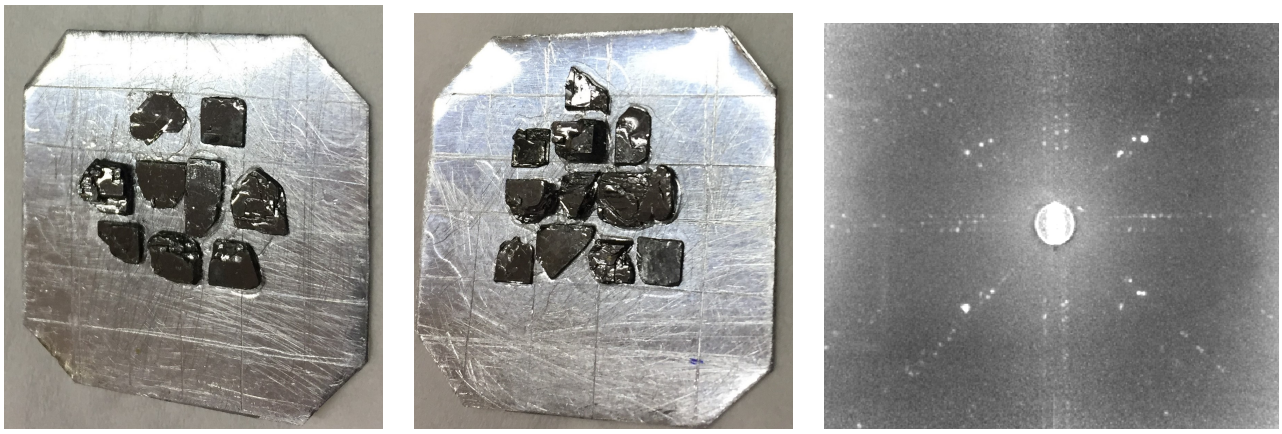

a) b) c)

Figure 3.2: a) and b) sample of $YbMnSb_2$ prepared for inelastic neutron scattering experiment, c) combined x-ray Laue pattern of the assembly of crystals. A version of this figure was originally published in the Supplemental Material of reference [1]. Copyright American Physical Society (2023).

3.2.1 X-ray diffraction

One representative crystal of $YbMnSb_2$ was examined on a four-circle κ X-ray diffractometer (Agilent Oxford Diffraction SuperNova) to determine the structure at room temperature. Fitting the data from this experiment, I found that the reflections were best indexed by the $P4/nmm$ space group, rather than the larger unit cell of the $Pnma$ space group. Reciprocal space slices are shown in Figure 3.3. One or two small secondary crystallites are misaligned compared to the main crystal. This is likely due to the 'terraced' appearance of the platelet crystals as seen in Figure 3.2.

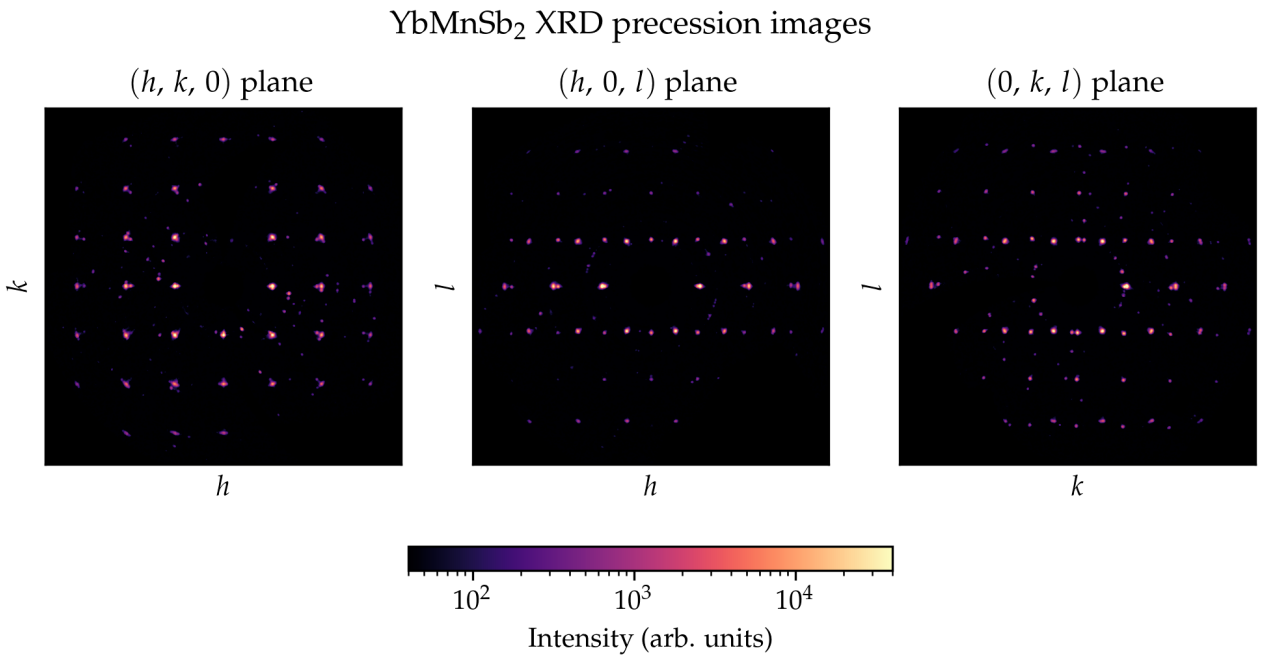

Figure 3.3: $YbMnSb_2$ XRD precession images showing different planes in reciprocal space. Image data read using the FABIO Python package [39].

3.2.2 Magnetometry

Magnetisation measurements were performed on a superconducting quantum interference device (SQUID) magnetometer (Quantum Design MPMS3) with magnetic field applied parallel and perpendicular to the crystal c axis. Measurements were performed in the temperature range 2 K $< T <$ 400 K and in fields of up to 3 T. The magnetisation curves diverge at $T_N \approx 345$ K, indicating antiferromagnetic ordering (Figure 3.4). Given that the bifurcation occurs for fields applied parallel and perpendicular to the c axis, and that the M curve is lower for $H \parallel C$, this suggests the magnetic moments preferentially align along the c axis. This is consistent with a previous report [4].

Magnetisation measurements were also made with the applied magnetic field along the b axis. This was to mimic one set of experimental conditions utilised in the half-polarised neutron diffraction experiment described later. Field sweeps from 2 T to -2 T and back to 2 T were performed at several different temperatures as shown in Figure 3.5. This enables the field-induced magnetisation to be estimated as $M = 0.001\ \mu_B$ f.u.$^{-1}$ at $\mu_0 H = 0.4$ T, which was the applied magnetic field for the half-polarised neutron diffraction experiment. The field dependence is linear, bar a small hysteresis loop that was present at all temperatures, which is likely due to a small ferromagnetic impurity such as MnSb ($T_C \approx 560$ K) [40].

3.2.3 Resistivity

Electrical transport measurements were performed on a Physical Property Measurement System (PPMS, Quantum Design) with the resistivity option, in the temperature range $2\,\mathrm{K} < T < 400\,\mathrm{K}$ in zero field. Below T_N, the in-plane resistivity decreases in line with metallic behaviour (Figure 3.4. The resistance peaks at T_N. The broad shape of the peak reflects the layered nature and reduced dimensionality of the material with increased scattering as the moments order antiferromagnetically in-plane (discussed in later sections).

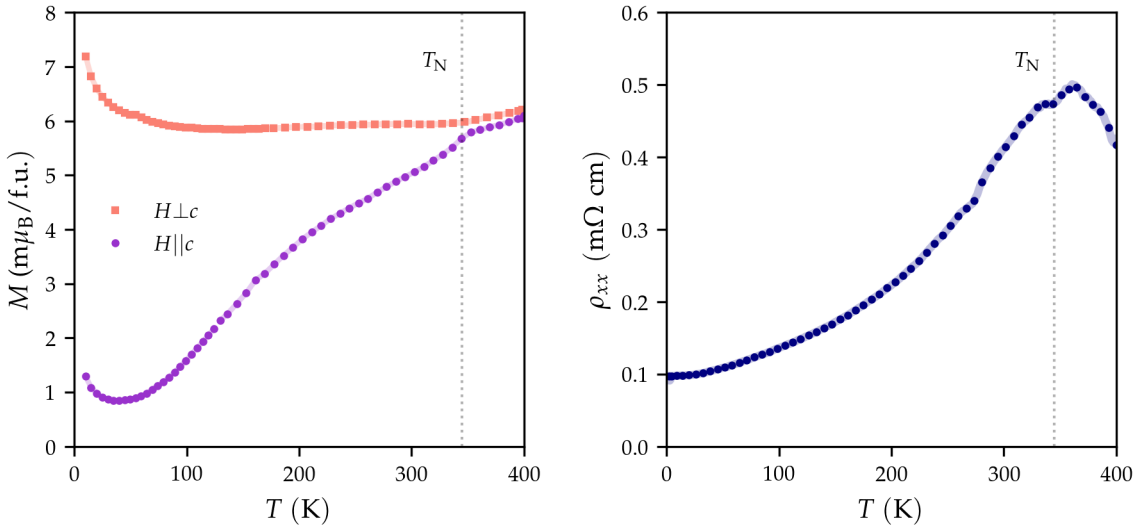

Figure 3.4: Bulk magnetisation and resistivity for $YbMnSb_2$. A version of this figure was originally published in the Supplemental Material of reference [15]. Copyright American Physical Society (2021).

3.3 Single crystal neutron diffraction of $YbMnSb_2$

To elucidate the magnetic structure of $YbMnSb_2$ we turned to neutron diffraction, which is a direct probe of magnetic order. In particular, given the scattering lengths of Yb (12.43 fm), Mn (−3.73 fm), and Sb (5.57 fm) are reasonably distinct, a single crystal neutron diffraction experiment would reveal the crystal structure of the unit cell and the presence of any stacking faults along the c axis, which is common in layered materials such as $AMnX_2$ compounds.

3.3.1 Method

Single crystal neutron diffraction with unpolarised neutrons of wavelength $\lambda = 2.36\,\text{Å}$ was performed on the four-circle diffractometer D10 at the Institut Laue–Langevin (ILL). The scattered neutrons were recorded on a $94 \times 94\ \mathrm{mm}^2$ area detector. To determine the magnetic and crystal

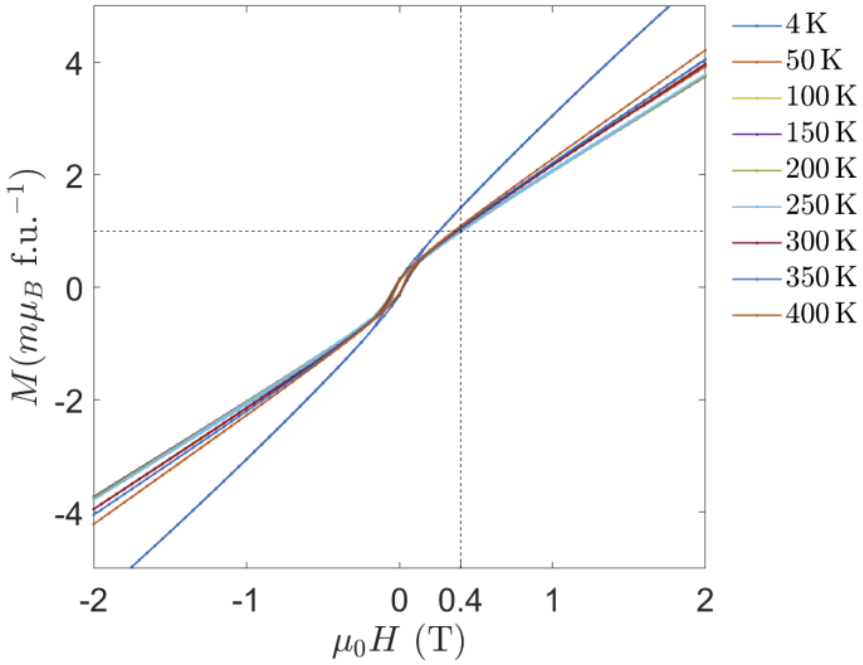

Figure 3.5: Bulk field-dependent magnetisation for $YbMnSb_2$ with applied $\mu_0 H \parallel b$ axis. Dashed line indicates $M = 0.001 \mu_B$ f.u.$^{-1}$ at $\mu_0 H = 0.4$ T (the applied magnetic field for the half-polarised neutron diffraction experiment). This figure was originally published in the Supplemental Material of reference [15].

structure of $YbMnSb_2$, a total of 382 and 386 *hkl* reflections were collected below and above the magnetic ordering temperatures, at $T = 2$ K and 400 K, respectively. At 2 K, measurements were also taken at 92 non-integer l corresponding to the G-type AFM structure with propagation vector (0, 0, 1/2); however, no significant intensity was recorded at these positions. To ascertain if there is a canting of the Mn moments away from the crystal c axis, the temperature dependence of several reflections was measured in the temperature range from 2 K to 420 K.

3.3.2 Description of data analysis

The D10 area detector gives a 2D snapshot of reciprocal space. This is extended to 3D via the generation of RACER ellipsoids, which are then used to calculate the observed integrated intensity at each reflection. Comparing the observed integrated intensities with calculated integrated intensities for various structure models enables the refinement of the (magnetic) structure. After Lorentz correction and RACER integration, the similarity of symmetry equivalent reflections R_{int} was 3.10 %, 3.18 %, and 9.44 % for the 400 K integer *hkl*, 2 K integer *hkl*, and 2 K non-integer l datasets respectively.

An earlier study on $YbMnSb_2$ [30] provided a good reference and starting point for our own refinement of the crystal structure. My lab XRD results on our sample also confirmed the structure,

so it was just a matter of further refining various parameters in the paramagnetic phase. I fixed the occupancy of all sites to 1 and the positions of the atoms on the 2*c* Wyckoff positions. For the $T = 400\,\mathrm{K}$ data, I varied the extinction parameters, the thermal displacement parameters B_{iso} and the z coordinate of the atoms not on the high symmetry sites.

I adopted a representation analysis approach for the task of refining the magnetic structure. Nearly all of the proposed magnetic structures for $YbMnSb_2$ have a magnetic unit cell that is identical in dimension to the structural unit cell, with a propagation vector of $\mathbf{q} = (0, 0, 0)$. The exception is the G-AFM in-plane structure, which has $\mathbf{q} = (0, 0, 1/2)$; however, we can rule this out as a possibility because no intensity was observed at non-integer reflections consistent with a non-zero $\mathbf{q}$.

I used the software package MAG2POL [41] to find the irreducible representations ('irreps') of the little group $G_{\mathbf{q}}$. The symmetry operations that are in $G_{\mathbf{q}}$ are a subset of the symmetry operations of the structural space group, and return $\mathbf{q}$ or $\mathbf{q}$ plus a translation when applied to $\mathbf{q}$. Each irrep has associated basis vectors, which specify the orientation of spins on the Mn sites. The magnetic structure will be a linear combination of these basis vectors. MAG2POL generated the irreps

$$\Gamma_3 + \Gamma_6 + \Gamma_9 + \Gamma_{10}.$$

Basis vectors for each of these irreps are listed in Table 3.1.

Table 3.1: Possible basis vectors given by MAG2POL for $\mathbf{q} = (0, 0, 0)$.

Irrep	Basis vector	Site 1 (0, 0, 0)	Site 2 $(\frac{1}{2}, \frac{1}{2}, 0)$
Γ_3	ψ_1	$[0, 0, 1]$	$[0, 0, 1]$
Γ_6	ψ_1	$[0, 0, 1]$	$[0, 0, -1]$
Γ_9	ψ_1	$[1, -i, 0]$	$[1, -i, 0]$
	ψ_2	$[-1, -i, 0]$	$[-1, -i, 0]$
Γ_{10}	ψ_1	$[1, i, 0]$	$[-1, -i, 0]$
	ψ_2	$[1, -i, 0]$	$[-1, i, 0]$

By the Landau theory of phase transitions, a second-order magnetic phase transition will have the symmetry of one irrep of $G_{\mathbf{q}}$ only. We can match the irreps to the proposed magnetic structures as follows:

- C-AFM with moments in-plane corresponds to Γ_{10} with $\mathbf{q} = (0, 0, 0)$
- C-AFM with moments along c corresponds to Γ_6 with $\mathbf{q} = (0, 0, 0)$

- C-AFM with moments primarily along c + FM in-plane canting, there is more than one irrep involved, $\Gamma_6 + \Gamma_9$.

We discounted the purely FM structures associated with Γ_3 and Γ_9, as no evidence of FM was seen in magnetisation data. Furthermore, below T_N intensity was seen at some integer reflections forbidden by the structural space group. This is inconsistent with a purely FM structure.

3.3.3 Refinement results

Table 3.2: Structural and extinction parameters for the paramagnetic phase of $YbMnSb_2$ determined by refinement in the space group $P4/nmm$ against integrated intensities collected at 400 K. $R_F = 1.46\,\%$ and $\chi^2_R = 1.73$ for this refinement

Atom	Wyckoff position	x	y	z	B_{iso}
Yb	2c	0.25	0.25	0.7274(1)	0.60
Mn	2a	0.75	0.25	0.00	0.4(1)
Sb	2b	0.75	0.25	0.50	0.78(7)
Sb	2c	0.25	0.25	0.1595(3)	0.49(8)

Extinction Parameter	Value
x_{11}	0.8(2)
x_{22}	0.72(7)
x_{33}	0.091(3)
x_{12}	0.3(3)
x_{23}	0.08(4)
x_{13}	0.08(7)

Table 3.3: Magnetic, structural and extinction parameters for $YbMnSb_2$ determined by refinement in the space group $P4/nmm$ and irrep Γ_6 against integrated intensities collected at 2 K. $R_F = 1.77\,\%$ and $\chi^2_R = 1.5$ for this refinement.

Atom	Wyckoff position	x	y	z	B_{iso}
Yb	2c	0.25	0.25	0.7282(1)	0.10
Mn	2a	0.75	0.25	0.00	0.283
Sb	2b	0.75	0.25	0.50	0.322
Sb	2c	0.25	0.25	0.16012(1)	0.322

Extinction Parameter	Value
x_{11}	0.519(1)
x_{22}	0.448(1)
x_{33}	0.0968(1)
x_{12}	0.270(1)
x_{23}	0.08102(5)
x_{13}	0.2712(5)

Spin	Moment (μ_B)
Mn^{2+}	3.46(1)

Results from the MAG2POL refinements of magnetic structure are shown in Figure 3.6. Refinements were performed for C-type AFM with moments $\perp c$ (Γ_{10}), C-type AFM with moments $\parallel c$ (Γ_6), and

G-type AFM with moments $\parallel c$. Although G-type AFM was ruled out based on the combination of no non-integer reflections with any significant intensity in the D10 data and parent $P4/nmm$ space group, I nevertheless performed a refinement with this magnetic order for completeness given this was the magnetic structure assumed in [31]. The best fit is achieved with the refinement using C-type AFM with moments $\parallel c$ as the model.

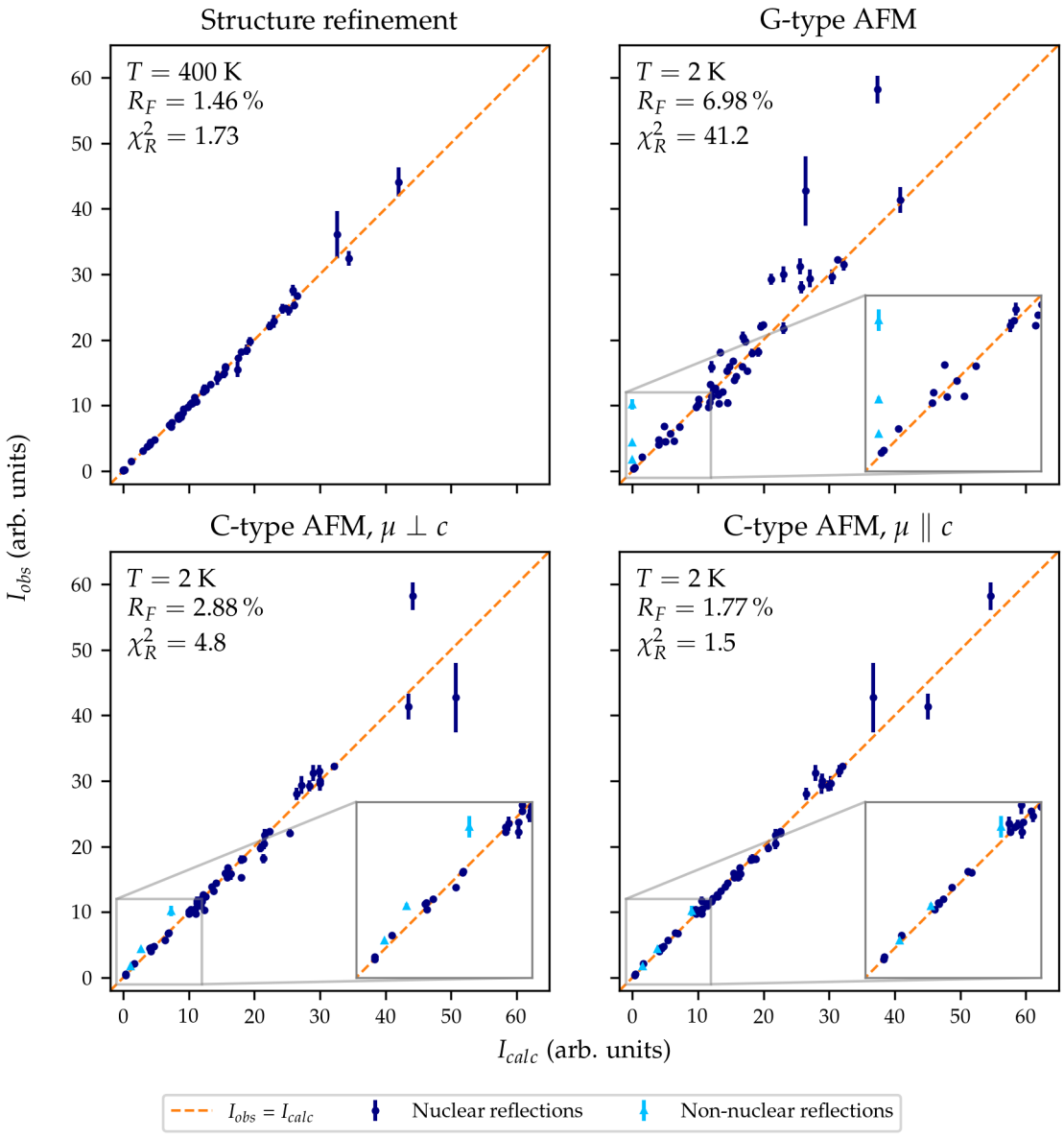

Figure 3.6: Plots showing calculated vs observed intensities of reflections from $YbMnSb_2$ D10 experiment. The dark blue points denote the intensities of reflections allowed by the $P4/nmm$ space group, while light blue points denote the intensities of reflections forbidden by the $P4/nmm$ space group.

3.3.4 Magnetic space group

Another approach to solving the magnetic structure is to consider magnetic space groups (MSGs). I will quickly go through the MSG approach here. To generate a MSG, basically start with a (structural) space group and then time reverse all the current loops (magnetic dipoles) and see which symmetry operations still work. Lattice points are either black or white, and time reversal (anti-symmetry) turns white points black and vice versa. The anti-symmetry operator $1'$ is not a symmetry operator of any magnetic space group that corresponds to magnetic order but has to piggyback on another operator e.g. m' is an 'antimirror' = mirror plane + colour change/time reversal. MSGs for paramagnetic 'structure' do have $1'$ as a symmetry operator.

There are different ways of classifying magnetic space groups, here I choose the Belov-Neronova-Smirnova (BNS) setting, where the magnetic unit cell $\equiv$ the unit cell for the space group. There are different types of magnetic space groups:

- Type I: single colour, no primes, FM unless $\mathbf{q} \neq (0,0,0)$
- Type II: colour is grey, $1'$ is a symmetry operation, paramagnetic only.
- Type III: black and white groups, AFM and FM possible.
- Type IV: black and white groups, 'antitranslations' are possible! Magnetic unit cell > structural unit cell i.e. $\mathbf{q} \neq (0,0,0)$, only AFM is possible.

The possible MSGs derived from space group $P4/nmm$ for $\mathbf{q} = (0,0,0)$ are listed in Table 3.4.

The only suitable MSG is $P4'/n'm'm$, which is the same as some other $A\mathrm{Mn}X_2$ compounds [28, 43, 44]. This is consistent with the representation analysis described above.

3.3.5 Temperature dependence of reflections

The structurally forbidden (100) reflection shows a clear temperature dependence akin to a Landau order parameter (Fig. 3.7). Fitting an equation of the form

$$\text{intensity} = A\left(\frac{T - T_N}{T_N}\right)^{2\beta} \tag{3.1}$$

yielded a critical exponent of $\beta = 0.308(3)$ and $T_N = 345.9(1)$ K. The input for the fit was data in the temperature range 220 K – 400 K.

Temperature dependent measurements were also made of (001) and (002) reflections. For both of these structurally-permitted reflections, we would expect the intensity of the peak to decrease

Table 3.4: Magnetic space groups derived from space group $P4/nmm$ (BNS setting = magnetic unit cell is the unit cell) from MAXMAGN on the Bilbao Server [42], with notes on admissible types of magnetism according to MWYCKPOS on the Bilbao Server.

MSG	Type	Notes
$P4/nmm$	I	Discount ⋱ FM
$P4/nmm1'$	II	Discount ⋱ paramagnetic
$P4/n'mm$	III	Discount ⋱ no AFM $\parallel c$ on $2a$ sites
$P4'/nm'm$	III	Discount ⋱ no AFM $\parallel c$ on $2a$ sites
$P4'/nmm'$	III	Discount ⋱ no AFM $\parallel c$ on $2a$ sites
$P4'/n'm'm$	III	Compatible with AFM $\parallel c$
$P4/nm'm'$	III	Discount ⋱ FM only in c direction
$P4'/n'mm'$	III	Discount ⋱ no AFM $\parallel c$ on $2a$ sites
$P4/n'm'm'$	III	Discount ⋱ no AFM $\parallel c$ on $2a$ sites
P_C4/nmm	IV	Discount ⋱ $\mathbf{k} \neq (0,0,0)$
P_C4/nmm	IV	Discount ⋱ $\mathbf{k} \neq (0,0,0)$
P_I4/nmm	IV	Discount ⋱ $\mathbf{k} \neq (0,0,0)$

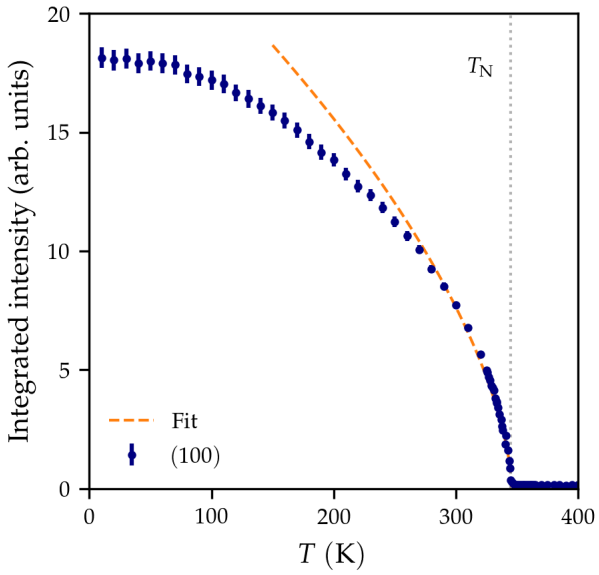

Figure 3.7: Temperature dependence of structurally forbidden (100) reflection of $YbMnSb_2$. The orange dashed line is a fit to Equation 3.1 over the temperature range 220 K – 400 K. A version of this figure was originally published in reference [15]. Copyright American Physical Society (2021).

in line with the Debye-Waller factor as temperature increases. A slight but unpredicted increase in integrated intensity for both of these peaks at temperatures $> T_N \approx 346$ K can be seen in Figure 3.8. A possible explanation is the presence of a ferromagnetic impurity such as MnSb, which has $T_C \approx 560$ K [40, 45].

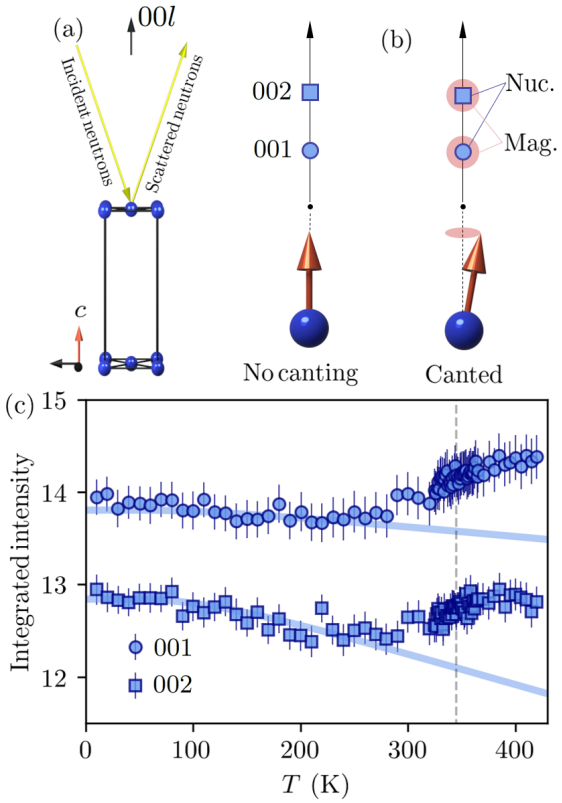

Figure 3.8: (a) Unpolarised neutrons were used on the D10 instrument (ILL), with the scattering vector **Q** along 00l. (b) Since magnetic neutron diffraction is sensitive to the component of **M** perpendicular to **Q**, namely $\mathbf{M}_{\perp}$, a canting of the Mn moments away from the crystal c axis will produce a magnetic contribution to the nuclear Bragg reflections along 00l. (c) The temperature dependence of the integrated intensities of the (001) and the (002) reflections. The line corresponds to the fit to the Debye-Waller factor. This figure was originally published in reference [15]. Copyright American Physical Society (2021).

3.4 Half-polarised neutron diffraction of $YbMnSb_2$

We conducted the experiment with the 'half-polarised' set-up, in which the incident beam is polarised but there is no polarisation analysis of the scattered beam. There were two distinct motivations for performing a half-polarised experiment on $YbMnSb_2$. The first objective was to measure any canting of the spins away from the c axis. The second objective was to perform a magnetic structure factor measurement so that the magnetisation density could be mapped throughout the unit cell, and that the field-induced moments on the Mn^{2+} ions could be calculated.

3.4.1 Method

Half-polarised neutron diffraction was conducted on the D3 diffractometer at the ILL [46]. A single crystal of $YbMnSb_2$ was prealigned using the ILL's neutron Laue diffractometer OrientExpress [47]. Polarised neutrons of wavelength $\lambda = 0.832$ Å were produced by a Heusler monochromator, and

a cryoflipper was used to switch their spin states from parallel to antiparallel with the external magnetic field. Two erbium filters were placed in the incident beam to minimise $\lambda/2$ contamination.

To check for canting of spins away from the c axis, the crystal was oriented such that the b axis was at a normal to the horizontal scattering plane, and the magnetic field was applied along the b axis direction. Hence the $h0l$ reflections would be sensitive to any magnetic components along the b axis. The crystal was cooled from 600 K to 400 K in a magnetic field of 3 T (along b axis) provided by a superconducting magnet. This was done to promote the formation of a single FM canted domain, i.e. all spins would cant towards the positive b axis. At 400 K, the magnetic field was reduced to 0.4 T. This was the minimum field needed to maintain the neutron polarisation. The field-induced moment of the Mn spins is miniscule with an external field of 0.4 T according to the magnetisation data seen in Figure 3.5. Flipping ratios (i.e. the ratio of the diffracted intensities for neutrons with spins parallel and antiparallel to the applied field) of different reflections were measured.

For the magnetic structure factor measurement, the crystal remained in the same orientation: the magnetic field applied along the vertical direction, parallel to the b axis. A larger field of $\mu_0 H = 9.0$ T was used. The sample was measured in the paramagnetic phase at a temperature of 400 K, with any ferromagnetism manifesting solely due to the applied magnetic field. Flipping ratios were measured at 25 $h0l$ reflections, as well as 20 hkl reflections with $k = 1, 2$ that were accessible.

3.4.2 Results

The beauty of the half polarised technique is that the ratio of nuclear and magnetic scattering can be distilled into one quantity, the flipping ratio. This offers higher sensitivity when dealing with small amounts of magnetic scattering, compared to integrating peak intensities directly when the peaks contain both nuclear and magnetic scattering. For $YbMnSb_2$, assuming a centrosymmetric structure and the magnetic field perpendicular to $\mathbf{Q}$, the flipping ratio R (Equation 2.33) simplifies to

$$R(\mathbf{Q}) = 1 + 4\frac{F_M(\mathbf{Q})}{F_N(\mathbf{Q})} \tag{3.2}$$

where $F_M(\mathbf{Q})$ is the magnetic structure factor (MSF, Equation 2.31) and $F_N(\mathbf{Q})$ is the nuclear structure factor (NSF, Equation 2.18), with $F_M(\mathbf{Q}) \ll F_N(\mathbf{Q})$. To calculate the magnetic form factor $f_{Mj}(\mathbf{Q})$ (MFF) input into the MSF, I used the approximation [48, 49]

$$f_{Mj}(\mathbf{Q}) = A\exp\left[-a\left(\frac{Q}{4\pi}\right)^2\right] + B\exp\left[-b\left(\frac{Q}{4\pi}\right)^2\right] + C\exp\left[-c\left(\frac{Q}{4\pi}\right)^2\right] + D. \tag{3.3}$$

Since I only had Mn^{2+} to worry about, there is no j dependence for the MFF and I used the MFF approximation with the following parameters for Mn^{2+} [48]:

$$\begin{aligned} A &= 0.4220, \quad a = 17.6840, \\ B &= 0.5948, \quad b = 6.0050, \\ C &= 0.0043, \quad c = -0.6090, \\ D &= -0.0219. \end{aligned}$$

Search for canting

For the field-cooled measurement at 400 K with 0.4 T applied, all flipping ratios at symmetry distinct **Q** were approximately 1. This indicates there is no spontaneous in-plane FM component at high temperature. The results are shown in Figure 3.9, together with calculated flipping ratios for in-plane FM moments of 0.01 μ_B, 0.02 μ_B and 0.03 μ_B by way of comparison. In this way, any canted (in-plane FM) moments of the Mn were constrained to $< 0.01\mu_B$.

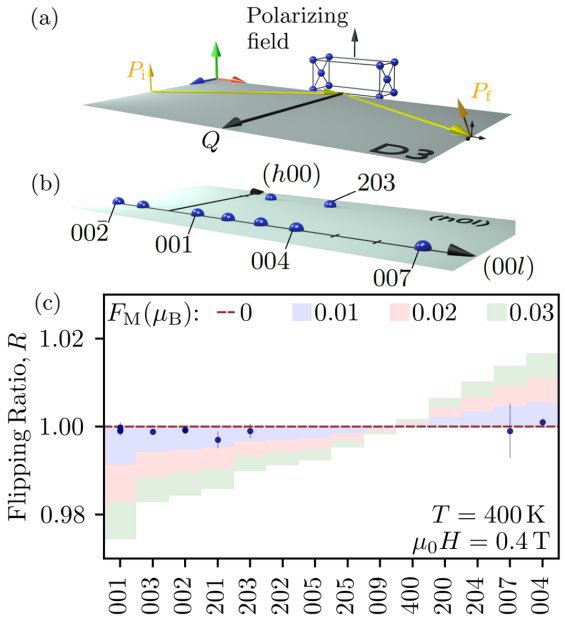

Figure 3.9:] (a) To access the $(h0l)$ reflections in the half-polarised experimental setup on D3, a $YbMnSb_2$ single crystal was aligned with the crystal b axis vertical. The incident neutrons are polarised along z ($P_i \parallel z$) and the scattered neutron polarisation P_f is not analysed. (b) Reciprocal space plot of the measured reflections (blue spheres) in the $(h0l)$ scattering plane. (c) Measured flipping ratios (blue circles) along with the calculated R for zero in-plane moment (dashed line) and several non-zero values up to 0.03 μ_B (coloured bars). This figure was originally published in reference [15]. Copyright American Physical Society (2021).

Structure factor measurement

The flipping ratios measured at 9 T were converted to field-induced magnetic structure factors by the method described in [49]. As the flipping ratios are all close to unity there is no ambiguity in the obtained magnetic structure factors, which are plotted in Figure 3.10 and Figure 3.11. The non-zero MSF agree with the reflection condition $h + k = 2n$. This is consistent with the field-induced ferromagnetic phase having the same symmetry as the underlying crystal structure with space group $P4/nmm$. The reflections $h = 1$, $k = 0$ do not obey the reflection condition $h + k = 2n$. Nearly all of these have zero F_M to within experimental uncertainty, except for (106).

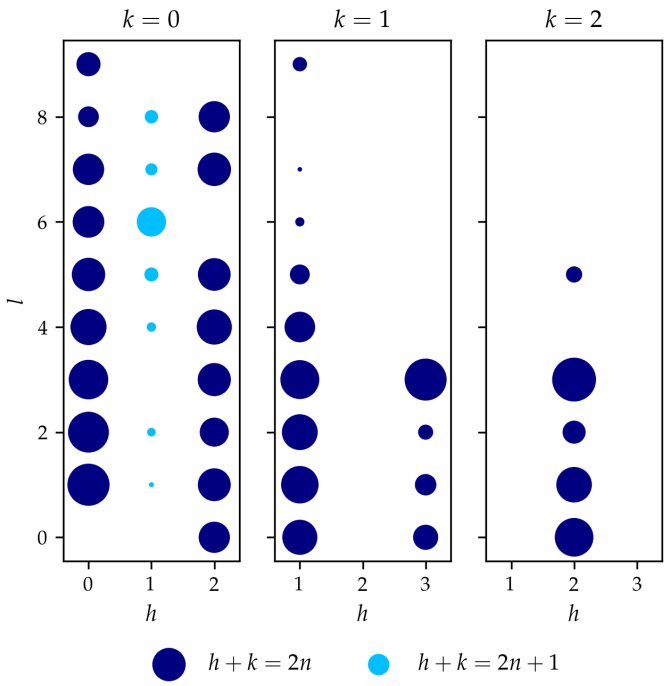

Figure 3.10: Magnetic structure factors calculated from measured flipping ratios. The radius of the circles is proportional to the magnetic structure factor at that *hkl* reflection. Dark blue indicates structurally allowed reflections obeying the selection rule $h + k = 2n$ for the $P4/nmm$ space group, light blue indicates reflections that are structurally forbidden ($h + k = 2n + 1$). A version of this figure was originally published in reference [1]. Copyright American Physical Society (2023).

The MSFs were utilised in a Bayesian reconstruction of the magnetisation distribution within the unit cell, shown in Figure 3.12. This was performed using a maximum entropy method (MaxEnt) implemented at the ILL, using routines from the MEMSYS library [50]. This method has advantages over directly Fourier transforming the MSFs because a Fourier transform assumes the input MSFs are a complete set with equal weight given to each MSF, whereas the maximum entropy method assumes nothing about the absent structure factors [51].

Cross-sections through the calculated magnetisation distribution in the Mn and Sb planes are shown

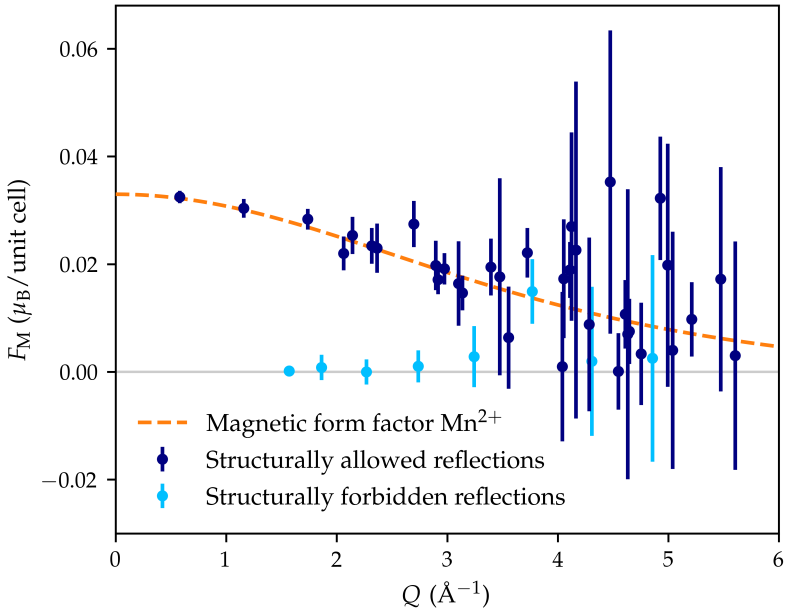

Figure 3.11: Magnetic structure factors calculated from measured flipping ratios as a function of Q, compared to the free-ion magnetic form factor of Mn^{2+} calculated using Equation 3.3 (orange dashed line). Dark blue indicates structurally allowed reflections obeying the selection rule $h + k = 2n$ for the $P4/nmm$ space group, light blue indicates reflections that are structurally forbidden ($h + k = 2n + 1$). A version of this figure was originally published in reference [1]. Copyright American Physical Society (2023).

in Figure 3.13. These slices show that the bulk of the magnetism induced by the external field is localised around the Mn sites and is approximately isotropic. Hence, we infer that all five Mn $3d$ orbitals are roughly equally populated, as predicted for the high spin state of Mn^{2+} ($3d^5$, $S = 5/2$). Integrating a volume around a Mn site yields an estimate of the total induced magnetic moment 0.011(4) μ_B per Mn. This integration followed a method developed by Markvardsen to obtain these moment values and their estimated uncertainties [52].

Note that a region of small negative magnetisation is observed around the Sb sites in the central layer at $z = 0.5$, with the induced moment calculated to be $-0.0002(6)\,\mu_B$ per Sb. The MaxEnt method uses a prior probability of uniform magnetisation throughout the unit cell and is designed to attribute a non-zero magnetisation only when there is evidence for it in the data. Nevertheless, the size of the uncertainty in the Sb moment is comparable with the moment itself, and so I would read into this small 'anti' magnetisation density with caution.

3.5 Discussion of magnetic structure of $YbMnSb_2$

The results from the experiments on $YbMnSb_2$ on ILL's D10 and D3 instruments and magnetometry indicate that the material exhibits C-type AFM along the c axis with negligible or no canting of

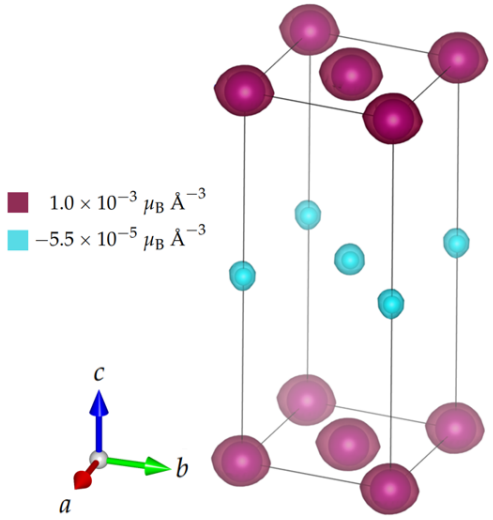

Figure 3.12: Magnetisation density distribution in the unit cell of $YbMnSb_2$, with isosurfaces showing strong concentration of magnetisation on Mn sites and a very small negative magnetisation on Sb sites in the middle of the unit cell. This figure was originally published in reference [1]. Copyright American Physical Society (2023).

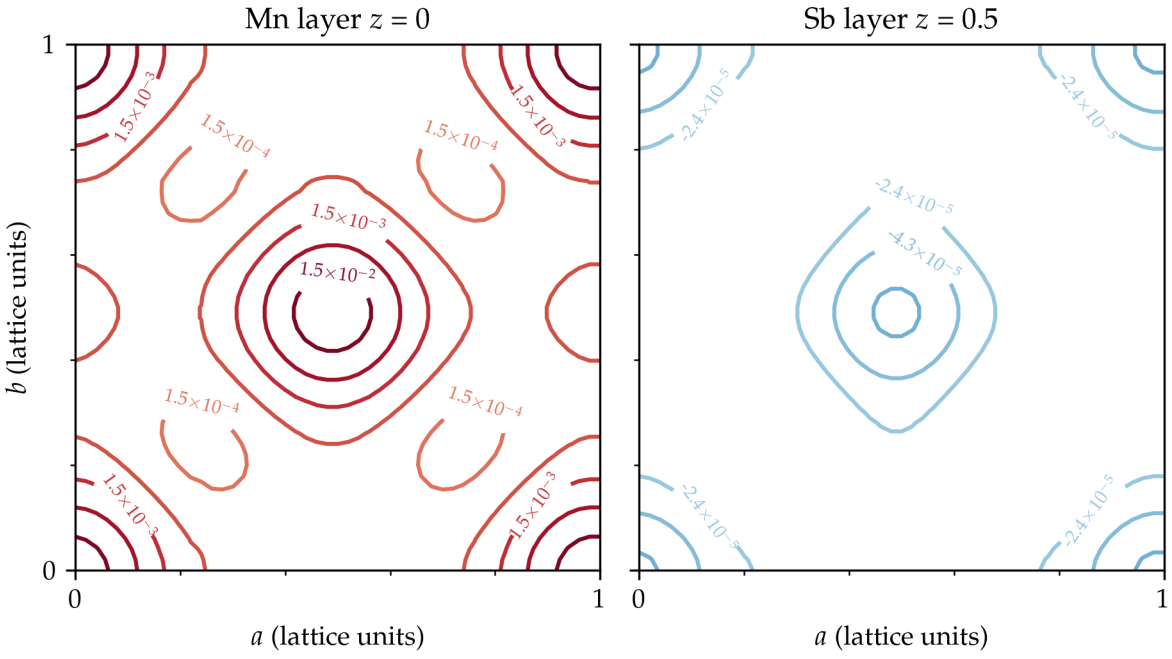

Figure 3.13: Slices through the ab plane showing magnetisation density map reconstructed from ILL D3 data. Contour lines show magnetisation density in units of μ_B Å^{-3}. A version of this figure was originally published in reference [1]. Copyright American Physical Society (2023).

Mn^{2+} spins (in-plane FM component $< 0.01\ \mu_B$) below $T_N \approx 346$ K. This agrees with a recent report on the magnetism of $YbMnSb_2$ which also made use of neutron diffraction, polarised neutron diffraction, x-ray diffraction and transport measurements [14]. The magnetic moments are well localised on the Mn sites with magnitude of 3.46 μ_B (in [14], 3.17 μ_B); however, the size of the

moment is less than moment predicted for Mn^{2+} in the high-spin state, 5 μ_B. The critical exponent of the magnetic phase transition is $\beta \approx 0.308$ (in [14], $\beta \approx 0.24$), which is significantly smaller than the $\beta = 0.36$ predicted for a 3D Heisenberg AFM and closer to $\beta = 0.32$ predicted for a 3D Ising AFM. However, the $\beta \approx 0.308$ was determined from a fit of the data in the temperature range 220 – 400 K, and this model over-estimates the intensity at the lowest temperatures (< 100 K), where a smaller critical exponent may apply. A smaller β is associated with a lower dimensionality of the lattice and a lower dimensionality of the order parameter, and so this indicates the quasi-2D nature and Ising-like anisotropy of the magnetism of $YbMnSb_2$.

Where the work [14] and our results described here (published in [15]) differ is the precise crystal and magnetic structure of $YbMnSb_2$. Here I contend that the magnetic space group of $YbMnSb_2$ is $P4'/n'm'm$, whereas the magnetic structure of $YbMnSb_2$ is ascribed to the orthorhombic $Pn'm'a'$ magnetic space group in [14]. The orthorhombicity is very slight ($\approx 0.31\%$) and the averaged lattice parameters $(b+c)/2 = 4.3167$ Å and $a/2 = 10.79815$ Å in [14] agree with the parameters of our refinement to within 0.1% and 0.3% for $a = b$ and c in $P4/nmm$ respectively. The shift in positions of atoms is similarly small. Like $P4/nmm$, $Pnma$ is centrosymmetric and has a glide symmetry in the Sb 'square net' plane. For the $AMnX_2$ family of materials, there are more significant implications for band structure topology if the space group symmetry further reduces to a polar space group, e.g. in the case of $BaMnSb_2$ [11].

Our work [15] also includes DFT calculations of the electronic band structure of $YbMnSb_2$, which used the empirically determined magnetic structure $P4'/n'm'm$ as a starting point (rather than assuming a favoured magnetic ground state based on *ab initio* calculations). The DFT calculations were performed by Dr Jian-Rui Soh and a spaghetti plot is shown in Figure 3.14. Linear band dispersion is found at anti-crossings close to the Fermi level at two points, one along the $\Gamma - M$ symmetry line and the other along $\Gamma - X$. The DFT result indicates that $YbMnSb_2$ is a gapped Dirac semimetal, with quasiparticle masses estimated to be 0.2 meV and 0.15 meV. The Fermiology presented in [14] is not so very different, with a reduced Brillouin zone and higher anisotropy of the hole/electron pockets due to the space group being $Pnma$. Interestingly, it is also suggested in [14] that the orthorhombic distortion raises the Fermi energy by ~ 50 meV. There are other mechanisms to tune E_F, including shifting the chemical potential via doping. Ultimately the conclusion as to the topological semimetal nature of $YbMnSb_2$ is that it is a gapped Dirac semimetal.

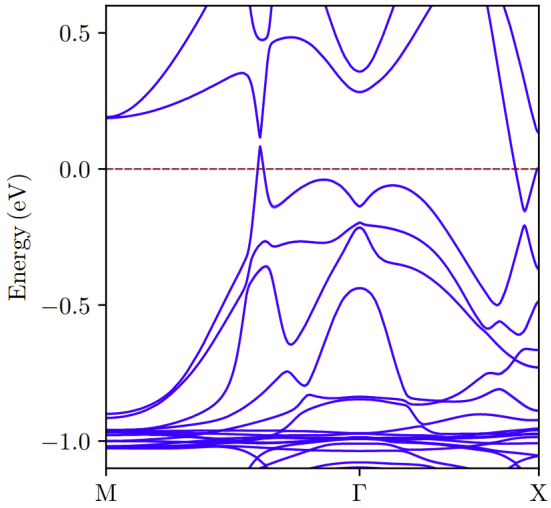

Figure 3.14: *Ab initio* electronic dispersion of $YbMnSb_2$ along in-plane high symmetry directions. The calculation assumes the magnetic structure determined in this work. This figure was originally published in reference [15]. Copyright American Physical Society (2021).

3.6 Inelastic neutron scattering of $YbMnSb_2$

The motivation behind the inelastic scattering experiment on $YbMnSb_2$ was to characterise the spin wave excitations and therefore the exchange interactions present. This would inform us as to how the magnetic structure (determined through the diffraction experiments above in § 3.3) is stabilised and possible interplay between the magnetism and topological quasiparticle fermions hosted within $YbMnSb_2$.

3.6.1 Method

Triple-axis spectroscopy was performed on the IN8 instrument at the ILL. The assembly of crystals described in § 3.2 was used as the sample. The FLATCONE multiplexed analyser-detector system was used on IN8 [53]. The FLATCONE array of 36 detectors sweeps out arcs in reciprocal space, allowing for greater coverage compared to traditional TAS using only one detector. The $(h0l)$ and (hhl) planes were accessible via two different orientations of the sample plate, separated by 45°. The outgoing neutron wavevector of $k_f = 3\,\text{Å}^{-1}$ was fixed by Bragg reflection from the silicon (111) analyser crystals incorporated into FLATCONE. Meanwhile the incident wavevector k_i was varied to give a range of neutron energy transfers ΔE from 0 to 70 meV. To set k_i, two monochromators were used: the double-focusing Si (111) for lower energies ($\Delta E < 40$ meV), or a double-focusing pyrolytic graphite (002) monochromator for higher energies ($\Delta E \geq 40$ meV). The FLATCONE was kept FLAT at a tilt angle of 0°, and the sample was held at a temperature of 1.5 K in a liquid He 'orange' cryostat for the entire experiment.

3.6.2 Data analysis

The inelastic neutron scattering data from the IN8 experiment contained both powder rings and 'spurions'. Due to the geometry of FLATCONE, the constant ΔE reciprocal space maps are best visualised as Voronoi diagrams, rather than a regular Cartesian grid. The background was non-negligible and highly Q dependent, with several spurions making an unwelcome appearance. Hence, it was necessary to post-process the data. The 'correction' process was as follows. For each reciprocal space map at different ΔE, NPLOT [54] was used to remove the spurions by hand. The spin wave signal was also subtracted and the remaining background smoothed such that the background only depended on Q. This isotropic background was subtracted from the raw data, and the 'spurious' data points were removed such that the size of Voronoi cells increased for regions that had contained spurions. The Delaunay triangulation plots between Voronoi cells for both raw and corrected data are shown in Fig. 3.15 for an example reciprocal space map ($(h0l)$ plane, $\Delta E = 18$ meV).

The Voronoi diagrams were interpolated to map the intensities to regular Cartesian grid. Constant energy cuts through the data were made along directions of interest through reciprocal space. Due to geometry of the IN8 instrument and the Flatcone array, the data are distorted slightly at higher Q (for example, in the $h0l$ plane, the spin waves appear to curve away from lines of constant h). We accounted for this effect by symmetrising the data about Brillouin zone boundaries once the dimensionality of the data had been reduced by taking constant $\mathbf{Q}$ energy cuts. For each energy cut, a number of peaks with Gaussian lineshape and a linear background were fitted. This was done using a suite of custom PYTHON programs (built using packages including those described in [55–57]).

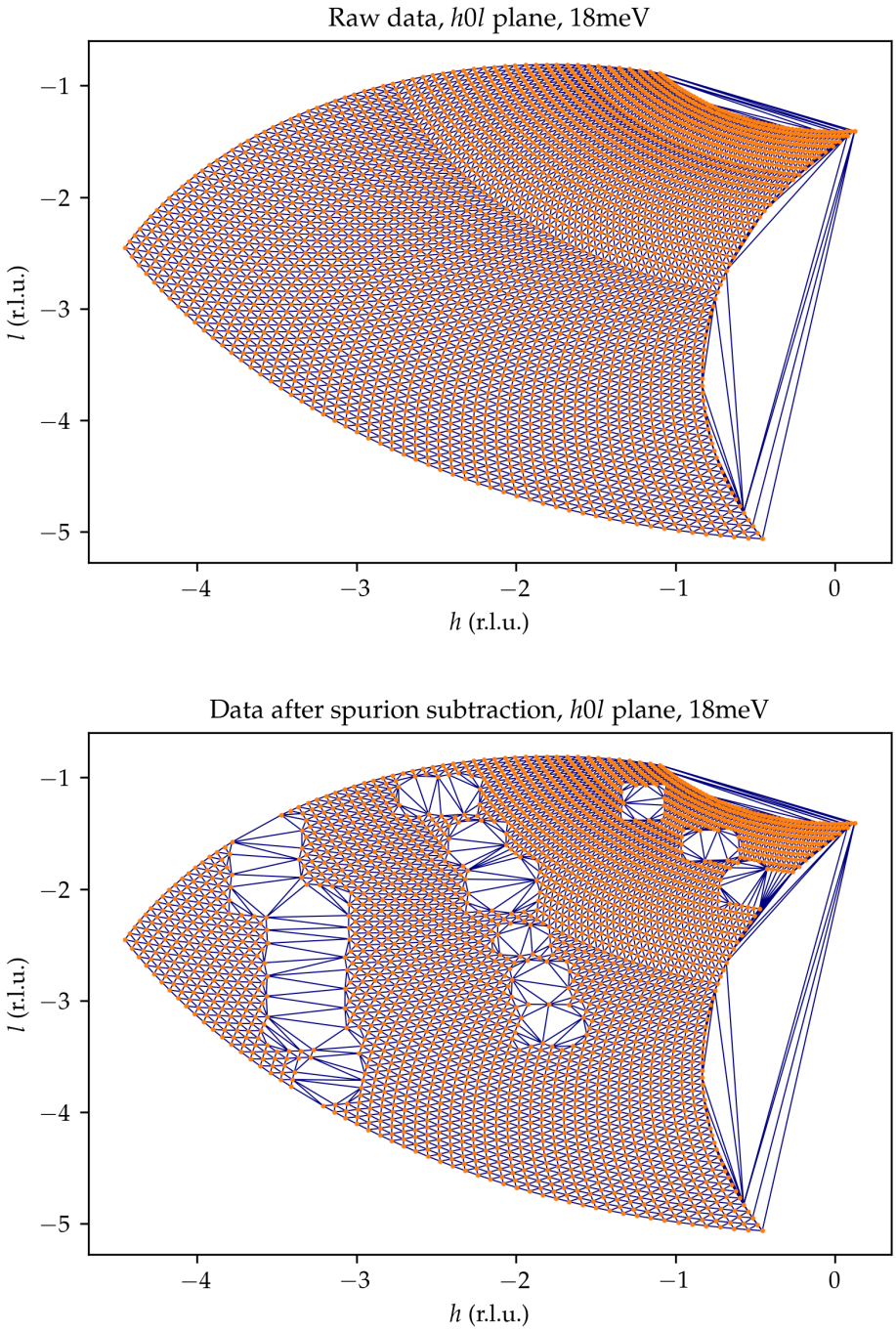

Figure 3.15: Delaunay triangulation plot for 18 meV *h*0*l* plane data. In the lower plot, the larger triangles indicate where data points have been removed due to spurions.

The high-symmetry lines used for cuts were $\Lambda = (0, 0, l)$, $U = (h, 0, \frac{1}{2})$, $\Delta = (h, 0, 0)$, $S = (h, h, \frac{1}{2})$ and $\Sigma = (h, h, 0)$. A selection of constant energy cuts together with peaks fitted are shown in Fig. 3.16. To improve the signal to noise ratio in the $h0l$ plane at $\Delta E \geq 40$ meV, and in the hhl plane at all energies, the integration was performed over specific detectors in the FLATCONE array that did not intersect Al powder rings. Next, the intensity maxima as a function of energy were found at the Γ and A points in order to anchor the turning points of the dispersion. Finally, the extracted peaks were assembled into the spin-wave dispersion along high-symmetry paths in reciprocal space shown in Figure 3.19.

3.6.3 Results

The IN8 data are shown as series of intensity maps for different ΔE in the $h0l$ (Figure 3.17) and hhl (Figure 3.18) planes. In the $h0l$ plane, the intensity is localised around the magnetic Γ positions at low energies. The intensity is highest at 10 meV, and decreases with energy until no signal is visible below about 5 meV (plotted in Figure 3.16). Above 10 meV, the intensity disperses outwards with increasing energy to form rings, which then evolve into a pattern resembling Neptune's necklace seaweed. The beads of seaweed eventually merge into rods of scattering running along the $(00l)$ direction at around 45 meV. In the hhl plane, rods of scattering along $(00l)$ are observed at all energies studied, with some intensity modulation along the rods at the lower energies. At higher energies the rods split into two; the newly-split rods then also move apart. By 55 meV, the signal is nearly indistinguishable from the background. I will now describe the model that demonstrates these features are consistent with the scattering from spin-wave excitations of antiferromagnetically ordered Mn local moments.

I modelled the magnetic interactions in $YbMnSb_2$ with a Heisenberg effective spin Hamiltonian of the form

$$\mathcal{H} = \sum_{i,j} J_{ij} \mathbf{S}_i \cdot \mathbf{S}_j - \sum_i D \left(S_i^z\right)^2, \tag{3.4}$$

and calculated the spin-wave spectrum using linear spin-wave theory (LSWT) for spins $\mathbf{S}_i$ localised on the Mn ions. This is similar to the approach used in works [58–60] for structurally related $A\mathrm{Mn}X_2$ compounds. For $\mathcal{H}$, I defined three isotropic exchange parameters, $J_{ij} = J_1, J_2$ for the nearest- and next-nearest Mn neighbours in the ab plane, and J_c for the nearest neighbour interaction along the c action. I also included a single-ion anisotropy parameter D, which in Equation 3.4 favours alignment of the Mn spins along the c axis. These parameters are displayed in Figure 3.20, and were sufficient to fit the data well. The parameter values were obtained from a global fit to the measured dispersion curves using both custom PYTHON programs (orthogonal distance regression)

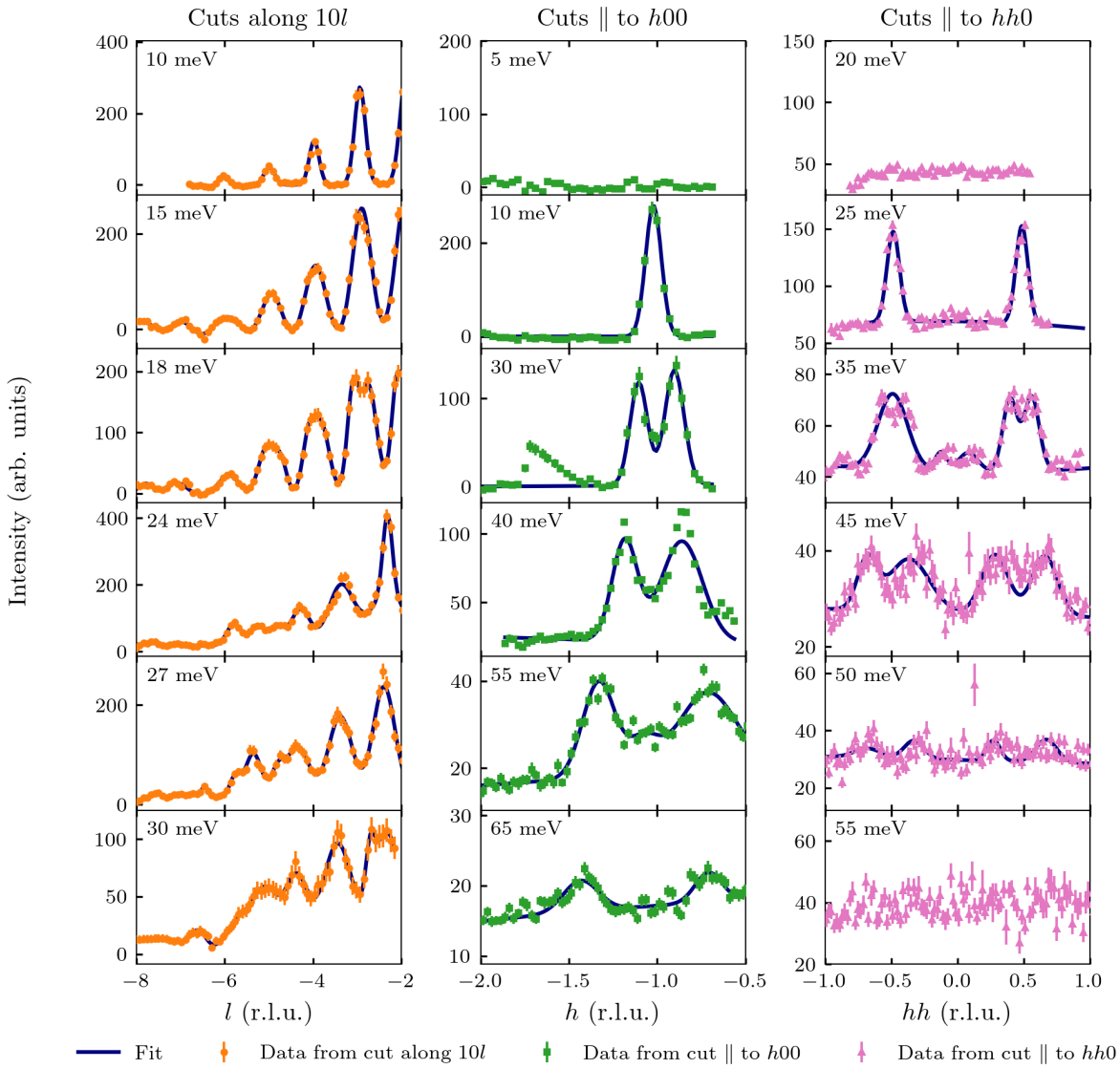

Figure 3.16: One dimensional cuts along $\mathbf{Q} = (10l)$ (orange) and parallel to $h00$ (green) of $h0l$ plane data for different ΔE. One dimensional cuts parallel to $hh0$ from the hhl plane data are also shown (pink) for different ΔE. Fits are shown in blue. A version of this figure was originally published in the Supplemental Material of [1]. Copyright American Physical Society (2023).

and the SpinW MATLAB library [61].

The calculated LSWT dispersion obtained from the best-fit parameters is shown in Figure 3.19 along with the data points. Along all symmetry directions, the model describes the data well. From the model, we can ascertain that the spin waves have a maximum energy of approximately 70 meV at the X-point in the Brillouin zone, where $X = (\frac{1}{2}, 0, 0)$, and a minimum gap of about 10 meV at the Γ-point.

The detail of the fit is also very satisfactory from a qualitative perspective, as seen by inspecting Figure 3.17 and Figure 3.18 closely. The rightmost column of these panels show simulations of the LSWT spectrum in the same region of reciprocal space and for the same energies that were probed experimentally. The magnetic form factor of Mn^{2+} is included in the simulations. It can be seen that the model reproduces the distribution of measured intensity throughout energy and momentum space very well.

The Hamiltonian parameters extracted from the LSWT fit are $SJ_1 = 28 \pm 2$ meV, $SJ_2 = 10.4(5)$ meV, $SJ_c = -0.73(7)$ meV and $SD = 0.44(5)$ meV (the spin quantum number S always multiplies the Hamiltonian parameters in LSWT). Here, positive values represent antiferromagnetic coupling, while negative values imply ferromagnetic coupling. The larger uncertainty in the SJ_1 value may be attributed to the inherent broadening of the dispersion in the ab plane, caused by the imperfect coalignment of the platelet crystals in this plane. According to the convention in Equation 3.4, the positive value of SD means that the Mn spins preferentially align along the c axis, which agrees with the magnetic structure determined for $YbMnSb_2$ in § 3.3. The exchange constants are presented in Table 3.5.

3.6.4 Discussion

In Table 3.5 I included the experimentally determined structural and exchange parameters for several other $AMnX_2$ materials for comparison with $YbMnSb_2$. There are a number of insights here. Firstly, the ordering temperature T_N seems to scale with the size of the exchange parameters, implying a more robust magnetically ordered phase. SJ_1, SJ_2 and SJ_c are all greater for $YbMnSb_2$ than other materials in the $AMnX_2$ family, especially SJ_c, and $YbMnSb_2$ has just about the highest T_N as discussed earlier. Second, the a lattice parameter of $YbMnSb_2$ is about 5 % smaller than that of the other materials, which likely explains why the SJ_1 and SJ_2 parameters are largest for $YbMnSb_2$. Third, the Mn-X-Mn bond angles associated with the the J_1 and J_2 superexchange paths both increase slightly, from 65.92° to 67.10° for J_1 and 100.60° to 102.82° for J_2, going from $YbMnBi_2$ to $YbMnSb_2$. These changes will tend to reduce the AFM superexchange contribution to J_1 and increase it for J_2, consistent with what is observed, although the effect is smaller than the overall increase in J_1 and J_2 associated with the decrease in a. The exchange parameters obtained through the analysis presented in this thesis are similar to those recently published by another group [37].

Finally, the distance between Mn atoms in the c direction is almost the same for all the compounds listed in Table 3.5, and yet SJ_c is around five times larger in $YbMnSb_2$ than in the Bi compounds. If not the exchange path geometry, what could be behind this? The p orbitals that mediate

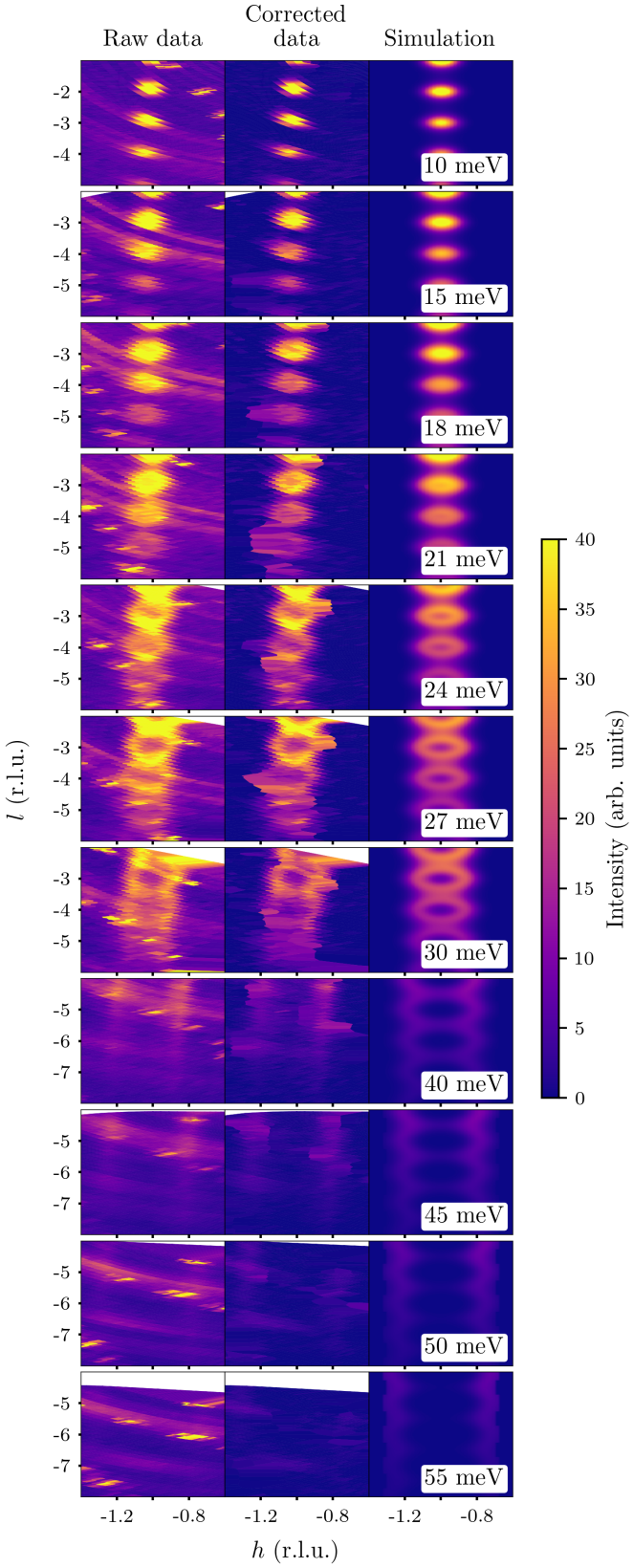

Figure 3.17: Spin-wave scattering and model for $h0l$ plane. Left column: raw neutron scattering data. Middle column: Data after the corrections described in the text. Right column: magnetic scattering simulated by linear spin-wave theory from our model. A version of this figure was originally published in reference [1]. Copyright American Physical Society (2023).

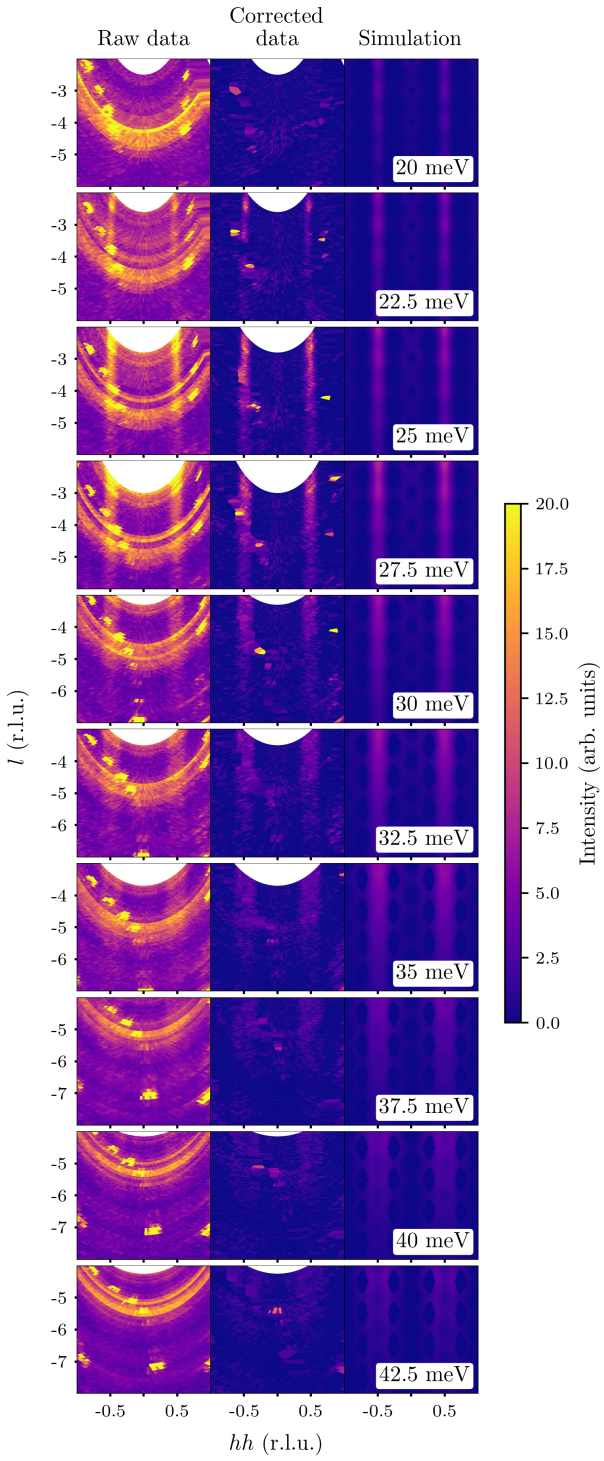

Figure 3.18: Spin wave data and model for *hhl* plane. The three columns show the experimental and simulated data as described in Figure 3.17. A version of this figure was originally published in reference [1]. Copyright American Physical Society (2023).

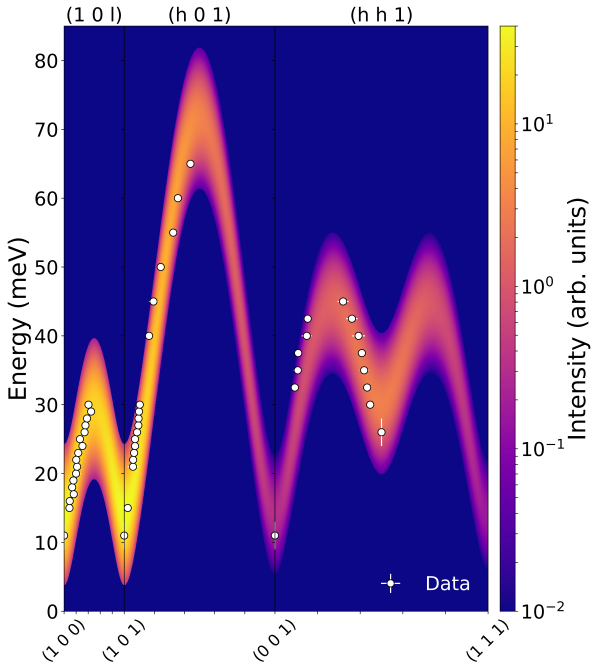

Figure 3.19: Spin-wave dispersion of $YbMnSb_2$. The data points are shown as white circles, and the spin-wave spectrum calculated from our model is shown as an intensity map with a logarithmic colour scale. The simulation includes a Gaussian energy broadening of 8 meV (FWHM). A version of this figure was originally published in reference [1]. Copyright American Physical Society (2023).

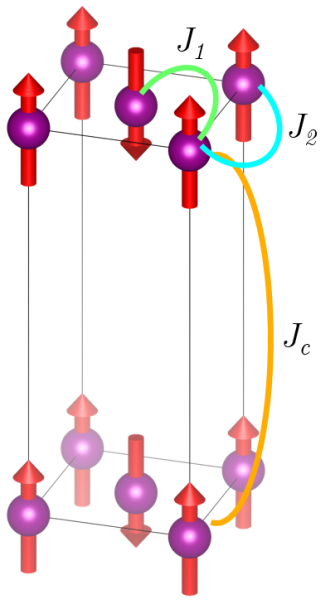

Figure 3.20: Magnetic unit cell of $YbMnSb_2$. Only the Mn ions are shown, together with moments indicated by red arrows and exchange interaction paths J_{ij} shown in blue, green and orange. A version of this figure was originally published in reference [1]. Copyright American Physical Society (2023).

Table 3.5: Experimentally determined parameters for $A\mathrm{Mn}X_2$. Exchange constants J_1, J_2 and J_c are defined in Figure 3.1, and D is the easy-axis anisotropy parameter. Mn-X-Mn bond angles: angle 1 is with one Mn located at the corner of the unit cell and the other in the centre of $z = 0$ face, and angle 2 is with the Mn located on neighbouring corners of the unit cell. Values in parentheses are errors in the last digits. A version of this table was originally published in reference [1]. Copyright American Physical Society (2023).

Material	Space group	a (Å)	c (Å)	T_N (K)	SJ_1 (meV)	SJ_2 (meV)	SJ_c (meV)	SD (meV)	Mn-X-Mn bond angle 1 (°)	Mn-X-Mn bond angle 2 (°)
$CaMnBi_2$ [58]	$P4/nmm$	4.50	11.07	264	23.4(6)	7.9(5)	-0.10(5)	0.18(3)	67.219(2)	103.04(1)
$SrMnBi_2$ [58]	$I4/nmm$	4.58	23.14	287	21.3(2)	6.39(15)	0.11(2)	0.31(2)	68.047(1)	104.614(1)
$YbMnBi_2$ [59]	$P4/nmm$	4.49	10.86	290	22.6(5)	7.8(5)	$-0.13(5)$	0.37(4)	65.92(4)	100.60(7)
$YbMnBi_2$ [60][a]	$P4/nmm$	4.48	10.8	290	22.7(3)	7.8(2)	$-0.16(3)$	0.43(4)		
$YbMnSb_2$ (this work [1, 15])	$P4/nmm$	4.31(2)	10.85(1)	345	28 ± 2	10.4(5)	$-0.73(7)$	0.44(5)	67.10(4)	102.82(7)
$YbMnSb_2$ [37]	$P4/nmm$	4.31(2)	10.85(1)	345	28.1(1)	10.7(1)	-0.597 ± 0.023	0.13(1)		

[a] The quoted parameters are from an analysis method which is similar to that used to obtain the other parameters listed in this table. A resolution-corrected fitting method gave the following parameters: $SJ_1 = 25.9(2)$ meV, $SJ_2 = 10.1(3)$ meV, $SJ_c = -0.130(3)$ meV, and $SD = 0.20(1)$ meV.

superexchange are lower in energy in Sb than in Bi. Assuming that J_c is determined by a competition between FM metallic double exchange and AFM superexchange [43], we expect a weaker AFM superexchange and hence a stronger net FM J_c in Sb relative to Bi, as observed. One interpretation of the small antimagnetisation density on the Sb 'square net' plane sites revealed by the D3 data (§ 3.4.2) is that the Mn-Sb exchange (however small) is AFM, further favouring a FM Mn-Mn coupling along the c axis. This implies that coupling between magnetism and the Dirac-like quasiparticle fermions may play a more important role in $YbMnSb_2$ than in the Bi compounds.

Indeed this is contended in the recent study [37], which presents stronger broadening of the spin waves as evidence for enhanced magnon-fermion coupling. The hypothesis behind this is that at low temperature, magnons primarily decay into electron-hole excitations involving the Sb 'square net' electron, rather than broadening mechanisms such as magnon-magnon or magnon-phonon decay. The research utilised TOF spectroscopy rather than TAS to measure the spin waves in $YbMnSb_2$. The spin wave model was different to the one described here in that it accounted for finite magnon lifetime, but it featured the same exchange parameters as inputs. The fitting procedure also considered the Q- and energy-dependent resolution function of the TOF spectrometer, which is far more difficult to constrain for a TAS instrument. The spin wave damping parameter was estimated to be twice that of $YbMnBi_2$, pointing to stronger out-of-plane interactions between the electrons responsible for the Mn magnetism and those in the topological quasiparticle Sb layer. This is an interesting result that highlights the utility of different instrumentation even within a single technique such as inelastic neutron scattering. However, to test whether the damping parameter is a good indicator of the influence of electronic band structure topology on spin waves will require inelastic neutron scattering measurements on a broad portfolio of different topological semimetals. This is challenging for two fairly plain reasons: the empirical verification of band structure topology primarily relies on fuzzy ARPES images of surface states, and the lack of large single crystals for bulk INS measurements.

3.7 Conclusions regarding the magnetism of $YbMnSb_2$

Our experiments have shown that the magnetic moments in $YbMnSb_2$ are well localised on the Mn atoms, and so a semiclassical spin-wave description of the magnetic dynamics in the antiferromagnetically ordered phase is appropriate.

The exchange interactions determined in this work from the magnon dispersion of $YbMnSb_2$ are all larger than in several related compounds containing Bi instead of Sb which have been studied

recently. The value of the interlayer coupling J_c is particularly notable, being around five times larger in $YbMnSb_2$ than in the Bi compounds. Considering the different superexchange and metallic contributions to J_c, we argue that the coupling between Dirac fermions and local spin moments on Mn may be more prominent in $YbMnSb_2$ than in the related Bi compounds. This suggests that $YbMnSb_2$ is a promising system with which to investigate the interplay between magnetism and topological band electrons.

Acknowledgements for this chapter

The crystal synthesis of $YbMnSb_2$ was performed by Hao Su and Yanfeng Guo of Shanghai Tech University.

The ILL D10 experiment was performed by Jian-Rui Soh, Siobhan Tobin, Andrew Boothroyd, Bachir Ouladdiaf and Ketty Beauvois. Data from this experiment are available via proposal number 5-41-1049. The proposal numbers for the crystal alignment experiments were EASY-671 (CYCLOPS) and EASY-667 (OrientExpress).

The ILL D3 experiment was performed by Jian-Rui Soh, Siobhan Tobin, Andrew Boothroyd, Anne Stunault and J. Alberto Rodriguez-Velamazan. Data from this experiment is available via proposal number 5-53-305 [62].

The ILL IN8 experiment was performed by Siobhan Tobin, Jian-Rui Soh, Andrew Boothroyd and Andrea Piovano. Data from this experiment are available via proposal number 4-01-1684 [63].

References

[1] S. M. Tobin, J.-R. Soh, H. Su, A. Piovano, A. Stunault, J. A. Rodríguez-Velamazán, Y. Guo, and A. T. Boothroyd. "Magnetic excitations in the topological semimetal $YbMnSb_2$". *Physical Review B* 107.19 (2023). DOI: 10.1103/PhysRevB.107.195146 (cited on pages 50, 55, 56, 68–70, 76, 78–81).

[2] J. Liu et al. "Nearly massless Dirac fermions hosted by Sb square net in $BaMnSb_2$". *Scientific Reports* 6.1 (2016). DOI: 10.1038/srep30525 (cited on pages 50, 52).

[3] J. B. He et al. "Quasi-two-dimensional massless Dirac fermions in $CaMnSb_2$". *Physical Review B* 95.4 (2017). DOI: 10.1103/PhysRevB.95.045128 (cited on page 50).

[4] Y.-Y. Wang, S. Xu, L.-L. Sun, and T.-L. Xia. "Quantum oscillations and coherent interlayer transport in a new topological Dirac semimetal candidate $YbMnSb_2$". *Physical Review Materials* 2.2 (2018). DOI: 10.1103/PhysRevMaterials.2.021201 (cited on pages 50, 53–55, 57).

[5] S. Klemenz, S. Lei, and L. M. Schoop. "Topological Semimetals in Square-Net Materials". *Annual Review of Materials Research* 49.1 (2019). DOI: 10.1146/annurev-matsci-070218-010114 (cited on pages 50, 51).

[6] S. Klemenz, A. K. Hay, S. M. L. Teicher, A. Topp, J. Cano, and L. M. Schoop. "The Role of Delocalized Chemical Bonding in Square-Net-Based Topological Semimetals". *Journal of the American Chemical Society* 142.13 (2020). DOI: 10.1021/jacs.0c01227 (cited on page 51).

[7] D. Gong, S. Huang, F. Ye, X. Gui, J. Zhang, W. Xie, and R. Jin. "Canted Eu magnetic structure in $EuMnSb_2$". *Physical Review B* 101.22 (2020). DOI: 10.1103/PhysRevB.101.224422 (cited on page 51).

[8] J.-R. Soh, P. Manuel, N. M. B. Schröter, C. J. Yi, F. Orlandi, Y. G. Shi, D. Prabhakaran, and A. T. Boothroyd. "Magnetic and electronic structure of Dirac semimetal candidate $EuMnSb_2$". *Physical Review B* 100.17 (2019). DOI: 10.1103/PhysRevB.100.174406 (cited on pages 51, 53).

[9] Q. Zhang, J. Liu, H. Cao, W. A. Phelan, J. F. DiTusa, D. A. Tennant, and Z. Mao. "Tuning quantum transport by controlling spin reorientations in Dirac semimetal candidates $Eu_{1-x}Sr_xMnSb_2$". *arXiv:2010.10405 [cond-mat]* (2021). DOI: 10.21203/rs.3.rs-799050/v1 (cited on pages 51, 53).

[10] S. Borisenko et al. "Time-reversal symmetry breaking type-II Weyl state in $YbMnBi_2$". *Nature Communications* 10.1 (2019). DOI: 10.1038/s41467-019-11393-5 (cited on pages 51–53).

[11] H. Sakai. "High-field Studies on Layered Magnetic and Polar Dirac Metals: Novel Quantum Transport Phenomena Coupled with Spin-valley Degrees of Freedom". *Journal of the Physical Society of Japan* 91.10 (2022). DOI: 10.7566/JPSJ.91.101001 (cited on pages 51–53, 71).

[12] K. Zhao, X. Chen, Z. Wang, J. Liu, J. Wu, C. Xi, X. Lv, L. Li, Z. Zhong, and P. Gegenwart. "Magnetic tuning of band topology evidenced by exotic quantum oscillations in the Dirac semimetal $EuMnSb_2$". *Physical Review B* 107.8 (2023). DOI: 10.1103/PhysRevB.107.L081112 (cited on page 51).

[13] A. F. May, M. A. McGuire, and B. C. Sales. "Effect of Eu magnetism on the electronic properties of the candidate Dirac material $EuMnBi_2$". *Physical Review B* 90.7 (2014). DOI: 10.1103/PhysRevB.90.075109 (cited on page 51).

[14] D. Bhoi et al. "Fermi surface reconstruction due to the orthorhombic distortion in Dirac semimetal $YbMnSb_2$". *arXiv:2306.12732 [cond-mat]* (2023). DOI: 10.48550/arXiv.2306.12732 (cited on pages 51, 53, 54, 70, 71).

[15] J.-R. Soh, S. M. Tobin, H. Su, I. Zivkovic, B. Ouladdiaf, A. Stunault, J. A. Rodríguez-Velamazán, K. Beauvois, Y. Guo, and A. T. Boothroyd. "Magnetic structure of the topological semimetal $YbMnSb_2$". *Physical Review B* 104.16 (2021). DOI: 10.1103/PhysRevB.104.L161103 (cited on pages 51, 53–55, 58, 59, 64, 65, 67, 71, 72, 81).

[16] J. S. You, I. Lee, E. S. Choi, Y. J. Jo, J. H. Shim, and J. S. Kim. "Shubnikov-de Haas oscillations of massive Dirac fermions in a Dirac antiferromagnet $SrMnSb_2$". *Current Applied Physics* 19.3 (2019). DOI: 10.1016/j.cap.2018.10.022 (cited on pages 52, 53).

[17] J. Deng, D. Shao, J. Gao, C. Yue, H. Weng, Z. Fang, and Z. Wang. "Twisted nodal wires and three-dimensional quantum spin Hall effect in distorted square-net compounds". *Physical Review B* 105.22 (2022). DOI: 10.1103/PhysRevB.105.224103 (cited on page 52).

[18] H. Ryu, S. Y. Park, L. Li, W. Ren, J. B. Neaton, C. Petrovic, C. Hwang, and S.-K. Mo. "Anisotropic Dirac

Fermions in $BaMnBi_2$ and $BaZnBi_2$". *Scientific Reports* 8.1 (2018). DOI: 10.1038/s41598-018-33512-w (cited on page 52).

[19] M. Kondo et al. "Tunable spin-valley coupling in layered polar Dirac metals". *Communications Materials* 2.1 (2021). DOI: 10.1038/s43246-021-00152-z (cited on page 52).

[20] Z. Zhang, Z. Guo, J. Lin, F. Sun, X. Han, G. Wang, and W. Yuan. "Effect of Cu Doping on Structure and Physical Properties in the Antiferromagnetic Dirac Semimetal $CaMnBi_2$". *Inorganic Chemistry* 61.11 (2022). DOI: 10.1021/acs.inorgchem.1c03410 (cited on page 53).

[21] Y. Xia et al. "Doping-induced spin reorientation and magnetic phase diagram of $EuMn_{1-x}Zn_xSb_2$ ($0 \leq x \leq 1$)". *Physical Review B* 107.18 (2023). DOI: 10.1103/PhysRevB.107.184415 (cited on page 53).

[22] J. Y. Liu et al. "A magnetic topological semimetal $Sr_{1-y}Mn_{1-z}Sb_2$ ($y, z < 0.1$)". *Nature Materials* 16.9 (2017). DOI: 10.1038/nmat4953 (cited on page 53).

[23] H. Rong et al. "Electronic structure examination of the topological properties of $CaMnSb_2$ by angle-resolved photoemission spectroscopy". *Physical Review B* 103.24 (2021). DOI: 10.1103/PhysRevB.103.245104 (cited on page 53).

[24] S. V. Ramankutty et al. "Electronic structure of the candidate 2D Dirac semimetal $SrMnSb_2$: a combined experimental and theoretical study". *SciPost Physics* 4.2 (2018). DOI: 10.21468/SciPostPhys.4.2.010 (cited on page 53).

[25] Q. Zou, S. Huang, W. Ko, M. Fu, Y. Yang, K. Zhao, S. R. Crittenden, E. W. Plummer, R. Jin, and Z. Gai. "Exploration of two surfaces observed in Weyl semimetal $BaMnSb_2$". *npj Quantum Materials* 7.1 (2022). DOI: 10.1038/s41535-022-00494-y (cited on page 53).

[26] A. Pal, M. Chinotti, L. Degiorgi, W. J. Ren, and C. Petrovic. "Optical properties of $YbMnBi_2$: A type II Weyl semimetal candidate". *Physica B: Condensed Matter* 536 (2018). DOI: 10.1016/j.physb.2017.09.079 (cited on page 53).

[27] X.-S. Ni, C.-Q. Chen, D.-X. Yao, and Y. Hou. "Origin of the type-II Weyl state in topological antiferromagnetic $YbMnBi_2$". *Phys. Rev. B* 105 (13 2022). DOI: 10.1103/PhysRevB.105.134406 (cited on pages 53, 54).

[28] J. Y. Liu et al. "Unusual interlayer quantum transport behavior caused by the zeroth Landau level in $YbMnBi_2$". *Nature Communications* 8.1 (2017). DOI: 10.1038/s41467-017-00673-7 (cited on pages 53, 63).

[29] Y. Pan, C. Le, B. He, S. J. Watzman, M. Yao, J. Gooth, J. P. Heremans, Y. Sun, and C. Felser. "Giant anomalous Nernst signal in the antiferromagnet $YbMnBi_2$". *Nature Materials* 21.2 (2022). DOI: 10.1038/s41563-021-01149-2 (cited on pages 53, 54).

[30] R. Kealhofer et al. "Observation of a two-dimensional Fermi surface and Dirac dispersion in $YbMnSb_2$". *Physical Review B* 97.4 (2018). DOI: 10.1103/PhysRevB.97.045109 (cited on pages 53–55, 59).

[31] Z. Qiu, C. Le, Z. Liao, B. Xu, R. Yang, J. Hu, Y. Dai, and X. Qiu. "Observation of topological nodal-line semimetal in $YbMnSb_2$ through optical spectroscopy". *Physical Review B* 100.12 (2019). DOI: 10.1103/PhysRevB.100.125136 (cited on pages 53–55, 62).

[32] Y. Pan et al. "Thermoelectric Properties of Novel Semimetals: A Case Study of $YbMnSb_2$". *Advanced Materials* 33.7 (2021). DOI: 10.1002/adma.202003168 (cited on page 53).

[33] S. Baranets and S. Bobev. "Transport properties and thermal behavior of $YbMnSb_2$ semimetal above room temperature". *Journal of Solid State Chemistry* 303 (2021). DOI: 10.1016/j.jssc.2021.122467 (cited on page 53).

[34] K. Behnia and H. Aubin. "Nernst effect in metals and superconductors: a review of concepts and experiments". *Reports on Progress in Physics* 79.4 (2016). DOI: 10.1088/0034-4885/79/4/046502 (cited on page 54).

[35] A. Sakai et al. "Giant anomalous Nernst effect and quantum-critical scaling in a ferromagnetic semimetal". *Nature Physics* 14.11 (2018). DOI: 10.1038/s41567-018-0225-6 (cited on page 54).

[36] S. Xu, C. Jiang, S.-X. Li, J.-J. Mi, Z. Li, T.-L. Xia, Q. Tao, and Z.-A. Xu. "Large Nernst effect and possible temperature-induced Lifshitz transition in topological semimetal $YbMnSb_2$". *Physical Review B* 107.24 (2023). DOI: 10.1103/PhysRevB.107.245138 (cited on page 54).

[37] X. Hu, A. Sapkota, Z. Hu, A. T. Savici, A. I. Kolesnikov, J. M. Tranquada, C. Petrovic, and I. A. Zaliznyak. "Coupling of magnetism and Dirac fermions in $YbMnSb_2$". *Physical Review B* 107.20 (2023). DOI: 10.1103/PhysRevB.107.L201117 (cited on pages 55, 77, 81, 82).

[38] K. C. Rule, R. A. Mole, and D. Yu. "Which glue to choose? A neutron scattering study of various adhesive materials and their effect on background scatter-

ing". *Journal of Applied Crystallography* 51.6 (2018). DOI: 10.1107/S1600576718014930 (cited on page 56).

[39] E. B. Knudsen, H. O. Sørensen, J. P. Wright, G. Goret, and J. Kieffer. "FabIO: easy access to two-dimensional X-ray detector images in Python". *Journal of Applied Crystallography* 46.2 (2013). DOI: 10.1107/S0021889813000150 (cited on page 57).

[40] Y. Liu et al. "Crystal growth, microstructure, and physical properties of $SrMnSb_2$". *Physical Review B* 99.5 (2019). DOI: 10.1103/PhysRevB.99.054435 (cited on pages 57, 64).

[41] N. Qureshi. "Mag2Pol: a program for the analysis of spherical neutron polarimetry, flipping ratio and integrated intensity data". *Journal of Applied Crystallography* 52.1 (2019). DOI: 10.1107/S1600576718016084 (cited on page 60).

[42] J. Perez-Mato, S. Gallego, E. Tasci, L. Elcoro, G. de la Flor, and M. Aroyo. "Symmetry-Based Computational Tools for Magnetic Crystallography". *Annual Review of Materials Research* 45.1 (2015). DOI: 10.1146/annurev-matsci-070214-021008 (cited on page 64).

[43] Y. F. Guo, A. J. Princep, X. Zhang, P. Manuel, D. Khalyavin, I. I. Mazin, Y. G. Shi, and A. T. Boothroyd. "Coupling of magnetic order to planar Bi electrons in the anisotropic Dirac metals $A\,MnBi_2$ (A = Sr, Ca)". *Physical Review B* 90.7 (2014). DOI: 10.1103/PhysRevB.90.075120 (cited on pages 63, 82).

[44] A. Wang, I. Zaliznyak, W. Ren, L. Wu, D. Graf, V. O. Garlea, J. B. Warren, E. Bozin, Y. Zhu, and C. Petrovic. "Magnetotransport study of Dirac fermions in $YbMnBi_2$ antiferromagnet". *Physical Review B* 94.16 (2016). DOI: 10.1103/PhysRevB.94.165161 (cited on page 63).

[45] W. J. Takei, D. E. Cox, and G. Shirane. "Magnetic Structures in the MnSb-CrSb System". *Physical Review* 129.5 (1963). DOI: 10.1103/PhysRev.129.2008 (cited on page 64).

[46] E. Lelièvre-Berna et al. "ILL polarised hot-neutron beam facility D3". *Physica B: Condensed Matter*. Proceedings of the Fifth International Workshop on Polarised Neutrons in Condensed Matter Investigations 356.1 (2005). DOI: 10.1016/j.physb.2004.10.065 (cited on page 65).

[47] B. Ouladdiaf, J. Archer, G. J. McIntyre, A. W. Hewat, D. Brau, and S. York. "OrientExpress: A new system for Laue neutron diffraction". *Physica B: Condensed Matter* 385-386 (2006). DOI: 10.1016/j.physb.2006.05.337 (cited on page 65).

[48] P. J. Brown. "Magnetic Form Factors". *International Tables for Crystallography*. Vol. C. Kluwer Academic Publishers, 2004 (cited on pages 66, 67).

[49] A. T. Boothroyd. *Principles of Neutron Scattering from Condensed Matter*. Oxford University Press, 2020 (cited on pages 66, 68).

[50] S. Gull and J. Skilling. *MEMSYS III Quantified Maximum Entropy Subroutine Library*. 1989 (cited on page 68).

[51] R. J. Papoular and B. Gillon. "Maximum Entropy Reconstruction of Spin Density Maps in Crystals from Polarized Neutron Diffraction Data". *Europhysics Letters* 13.5 (1990). DOI: 10.1209/0295-5075/13/5/009 (cited on page 68).

[52] A. J. Markvardsen. "Polarised neutron diffraction measurements of $PrBa_2Cu_3O_{6+x}$ and the Bayesian statistical analysis of such data". PhD thesis. University of Oxford, 2000 (cited on page 69).

[53] M. Kempa, B. Janousova, J. Saroun, P. Flores, M. Boehm, F. Demmel, and J. Kulda. "The FlatCone multianalyzer setup for ILL's three-axis spectrometers". *Physica B: Condensed Matter* 385-386 (2006). DOI: 10.1016/j.physb.2006.05.371 (cited on page 72).

[54] P. Steffens. *nplot*. 2019 (cited on page 73).

[55] J. D. Hunter. "Matplotlib: A 2D Graphics Environment". *Computing in Science & Engineering* 9.3 (2007). DOI: 10.1109/MCSE.2007.55 (cited on page 73).

[56] C. R. Harris et al. "Array programming with NumPy". *Nature* 585.7825 (2020). DOI: 10.1038/s41586-020-2649-2 (cited on page 73).

[57] P. Virtanen et al. "SciPy 1.0: fundamental algorithms for scientific computing in Python". *Nature Methods* 17.3 (2020). DOI: 10.1038/s41592-019-0686-2 (cited on page 73).

[58] M. C. Rahn, A. J. Princep, A. Piovano, J. Kulda, Y. F. Guo, Y. G. Shi, and A. T. Boothroyd. "Spin dynamics in the antiferromagnetic phases of the Dirac metals $A\,MnBi_2$ (A = Sr, Ca)". *Physical Review B* 95.13 (2017). DOI: 10.1103/PhysRevB.95.134405 (cited on pages 75, 81).

[59] J.-R. Soh et al. "Magnetic structure and excitations of the topological semimetal $YbMnBi_2$". *Physical Review B* 100.14 (2019). DOI: 10.1103/PhysRevB.100.144431 (cited on pages 75, 81).

[60] A. Sapkota, L. Classen, M. B. Stone, A. T. Savici, V. O. Garlea, A. Wang, J. M. Tranquada, C. Petrovic, and I. A. Zaliznyak. "Signatures of coupling between spin waves and Dirac fermions in $YbMnBi_2$". *Physical Review B*

101.4 (2020). DOI: 10.1103/PhysRevB.101.041111 (cited on pages 75, 81).

[61] S. Toth and B. Lake. "Linear spin wave theory for single-Q incommensurate magnetic structures". *Journal of Physics: Condensed Matter* 27.16 (2015). DOI: 10.1088/0953-8984/27/16/166002 (cited on page 76).

[62] J.-R. Soh, K. Beauvois, A. T. Boothroyd, J. A. Rodríguez-Velamazán, A. Stunault, and S. M. Tobin. "Structural investigation of a possible magnetically-induced Weyl Semi-Metal $YbMnSb_2$". *Institut Laue-Langevin (ILL)* (2021). DOI: 10.5291/ILL-DATA.5-53-305 (cited on page 83).

[63] J.-R. Soh, A. T. Boothroyd, A. Piovano, J. Sun, and S. M. Tobin. "Magnon spectrum in a candidate topological semi-metal with magnetic order". *Institut Laue Langevin* (2021). DOI: 10.5291/ILL-DATA.4-01-1684 (cited on page 83).

A mega table of $AMnX_2$ materials and their properties

Table 3.6: $AMnX_2$ materials overview

Material	Space group	Magnetism	Topology	Other notes
$EuMnSb_2$	$P4/nmm$ [1], $Pnma$ [2]	Mn moments: C-type AFM along c axis, $T_N \sim 346$ K [1, 2], Eu moments: canted A-type AFM, $T_N \sim 21$ K, from single crystal neutron and X ray diffraction [1, 2]. Contrasting conclusion was reached in [3], which has Eu moments entirely in ab plane and $\perp$ to Mn moments.	Dirac semimetal, from ARPES in [2]. Not a semimetal according to [3].	Ordering of Eu moments suppresses inter-layer magnetic coupling. Expected coupling between magnetic sublattices is via Eu $4f$ and Mn $3d$ electrons.
$EuMnBi_2$	$I4/mmm$	G-type AFM on Mn moments, Eu moments also AFM order along c axis below 20 K [4]	Gapped Dirac semimetal ARPES and calculations [4]	Potential to control spin splitting through canting angle of Eu spins [5]
$Eu_{(1-x)}Sr_xMnSb_2$	$Pnma$	C-type AFM, $T_N \sim 300$ K. Eu moments: canted A-type AFM in ac plane $T_N \sim 17$ K, '+ + - -' along c axis and '+ - + -' along a axis, swapping to '+ - + -' along both a and c axes below 10 K [3]	Dirac semimetal, driven by Sr doping [3]	For $x \geq 0.5$, Eu spin canting and intra- (inter-) layer conductivity (decreases) increases with x [3].
$CaMnSb_2$	$Pnma$	C-type AFM, $T_N = 302$ K [6].	Gapped Dirac semimetal based on dHvA oscillations, SdH oscillations and electronic transport in [6, 7]	Sb square distorted to zig-zag in b axis

Material	Space group	Magnetism	Topology	Other notes
$CaMnBi_2$	$P4/nmm$	in ab plane AFM, $T_N \sim 250$ K[8]. Contradictory evidence from neutron powder diffraction presented in [9] C-type AFM along c axis, $T_N \sim 300$ K. Neutron single crystal diffraction in [10] showed C-type AFM along c axis, $T_N = 264$ K.	Dirac semimetal from SdH oscillations in [8] and calculations in [9].	-
$CaMn_{(1-x)}Cu_xBi_2$	$P4/nmm$	Cu doping suppresses AFM order ($T_N \approx 85$ K), while probably increasing spin canting [11].	-	-
$BaMnSb_2$ (actually $Ba_{1-y}Mn_zSb_2$ in [12])	$I4/mmm$ [12], $Imm2$ [13, 14]	G-type AFM along c axis, $T_N = 283$ K, from neutron diffraction and magnetisation measurements in [12]	Dirac semimetal from SdH oscillations [12]; Weyl semimetal [14, 15]	Speculated local deficiencies in Ba or Mn may lead to some small canted FM moments [12]. Out-of-plane resistivity displays curious local minimum (rather than local maximum as for $Ca/Sr/BaMnBi_2$) as temperature decreases.
$BaMnBi_2$	$Imm2$ [16] (very slight orthorhombic distortion), $I4/mmm$ [17, 18]	AFM $T_N \sim 290$ K	Gapped Dirac semimetal [16, 17]	Lattice is less distorted than for $BaMnSb_2$ but band structure is similar [5, 16]
$SrMnBi_2$	$I4/mmm$	G-type AFM, $T_N \sim 300$ K result from neutron powder and single crystal diffraction [9]. The work [10] had the same magnetic structure but refined $T_N = 287$ K.	Dirac semimetal from calculations [9, 19] and SdH oscillations [20]	-

Material	Space group	Magnetism	Topology	Other notes
$SrMnSb_2$	*Pnma* [21]	AFM $T_N \sim 300$ K [21]	Gapped Dirac semimetal with larger gap than $SrMnBi_2$ [21], not a topological semimetal according to [22]	$SrMnSb_2$ has fewer charge carriers and higher resistivity than $SrMnBi_2$ [21].
$Sr_{1-y}Mn_zSb_2$	*Pnma*	C-type AFM along *c* axis with FM component in *ab* plane $T_N \sim 304$ K, FM in *ab* plane $T_C \sim 565$ K, from neutron diffraction and transport in [23]	Argued for Dirac semimetal under pressure in [23]	Larger Sr deficiency associated with increased FM, larger Mn deficiency associated with weaker FM [23]

Material	Space group	Magnetism	Topology	Other notes
$YbMnBi_2$	$P4/nmm$	C-type AFM along c axis, $T_N = 290\,K$ single crystal neutron diffraction, any canting away from the c axis constrained to within 3° [2]. The neutron diffraction and HRTEM study [24] concurred. In [4] they had Mn spins canted 10° away from c axis. Magnetometry measurements yielded a miniscule canting of 0.018° in [25].	Weyl semimetal from ARPES measurements and calculations [4]. A Weyl semimetal based on transport measurements in [25]. Not Weyl, potential Dirac semimetal in [2]. Based on SdH oscillations results, [24] declared $YbMnBi_2$ to be a Dirac semimetal. The work in [26] interpreted their SdH oscillations and transport measurements in terms of a band structure featuring both Weyl and Dirac bands.	In this theoretical study [27], it was argued that transition from Dirac to type-II Weyl state is due to Bi vacancies and subsequent in ab plane canting of Mn moments from increased DM interactions. Optical spectroscopy on this material is presented in the work [28], which leaves the door open to interpret results as either Dirac or Weyl semimetal.

Material	Space group	Magnetism	Topology	Other notes
$YbMnSb_2$	$P4/nmm$	C-type in-plane AFM argued for in [29] but no measurements of magnetic phase transition presented. Magnetic hysteresis was observed in $YbMnSb_2$ [30] C-type AFM along the c axis, with canted spins so FM component in the ab plane. G-type AFM argued for in [31] (optical spectroscopy study). Single crystal neutron diffraction shows C-type AFM along c axis [32]. $T_N \sim 345$ K [32].	Dirac semimetal based on calculations, ARPES and SdH oscillations in [29]. Nodal line semimetal based on calculations in [31]. Reference [30] had $YbMnSb_2$ as a Weyl semimetal, assuming canted Mn spins. DFT calculations in [32] has $YbMnSb_2$ as a Dirac semimetal.	-

4

The magnetic order of the topological semimetal $MnSb_4Te_7$

4.1 Introduction

The magnetism and band structure of materials have a complex relationship, leading to exotic quantum materials phenomena such as the Quantum Anomalous Hall Effect (QAHE) and axion insulator states. Materials with a quasi-2D layered structure are of prime interest, both at their surface, and in their bulk crystalline form, as magnetic topological insulator and topological semimetal candidates. These van der Waals materials possess anisotropic electronic properties, as well as being ripe for heterostructural device engineering.

One particular crystal family is the rhombohedral family X_2Y_3, where the linear dispersion in the electronic bands are induced by the strong spin-orbit coupling arising from the heavy constituent ions X = Sb, Bi and Y = Se, Te [1–3]. These materials have 'quintuple' layers as building blocks and are three-dimensional examples of topological insulators. However, one of the major stumbling blocks in developing these TIs for technological applications is that the topological electronic bands cannot be easily controlled. Incorporating a magnetic ion such as Mn^{2+} has implications for the crystal structure, magnetism and band structure (§ 4.2). Hence, the idea of producing materials featuring topological quintuple X_2Y_3 layers interspersed with magnetic septuple MnX_2Y_4 has come to fruition.

There is now a proliferation of studies on the $(MnX_2Y_4)(X_2Y_3)_m$ family of materials, where $m = 0, 1, 2\ldots$ denotes the number of (potentially topological) quintuple layers. A smörgåsbord of topological electronic states and magnetic phenomena has been reported. In this chapter, I briefly

introduce the potential applications of the Mn-X-Y van der Waals family. Then I primarily focus on reviewing work done on $MnBi_2Te_4$ (§ 4.2.1), $MnSb_2Te_4$ (§ 4.2.4) and $MnSb_4Te_7$ (§ 4.2.5). Finally I present experimental work on the magnetism of $MnSb_4Te_7$ (§ 4.4 and § 4.4.4).

4.1.1 Potential applications of $(MnX_2Y_4)(X_2Y_3)_m$

Topological insulator systems with intrinsic magnetic order may pave the way for advances in spintronics, with tuneable spin structures and superior charge transport. An exciting proof-of-principle experiment [4] demonstrated electric field control of the canted AFM–AFM transition and associated Chern insulator state in $MnBi_2Te_4$.

Beyond quantum technology development, the axion insulator topological state is a focus of the dark matter physics community. It is hypothesised that quasiparticles hosted by axion insulators will interact with dark axions, a proposed candidate for dark matter [5]. This highlights the importance of topological materials as a testing ground for high energy particle physics.

Another application for materials considered here is phase change memory. The current material of choice is a Ge-Se-Te alloy, but other materials such as $MnBi_2Te_4$ have been identified as suitable phase change memory candidates [6]. $MnBi_2Te_4$ is particularly attractive given its high optoelectric contrast and magnetic storage potential [6].

Bi_2Se_3 is a common thermoelectric material, and it follows that the materials with quintuple layers of X_2Y_3, X = Sb, Bi and Y = Se, Te would also demonstrate good thermoelectric properties. Some examples of thermoelectric figures of merit ($MnBi_4Te_7$ and $MnBi_6Te_{10}$) are given in the work [7].

4.2 Quantum materials of interest

Considering the X_2Y_3 family, several approaches to manipulate the topology of the band structure have been made. One concept is to create heterostructures, for example, by epitaxially layering X_2Y_3 with magnetic EuS layers, but these are very prone to defects [8–10]. A different approach is to dope the parent X_2Y_3 compound with a magnetic ion such as Cr or Mn. An example of doping Bi_2Te_3 and Bi_2Se_3 with a non-magnetic ion is reported in [3]. This does not change the topological character of the band structure but does adjust the Fermi energy. Cr was utilised as a magnetic dopant in [11] for thin films of $Cr_{0.15}(Bi_{0.1}Sb_{0.9})_{1.85}Te_3$, which displayed the anomalous Hall effect.

One example of doping with a magnetic ion is $Bi_{2-x}Mn_xTe_3$. For x = 0.02 and x = 0.015, ferromagnetism was observed below T_C = 10 K and 17 K respectively [12]. At this concentration, the magnetic dopants did not incorporate well. A similar study with x = 0.04 demonstrated param-

agnetism at temperatures as low as 2 K [13]. Increasing the amount of magnetic dopant could degrade the sample quality, and additionally hinder charge carrier mobility. However, a comprehensive experimental work [14] covering x = 0, 0.005, 0.01, 0.02, 0.04, 0.09, found the material was ferromagnetic for x = 0.04, 0.09, with T_C = 9 K, 12 K respectively. This paper described the Mn dopant ions substituting on Bi sites, but hints of Mn intercalation layers were seen in STM data. The Fermi energy increased with increased concentration of Mn and the charge carriers transitioned from n-type to p-type. The Dirac surface state of Bi_2Te_3 was preserved for x = 0.09 as evidenced by ARPES data. The range of results among [12–14] highlight the sensitivity of $Bi_{2-x}Mn_xTe_3$ to sample synthesis parameters. None of these works gave a satisfying explanation for the onset of magnetic order. In terms of achieving the QAHE, impurities – whether magnetic or not – can introduce undesirable bands near the Dirac point [8] and shift the Fermi energy [3]. Meanwhile, first principles calculations showed the potential of Mn doping to adjust band structure topology of Bi_2Te_3 [15] and so experimental investigations along this line continued.

Interestingly, a structure of quintuple Bi_2Te_3 and septuple $MnBi_2Te_4$ layers emerged in epitaxially grown samples [10, 16]. The concentration of Mn determined the relative number of quintuple Bi_2Te_3 and septuple $MnBi_2Te_4$ layers. DFT calculations showed that such a structure was energetically favourable compared to random Mn placement [10]. The significance of the layers is that Bi_2Te_3 is a topological insulator in its own right and $MnBi_2Te_4$ is a magnetic topological insulator (more below). The self-organisation into the quintuple and septuple layers persists with other crystal growth methods. This quintuple/septuple layer structure is in contrast to the earlier works, where Mn ions were random impurities within X_2Y_3. This is a very promising approach: now the magnetic and the heavy ions reside on well-defined crystalline positions. We pursue such crystals with intrinsic magnetic order, heavy ions, strong spin-orbit coupling and inherent van der Waals anisotropy.

4.2.1 $MnBi_2Te_4$

$MnBi_2Te_4$ was the first intrinsic magnetic topological insulator. For a very recent review, see reference [17]. It has a septuple layered structure with van der Waals bonding and antiferromagnetic coupling between the layers [18, 19] (see Figure 4.1). $MnBi_2Te_4$ has been hypothesised to harbour the axion insulator state, in which quasiparticles analogous to axions manifest in a topological insulator [20]. The concentration of lattice defects in the material $MnBi_2Te_4$ is low, around a few percent [21].

Experimental evidence of an axion insulator state was found in even-layer number samples of

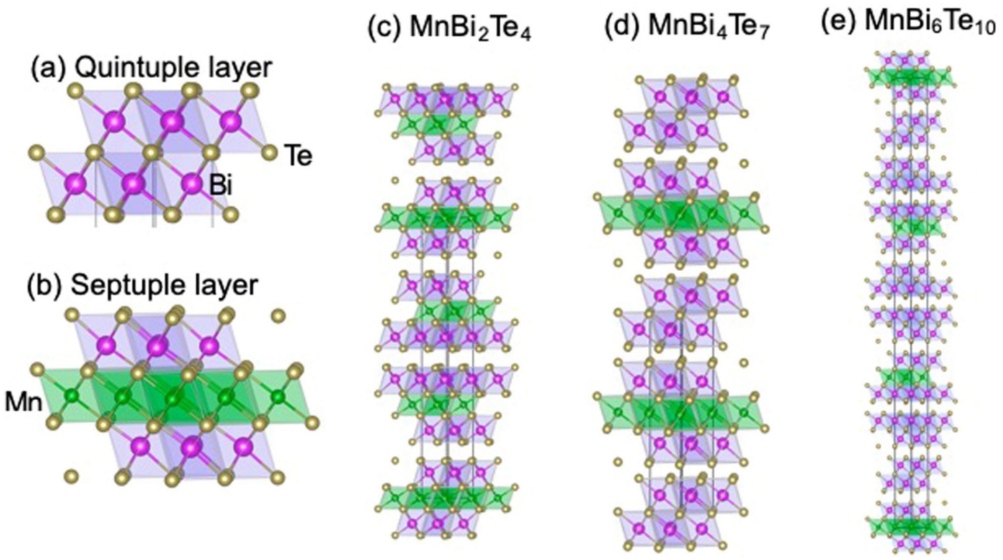

Figure 4.1: Quintuple and septuple layers, $(MnBi_2Te_4)(Bi_2Te_3)_m$ structure. The same structure applies to other members of the $(MnX_2Y_4)(X_2Y_3)_m$ family. Figure from reference [22], reproduced with permission. Copyright American Physical Society (2020).

$MnBi_2Te_4$ [23]. Samples of six septuple layer thickness were fabricated into Hall bar geometry and a detailed transport study undertaken. Magnetoresistance with different gate voltages revealed hole-type carriers dominate the transport below a gate voltage of 14 V (negative slope of Hall resistance vs. magnetic field, Fermi energy lies in the valence band), while electron-type carriers dominate the transport above a gate voltage of 38 V (positive slope and the Fermi energy lies in the conduction band). The work suggests spins begin to flip in the antiferromagnetically-coupled septuple layers from 2.5 T and are completely aligned with the external magnetic field by 5 T. The highlight of this work [23] is the signature of an axion insulator state (quantised Hall plateau and large longitudinal resistivity at zero external magnetic field) for gate voltages 22–30 V (the Fermi energy lies in the surface band gap for this range). For a high external magnetic field of 9 T and the same gate voltage range, indications of a Chern insulator state are seen instead: negligible longitudinal resistivity and quantised Hall resistivity plateau (see Figure 4.2).

$MnBi_2Te_4$ was shown to have Dirac dispersion via ARPES; a gap was noticeable between the Dirac cones in the ARPES data [16, 24]. Interestingly, the band structure changed slightly with bands seen to merge/hybridise above T_N [24]. The authors in [24] also suggested the magnetism at the surface was FM rather than AFM, and that multi-domains at the surface were responsible for the gapped Dirac band structure. Another ARPES investigation found a very sharp, *gapless* Dirac cone dispersion for $MnBi_2Te_4$ [19]. They too concluded the surface-level magnetism must differ from that of the bulk material (which is A-type AFM along the c axis), and proposed the following alternatives

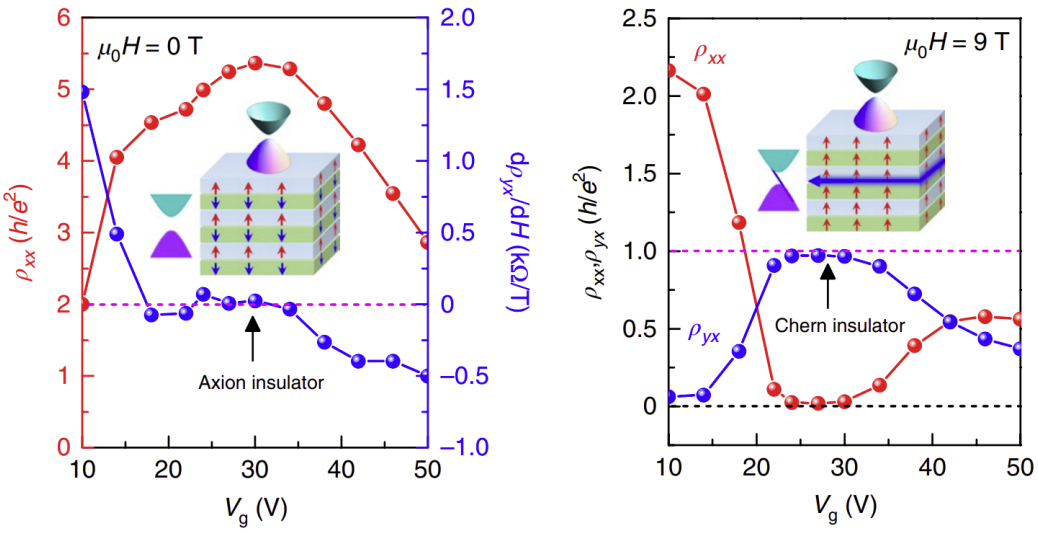

Figure 4.2: Six septuple layer $MnBi_2Te_4$ demonstrates characteristics of the axion insulator state at zero magnetic field, and the Chern insulator state at high magnetic field. Figure from reference [23], reproduced with permission from Springer Nature.

from symmetry arguments and DFT calculations: A-type AFM with an in-plane moment, G-type AFM, C-type AFM in-plane, or paramagnetism [19]. A spin-flop transition occurs at a critical field of 3 T, with magnetisation saturating at a field of 8 T [19].

Studying $MnBi_2Te_4$ at even higher magnetic fields reveals magnetic moments of Mn initially saturating at 3.9 μ_B at 10 T (similar to [19] above) before finally plateauing at a higher value of 4.6 μ_B at 50 T [25]. This suggests Mn antisite defects couple antiferromagnetically with the main layer of Mn, and gradually spin-flip to co-align with the Mn on the main sites as they are exposed to an increasing magnetic field. The same (canted) spin-flop phase at ≈ 3.7 T was observed in both [19] and [25]. While the magnetic moment of 4.6 μ_B is lower than the 5 μ_B expected for the $S = 5/2$ Mn^{2+}, this is attributed to orbital hybridization found via DFT calculations [25].

Exchange parameters for $MnBi_2Te_4$ are estimated in [25] based on the difference between magnetisation plateaus at 10 T and 50 T. These are presented in Table 4.1 together with those obtained via inelastic neutron scattering of a powder sample of $MnBi_2Te_4$ in [26]. The Heisenberg Hamiltonian

$$\mathcal{H} = -\sum_{\langle ij \rangle_\parallel} J_{ij} \mathbf{S}_i \cdot \mathbf{S}_j - J_c \sum_{\langle ij \rangle_\perp} \mathbf{S}_i \cdot \mathbf{S}_j - D \sum_i S_{i,z}^2 \tag{4.1}$$

was used to model the exchange interactions. Interactions within the Mn plane ($\langle ij \rangle_\parallel$) considered in [26] were 1st, 2nd and 4th nearest neighbours (nn), whereas [25] considered 1st nn $\langle ij \rangle_\parallel$ interactions, and intra(septuple)layer – but out-of-plane ($\langle ij \rangle_\perp$) – antisite Mn interactions on different Mn_{Bi} sites. The mechanism for the Q-dependent broadening of the spin waves seen in [26] is unknown, but

Table 4.1: Exchange parameters for $MnBi_2Te_4$ and $MnSb_2Te_4$. Note that the same parameters were obtained for both FM and AFM samples of $MnSb_2Te_4$ in [25]. Here a negative sign denotes AFM exchange.

Parameter	Description	$MnBi_2Te_4$ value [25] (meV)	$MnBi_2Te_4$ value [26] (meV)	$MnSb_2Te_4$ value [25] (meV)
SJ_1	nearest-neighbour (nn) coupling within Mn layer	0.35	0.3	-
SJ_2	next nn coupling within Mn layer	-	-0.083	-
SJ_4	4th nn coupling within Mn layer	-	0.023	-
SJ'	coupling between antisite $Mn_{Bi/Sb}$ and main Mn layer	-1.2	-	-2.1
SJ_c	coupling between nn septuple blocks	-0.085	-0.055	-0.01
SD	single ion anisotropy	0.075	0.12	0.07

suggestions included lifetime broadening due to J_1–J_2 frustration, magnon-electron or magnon-phonon coupling. Single-crystal inelastic neutron scattering data is needed to resolve this puzzle and refine models of spin dynamics in $MnBi_2Te_4$.

Another approach to probe the exchange interactions in $MnBi_2Te_4$ is described in [27], which utilised ultrafast electron diffused scattering and resonant soft x-ray scattering. This study specifically aimed at ascertaining the coupling strength responsible for the energy gap between the Dirac cones, attributed to interactions between well-localised $3d$ Mn spins and more itinerant $4p/5p$-like spins on Bi and Te atoms (much smaller magnetic moment of $0.03\,\mu_B$). Ultrafast electron diffused scattering was utilised to probe non-equilibrium electron-phonon dynamics. Meanwhile resonant soft x-ray reflectivity was used to examine the Mn L edge and dynamics associated with Mn spins. This was also in conjunction with an optical probe to measure magneto-optic Kerr rotation of Bi and Te spins. The $4p/5p$ bands of Bi and Te are spin-polarised. Disorder of itinerant and localised spins happens simultaneously when pumped by the ultrafast electrons; in absence of this pump, the disordering of Mn spins happens far more slowly. The size of the exchange coupling between (tiny) Bi/Te itinerant spins and (large) localised Mn spins is estimated at > 10 meV. The study [27] proposes the gapless nature of the Dirac surface state in $MnBi_2Te_4$ is due to topological surface states penetrating the bulk of the material, rather than microdomains at the surface or weak coupling between itinerant and localised spins.

Variations on septuple/quintuple layers: $(MnBi_2Te_4)(Bi_2Te_3)_m$

Variations on $MnBi_2Te_4$ have been studied. The work [18] examined the family of materials $(MnBi_2Te_4)(Bi_2Te_3)_m$. $MnBi_2Te_4$ corresponds to $m = 0$; $MnBi_4Te_7$ to $m = 1$; etc. For $m = 0$, 1, 2, the magnetism is AFM, whereas for $m = 3$, it is FM. For $m > 3$, neither description applies. Instead, the Mn moments present in the $MnBi_2Te_4$ layers are disordered along the [0001] direction, although FM-ordered within the layer [18]. This interesting phase is termed a 'single layer magnet'. For the $m = 1$ case, there is evidence of strong FM interactions despite the overall domination of A-type AFM order. The T_N for $m = 0$, 1, 2 are 25 K, 13 K and 11 K respectively; this indicates a diminishing return on the AFM phase for increasing m, and a much weaker interlayer exchange coupling for $m = 1$ compared to $m = 0$. $m = 3, 4$ display nearly purely FM behaviour in the form of a clear hysteresis loops at 2 K. For $m = 0, 1, 2$, there are spin-flip transitions at fields of 3.5 T, 0.2 T and 0.07 T respectively at 10 K. ARPES performed on both the $m = 1$ and $m = 2$ compounds revealed these to be Dirac semimetals [18]. The variation in surface terminations present within this family of materials (i.e. is the surface a quintuple or septuple layer) and the implications for measurements were also discussed: different dispersion bands are present in the ARPES data and are attributed to these different surface terminations.

Neutron scattering studies [28, 29] on the same $(MnBi_2Te_4)(Bi_2Te_3)_m$ compounds yielded consistent results: A-type AFM for $m = 0, 1, 2$ [28, 29] and FM for $m = 3$ [28]. Using polarised neutron diffraction, the magnetic moments were well-localised to the Mn sites [28]. It was determined that the magnetic moment per site decreased monotonically with m, from $\approx 3.8\,\mu_B$ to $\approx 3.0\,\mu_B$ for $m = 0$ to $m = 3$ [28]. In [29], the magnetic moment per site was also lower ($\approx 4\,\mu_B$) than expected ($5\,\mu_B$) for the $S = 5/2$ state of Mn^{2+} for the $m = 0$ compound.

Examining the magnetic order parameter for the $m = 0$ and $m = 1$ case in [29] gave critical exponents $\beta = 0.50(2)$ and $\beta = 0.45(3)$ respectively. Considering the data from a smaller, lower temperature range yielded near-identical β for both $m = 0$ and $m = 1$, $\beta = 0.32(2)$. This compares favourably to the theoretical value $\beta = 0.325$ from a 3D Ising model. In [29], it is suggested there is a transition from 3D to 2D magnetism upon cooling, especially for the $m = 1$ case.

Some evidence of site mixing disorder was seen as the same decrease in m coincided with a marked decrease in the Mn site occupancies from 85 % to 60 % [28]. The work [29] also reported Mn deficiencies and presence of 18 % ($m = 0$) and 28 % ($m = 1$) Bi at Mn sites. Interestingly, structural analysis did not reveal prevalent stacking faults between layers – something expected with van der Waals materials.

The materials $(MnBi_2Te_4)(Bi_2Te_3)_m$ have demonstrated the QAHE, in epitaxially-thin samples ($m = 0$) and in bulk samples ($m \approx 4$). Odd-layer number flakes of $MnBi_2Te_4$ demonstrated the anomalous Hall effect [30]. An odd number of layers (three or five septuple layers in the paper) rendered the flakes ferro/ferrimagnetic overall, while an even number of layers (four septuple layers in the paper) preserved the bulk antiferromagnetism. The quantisation temperature was 1.4 K, rising to 6.5 K when a magnetic field was applied to align all the layers ferromagnetically.

$(MnBi_2Te_4)(Bi_2Te_3)_m$ has also demonstrated the QAHE in a bulk crystal [31]. Samples with a very dilute concentration of Mn (2 %), were shown to correspond approximately to the $(MnBi_2Te_4)(Bi_2Te_3)_m$ $m = 4$ structure via EDX and STEM. Some Mn ions were detected in quintuple, rather than septuple, layers. These demonstrated ferromagnetism with $5\ \text{K} \lesssim T_C \lesssim 10\ \text{K}$. The samples were originally n-type semiconductors with the Fermi surface well above the Dirac gap. To tune the band structure by introducing vacancies, samples were then subjected to electron irradiation and annealing. This lowered the Fermi surface while raising the surface energy bands. The work [31] indicates edge states are responsible for the anomalous Hall conductance measured, i.e. the bulk crystal remains n-type semiconducting.

4.2.2 Sb-doped $MnBi_2Te_4$ / Bi-doped $MnSb_4Te_7$

Synthesised $MnBi_2Te_4$ tends toward strong n-type doping with the Fermi level in the bulk conduction bands rather than in the gap (as desired for topological transport phenomena). This motivated the investigation of $Mn(Sb_xBi_{(1-x)})_2Te_4$ family in [32]. All crystals were grown using a flux method. Dirac-like dispersion was seen on the surface of $MnBi_2Te_4$ crystals using ARPES (confirming the result of [24]). Sb, being smaller than Bi, was easily substituted into the lattice without causing defects. For $x \sim 0.3$, the Fermi level lay near the bulk gap (ARPES) and a transition between n- and p-carriers took place (indicated by the derivative of the Hall resistivity changing sign w.r.t applied magnetic field, showing bulk carrier suppression). Furthermore the Hall resistivity vs temperature plot did not show metallic behaviour for the key dopant concentration of $x = 0.3$ (whereas other concentrations above and below this were clearly metallic). The phase diagram is shown in Figure 4.3. Further increasing x drove the Fermi level into the valence band (ARPES). Examining magnetisation data, this work found evidence for AFM, canted AFM and FM ordering in $Mn(Sb_xBi_{(1-x)})_2Te_4$ samples.

A recent work [33] probed the properties of $Mn(Bi_{0.15}Sb_{0.85})_4Te_7$ as compared to $MnSb_4Te_7$ (§ 4.2.5). The Bi substitution raised the Fermi energy by 120 meV, while leaving the band structure qualitatively unchanged according to ARPES data.

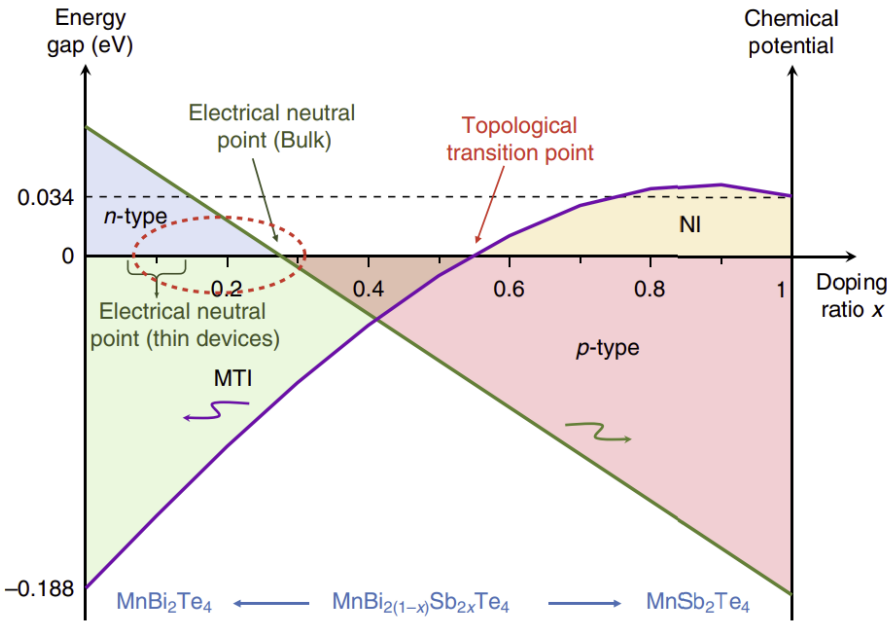

Figure 4.3: $n \rightarrow p$ carrier transition and topological phase diagram of $Mn(Sb_xBi_{(1-x)})_2Te_4$. Figure from reference [32], used under CC BY 4.0.

Intriguingly, Weyl (rather than Dirac) dispersion was observed in $Mn(Sb_xBi_{(1-x)})_2Te_4$ for lightly hole-doped samples $x = 0.26$, which are ferromagnetic under the influence of an external magnetic field of ~ 7 T [34]. Although they did not observe Fermi arcs via ARPES, they did find that the average chemical potential for $x = 0.26$ was almost at the top of the bulk valence band. Instead, evidence for the Weyl state was obtained through transport measurements, namely the nonlinearity of ρ_{yx} for lightly hole-doped $x = 0.26$ samples with respect to magnetic field and temperature. This indicates the coexistence of hole and electron pockets in the Fermi surface, touching as required for a Weyl node. More heavily doped samples show no evidence of a change in Fermi surface topology in ρ_{yx} measurements with respect to temperature and magnetic field.

4.2.3 $MnSb_2Se_4$

$(MnBi_2Se_4)(Bi_2Se_3)_m$ is another compound exhibiting the same structure consisting of magnetic septuple and topological quintuple layers. For $m = 0$, the material is antiferromagnetic with $T_N = 14$ K. For a heterostructure of six septuple layers between quintuple layers, ferromagnetism was evident from magnetisation data (both at 4 K and 300 K) and XMCD measurements in [8]. This work also uncovered a gapped Dirac state with a large gap of ~ 80 meV through ARPES. The T_C is certainly above room temperature for this material.

4.2.4 $MnSb_2Te_4$

Recently, $MnSb_2Te_4$ has burst onto the scene as a septuple van der Waals compound with nontrivial band structure topology and magnetism. It is structurally similar to $MnBi_2Te_4$, with space group $R\bar{3}m$. The presence of Sb rather than Bi may contribute to stronger spin-orbit coupling between the septuple layers. Sb ions are also closer in size and in electronegativity to Mn compared with Bi, which makes site mixing of Mn and Sb more likely [35]. Hence, the material $MnSb_2Te_4$ offers potentially greater options for tuning the magnetic and topological nature of a van der Waals compound through synthesis. Obtaining single crystal samples is a challenge as with any van der Waals material.

Table 4.2: Structure parameters for $MnSb_2Te_4$. Space group $P\bar{3}m$ (#166) with lattice parameters $a = b = 4.244$ Å, $c = 40.89$ Å, $\alpha = \beta = 90°$ and $\gamma = 120°$.

Atom	Site	x	y	z	Occupancy
Mn	3*a*	0	1	0.5	1
Sb	6*c*	0.3̇	0.6̇	0.408	1
Te (1)	6*c*	0.6̇	0.3̇	0.459	1
Te (2)	6*c*	1	0	0.368	1

$MnSb_2Te_4$ has been investigated through first-principles calculations in [36], which concluded that it was a Weyl semimetal with ferromagnetic order between septuple layers, and under pressure, would display the QAHE. Similar conclusions were reached in other theoretical works: calculations with spin orbit coupling and assumed ferromagnetism yielded a Weyl semimetal state, either type I [37] or type II [38]. Without spin orbit coupling, AFM order is favoured [37–39]. The latter work [39] contended that $MnSb_2Te_4$ is inherently antiferromagnetic, with a ferromagnetic phase and potential Weyl semimetal state only shown under strain. Further theoretical calculations contended that there was topological phase transition to an axion insulator state for $MnSb_2Te_4$ without site mixing [40].

The experimental reality for $MnSb_2Te_4$ is quite different, with a variety of FM, AFM, canted AFM, and ferrimagnetic orders reported. Site mixing between Mn and Sb introduced intra-layer ferrimagnetism at $T_C = 31$ K as seen in [41], which utilised laboratory XRD and magnetometry. A similar work, which also utilised powder XRD and magnetisation measurements, also supported ferrimagnetic order with $T_C = 25$ K [38]. Ferrimagnetism in the case of $MnSb_2Te_4$ would manifest as AFM intra-layer coupling and FM inter-layer coupling, but this is debated. For a sample with

composition $(Mn_{0.66}Sb_{0.34})(Sb_{0.83}Mn_{0.17})_2Te_4$, magnetic moments were determined for the Mn ions on the 6*c* (originally Sb) site and 3*a* (usual Mn) site: 3.1 μ_B and 4.2 μ_B respectively [38]. A neutron diffraction and STM study [35] showed either inter-layer ferromagnetic (T_C = 24 K) or antiferromagnetic (T_N = 19 K) order was possible for $MnSb_2Te_4$ depending on site mixing. In [25], near stoichiometric $MnSb_2Te_4$ was FM while Mn-deficient $MnSb_2Te_4$ was AFM, with significant compensation from antisite defects driving down the overall magnetisation in the latter sample. Both samples show similar overall trends in magnetisation per ion vs. magnetic field: a plateau is reached at $\sim 2\,\mu_B$ at ~ 1 T, then magnetisation gradually increases with magnetic field, peaking at 4.9 μ_B for the AFM sample and 5 μ_B for the FM sample. This is attributed to ferrimagnetism combined with a spin-flip transition at 0.5 T for the AFM $MnSb_2Te_4$ sample (as oppposed to $MnBi_2Te_4$ which displayed a spin-flop transition, and higher magnetisation per Mn^{2+} ion) [25]. Ferrimagnetism is also reported in [42].

A slightly different result was reported in [37, 43], with both AFM $\rightarrow$ canted AFM and canted AFM $\rightarrow$ FM transitions (a staggered spin-flip) observed at critical fields ($\mathbf{H} \parallel c$) of 0.6 T and 1.4 T. The $T_N \sim 19$ K appearing in [37] is consistent with [35], suggesting this was also a Mn-deficient sample. The magnetic moment of Mn^{2+} was determined to be 1.75 μ_B, similar to [25]. However, the studies presented in references [37, 43] did not use any diffraction methods to probe the canted AFM state or crystal structure, and there may be other explanations for the magnetometry data with $H \parallel c$ that do not involve a spin component perpendicular to the c axis, such as site mixing.

Transport measurements in [37] revealed that holes are the primary charge characters, as well as the anomalous Hall effect and non-linear magnetoresistance ρ_{xy}. This is different to $MnBi_2Te_4$ but consistent with works on Sb-doped $MnBi_2Te_4$ [32–34] (see Figure 4.3).

Estimated exchange constants for $MnSb_2Te_4$ are shown in Figure 4.1. Vacancies in the Mn layer enhance AFM coupling between the Mn layer and Mn_{Bi} sites, but this depends on the local configuration of magnetic defects [25]. The variety of magnetic orders observed in $MnSb_2Te_4$ sets the stage for exchange mechanisms including superexchange and RKKY interactions. Since the oxidation state of Mn is +2, Sb is +3 and Te is -2, the 5*p* orbital of Te is full and the 3*d* orbital of Mn is partly full. The Goodenough-Kanamori rules then favour ferromagnetic intra-layer superexchange. Meanwhile the RKKY interaction mediates inter-layer coupling between localised Mn moments via Sb conduction electrons. This could explain the differences in magnetic ordering phenomena among the members of the $(MnSb_2Te_4)(Sb_2Te_3)_m$ family. Introducing site mixing could add double exchange into the mix as well, potentially between Mn_{Mn} and Mn_{Bi}.

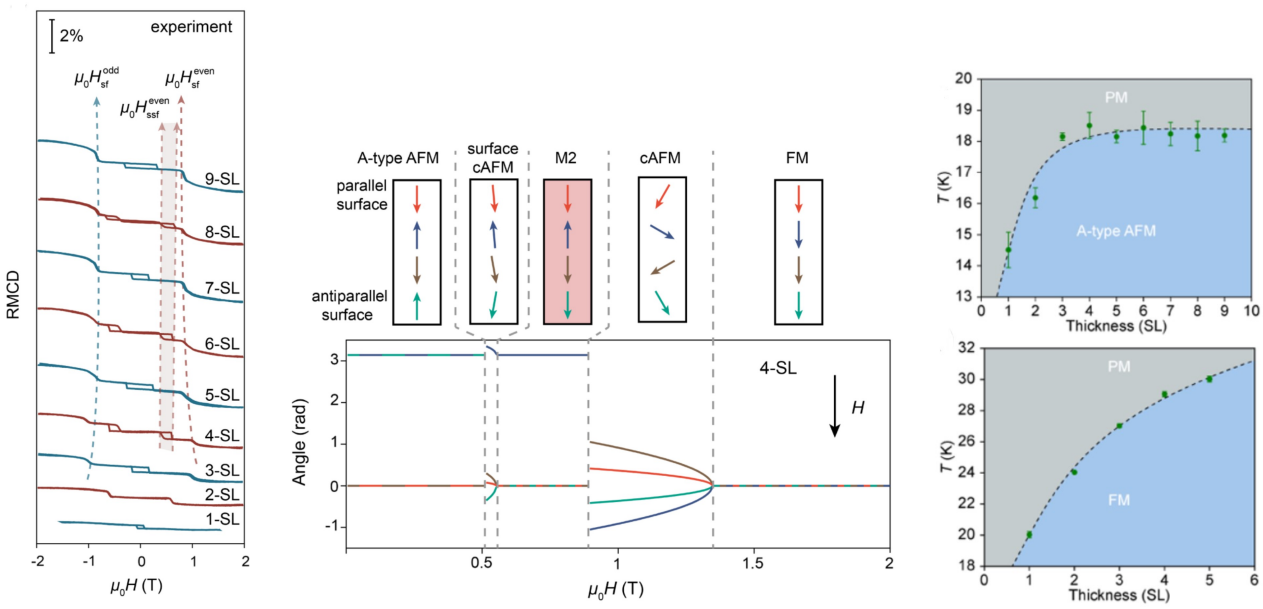

Figure 4.4: Layer-number dependent magnetism in $MnSb_2Te_4$. a) RMCD signals of 1- to 9-septuple-layer (-SL) AFM-$MnSb_2Te_4$ flakes measured at 2 K. b) Calculated magnetic state evolution of 4-SL flake under an external field. The upper (lower) panel denotes the spin configuration (angle of 'macrospin' in each SL) at each state. c) Thickness-temperature phase diagrams of AFM $MnSb_2Te_4$ and FM $MnSb_2Te_4$. The dashed lines denote the phase boundaries. Subfigures and caption adapted from reference [44], reproduced with permission. Copyright American Physical Society (2022).

Thin flakes of $MnSb_2Te_4$ display different magnetic orders and transitions depending on the number N of septuple layers present in the sample, as well as the composition of the sample [44]. The experimental probe used here was reflective magnetic circular dichroism (RMCD). In $MnSb_2Te_4$ samples with AFM order, N odd means the bulk magnetisation is uncompensated; hence, magnetic hysteresis is observed. On the other hand, hysteresis is seen for AFM samples with N even. AFM odd-number ($N \geq 3$) septuple layer samples undergo a single spin flip transition with increasing magnetic field, whereas AFM even-number ($N \geq 4$) septuple layer samples demonstrate distinct surface spin flip and bulk spin flip transitions via canted AFM states. These transitions are shown in Figure 4.4.

The magnetisation measurements on $MnSb_2Te_4$ in [45] showed a distinct split between zero field-cooled and 0.01 T field-cooled data below $T_C \sim 24$ K for both $\mathbf{H} \parallel ab$ and $\mathbf{H} \parallel c$. Together with frequency-dependence of the AC susceptibility peak, this was interpreted as evidence of a spin-glass state, arising from the frustration between intra-and inter-layer coupling. Magnetisation relaxation measurements in the same work show cluster-like dynamics in the magnetically 'ordered' phase are present on a time scale of minutes in the ZFC sample.

Epitaxially-grown, Mn-rich $MnSb_2Te_4$ displays ferromagnetic order at a much higher temperature ($T_C \sim 46$ K), while ARPES measurements also show that this is a Dirac semimetal [46]. A magnetic force microscopy study on flux-grown $MnSb_2Te_4$ demonstrated ferromagnetism with $T_C = 33$ K [47] with weak domain wall pinning (observed by saturating the magnetisation by applying a field of 0.1 T and then removing it) and little hysteresis. The work [47] in fact examined two sets of samples that were grown by different groups under similar conditions but displayed slightly different characteristics in regard to domain formation.

Growing single crystals of $MnSb_2Te_4$ is a challenge; many samples are polycrystalline and small. One new approach detailed in [45] is first to prepare the materials MnTe and Sb_2Te_3. These were then combined at 1173 K, cooled slowly to 893 K and held at that temperature for two weeks in order to anneal. When the sample was quenched in air and cracked, the result was millimetre-sized crystals. Thin samples were exfoliated from these crystals. The composition was determined to be $Mn_{1.09(7)}Sb_{1.90(3)}Te_{3.95(1)}$. Other examples of single crystal $MnSb_2Te_4$ have been prepared via the flux method [42] from a 1:10:16 molar mixture of Mn, Sb, and Te heated to 700°C for 20 hours and cooled at 0.5°C/hour to 630°C.

4.2.5 $MnSb_4Te_7$

The hexagonal $MnSb_4Te_7$ is another example of a van der Waals material, another member of the $(MnSb_2Te_4)(Sb_2Te_3)_m$ family. The unit cell can be described by the $P\bar{3}m1$ space group, where the Sb_2Te_3 topological layers are sandwiched between magnetic $MnSb_2Te_4$ septuple layers.

Theoretical calculations indicate that different spin arrangements of the Mn magnetic sublattice can strongly influence the topology of the charge carriers in the Sb_2Te_3 quintuple layers [33]. Magnetisation measurements in [33] are consistent with A-type AFM along the c axis ($T_N = 13.5$ K), with a spin flip transition to FM order when a magnetic field of 0.15 T is applied along the c axis. Symmetry analysis and theoretical calculations indicate that the axion insulator state usually associated with A-type AFM order will in fact persist even when the material becomes FM ordered along the c axis in the presence of an external magnetic field [33]. Intriguingly, there is the possibility of a Weyl semimetal state coexisting with the axion insulator state in $MnSb_4Te_7$, not seen in the Bi equivalent compound. It is hypothesised this would occur for $MnSb_4Te_7$ doped with either electron acceptors or donors, while enforcing FM order via an external magnetic field [33].

The topological nature of the surface state will be governed by the terminating layer of the material, according to calculations in [33]. If it is a quintuple layer, the surface band gap is calculated to be much larger and the surface bands more parabolic. If it is a magnetic septuple layer, Dirac

dispersion will occur, with the band crossing near the Fermi energy. This theoretically aligns with the behaviour of $(MnBi_2Te_4)(Bi_2Te_3)_m$ band structure; however, in the ARPES data in [33], the two different surface terminations of $MnSb_4Te_7$ could not be distinguished.

Since the topology of the electronic bands depend on the fine details of the spin configuration, a study of the arrangement of the Mn ions was in order. Furthermore, the ground state magnetic structure, and the evolution of the spins in an applied field had not yet been directly observed in any prior work. Neutron diffraction was selected as the chief experimental probe to investigate the magnetism of $MnSb_4Te_7$, being particularly well suited to nailing down the positions of Mn and Sb within the unit cell because of the opposing scattering lengths of Mn ($b_{coh} = -3.73$ fm [48]) and Sb ($b_{coh} = 5.57$ fm [48]). Single crystal neutron diffraction is often able to pinpoint the magnetic structure of a material among several possibilities gleaned from magnetisation measurements. Here we present the results of our single crystal neutron diffraction experiment on $MnSb_4Te_7$.

4.3 $MnSb_4Te_7$ samples and initial characterisation

The single crystal we studied was kindly provided to us by Xin Zhang and Dr Yan-Feng Guo of ShanghaiTech University, who were the first to synthesise single crystals of $MnSb_4Te_7$ [33]. A self-flux method was used, as specified in reference [33] by the ShanghaiTech University group:

1. Mn, Sb and Te were mixed in a 1:10:15 molar ratio in an alumina crucible.
2. The crucible was heated to 750°C and held at this temperature for 10 hours.
3. It was slowly cooled at a rate 2°C per hour to 613°C.
4. The melt was centrifuged and platelet-type crystals were obtained.

The XRD, magnetisation and resistivity measurements performed by my ShanghaiTech University collaborators (on crystals from the same batch as the one I measured) were published in reference [33] and are reproduced in Figure 4.5. The structural parameters for $MnSb_4Te_7$ obtained by refining the XRD data are given in Table 4.3. No superstructural peaks were observed by XRD. The magnetisation data in Figure 4.5 d) are characteristically anisotropic as is expected for the van der Waals crystals, although the splitting between the FC and ZFC curves is not strong. The magnetoresistance data from reference [33] is reproduced in Figure 4.6. The field-dependent magnetic order (shown in Figure 4.5 e)) has a pronounced effect on charge transport. Of note is Figure 4.6 e), which shows the largest calculated anomalous Hall conductivity is for FM order with moments along z (the c axis direction).

Table 4.3: Structure parameters for $MnSb_4Te_7$ from XRD data and refinement published in reference [33]. Space group $P\bar{3}m1$ (#164) with lattice parameters $a = b = 4.25$ Å, $c = 23.76$ Å, $\alpha = \beta = 90°$ and $\gamma = 120°$. NB: The position of Mn (2) = position of Sb (2); and position of Sb (3) = position of Mn (1).

Atom	Site	x	y	z	Occupancy
Mn (1)	1*a*	0	0	0	1
Sb (1)	2*d*	1/3	2/3	0.416̇	1
Sb (2)	2*d*	1/3	2/3	0.1579	1
Te (1)	1*b*	0	0	0.5	1
Te (2)	2*d*	2/3	1/3	0.3457	1
Te (3)	2*c*	0	0	0.2271	1
Te (4)	2*d*	2/3	1/3	0.0711	1

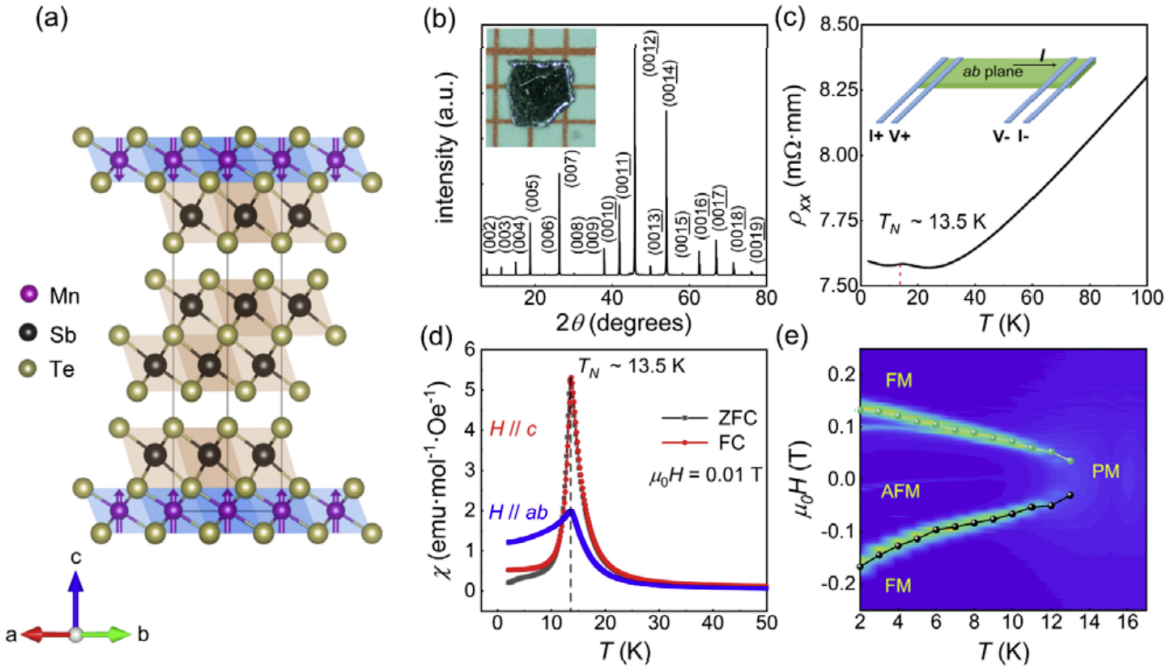

Figure 4.5: (a) The schematic crystal structure of $MnSb_4Te_7$. The blue arrows represent the Mn^{2+} spins in the A-type AFM structure. Green block: edge-sharing $SbTe_6$ octahedra. Blue block: edge-sharing $MnTe_6$ octahedra. (b) The room temperature powder x-ray diffraction peaks from the ab plane of $MnSb_4Te_7$ crystal. Inset: Image of a typical $MnSb_4Te_7$ single crystal synthesized in this work. (c) The temperature dependence of transverse resistivity ρ_{xx} at $\mu_0 H = 0$ T measured from 2 to 100 K. The sketch for the four-probe measurements configuration is inserted. (d) The temperature dependent magnetic susceptibility χ under $\mu_0 H = 0.01$ T for $H \parallel c$ (green and red dotted lines) and $H \parallel ab$ plane (blue lines). (e) The magnetic phase diagram of $MnSb_4Te_7$. The solid dots and dotted line represent the critical magnetic fields as a function of temperature. Figure from reference [33], reproduced with permission. Copyright American Physical Society (2021).

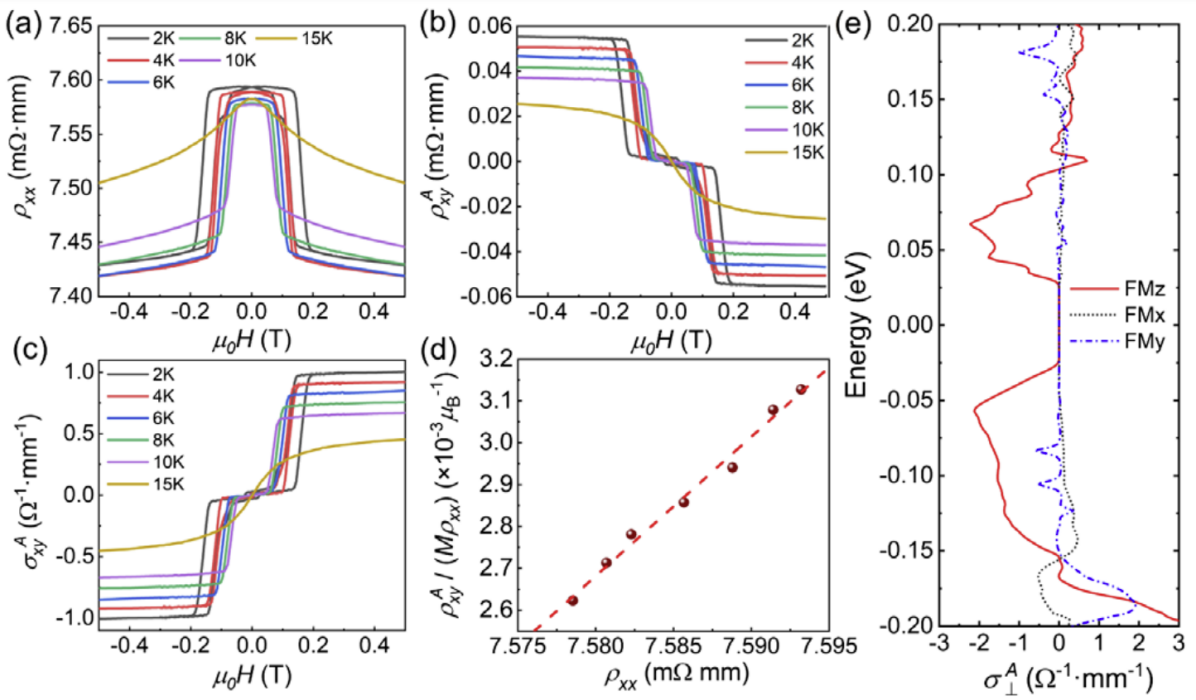

Figure 4.6: (a) Magnetoresistance ρ_{xx} with $I \parallel ab$ plane and $H \parallel c$ at various temperatures. (b) The anomalous Hall resistivity ρ^A_{xy}. (c) The anomalous Hall conductivity σ^A_{xy} at various temperatures. (d) The plot of $\rho^A_{xy}/(M\rho_{xx})$ vs ρ_{xx}, where the red dashed line denotes the linear fit when the temperature is below 8 K. (e) The calculated anomalous Hall conductivities of $MnSb_4Te_7$ for the three different ferromagnetic states as a function of varied Fermi energy, where the actual Fermi energy is set as zero. Figure from reference [33], reproduced with permission. Copyright American Physical Society (2021).

4.4 Single crystal neutron diffraction of $MnSb_4Te_7$ at ILL D10

4.4.1 Zero-field diffraction

We inspected the single crystal of $MnSb_4Te_7$ using the Cyclops neutron Laue diffractometer [49] at the ILL to check it was a single grain. The diffraction spots appear slightly elongated in the radial direction, rather than being perfect points. This probably indicates a stress-induced spread in d spacing from the "stacked platelet" macroscopic structure of the sample, which is typical of van der Waals materials. No signs of twinning were seen, i.e. there is only a single orientation of symmetric spots in Figure 4.7.

We then measured it on the D10 four circle diffractometer, also at the ILL. The sample was mounted on a pin, which was then attached to the Eulerian cradle (Figure 2.8) with the Displex closed-cycle cryostat. A constant wavelength of 2.36 Å was used. At 2 K and zero field we measured 394 unique structural Bragg peaks (113 symmetry-inequivalent peaks) and 26 unique non-integer, 'non-nuclear' Bragg peaks (8 symmetry-inequivalent peaks), which were presumed to be of magnetic origin. The

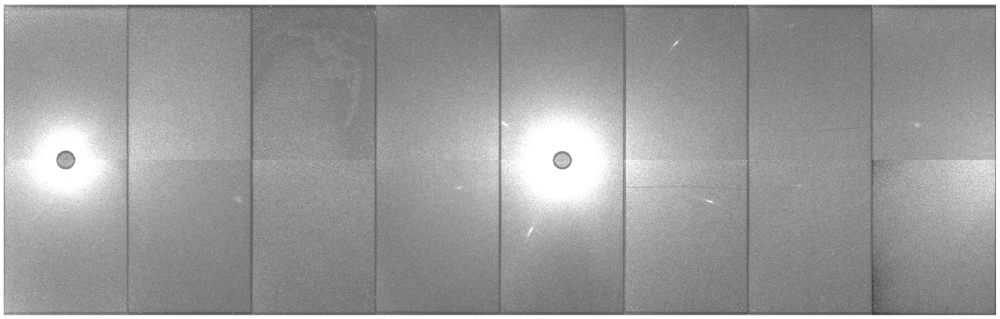

Figure 4.7: $MnSb_4Te_7$ neutron Laue diffraction on ILL Cyclops.

self-consistency of the integrated intensities of symmetry-equivalent peaks after Lorentz factor corrections was R_{int} = 7.6 % for nuclear reflections and R_{int} = 6.8 % for non-nuclear reflections.

The temperature dependence of the intensity of one 'non-nuclear' reflection (1 0 0.5) was measured in the range 2 K – 18 K.

4.4.2 Magnetic structure analysis and results

Intensity was observed at non-integer positions in reciprocal space for $l = (2n + 1)/2$, suggesting the propagation vector is $\mathbf{q} = (0, 0, 1/2)$. This is consistent with some form of AFM order along the c axis, as indicated by the earlier magnetisation measurements. When refining the crystal and magnetic structure of $MnSb_4Te_7$, I considered models with and without site mixing of Mn and Sb, shown in the diagrams in Figure 4.8.

No site mixing

For the case with no site mixing, I used the structural parameters from refinement of XRD data (Table 4.3) as the starting point, setting $\epsilon = \zeta = 0$. With no site mixing, there is just the one magnetic site:

- site 1: Mn^{2+} at (0, 0, 0), a symmetry-protected location.

MAG2POL generates the following irreps for the unit cell given the propagation vector $\mathbf{q} = (0, 0, 1/2)$:

$$\Gamma_3 + \Gamma_5.$$

The basis vectors are presented in Table 4.4. The only irrep consistent with moments along the c axis is Γ_3.

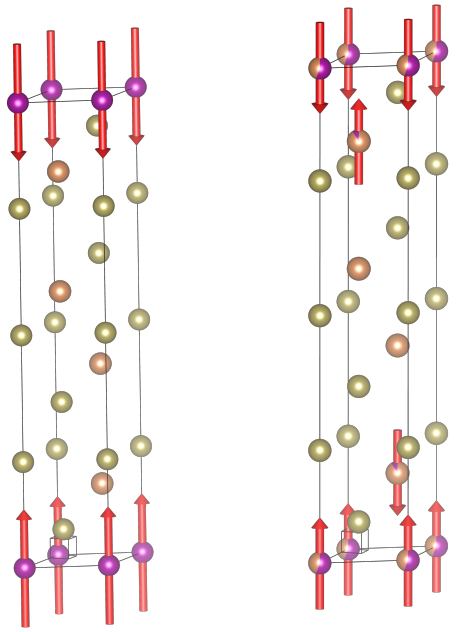

(a) AFM order, no site-mixing

(b) ferriM order/averaged AFM order, site-mixing

Figure 4.8: Possible magnetic structures of $MnSb_4Te_7$. Drawn in VESTA [50].

Site mixing

In the MST family, there is evidence of site mixing between Mn and its nearest Sb neighbour. I defined the site-mixing as follows:

- the position of Mn (2) $\equiv$ the position of Sb (2)
- the position of Sb (3) $\equiv$ the position of Mn (1)
- Mn (1) occupancy $1 - \epsilon$
- Mn (2) occupancy ϵ
- Sb (2) occupancy $1 - \zeta$
- Sb (3) occupancy ζ.

By having two occupancy parameters ϵ and ζ, I allowed for the possibility of a deficiency or excess of Sb relative to Mn and the nominal stoichiometry $MnSb_4Te_7$. Hence I considered two(ish) magnetic sites:

- site 1: Mn^{2+} at (0, 0, 0)
- site 2.1: Mn^{2+} at (1/3, 2/3, ≈ 0.16)

Table 4.4: Possible basis vectors for irreps describing $MnSb_4Te_7$ magnetic structure given by MAG2POL

Irrep	Basis vector	Site 1 (0, 0, 0)	Site 2.1 (1/3, 2/3, ≈ 0.16)	Site 2.2 (2/3, 1/3, ≈ 0.84)
Γ_2	ψ_1	–	$\begin{bmatrix}0\\0\\1\end{bmatrix}$	$\begin{bmatrix}0\\0\\-1\end{bmatrix}$
Γ_3	ψ_1	$\begin{bmatrix}0\\0\\1\end{bmatrix}$	$\begin{bmatrix}0\\0\\1\end{bmatrix}$	$\begin{bmatrix}0\\0\\1\end{bmatrix}$
Γ_5	ψ_1	$\begin{bmatrix}0.612-0.345i\\-0.707i\\0\end{bmatrix}$	$\begin{bmatrix}0.612-0.345i\\-0.707i\\0\end{bmatrix}$	$\begin{bmatrix}0.612-0.345i\\-0.707i\\0\end{bmatrix}$
	ψ_2	$\begin{bmatrix}-0.707i\\0.612-0.345i\\0\end{bmatrix}$	$\begin{bmatrix}-0.707i\\0.612-0.345i\\0\end{bmatrix}$	$\begin{bmatrix}-0.707i\\0.612-0.345i\\0\end{bmatrix}$
Γ_6	ψ_1	–	$\begin{bmatrix}0.612-0.345i\\-0.707i\\0\end{bmatrix}$	$\begin{bmatrix}-0.612+0.345i\\0.707i\\0\end{bmatrix}$
	ψ_2	–	$\begin{bmatrix}0.707i\\-0.612+0.345i\\0\end{bmatrix}$	$\begin{bmatrix}-0.707i\\0.612-0.345i\\0\end{bmatrix}$

- site 2.2: Mn^{2+} at (2/3, 1/3, ≈ 0.84), the symmetry-equivalent site to site 2.1.

This meant adding two extra atoms to the unit cell, Mn (2) and Sb (3), subject to the constraints as per Table 4.3. The position of Mn (2) ≡ position of Sb (2); and position of Sb (3) ≡ position of Mn (1). MAG2POL generates the following irreps for the site-mixed unit cell given the propagation vector $\mathbf{q} = (0, 0, 1/2)$:

$$\text{site 1: } \Gamma_3 + \Gamma_5$$

$$\text{site 2: } \Gamma_2 + \Gamma_3 + \Gamma_5 + \Gamma_6.$$

The basis vectors are presented in Table 4.4. The only irreps consistent with moments along the *c* axis are Γ_2 and Γ_3.

Refinement

The software package MAG2POL [51] was used to refine the zero-field data from the ILL D10 experiment on $MnSb_4Te_7$. The various structural and magnetic parameters were refined in the following order:

1. scale factor between integrated intensity data and calculated intensities
2. diagonal extinction factor terms x_{ii}
3. occupancy / degree of site mixing between Mn (1) and Sb (2) sites
4. atomic positions z coordinates
5. isotropic thermal displacement B
6. off-diagonal extinction factor terms x_{ij}
7. magnetic moments μ_B per Mn (refined using magnetic reflections only).

Now I describe the details of the refinement procedure. First the nuclear Bragg peak dataset was used to refine structural parameters only excluding site mixing (i.e. occupancy for all sites held constant at one). The thermal displacement parameters B and the diagonal extinction parameters x_{11}, x_{22}, x_{33} were all constrained to be positive. Additionally, B was equal for all atoms of the same type. This first round of refinement was not very good and became worse still when the magnetic peak dataset was included – after that, the fit would not converge if any parameter beyond the scale factor was varied.

A second round of refinement used the nuclear Bragg peak dataset, but with the degree site mixing (occupancy) allowed to vary on the Mn (1), Mn (2), Sb (2) and Sb (3) sites, i.e. non-zero ϵ and ζ (see Table 4.3). Adjusting the occupancy had the biggest effect on the agreement factor of the refinement. The magnetic moments were refined separately using the magnetic peak dataset, before combining both datasets (weights were 0.9 for the nuclear peak dataset and 0.1 for the magnetic peak dataset) for a final refinement. The results of the refinements with and without site-mixing are shown in Figure 4.9, and the fit parameters from the best refinement with site mixing are given in Table 4.5. The agreement factor $R_F = 8.7\,\%$ of this refinement is comparable to the variation among symmetry-equivalent peaks of $R_{\text{int}} = 7.6\,\%$.

Table 4.5: Structure refinement for $MnSb_4Te_7$ in the space group $P\bar{3}m1$ (#164) with lattice parameters $a = b = 4.25$ Å, $c = 23.76$ Å, $\alpha = \beta = 90°$ and $\gamma = 120°$. For this refinement, $R_F = 8.7\,\%$ and $\chi^2_R = 1.18$.

Atom	Wyckoff position	x	y	z	B_{iso}	Occupancy
Mn (1)	1*a*	0	0	0	1.531	0.559
Mn (2)	2*d*	1/3	2/3	0.1590	1.531	0.089
Sb (1)	2*d*	1/3	2/3	0.4166	0.789	1
Sb (2)	2*d*	1/3	2/3	0.1590	0.789	0.911
Sb (3)	1*a*	0	0	0	0.789	0.441
Te (1)	1*b*	0	0	0.5	0.124	1
Te (2)	2*d*	2/3	1/3	0.3455	0.124	1
Te (3)	2*c*	0	0	0.2278	0.124	1
Te (4)	2*d*	2/3	1/3	0.0718	0.124	1

Extinction parameter	Value
x_{11}	0
x_{22}	0
x_{33}	0.00340
x_{12}	−0.07420
x_{23}	0.01750
x_{13}	−0.01716

Irrep	ψ_1
Γ_2	−2.29
Γ_3	2.40

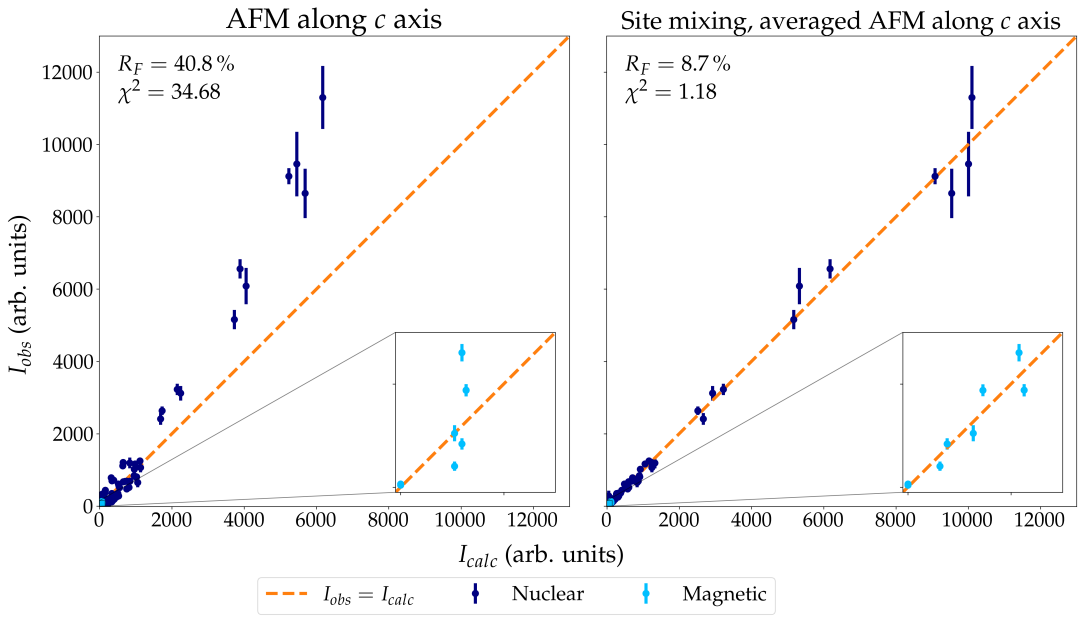

Figure 4.9: $MnSb_4Te_7$ magnetic structure refinement results: left, A-type AFM along *c* axis with no site mixing; and right, averaged AFM along *c* axis resulting from ferrimagnetic, site-mixed septuple layers.

4.4.3 Temperature dependence of a magnetic peak

We measured the temperature dependence of one non-nuclear reflection, the (1 0 0.5) reflection. The data are shown in Figure 4.10. The intensity of this peak is reminiscent of a Landau order parameter, showing a clear up-tick in intensity at 14 K. This is consistent with the ordering temperature obtained from magnetisation data. Fitting an equation of the form

$$\text{intensity} = A\left(\frac{T - T_N}{T_N}\right)^{2\beta} \tag{4.2}$$

yielded a critical exponent of $\beta = 0.31(2)$ and $T_N = 13.9(1)$ K.

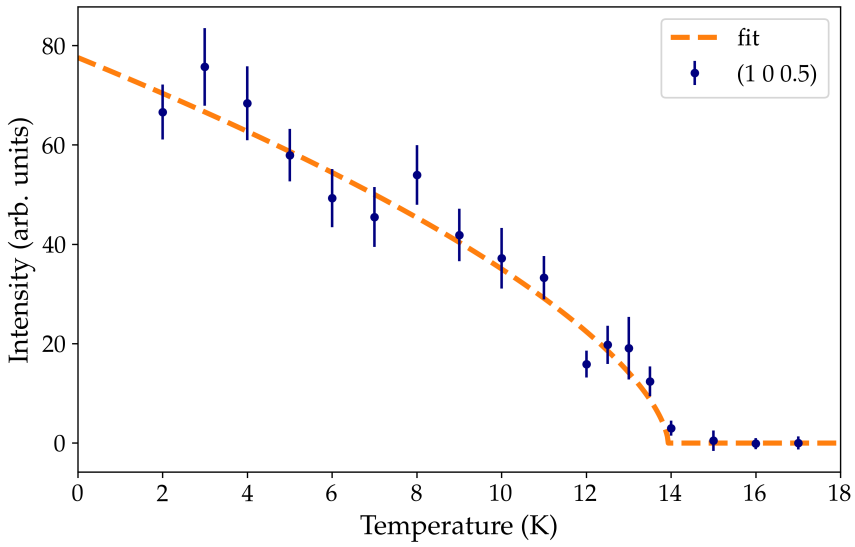

Figure 4.10: $MnSb_4Te_7$ reflection intensity vs. temperature for a non-nuclear reflection (1 0 0.5).

4.4.4 Diffraction in a magnetic field

The magnetic field-dependence of several reflections was also studied on ILL D10. This part of the experiment utilised the vertical cryomagnet (Figure 2.8b) to provide an external magnetic field along the c axis of the crystal. The field dependence of two reflections was measured: the (0 1 0.5) reflection, as it is sensitive to AFM order along the c axis; and the (0 1 1) reflection, as it is a good indicator of any FM order along the c axis because it is structurally weak and at low Q. The magnetic field was swept from 0 T to 1 T and then back down to 0 T at a temperature of 2 K, before repeating the procedure at a temperature of 6 K. The results are shown in Figure 4.11.

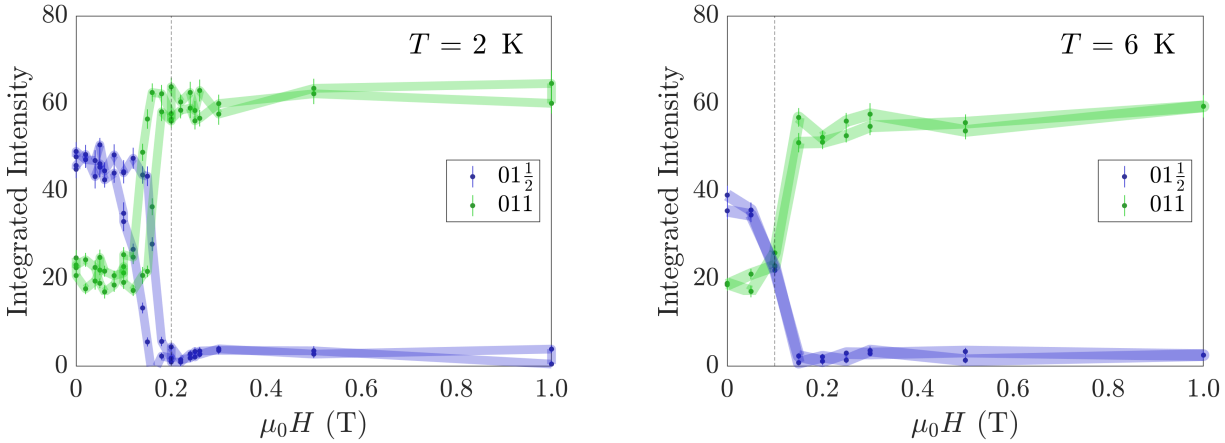

(a) 2 K **(b)** 6 K

Figure 4.11: $MnSb_4Te_7$ reflection intensities vs. magnetic field for two different temperatures. The lines are guides for the eye.

4.4.5 Discussion

Crystal and magnetic structure

The refinement (parameters in Table 4.5) shows that the composition of the crystal is not stoichiometric $MnSb_4Te_7$, but rather $(Mn_{0.56}Sb_{0.44})(Sb_{0.91}Mn_{0.09})_2Te_4(Sb_2Te_3)$. There is a deficiency of Mn relative to Sb, and a high degree of site-mixing. The positions of the atoms within the unit cell are very similar to those determined by XRD on crystals from the same batch (Table 4.3). The ability of our experiment to detect site-mixing is due to the increased contrast between Mn and Sb for neutrons compared with x-rays. The non-integer reflections with $l = (2n+1)/2$ we measured in the ILL D10 experiment are the smoking gun for a magnetic supercell with AFM order along the c axis. However, we did not measure any other non-integer or satellite positions consistent with AFM order along the a or b axes, such as the canted AFM state proposed in reference [43] for $MnSb_2Te_4$. In my refinement, the moment per Mn ion for the 1a site (Mn_{Mn}) was 2.40 μ_B, while the moment per Mn ion for the 2d site (Mn_{Sb}) was 2.3 μ_B.

Temperature dependence

The critical exponent that describes the temperature dependence of the (1 0 0.5) reflection in $MnSb_4Te_7$ is $\beta = 0.31(2)$, which is very close to the critical exponent for $MnBi_4Te_7$ and that of a 3D system with Ising-like interactions $\beta \approx 0.32$ [28]. It is lower than the critical exponent for a 3D system with Heisenberg interactions ($\beta \approx 0.36$) or XY-like interactions ($\beta \approx 0.34$) [52], and than the critical exponent for $MnSb_2Te_4$, $\beta \approx 0.44$ [43]. Ising-like interactions could contribute to shorter-range magnetic order in these materials and possibly explain the prevalence of different

AFM 'domains' seen in surface probes such as STM.

Spin-flip transition in field

The AFM → FM transition is of interest as the change in magnetic order might leave the hypothetical axion insulator state unchanged [33]. The results in 4.11 show a spin-flip transition (AFM → FM) at 0.2 T for 2 K, ∼ 0.15 T for 6 K. $MnBi_4Te_7$ exhibited a spin-flip transition at the same field but at a higher temperature of 10 K [18]. This is consistent with less μ_B/Mn in $MnSb_4Te_7$ compared to $MnBi_4Te_7$.

Given the extremely high fields needed to saturate the magnetic moments of Mn^{2+} ions in $MnBi_2Te_4$ (discussed in § 4.2.1), the spin-flip transition at 0.2 T is likely to be one of several in-field transitions for $MnSb_4Te_7$. The near-zero intensity of the non-integer reflection (0 1 0.5) for fields higher than 0.2 T demonstrates that the magnetic unit cell is no longer twice the size of the structural unit cell along the c axis, corresponding to the AFM coupling between successive septuple layers being overcome. However, it is very likely that the stronger intra-layer AFM between site-mixed Mn_{Sb} and main-layer Mn_{Mn} persists. Another way to look at this is to compare the energy $\sim g \times 0.2\,\mathrm{T} \times 4.7\mu_B \approx 5.4 \times 10^{-5}$ eV for the observed spin-flip transition here with the estimated exchange parameter between layers $SJ_c \sim 5 \times 10^{-5}$ eV for the similar $MnBi_2Te_4$ system in Table 4.1. In the case of $MnSb_4Te_7$, the interlayer exchange is likely weaker than the quoted SJ_c for $MnBi_2Te_4$ due to the increased distance between septuple layers.

A hysteresis loop opens up at a temperature of 2 K, which is not seen in the 6 K data. This is consistent with the magnetisation data reported in reference [33], where hysteresis increased as temperature decreased – additionally in that reference, no hysteresis was seen with the field parallel to the ab plane. This suggests increasing magnetic anisotropy with decreasing temperature, and a shift to the magnetism being dominated by more 2D interactions or at least more intra- (rather than inter-) layer interactions. The decreased spin-flip field and lack of hysteresis in the higher temperature data suggests the energy barrier associated with the AFM → FM transition has diminished as the temperature has increased.

4.5 Conclusion

Different materials of the $(MnX_2Y_4)(X_2Y_3)_m$ family exhibit a range of magnetic ordering phenomena; however, there are two evident commonalities:

- Mn^{2+} moments in the same ab plane are ferromagnetically aligned;

- materials with site mixing between Mn and X sites have ferrimagnetic septuple layers.

The interlayer magnetic coupling does vary along the c axis, and depends on the number of (non-magnetic) quintuple layers, Mn^{2+} content/stoichiometry, layer number in thin film samples, proportion of Sb/Bi, as well as site mixing – all susceptible to variation in synthesis conditions [35]. Our ILL D10 zero-field data for $MnSb_4Te_7$ (grown under the conditions described in [33]) provides evidence that

- our $MnSb_4Te_7$ crystal is deficient in Mn (% less than stoichiometric) and rich in Sb (% in excess);
- the composition of our $(MnSb_2Te_4)(Sb_2Te_3)$ crystal is in fact $(Mn_{0.56}Sb_{0.44})(Sb_{0.91}Mn_{0.09})_2Te_4(Sb_2Te_3)$;
- the magnetic order consists of ferrimagnetism within the site-mixed septuple $MnSb_2Te_4$ layers;
- and interlayer AFM along the c axis, giving an overall AFM on average with propagation vector $\mathbf{q} = (0\,0\,\frac{1}{2})$.

The magnetic ordering is similar to Mn-deficient $MnSb_2Te_4$, which lacks the Sb_2Te_3 quintuple layer of $MnSb_4Te_7$. The refined moments of 2.4 μ_B/Mn on the Mn site and 2.3 μ_B/Mn on the Sb site are comparable to prior $MnSb_2Te_4$ results [25, 35]. On the other hand, the Bi compound $MnBi_4Te_7$ has more μ_B per Mn, together with less site mixing [28, 29].

Our field-dependent D10 data revealed a spin-flip transition to FM order with 0.2 T applied along the c axis, at a temperature of 2 K. However, it is likely the site-mixed Mn_{Sb} spins are still antiferromagnetically coupled to the Mn_{Mn} spins within the structural unit cell. Measurements at higher fields would be required to test this hypothesis. Furthermore, the hysteresis loop seen in our field-dependent 2 K data supports the notion that the magnetism is increasingly 2D rather than 3D at low temperatures [29].

Acknowledgements for this chapter

Affiliations are the University of Oxford unless otherwise stated.

The crystal synthesis and magnetisation measurements of $MnSb_4Te_7$ was performed by Xin Zhang and Yan-Feng Guo (Shanghai Tech University).

The ILL Cyclops experiment was performed by Siobhan Tobin and Jian-Rui Soh (EPFL).

The ILL D10 experiment was performed by Siobhan Tobin, Jian-Rui Soh (EPFL), Bachir Ouladdiaf

(ILL), Ketty Beauvois (ILL) and Andrew Boothroyd. Data from this experiment are available via proposal number 5-41-1155 [53].

References

[1] Y. L. Chen et al. "Experimental Realization of a Three-Dimensional Topological Insulator, Bi_2Te_3". *Science* 325.5937 (2009). DOI: 10.1126/science.1173034 (cited on page 93).

[2] H. Zhang, C.-X. Liu, X.-L. Qi, X. Dai, Z. Fang, and S.-C. Zhang. "Topological insulators in Bi_2Se_3, Bi_2Te_3 and Sb_2Te_3 with a single Dirac cone on the surface". *Nature Physics* 5.6 (2009). DOI: 10.1038/nphys1270 (cited on page 93).

[3] D. Hsieh et al. "A tunable topological insulator in the spin helical Dirac transport regime". *Nature* 460.7259 (2009). DOI: 10.1038/nature08234 (cited on pages 93–95).

[4] J. Cai et al. "Electric control of a canted-antiferromagnetic Chern insulator". *Nature Communications* 13.1 (2022). DOI: 10.1038/s41467-022-29259-8 (cited on page 94).

[5] D. J. E. Marsh, K. C. Fong, E. W. Lentz, L. Šmejkal, and M. N. Ali. "Proposal to Detect Dark Matter using Axionic Topological Antiferromagnets". *Physical Review Letters* 123.12 (2019). DOI: 10.1103/PhysRevLett.123.121601 (cited on page 94).

[6] Y.-T. Liu, X.-B. Li, H. Zheng, N.-K. Chen, X.-P. Wang, X.-L. Zhang, H.-B. Sun, and S. Zhang. "High-Throughput Screening for Phase-Change Memory Materials". *Advanced Functional Materials* 31.21 (2021). DOI: 10.1002/adfm.202009803 (cited on page 94).

[7] D. Souchay et al. "Layered manganese bismuth tellurides with $GeBi_4Te_7$- and $GeBi_6Te_{10}$-type structures: towards multifunctional materials". *Journal of Materials Chemistry C* 7.32 (2019). DOI: 10.1039/C9TC00979E (cited on page 94).

[8] T. Hirahara et al. "Large-Gap Magnetic Topological Heterostructure Formed by Subsurface Incorporation of a Ferromagnetic Layer". *Nano Letters* 17.6 (2017). DOI: 10.1021/acs.nanolett.7b00560 (cited on pages 94, 95, 101).

[9] F. Katmis et al. "A high-temperature ferromagnetic topological insulating phase by proximity coupling". *Nature* 533.7604 (2016). DOI: 10.1038/nature17635 (cited on page 94).

[10] J. A. Hagmann et al. "Molecular beam epitaxy growth and structure of self-assembled Bi_2Se_3/Bi_2MnSe_4 multilayer heterostructures". *New Journal of Physics* 19.8 (2017). DOI: 10.1088/1367-2630/aa759c (cited on pages 94, 95).

[11] C.-Z. Chang et al. "Experimental Observation of the Quantum Anomalous Hall Effect in a Magnetic Topological Insulator". *Science* 340.6129 (2013). DOI: 10.1126/science.1234414 (cited on page 94).

[12] J. Choi, S. Choi, J. Choi, Y. Park, H.-M. Park, H.-W. Lee, B.-C. Woo, and S. Cho. "Magnetic properties of Mn-doped Bi_2Te_3 and Sb_2Te_3". *physica status solidi (b)* 241.7 (2004). DOI: 10.1002/pssb.200304527 (cited on pages 94, 95).

[13] J. Dyck, P. Svanda, P. Lošťák, J. Horák, W. Chen, and C. Uher. "Magnetic and transport properties of the V_2–VI_3 diluted magnetic semiconductor $Sb_{2-x}Mn_xTe_3$". *Journal of Applied Physics* 94 (2003). DOI: 10.1063/1.1626803 (cited on page 95).

[14] Y. S. Hor et al. "Development of ferromagnetism in the doped topological insulator $Bi_{2-x}Mn_xTe_3$". *Physical Review B* 81.19 (2010). DOI: 10.1103/PhysRevB.81.195203 (cited on page 95).

[15] J. Henk, M. Flieger, I. V. Maznichenko, I. Mertig, A. Ernst, S. V. Eremeev, and E. V. Chulkov. "Topological Character and Magnetism of the Dirac State in Mn-Doped Bi_2Te_3". *Physical Review Letters* 109.7 (2012). DOI: 10.1103/PhysRevLett.109.076801 (cited on page 95).

[16] E. D. L. Rienks et al. "Large magnetic gap at the Dirac point in $Bi_2Te_3/MnBi_2Te_4$ heterostructures". *Nature* 576.7787 (2019). DOI: 10.1038/s41586-019-1826-7 (cited on pages 95, 96).

[17] S. Li, T. Liu, C. Liu, Y. Wang, H.-Z. Lu, and X. C. Xie. "Progress on the antiferromagnetic topological insulator $MnBi_2Te_4$". *National Science Review* 11.2 (2024). DOI: 10.1093/nsr/nwac296 (cited on page 95).

[18] I. I. Klimovskikh et al. "Tunable 3D/2D magnetism in the $(MnBi_2Te_4)(Bi_2Te_3)_m$ topological insulators family". *npj Quantum Materials* 5.1 (2020). DOI: 10.1038/s41535-020-00255-9 (cited on pages 95, 99, 116).

[19] Y.-J. Hao et al. "Gapless Surface Dirac Cone in Antiferromagnetic Topological Insulator $MnBi_2Te_4$". *Physical Review X* 9.4 (2019). DOI: 10.1103/PhysRevX.9.041038 (cited on pages 95–97).

[20] D. Zhang, M. Shi, T. Zhu, D. Xing, H. Zhang, and J. Wang. "Topological Axion States in the Magnetic Insulator $MnBi_2Te_4$ with the Quantized Magnetoelectric Effect". *Physical Review Letters* 122.20 (2019). DOI: 10.1103/PhysRevLett.122.206401 (cited on page 95).

[21] J.-Q. Yan, Q. Zhang, T. Heitmann, Z. L. Huang, W. D. Wu, D. Vaknin, B. C. Sales, and R. J. McQueeney. "Crystal growth and magnetic structure of $MnBi_2Te_4$". *Physical Review Materials* 3.6 (2019). DOI: 10.1103/PhysRevMaterials.3.064202 (cited on page 95).

[22] J.-Q. Yan, Y. H. Liu, D. S. Parker, Y. Wu, A. A. Aczel, M. Matsuda, M. A. McGuire, and B. C. Sales. "A-type antiferromagnetic order in $MnBi_4Te_7$ and $MnBi_6Te_{10}$ single crystals". *Physical Review Materials* 4.5 (2020). DOI: 10.1103/PhysRevMaterials.4.054202 (cited on page 96).

[23] C. Liu, Y. Wang, H. Li, Y. Wu, Y. Li, J. Li, K. He, Y. Xu, J. Zhang, and Y. Wang. "Robust axion insulator and Chern insulator phases in a two-dimensional antiferromagnetic topological insulator". *Nature Materials* 19.5 (2020). DOI: 10.1038/s41563-019-0573-3 (cited on pages 96, 97).

[24] Y. Chen et al. "Topological Electronic Structure and Its Temperature Evolution in Antiferromagnetic Topological Insulator $MnBi_2Te_4$". *Physical Review X* 9.4 (2019). DOI: 10.1103/PhysRevX.9.041040 (cited on pages 96, 100).

[25] Y. Lai, L. Ke, J. Yan, R. D. McDonald, and R. J. McQueeney. "Defect-driven ferrimagnetism and hidden magnetization in $MnBi_2Te_4$". *Physical Review B* 103.18 (2021). DOI: 10.1103/PhysRevB.103.184429 (cited on pages 97, 98, 103, 117).

[26] B. Li, J.-Q. Yan, D. M. Pajerowski, E. Gordon, A.-M. Nedić, Y. Sizyuk, L. Ke, P. P. Orth, D. Vaknin, and R. J. McQueeney. "Competing Magnetic Interactions in the Antiferromagnetic Topological Insulator $MnBi_2Te_4$". *Physical Review Letters* 124.16 (2020). DOI: 10.1103/PhysRevLett.124.167204 (cited on pages 97, 98).

[27] H. Padmanabhan et al. "Large Exchange Coupling Between Localized Spins and Topological Bands in $MnBi_2Te_4$". *Advanced Materials* 34.49 (2022). DOI: 10.1002/adma.202202841 (cited on page 98).

[28] L. Ding, C. Hu, E. Feng, C. Jiang, I. A. Kibalin, A. Gukasov, M. Chi, N. Ni, and H. Cao. "Neutron diffraction study of magnetism in van der Waals layered $MnBi_{2n}Te_{3n+1}$". *Journal of Physics D: Applied Physics* 54.17 (2021). DOI: 10.1088/1361-6463/abe0dd (cited on pages 99, 115, 117).

[29] L. Ding, C. Hu, F. Ye, E. Feng, N. Ni, and H. Cao. "Crystal and magnetic structures of magnetic topological insulators $MnBi_2Te_4$ and $MnBi_4Te_7$". *Physical Review B* 101.2 (2020). DOI: 10.1103/PhysRevB.101.020412 (cited on pages 99, 117).

[30] Y. Deng, Y. Yu, M. Z. Shi, Z. Guo, Z. Xu, J. Wang, X. H. Chen, and Y. Zhang. "Quantum anomalous Hall effect in intrinsic magnetic topological insulator $MnBi_2Te_4$". *Science* 367.6480 (2020). DOI: 10.1126/science.aax8156 (cited on page 100).

[31] H. Deng et al. "High-temperature quantum anomalous Hall regime in a $MnBi_2Te_4/Bi_2Te_3$ superlattice". *Nature Physics* 17.1 (2021). DOI: 10.1038/s41567-020-0998-2 (cited on page 100).

[32] B. Chen et al. "Intrinsic magnetic topological insulator phases in the Sb doped $MnBi_2Te_4$ bulks and thin flakes". *Nature Communications* 10.1 (2019). DOI: 10.1038/s41467-019-12485-y (cited on pages 100, 101, 103).

[33] S. Huan et al. "Multiple Magnetic Topological Phases in Bulk van der Waals Crystal $MnSb_4Te_7$". *Physical Review Letters* 126.24 (2021). DOI: 10.1103/PhysRevLett.126.246601 (cited on pages 100, 103, 105–108, 116, 117).

[34] S. H. Lee et al. "Evidence for a Magnetic-Field-Induced Ideal Type-II Weyl State in Antiferromagnetic Topological Insulator $Mn(Bi_{1-x}Sb_x)_2Te_4$". *Physical Review X* 11.3 (2021). DOI: 10.1103/PhysRevX.11.031032 (cited on pages 101, 103).

[35] Y. Liu et al. "Site Mixing for Engineering Magnetic Topological Insulators". *Physical Review X* 11.2 (2021). DOI: 10.1103/PhysRevX.11.021033 (cited on pages 102, 103, 117).

[36] X. Zhang et al. "Tunable intrinsic ferromagnetic topological phases in bulk van der Waals crystal $MnSb_6Te_{10}$". *arXiv:2111.04973 [cond-mat]* (2021). DOI: 10.48550/arXiv.2111.04973 (cited on page 102).

[37] S. Huan, D. Wang, H. Su, H. Wang, X. Wang, N. Yu, Z. Zou, H. Zhang, and Y. Guo. "Magnetism-induced ideal Weyl state in bulk van der Waals crystal $MnSb_2Te_4$". *Applied Physics Letters* 118.19 (2021). DOI: 10.1063/5.0047438 (cited on pages 102, 103).

[38] T. Murakami, Y. Nambu, T. Koretsune, G. Xiangyu, T. Yamamoto, C. M. Brown, and H. Kageyama. "Realization of interlayer ferromagnetic interaction in $MnSb_2Te_4$ toward the magnetic Weyl semimetal state". *Physical Review B* 100.19 (2019). DOI: 10.1103/PhysRevB.100.195103 (cited on pages 102, 103).

[39] L. Chen, D. Wang, C. Shi, C. Jiang, H. Liu, G. Cui, X. Zhang, and X. Li. "Electronic structure and magnetism of $MnSb_2Te_4$". *Journal of Materials Science* 55.29 (2020). DOI: 10.1007/s10853-020-05005-7 (cited on page 102).

[40] L. Zhou, Z. Tan, D. Yan, Z. Fang, Y. Shi, and H. Weng. "Topological phase transition in the layered magnetic compound $MnSb_2Te_4$: Spin-orbit coupling and interlayer coupling dependence". *Physical Review B* 102.8 (2020). DOI: 10.1103/PhysRevB.102.085114 (cited on page 102).

[41] D. Y. Yan, M. Yang, P. B. Song, Y. T. Song, C. X. Wang, C. J. Yi, and Y. G. Shi. "Site mixing induced ferrimagnetism and anomalous transport properties of the Weyl semimetal candidate $MnSb_2Te_4$". *Physical Review B* 103.22 (2021). DOI: 10.1103/PhysRevB.103.224412 (cited on page 102).

[42] M. Z. Gang Shi. "Anomalous Hall Effect in Layered Ferrimagnet $MnSb_2Te_4$". *Chinese Physics Letters* 37.4 (2020). DOI: 10.1088/0256-307X/37/4/047301 (cited on pages 103, 105).

[43] X. Yang, J. Pan, X. He, and D. Chu. "Critical behavior, magnetic phase diagram, and magnetic entropy change of $MnSb_2Te_4$". *Physical Review B* 109.9 (2024). DOI: 10.1103/PhysRevB.109.094408 (cited on pages 103, 115).

[44] Z. Zang et al. "Layer-Number-Dependent Antiferromagnetic and Ferromagnetic Behavior in $MnSb_2Te_4$". *Physical Review Letters* 128.1 (2022). DOI: 10.1103/PhysRevLett.128.017201 (cited on page 104).

[45] H. Li, Y. Li, Y.-K. Lian, W. Xie, L. Chen, J. Zhang, Y. Wu, and S. Fan. "Glassy magnetic ground state in layered compound $MnSb_2Te_4$". *Science China Materials* 65 (2022). DOI: 10.1007/s40843-021-1738-9 (cited on pages 104, 105).

[46] S. Wimmer et al. "Mn-Rich $MnSb_2Te_4$: A Topological Insulator with Magnetic Gap Closing at High Curie Temperatures of 45–50 K". *Advanced Materials* 2021 (2021). DOI: 10.1002/adma.202102935 (cited on page 105).

[47] W. Ge, P. M. Sass, J. Yan, S. H. Lee, Z. Mao, and W. Wu. "Direct evidence of ferromagnetism in $MnSb_2Te_4$". *Physical Review B* 103.13 (2021). DOI: 10.1103/PhysRevB.103.134403 (cited on page 105).

[48] *NIST Neutron Scattering Lengths List*. 2017. URL: https://www.nist.gov/ncnr/neutron-scattering-lengths-list (visited on 2022) (cited on page 106).

[49] B. Ouladdiaf, J. Archer, J. R. Allibon, P. Decarpentrie, M.-H. Lemée-Cailleau, J. Rodríguez-Carvajal, A. W. Hewat, S. York, D. Brau, and G. J. McIntyre. "CYCLOPS – a reciprocal-space explorer based on CCD neutron detectors". *Journal of Applied Crystallography* 44.2 (2011). DOI: 10.1107/S0021889811006765 (cited on page 108).

[50] K. Momma and F. Izumi. "VESTA 3 for three-dimensional visualization of crystal, volumetric and morphology data". *Journal of Applied Crystallography* 44.6 (2011). DOI: 10.1107/S0021889811038970 (cited on page 110).

[51] N. Qureshi. "Mag2Pol: a program for the analysis of spherical neutron polarimetry, flipping ratio and integrated intensity data". *Journal of Applied Crystallography* 52.1 (2019). DOI: 10.1107/S1600576718016084 (cited on page 112).

[52] A. T. Boothroyd. *Principles of Neutron Scattering from Condensed Matter*. Oxford University Press, 2020 (cited on page 115).

[53] J.-R. Soh, A. Boothroyd, B. Ouladdiaf, and S. M. Tobin. "Anti-ferromagnetic topological insulator candidate $MnSb_4Te_7$". *Institut Laue Langevin* (2021). DOI: 10.5291/ILL-DATA.5-41-1155 (cited on page 118).

5

The spin disorder and hourglass excitation spectrum of the charge-doped cobalt oxide $La_{2-x}Ba_xCoO_4$

5.1 Introduction

The layered transition metal oxides $La_{2-x}A_xMO_4$ – including cuprates, nickelates, cobaltates and manganites – are strongly correlated materials displaying a rich diversity of electronic and magnetic order confined largely to two dimensional MO_2 layers, where M is the transition metal. Hole-doping with a divalent ion (the dopant concentration is x) is crucial for manifesting superconductivity in the cuprates but the ordering of insulating phases at intermediate doping is also of interest [1–3]. Charge stripes are a form of electronic order (Figure 5.2) seen in these layered transition metal oxides (a typical crystal structure is shown in Figure 5.1). Charge order introduces symmetry-breaking lattice distortions (e.g. Jahn-Teller effect), which in turn affect phonon propagation. From the BCS theory, we know that coupling between electrons and phonons can play a significant role in superconductivity, yet BCS theory cannot explain the high temperature superconductivity in the cuprates [2]. On top of charge and structural effects, stripes also form domain walls between regions of antiferromagnetic order, implying that the exchange interactions between spins are also involved as well as Coulomb repulsion.

The interplay between these various electronic degrees of freedom is not fully understood, but is believed to play a crucial role in the development of the pseudogapped superconducting phase [3–5]. Static charge stripes are found in insulators and hinder superconductivity, but a transition

to dynamic charge stripe order could indicate a new transport mechanism that facilitates superconductivity. How charge stripes manifest in different materials, and what role they play in the physics of strongly correlated electronic systems, is up for discussion in the condensed matter community, with a number of models put forward in the literature. Furthermore, other forms of charge transport are found in the transition metal oxides, with La_2CoO_4/La_2CoO_3 also attracting interest as cathodes [6], catalyst materials [7–9] and conductors of ionic oxygen [10]. Probing materials that potentially exhibit charge stripe order is an important aspect of this discussion, and this chapter of my thesis looks at one such stripy candidate: $La_{2-x}Ba_xCoO_4$.

The structure of the chapter is as follows:

- Different charge and spin ordering possibilities and the associated terminology are introduced in § 5.1.1.
- The $La_{2-x}A_xMO_4$ family of materials are introduced in more detail in § 5.1.2, with a focus on $La_{2-x}Ba_xCoO_4$ in § 5.1.3.
- Several approaches to modelling the magnetic excitations of the $La_{2-x}A_xMO_4$ materials are described in § 5.2, with examples drawn from existing work on $La_{2-x}Sr_xCoO_4$.
- Then we move into the experimental work including characterisation of the samples (§ 5.3), elastic neutron scattering (§ 5.4) and inelastic neutron scattering (§ 5.5).
- Concluding remarks are presented in § 5.6.

5.1.1 Manifestations of charge and spin order

With the magnetic moment of any given ion determined by the unpaired electrons in its outermost shell, it follows that charge (and orbital) order are coupled to magnetic order. All of the $La_{2-x}A_xMO_4$ materials in this chapter have an element M that can be present as both magnetic and non-magnetic ions depending on the hole dopant concentration x, for example, Co^{2+} is magnetic ($S = 3/2$), while Co^{3+} is not ($S = 0$). Further complicating this is that other spin states are relatively low-lying in energy for cobalt ions; for example, Co^{3+} can access higher spin states ($S = 1$, $S = 2$), but the evidence favours non-magnetic Co^{3+} with $S = 0$ in materials such as $La_{1.5}Sr_{0.5}CoO_4$ in which the Co is surrounded by an octahedron of oxygen ions [11]. All adopt a similar kind of crystal structure seen in Figure 5.1: either a tetragonal space group as shown, or an orthorhombic distortion from this.

Here the focus is on phases where the charge and spin order is confined to the two dimensional

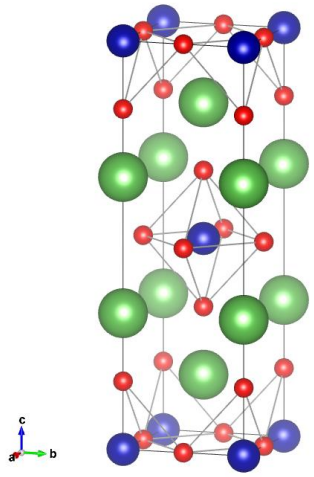

Figure 5.1: An example of the crystal structure of the transition metal oxides such as cuprates, nickelates and cobaltates belonging to tetragonal space group $I4/mmm$. Here in this thesis, my experimental work is on $La_{2-x}Ba_xCoO_4$, shown in this diagram as cobalt = blue, oxygen = red, and lanthanum/barium = green. Diagram drawn using VESTA [12].

ab plane of the crystal as the interactions along the *c* direction are considered to be much weaker than those within the *ab* plane. Due to the anisotropy and varying strength of the exchange and superexchange interactions present, an array of different layered magnetic structures is possible. The structural unit cell in the *ab* plane is a square (or approximately so) but the varying periodicity and range of the charge and spin orders leads to different superstructure reflections in reciprocal space. Some of these magnetic structures are shown in Figure 5.2, with only the transition metal element shown. In this case, Co^{2+} / Co^{3+} are used as the ionic species but the illustrations are also valid for Ni ions.

Distinguishing between checkerboard and stripe phases is key, yet is not entirely straightforward. All forms of order mentioned so far are effectively 2D, located in the *ab* plane. Across all layers, stripes are unlikely to be oriented along the same direction, and instead may run along perpendicular directions between successive layers. Looking at such a structure along the *c* axis, it could be confused with checkerboard ordering instead. However, checkerboard order has a higher symmetry than stripe order. By considering the mean periodicity and orientation of stripes as a form of long-range order, a charge stripe phase can be differentiated from a checkerboard phase [14].

Neutron scattering is a direct probe of magnetic order; however, it is an indirect probe of charge order, able only to detect superstructure reflections from structural distortions introduced by charge order. X-ray scattering experiments, including x-ray absorption spectroscopy and resonant elastic

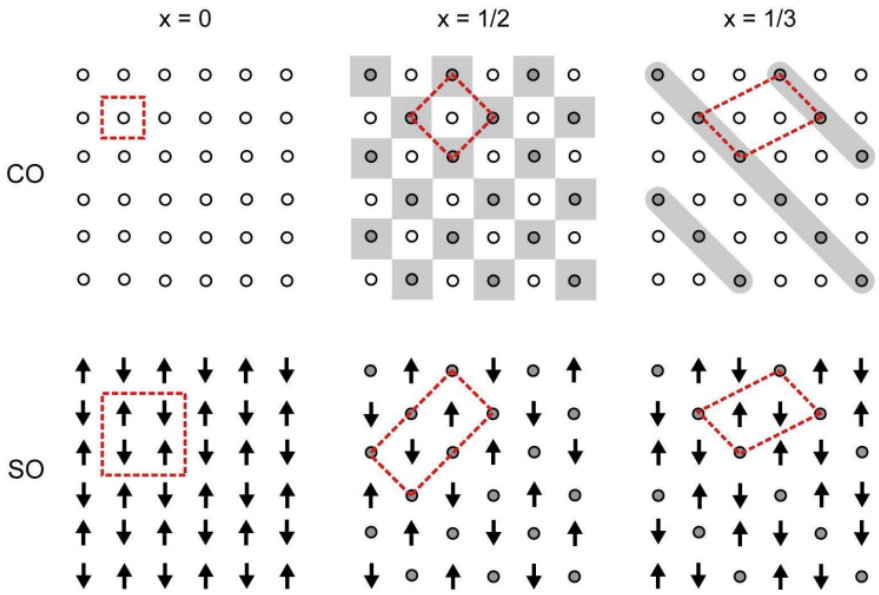

Figure 5.2: Charge order (CO) and spin order (SO) on a square lattice *ab* plane layer for materials such as the cobalt oxides with dopant concentration x. Nearest-neighbour AFM order prevails for x = 0. In checkerboard charge ordering for x = 1/2, equal amounts of Co^{3+} and Co^{2+} are present. Stripe order for x = 1/3 consist of stripes of Co^{3+} ions while regions of Co^{2+} ions lead to anisotropic AFM order between the stripes (spins are FM aligned along one diagonal and AFM along the other). Red dashed boxes mark primitive 2D unit cells. Source: [13], reproduced with permission. Copyright Lucy M. Helme (2006).

x-ray scattering, can provide a more robust indicator of charge order. An example using these x-ray techniques is given in reference [15], where the onset of charge stripe order coincides with a transition to a tetragonal structure.

An additional complication arises in the form of disorder and frustration in the layered transition metal oxides such as the cobaltates. No sample of any material is *perfectly* ordered – descriptions of samples as twinned, multi-domained, glassy, or even nanoscale phase-separated abound in the literature for the cobaltates. These terms can be thought of as being on a spectrum of short- to long-range order, but (in my opinion) the language can overlap (at the very least, it is opaque or maybe even *diffuse*[1]). For example, two different models for the specific case of $x = 1/3$ $La_{2-x}Sr_xCoO_4$ have been proposed. How different does nanoscale phase separation of checkerboard $x = 1/2$ and undoped $x = 0$ $La_{2-x}Sr_xCoO_4$ (the model suggested in reference [17]) look from cluster spin glass (proposed in reference [18]) in real and reciprocal space? Primarily, it is a matter of the range of the magnetic order. It's conceivable that the spin ordering of samples of the same material could occupy a range of correlation length scales, i.e. on a sliding scale from larger domains to cluster spin glass.

[1] Hello, here is a Nature paper that talks of "stripy charge-density-wave puddles" [16]!

Of course, among all this discussion of spin and charge stripes, the concepts of spin and charge density waves merit a mention. A charge density wave (CDW) is a one dimensional standing wave modulation of the charge on a particular lattice site in a metallic material. This charge modulation induces a periodic lattice distortion resulting in a superstructure, observable via diffraction techniques. The stripes associated with charge density waves have been observed in real space using electron microscopy techniques [19]. Naturally, a charge density wave may be accompanied by a spin density wave (SDW); for an example, see reference [20]. This is usually associated with itinerant magnetism in a metal, but may also accompany a metal-insulator transition [21]. This is because a SDW is essentially the superposition of out-of-phase spin-up and spin-down CDWs. In some cases, the nesting of the Fermi surface from one CDW with the other CDW may introduce a bandgap; hence, the result can be a Peierls insulator with a SDW. A SDW modulates not only the direction of the spins but their magnitude as well, which is a key difference from the effective spin 1/2 model that linear spin wave theory and the Heisenberg Hamiltonian are based on.

Examples of superconductors with CDW and/or SDW instabilities abound [22]. These are also labelled as electron liquid crystal states [2]. To my mind, the time-averaged picture of a SDW does not differ from that of fluctuating spin stripes at all. In the case of static order in an insulator, there is a clear difference qualitatively in real space but less so in reciprocal space – both models permit incommensurate and commensurate orders.

Having introduced some of the terminology and signatures of different forms of magnetic order, we now turn to specific material examples.

5.1.2 The $La_{2-x}A_xMO_4$ family of materials

The undoped cuprates are antiferromagnetic (AFM) Mott insulators. Undoped La_2MO_4 (where M = Co, Ni, or Cu) has La in the +3 oxidation state, M in the magnetic +2 oxidation state, and O in the -2 oxidation state. A simple model is that doping with an alkali earth metal A (typically Ca, Sr or Ba) disrupts the AFM order and the introduced holes form stripes as in Figure 5.2, with the periodicity and values of charge stripes affected by dopant concentration x. Some AFM order persists in domains bounded by charge stripes. Furthermore, superconductivity in the cuprate family can be enhanced by external pressure [23–25] and the dopant ion A can be seen as a source of internal 'chemical' pressure within the lattice [26–28]: increasing the concentration x or size difference between La and A ions presumably leads to structural, spin and charge order modifications that can tip the balance in favour of superconductivity.

Insights into the spin and charge order may be gleaned from studying isostructural compounds that share the same parent phase as the cuprates, but remain insulating at low temperatures and over a wide range of dopant concentrations. Members of this family include the nickel oxides (nickelates), the manganese oxides (manganites), and the cobalt oxides (cobaltates and cobaltites).

It is also worth mentioning that some of the nickelates and cobaltates of the $La_{2-x}A_xMO_4$ family exhibit other electronic transport phenomena, including mixed ionic conduction at higher temperatures [10, 29] and even temperature-dependent oxygen stoichiometry has been reported in reference [30]. This is because the nickelates and cobaltates $La_{2-x}A_xMO_{4+\delta}$ can accommodate a wider range of oxygen concentration ($\delta \lesssim 0.35$) than the cuprates ($\delta \lesssim 0.05$), with oxygen ions readily occupying interstitial sites. An excess of oxygen δ introduces holes, as does substituting x amount of a divalent ion A for La. This results in some Co^{2+} being swapped for Co^{3+}. $\delta = 0.25$ in $La_2CoO_{4+\delta}$ yields an equal amount of Co^{2+} and Co^{3+}, as does x = 1/2 in $La_{2-x}A_xO_4$. In general, combined doping of δ and x gives the charge balance [13]

$$La_{2-x}Sr_xCo^{2+}_{1-z}Co^{3+}_zO_{4+\delta}, \quad z = x + 2\delta. \tag{5.1}$$

These materials of general formula $La_{2-x}A_xMO_4$ or $La_{1-x}A_xMnO_3$ can be compared to the likes of $La_{2-x}Sr_xCuO_4$, a high-temperature superconductor that exhibits both static and dynamic charge-, and magnetic-stripe order [2]. With replacement of Sr by Ba, or additional Nd doping, the stripes in $La_{2-x}Sr_xCuO_4$ become static and superconductivity is suppressed near x = 1/8 [2], further emphasising the importance of the stripe phase in this system. Some examples of relevant cuprates are La_2CuO_4 [31], $La_{2-x}Sr_xCuO_4$ [14, 32], $La_{2-x}Ba_xCuO_4$ [14, 33], and $La_{1.6-x}Nd_{0.4}Sr_xCuO_4$ [1, 34]. A review of nickelates including $La_{2-x}A_xNiO_4$ (A = Sr, Ca), $Re_{1.67}A_{0.33}NiO_4$ (Re a rare earth and A = Sr, Ca), and $La_{2-x}Sr_xNiO_{4+\delta}$ is presented in reference [11]. The nickelates, like the cobaltates, are AFM Mott insulators except in the limit $x \sim 1$.

The manganites have a different perovskite crystal structure and show a zig-zag form of charge, orbital and magnetic order [11], which is quite different to the types of order present in the selection of cuprates and nickelates listed above. Perhaps what is more relevant here is lanthanum cobaltite with composition $La_{1-x}A_xCoO_3$ and perovskite structure, which is shown in the overview of cobalt oxides presented in Table 5.1 together with the lanthanum cobaltates. The lanthanum cobaltites have a distinct phase diagram from the lanthanum manganites, but feature the same (approximately) octahedral Co sites as the cobaltates, and can display a broad range of strongly correlated phenomena ranging from ferroelastic and semiconductor tendencies [35–37] to colossal magnetore-

sistance [38]. The spin state(s) of the Co ions is crucial to understanding these characteristics and I will now briefly discuss this.

The spin states of the Co ions

Here I briefly justify and summarise the assumptions made regarding the spin states of Co^{2+} and Co^{3+} for the remainder of this chapter; that is $S = 3/2$ for Co^{2+} and $S = 0$ for Co^{3+} surrounded by oxygen octahedra in many cobalt oxides.

The octahedral crystal field of the oxygen ions splits the $3d$ level into an e_g doublet and a t_{2g} triplet as shown in Figure 5.3. For Co^{2+} ($3d^7$), Co^{3+} ($3d^6$), and Co^{4+} ($3d^5$), the crystal field splitting (energy Δ_{CF}) is in competition with Hund's rule (interatomic exchange energy J_H) and so multiple spin states are conceivable; however, Hund's coupling dominates for Co^{2+} (as in La_2CoO_4) and the crystal field for Co^{4+}, resulting in the favoured spin states being high ($S = 3/2$) and low ($S = 1/2$) respectively [11, 39, 40]. The variety of spin states associated with different oxidation states of Co no doubt drives the rich array of electronic and magnetic order seen in the cobalt oxides: the relative chemical instability of Co^{4+} contributes to the ferromagnetic metallicity of $La_{1-x}A_xCoO_3$, whereas the strong localisation of Co^{2+} electrons in the high spin state (the nominated oxidation state in La_2CoO_4) renders the compounds $La_{2-x}A_xCoO_4$ ($0 \leq x < 1$) Mott insulators [39].

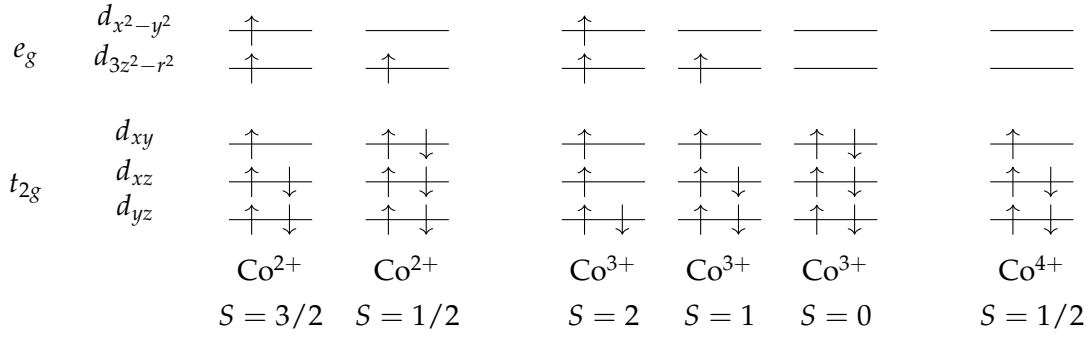

Figure 5.3: Possible spin states of different Co ions in an octahedral crystal field.

For Co^{2+} in the high spin state, including spin-orbit coupling introduces a further splitting of the t_{2g} levels, and S is no longer a good quantum number [13]. The usual $\mu = g\mu_B S$ ($g = 2$) for transition metal ions is no longer strictly true. Adding this interaction increases the magnetic moment per Co^{2+} ion to $\mu_{\text{eff.}} \approx 6.7\,\mu_B$, so this interaction accounts for experimental results without invoking a magnetic moment on the Co^{3+} ions in e.g. $La_{1.5}Sr_{0.5}CoO_4$ [13] (the spin-orbit interaction also contributes to the excitation spectra, see § 5.2.2).

In the case of Co^{3+}, there is a closer competition between J_H and Δ_{CF}, so the spin state can be affected

by structural distortions with changing temperature or pressure [39]. Indeed, the intermediate spin state is Jahn-Teller active [41]. The occupation of the high ($S = 2$) and intermediate ($S = 1$) spin states would imply that Co^{3+} has a non-zero magnetic moment. This is the case for $LaSrCoO_4$ (which ostensibly features Co^{3+} only) $\mu_{\text{eff.}} \approx 2.8\,\mu_{\text{B}}$, with the material remaining paramagnetic even at low temperatures [41] (similar paramagnetism of Co^{3+} ions but in the high spin state was explored in reference [42]). There is also the suggestion that the Co^{3+} ions are 'frozen' into a $M_S = 0$ singlet state (irrespective of S) in the case of low temperatures and strong planar anisotropy [40]. For doping concentrations $x < 1$, the bulk of experimental evidence favours the low spin $S = 0$ state of Co^{3+}, with an overall philosophy of "keep it simple" prevailing, given that the strength of the Co^{2+} ordered moments is sufficient to account for measurements (see the review [11] and an example in reference [43]).

Table 5.1: Some examples of cobalt oxides and their properties

Cobalt oxides[1]	Space group	Magnetic structure	Electronic properties
La_2CoO_4 [44]	$I4/mmm$, $Cmce$[2] above 135 K, $P4_2/ncm$ below 135 K	Nearest-neighbour AFM with strong XY anisotropy. Stacking along c axis is FM below 135 K and AFM above 135 K. No long range order above $T_N \approx 275$ K	AFM insulator.
$La_2CoO_{4+\delta}$, $0 < \delta < 0.32$ [10, 30]	$Fmmm$ for $\delta \approx 0.25$, $F4/mmm$ and $F112/m$, with incommensurate structural distortions [10, 45], $Bmab$ for $\delta \approx 0.22$, $Pmmm$ for $\delta \approx 0.32$ [30]	$T_N \sim 36$ K with checkerboard charge order and a magnetic unit cell double (at least) the structural unit cell in all directions [10]	Diffusion of ionic oxygen reported for $\delta \sim 0.25$.
$LaCoO_3$ [7, 35–37]	$R\bar{3}c$ [7, 35]	Short-range 2D antiferromagnetism, $T_N \approx 89$ K, accompanied by ubiquitous twinning with ferro/ferrimagnetic behaviour emerging when field-cooled. All magnetic order disappears at $T \approx 40$ K [35].	Diamagnetic semiconductor [36] with ferroelastic behaviour [37]
$La_{1-x}Sr_xCoO_3$ [38]	$R\bar{3}c$	Predominantly glassy ferromagnetic clusters for $x < 0.18$ with $T_{SG} = 40$ K – 100 K, predominantly FM $x \geq 0.18$ with $T_C \sim 60$ K and nn $J \approx 6.5$ meV[46]	$x \lesssim 0.18$: insulator, $x \gtrsim 0.18$: metallic, with a percolation-type metal-to-insulator transition.

[1] The naming conventions are ambiguous: La_2CoO_4 is often termed a *cobaltate*, while the IUPAC convention would be lanthanum cobalt(II) oxide. $LaCoO_3$ would then be lanthanum cobalt(III) oxide, but it can be called a *cobaltite* or a *perovskite*; both cobaltite (CoAsS) and perovskite ($CaTiO_3$) are actually minerals but the latter is used as a catch-all term for compounds with formula ABX_3 and structure with space group $Pnma$ (or close to this). Also the oxidation state of cobalt here varies with doping, which is kind of the whole point of this chapter. I have bigger fish to fry, but the reader should beware the nomenclature.

[2] The space groups $Cmce$ (formerly known as $Cmca$) and $Bmab$ are equivalent; $Cmce$ uses the conventional choice of b as the long side of the unit cell.

Cobalt oxides[1]	Space group	Magnetic structure	Electronic properties
$La_{2-x}Sr_xCoO_4$, x = 1/2 [40, 43, 47]	$I4/mmm$	Checkerboard charge order, strong XY anisotropy and planar AFM order with $T_N \approx 31$ K [43]. Glassy AFM with strong planar anisotropy and disorder along the c axis, $T_N \approx 36$ K and spin order independent of charge order at $T_{CO} \sim 750$ K [40, 47].	$La_{2-x}A_xCoO_4$: AFM insulator. x = 1/2 is the strongest insulator, correlated with the highest T_{CO}. Metallic for x $\sim$ 1 [11].
$La_{2-x}Sr_xCoO_4$, x = 1/3 [48–50]	$I4/mmm$	Short-range $\approx$ period-3 stripes onset at $\sim$ 100 K.	
$La_{2-x}Sr_xCoO_4$, $0.3 \leq x \leq 0.5$ [51]	$I4/mmm$	Short-range stripe order possibly coexisting with nanoscale phase separation of undoped and checkerboard-ordered regions.	
$La_{2-x}Ca_xCoO_4$ [42, 48]	$I4/mmm$, $A2mm$	Commensurate checkerboard charge order with much longer correlation length for e.g. $La_{1.5}Ca_{0.5}CoO_4$ than for $La_{1.5}Sr_{0.5}CoO_4$. There is commensurate AFM order across all x with four domains (2 structural twins $\times$ $\perp$ spin orientations) [42, 48]. Co^{3+} in the high spin state with sublattice order $\uparrow\uparrow\downarrow\downarrow$ but this is much weaker/diffuse away from x = 1/2, the sublattice of Co^{2+} spins is A/C-type AFM [42].	AFM insulator.

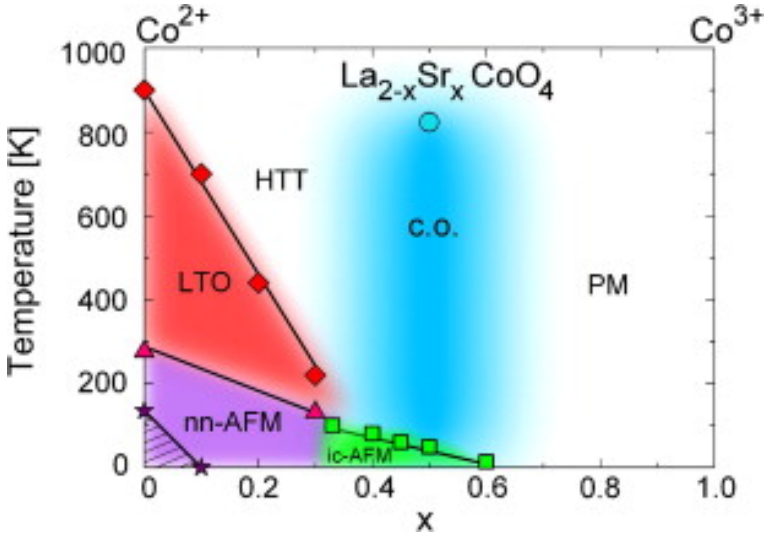

Figure 5.4: Phase diagram of Sr-doped cobaltates. Acronyms used to indicated different phases: HTT = high temperature tetragonal, LTO = low-temperature orthorhombic, c.o. = charge order, nn-AFM = nearest-neighbour antiferromagnetic, ic-AFM = incommensurate antiferromagnetic, PM = paramagnetic. A more recent phase diagram in reference [52] indicates the boundary between *nn*-AFM and incommensurate/glassy AFM lies closer to x ≈ 0.2 than x ≈ 0.3 at low temperatures, but agrees that the transition to PM lies at x ≈ 0.6. This figure is reproduced from reference [11] with permission. Copyright Elsevier (2012).

5.1.3 $La_{2-x}Ba_xCoO_4$

What motivated the selection of Ba as the dopant of our cobaltate? $La_{2-x}Ca_xCoO_4$ demonstrates checkerboard charge order over a wide range of x [42], so it is even less conducive to the formation of stripes than $La_{2-x}Sr_xCoO_4$. Ba is the ubiquitous dopant for the cuprates, with stripes in superconducting $La_{2-x}Ba_xCuO_4$ shown to be more stable than those found in $La_{2-x}Sr_xCuO_4$. Out of Ca^{2+} (0.99 Å), Sr^{2+} (1.13 Å), and Ba^{2+} (1.34 Å), Ba^{2+} has the largest ionic radius, and Ca^{2+} the smallest, which further encouraged us to investigate a Ba-doped cobaltate given there is some evidence for stripes and checkerboard ordering in Sr-doped cobaltates. A larger ionic radius goes some way to alleviating the structural mismatch evidenced by the change in the tilt axis of the oxygen octahedra (this structural transition is seen in La_2CuO_4, La_2NiO_4, and La_2CoO_4) [11], with the atomic radius of La^{3+} = 1.03 Å. Increasing x serves to reduce the octahedral tilting distortion and renders the structure less orthorhombic and then tetragonal at low temperatures [11]. $La_{2-x}Ba_xCoO_4$ may be an exclusively stripy cobaltate system – one in which period-3 charge stripes are present as a single phase – and so my work aimed to characterise its magnetic order and excitations. As far as I am aware, no previous reports of $La_{2-x}Ba_xCoO_4$ measurements exist.

5.2 A review of different models for magnetic excitations seen in cobalt oxides

Established members of the cobalt oxide family with x = 0 and x = 1/2 have well-defined magnetic excitations, but the case of intermediate doping concentrations is not as straightforward. The parent compound La_2CoO_4 orders as a nearest-neighbour antiferromagnet with spins in the *ab* plane. The excitation spectrum of $La_{2-x}Sr_xCoO_4$ has been extensively studied. $La_{2-x}Sr_xCoO_4$ with x = 1/2 exhibits checkerboard charge ordering of Co^{3+} and Co^{2+} ions, combined with AFM ordering of the magnetic moments of Co^{2+} [43]. A phase diagram for $La_{2-x}Sr_xCoO_4$ is shown in Figure 5.4 – the phase diagrams for the nickelates and hole-doped cuprates are remarkably similar, though a doping of just x = 0.02 is sufficient for the cuprates to depart from *nn*-AFM. The onset of charge order occurs at a much higher temperature $T_{C.O.}$ than any magnetic ordering, and as such, the charge order is assumed to be 'frozen in' by the time T_N is reached: for $La_{1.5}Sr_{0.5}CoO_4$, $T_{C.O.} \approx$ 750 K [40] and $T_N \approx 31$ K [40, 43], compared with undoped La_2CoO_4, $T_N = 275$ K [53]. This large difference in T_N suggests hole-doping diminishes the strength of the magnetic interactions as we would expect with a greater proportion of Co^{3+} ions. Furthermore, the difference between $T_{C.O.}$ (which is relatively constant across all dopant concentrations x) and T_N, as well as the fact that there is no noted temperature coincidence of structural and magnetic phase transitions, indicates that magnetic and charge orders are separate degrees of freedom (to a point). Away from x = 1/2, the charge order is no longer in a checkerboard configuration. The magnetic excitation spectrum of $La_{2-x}Sr_xCoO_4$, x = 1/3, has an hourglass shape in reciprocal space [49] extending up to ∼45 meV, which is similar to that of the cuprates; hence generating much interest and discussion of the magnetic ground state.

A more recent revision of the phase diagram of the cobaltates found the *nn*-AFM suppressed for x < 0.2 and the incommensurate/glassy AFM order prevailing between $0.2 \lesssim x \lesssim 0.6$ indicated by muon spin relaxation measurements [52]. The neutron scattering study of $La_{2-x}Sr_xCoO_4$ for x = 1/4 (reference [54]) also shows that this doping concentration cannot be described by a *nn*-AFM model, supporting the lower bound of $x \approx 0.2$ for incommensurate/glassy AFM in reference [52].

Here I discuss three different models for the magnetism of this material: the qualitative differences are best summed up by the diagrams in Figure 5.5. I also recap the magnetic excitations of La_2CoO_4, which is the x = 0 limit of the $La_{2-x}Sr_xCoO_4$ series – but how similar is its physics compared to that of its doped cousins? Read on.

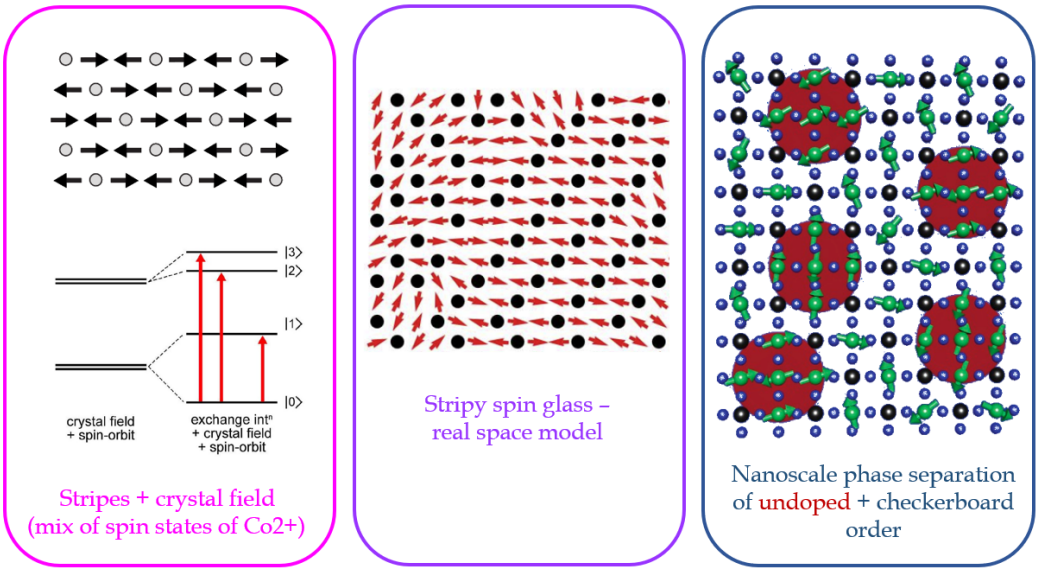

Figure 5.5: Three different approaches to modelling the excitation spectrum of $La_{2-x}Sr_xCoO_4$: left, long-range stripe order with crystal field splitting of Co^{2+}; middle, stripy spin glass real space model; right, nanoscale phase separation of undoped and checkerboard order (the undoped regions have a red background). Top left subfigure reproduced from reference [49] with permission from Springer Nature. Bottom left subfigure reproduced from reference [13]. Copyright Lucy M. Helme (2006). Middle subfigure reproduced with permission from reference [18]. Copyright American Physical Society (2012). Right subfigure reproduced from reference [51]. Copyright WILEY-VCH Verlag GmbH & Co. KGaA, Weinheim (2015).

5.2.1 No hourglass: Heisenberg exchange and crystal field anisotropy model for $x = 0$ and $x = 1/2$

The parent compound La_2CoO_4 ($x = 0$) and the half-doped $La_{1.5}Sr_{0.5}CoO_4$ ($x = 1/2$) material show similar behaviour in their excitation spectra, albeit with different periodicity (the magnetic unit cell for $x = 1/2$ is twice as large as that of $x = 0$). There is no 'hourglass' evident but instead a clear energy gap between two sharp, intense modes in the inelastic neutron scattering data. Both $x = 0$ and $x = 1/2$ exhibit commensurate (or very close to) long-range magnetic order, and in the case of $x = 1/2$, this extends to the 'checkerboard' charge order too. The excitations in both cases are well described by a Hamiltonian encompassing the crystal field and Heisenberg exchange interactions.

La_2CoO_4

First I will review the magnetic excitations of La_2CoO_4, which lacks the charge ordering superstructure of the doped compounds. Every Co site is occupied by Co^{2+}, and the magnetic excitations are confined to 2D planes, lacking any obvious signatures of inter-layer coupling [55]. The magnetic structure within these planes is nearest-neighbour antiferromagnetic order (*nn* AFM), leading

to a magnetic Bragg peak at the position (0.5, 0.5) within the (h,k) plane. The inelastic neutron scattering data in reference [55] exhibits strongly dispersive magnons stemming from these (0.5, 0.5) points in the (h,k) plane with an energy gap of $\sim 10\,\text{meV}$ and an energy maximum of $\sim 60\,\text{meV}$. A distinct feature is a much higher energy mode at $\sim 190\,\text{meV}$, which is rather flat compared to the low energy spin waves. In the simplest approximation, the lower level mode can be described by an effective spin-1/2 linear spin wave theory (LSWT) model utilising the Heisenberg Hamiltonian

$$\mathcal{H} = \sum_{\langle ij \rangle} J_{ij} S_i \cdot S_j = \sum_{\langle ij \rangle} J_{ij} \left(S_i^x S_j^x + S_i^y S_j^y + S_i^z S_j^z \right) \tag{5.2}$$

where J_{ij} is a parameter reflecting the strength of the exchange interaction, and $S_{i,j}$ are pairs of spins. An effective spin of $S = 1/2$ is assumed for Co^{2+}. Here in Figure 5.6, three exchange parameters

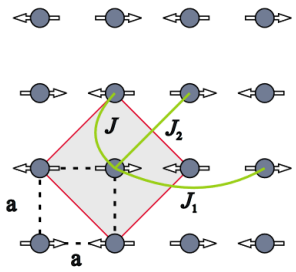

Figure 5.6: The magnetic structure and exchange interactions of La_2CoO_4, with the structural unit shown as a black dashed line; the magnetic unit cell as a shaded grey box outlined in red; and the exchange interactions represented by green lines. Figure from reference [55], reproduced with permission. Copyright American Physical Society (2010).

are defined: the *nn* interaction J and the *nnn* interaction J_1 along the x and y directions, and finally the J_2 interaction along the $x = \pm y$ diagonal. The anisotropy in J was parametrised as

$$\begin{aligned} J^x &= J(1+\epsilon), \\ J^y &= J, \\ J^z &= J(1-\delta), \end{aligned} \tag{5.3}$$

such that ϵ determined the degree of in ab plane anisotropy and δ, the out-of-plane anisotropy. With $J \gg J_{1,2}$, any anisotropy in the other exchange parameters was ignored. The parameters of the LSWT model were $J = 9.89(1)\,\text{meV}$, $J_1 = 0.04(1)\,\text{meV}$, $J_2 = 0.13(1)\,\text{meV}$, $\epsilon = 0.024(1)$, and $\delta = 0.383(5)$ [55].

To give a more complete picture of the spectrum, the following Hamiltonian was used:

$$\mathcal{H} = \underbrace{\sum_{\langle jk \rangle} J_{jk} \mathbf{S}_j \cdot \mathbf{S}_k}_{\text{Heisenberg}} + \sum_j \Bigg[\underbrace{\sum_{l,m} B_l^m O_l^m(\mathbf{L}_j)}_{\text{crystal field}} + \underbrace{\lambda \mathbf{L}_j \cdot \mathbf{S}_j}_{\substack{\text{spin-orbit} \\ \text{coupling}}} \Bigg] + \underbrace{\mathbf{H}_a \cdot \mathbf{S}}_{\substack{\text{in-plane} \\ \text{anisotropy} \\ \text{along x}}} . \tag{5.4}$$

Now the Heisenberg exchange term contains no anisotropy; rather the anisotropy is predominantly driven by the single-ion crystal field term, which has Stevens operators O_2^0, O_4^0 and O_4^4 with crystal field parameters B_2^0, B_4^0 and B_4^4 respectively. The last term in Equation 5.4 is a small anisotropy field term in the x direction. For La_2CoO_4, the parameters fitted to the data were J = 9.69(2) meV, J_1 = 0.14(2) meV, J_2 = 0.43(1) meV, $B_4^0 = -13.5$ meV, $B_4^4 = -8.0$ meV, $B_2^0 = 14.6(1)$ meV, and $|\mathbf{H}_a \cdot \mathbf{S}|$ = 0.66(6) meV.

$La_{1.5}Sr_{0.5}CoO_4$

As discussed earlier, doping concentration x introduces non-magnetic Co^{3+} into the equation, and so the exchange interaction paths are slightly different to those for undoped La_2CoO_4. One possibility consistent with strong in-plane anisotropy and Heisenberg interactions is the formation of stripes of spins (i.e. ferromagnetic alignment along one *ab* diagonal and antiferromagnetic/antiparallel alignment along the other *ab* diagonal). Analysis of $La_{2-x}Sr_xCoO_4$, x = 1/2 neutron scattering data using this model is presented in [13, 43]. A summary of these works is presented in Figure 5.7. Reasonably sharp magnons emerge from magnetic Bragg peaks at $\approx (0.5 \pm \eta, 0.5 \pm \eta, l)$, $\eta = 1/4$, plus the same vector in the perpendicular domain (picture swapping a and b around, and overlaying these layers), $\approx (0.5 \mp \eta, 0.5 \pm \eta)$, $\eta = 1/4$. Then there is a higher energy mode at around 30 meV, which is not as strongly dispersive.

As for the undoped compound La_2CoO_4, let us start by looking at the LSWT picture for $La_{1.5}Sr_{0.5}CoO_4$, which assumes the Co^{2+} ions carry effective $S = 1/2$ spins. The exchange interactions are nearest-neighbour Co^{2+} interactions J_1 and J_2, and next-nearest-neighbour Co^{2+} interaction J, which acts through superexchange via a Co^{3+} 'hole' (see Figure 5.7). The alternating magnetic stripes accompanying the checkerboard charge order can be pictured as two interpenetrating antiferromagnetic square lattices. However, if $J_1 = J_2 = 0$, then these would be uncoupled. In the case of $J \gg J_{1,2}$, then $J_1 = J_2 \equiv J'$ can be considered isotropic [43]. In this way, the *ab*-plane dispersion relation for

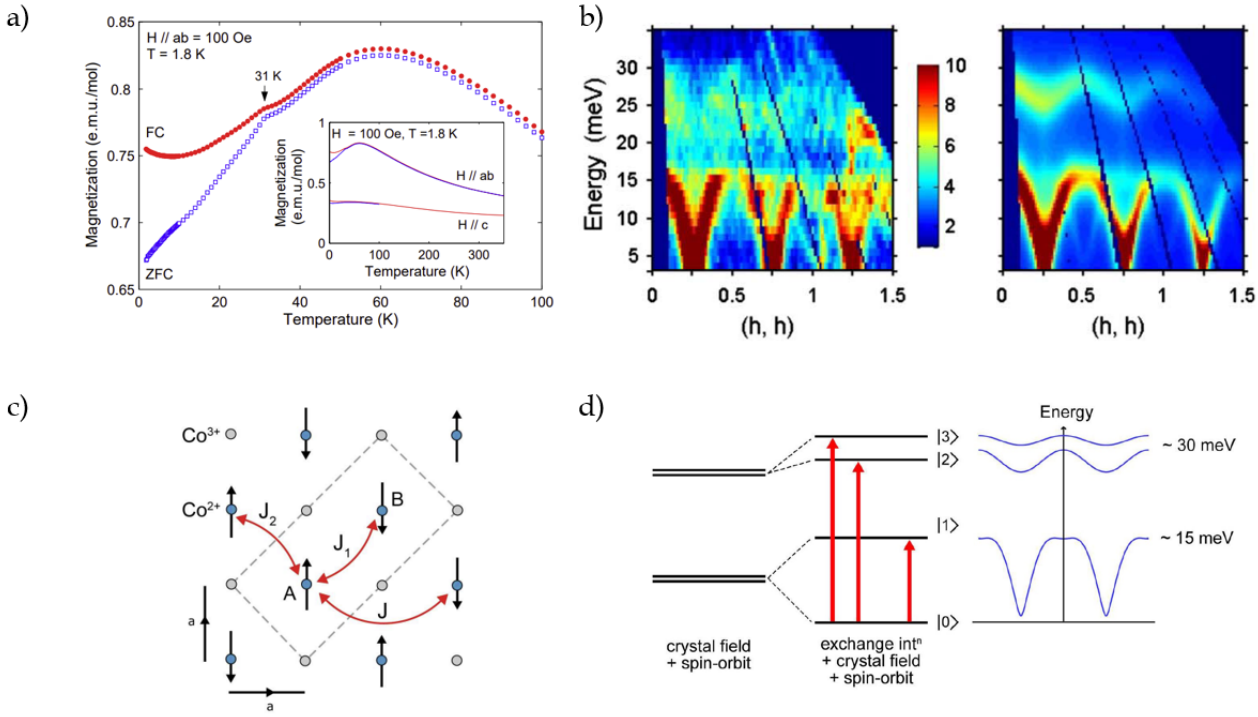

Figure 5.7: $La_{2-x}Sr_xCoO_4$, x = 1/2 a) temperature-dependent magnetisation data; b) *(left)* inelastic neutron scattering spectrum along $(h, h, 0)$ direction and *(right)* reconstruction of the data using a combined Heisenberg and crystal field Hamiltonian ;, c) magnetic structure and exchange interactions with the magnetic unit cell shown by the dashed grey line; d) schematic energy level diagram showing the splitting of the energy levels of Co^{2+} ions and how this correlates with the spectrum measured. Subfigures a) and b) reproduced from reference [43] with permission. Copyright American Physical Society (2009). Subfigures c) and d) reproduced from reference [13] with permission. Copyright Lucy M. Helme (2006).

checkerboard-ordered $La_{1.5}Sr_{0.5}CoO_4$ is [43]

$$\begin{aligned}
\hbar\omega_{1,2}(\mathbf{Q}) &= \sqrt{(A_\mathbf{Q} \pm B_\mathbf{Q})^2 - D_\mathbf{Q}^2} \quad \text{with} \\
A_\mathbf{Q} &= 2S\left(2J(1+\epsilon) + J_1 - J_2 + J_2\cos[\mathbf{Q}\cdot(\mathbf{a}-\mathbf{b})]\right) \\
B_\mathbf{Q} &= S\left(J\delta\cos(2\mathbf{Q}\cdot\mathbf{a}) + J\delta\cos(2\mathbf{Q}\cdot\mathbf{b})\right) \\
D_\mathbf{Q} &= 2S(J(1-\delta/2)\left[\cos(2\mathbf{Q}\cdot\mathbf{a}) + \cos(2\mathbf{Q}\cdot\mathbf{b})\right] \\
&\quad + J_1\cos\left(\mathbf{Q}\cdot(\mathbf{a}+\mathbf{b})\right)).
\end{aligned} \tag{5.5}$$

In [13, 43], the nearest-neighbour exchange was found to be small and effectively isotropic. On the other hand, significant anisotropy in the larger J parameter was required to reproduce the spin waves at low energies. The values obtained from a fit of the low-energy mode of $La_{1.5}Sr_{0.5}CoO_4$ were: $J' = J_{1,2} = -0.15$ meV, $J = 3.23$ meV, $\epsilon = 0.03$ and $\delta = 0.65$. The antiferromagnetic J value is consistent with a superexchange across the Co^{2+}– O – Co^{3+}– O – Co^{2+} bonds through 180°, while

the ferromagnetic $J' = J_{1,2}$ (acting through the Co^{3+} ion at a 90° angle) introduce an element of frustration in the *ab* plane, although the values are small. δ is comparatively large compared to ϵ, meaning that the spins are constrained to the *ab* plane or close to it. The in-plane anisotropy is essential to gap the modes and possibly stabilise the stripes at other doping concentrations, which is further discussed in the later publications [49, 50].

The lower energy mode does not intersect at all with the higher energy mode for x = 1/2. To account for this additional mode, the complete Hamiltonian (including the crystal field and anisotropy terms, Equation 5.4) was used. This model produced good agreement with the data with parameters $J = 1.4\,\text{meV}$, $J_{1,2} = J' = 0$, $\lambda = -18.7\,\text{meV}$, $B_4^0 = -13.5\,\text{meV}$, $B_4^4 = -8.0\,\text{meV}$, $B_2^0 = 13.0\,\text{meV}$, $|\mathbf{H}_a \cdot \mathbf{S}| = 0.22\,\text{meV}$.

5.2.2 Emergence of the hourglass at intermediate doping (x = 1/3)

The characteristic hourglass-shaped spectrum emerges for the intermediate doping x = 1/3 in $La_{2-x}Sr_xCoO_4$. The versatility of Equation 5.4 is shown in an inelastic neutron scattering study of $La_{1.67}Sr_{0.33}CoO_4$ [49]. Disorder is included in the model via phenomenological broadening of the spin wave spectrum. This was interpreted in terms of two orthogonal domains of charge stripes of Co^{3+} ions modulated by AFM ordering of the magnetic moments of Co^{2+} ions, with a periodicity of three in the *ab* plane. The combined effective Heisenberg and crystal field model with parameters $J = 11.5\,\text{meV}$, $J_{1,2} = J' = 0.55\,\text{meV}$, $\lambda = -18.7\,\text{meV}$, $B_4^0 = -13.5\,\text{meV}$, $B_4^4 = -8.0\,\text{meV}$, $B_2^0 = 13.0\,\text{meV}$ (the in-*ab*-plane anisotropy term in Equation 5.4 is not needed) successfully reproduces the characteristic 'hourglass' excitations emanating from $\approx (0.5 \pm \eta, 0.5 \pm \eta)$, $\eta = 1/6$.

The key features of the dispersion are seen in Figure 5.8. At the lowest energies, the spin waves resemble a four-leaf clover in reciprocal space. As energy increases, the excitations converge at (0.5, 0.5, 0), which is where the spectrum reaches its maximum intensity at approximately 17 meV. This is the 'waist' of the hourglass. From there, the spin waves diverge into four branches again, but these are rotated 45° about (0.5, 0.5, 0) relative to the low energy branches and spread out to the edges of the antiferromagnetic Brillouin zone. The dispersion in this model is anisotropic and four-fold symmetric at all energies from 3 meV to $\sim 50\,\text{meV}$. It is the large ratio of J/J' that is chiefly responsible for the hour-glass shape of the dispersion [49].

In a detailed polarised neutron diffraction study on the same single crystal, the magnetic and charge order wavevectors were found to be slightly incommensurate at positions $\approx$ (0.37, 0.37, 0) and $\approx$ (0.36, 0.36, 0) etc [50]. The superstructure reflections associated with the low temperature orthorhombic (LTO) phase favoured by $La_{2-x}Sr_xCoO_4$ for $x < 0.4$ were also seen but no peaks

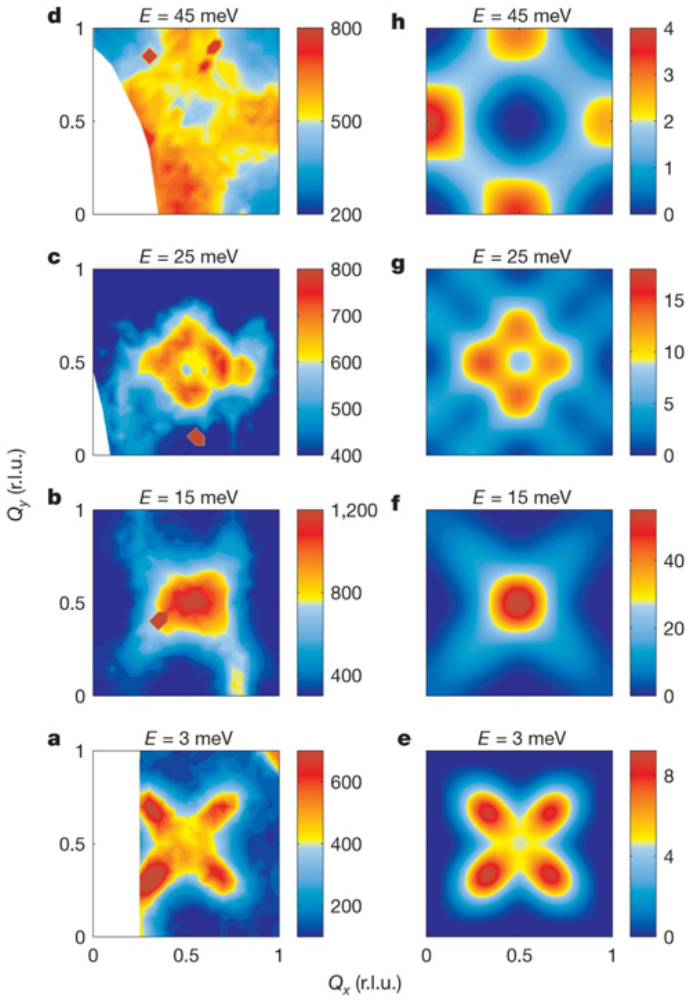

Figure 5.8: Constant energy slices of the $La_{2-x}Sr_xCoO_4$, x = 1/3 excitation spectrum. a) to d) are data where the intensity scale differs between plots; e) to h) are simulations on a shared intensity scale though colourmaps vary for individual subplots. Figure from reference [49], reproduced with permission from Springer Nature.

consistent with any undoped La_2CoO_4 were observed [50]. Polarised neutrons enabled the contributions of nuclear and magnetic scattering to be distinguished; hence, the consistent positioning of charge and magnetic peaks in reciprocal space lends further weight to the charge stripe model. The temperature dependence of the charge peaks between temperatures of 2 K and 300 K was minimal, but the intensity of both the magnetic and LTO reflections increased significantly below 100 K. This suggests that the orthorhombicity drives the in-planar anisotropy in the *ab* plane. There was also evidence for the checkerboard x = 1/2 phase (charge order peaks at 0.5 positions) being present alongside the stripe phase in [50]. This disordered coexistence of two phases contributes to the incommensurate and broad nature of the magnetic reflections being located away from the 'perfect' stripe positions of $(1/3, 1/3, l)$ etc.

The studies discussed above primarily probed the magnetic order and excitations in the (h, k) plane, rather than along the l direction where the interactions are expected to be far weaker. The stacking order along the c axis for x = 1/2 is discussed in references [13, 43] and for x = 1/3 in references [49, 50]. The Bragg peaks are broader along l than along h or k, consistent with shorter-range order along the c axis. Further compounding this disorder is the presence of two domains of orthorhombic distortions in these materials for $x < 0.4$, and two domains of charge stripes, which can run along either diagonal. Hence the combined charge stripe and crystal field description is an effective model of the interactions in the bulk and not necessarily the full picture at the microscopic level. The distribution and growth of domains is not explored, only the correlation length constrained to $\lesssim 1$ nm in [50].

5.2.3 Intermediate doping concentrations: a slightly stripy spin glass and a real-space modelling approach

Building on the idea of effective order through disorder, a different approach was taken in reference [18]: a real-space model of disordered stripes in the *ab* plane was constructed through Monte Carlo simulations on a 2D lattice, using the perfect period-three stripe model as a starting point with Ising-like distribution of Co^{2+} and Co^{3+}, within the charge-balance constraint imposed by x = 1/3. The magnetism of the Co^{2+} was governed by Heisenberg interactions J and J' (Equation 5.2), with the anisotropy of J defined as per Equation 5.3 (in this case, $\delta = 0.28$ and $\epsilon = 0.013$). The spin waves of this finite lattice of sites were then calculated using the dynamic susceptibility.

The advantage of this computational approach is that the correlation lengths along the charge stripes ($\xi_C^{\parallel}$) and perpendicular to the charge stripes ($\xi_C^{\perp}$) could be tuned by adjusting the Ising model of the charge distribution, and the magnetic order in between the charge stripes by the

relative strengths of the Heisenberg interactions J and J'. Thus the effect of the degree of disorder or 'glassiness' in the *ab* plane on the spin wave spectrum could be investigated. As found in the experimental study [50], the correlation lengths for the spin order and charge order were closely aligned ($\xi_C^{\parallel} \approx \xi_S^{\parallel}$). Additionally, the excitations for $La_{2-x}Sr_xCoO_4$ at other intermediate doping concentrations (e.g. x = 1/4 as in reference [54]) could be simulated by adjusting the charge-balance constraint for the Ising model.

This model of a slightly stripy spin glass can produce spectra closely resembling that of reference [49]. Furthermore, the same model was used to show that the disordered stripe model and hourglass excitations persist at an even lower doping of x = 1/4 [54, 56], in contrast to the previous hypothesis that *nn*-AFM would prevail for x < 1/3 [11]. However, exploring the parameter space reveals other key features and possibilities for magnetic excitation spectra, which could be relevant for materials other than $La_{2-x}Sr_xCoO_4$ including cuprates displaying glassy tendencies [18].

- Increasing disorder – manifesting as stronger frustration between domains of locally stripe-ordered spins – concentrates the intensity around the waist of the hourglass (energy ω_S) at (0.5, 0.5) in the $(h,\ k)$ plane, lowers ω_S and broadens the excitations (see Figure 5.9), as well as quashing the intensity in the branches heading towards (0, 0).

- Increasing the ratio of J/J' concentrates the intensity into lower energies and more distinct 'legs' of the hourglass. Even when the disorder parameters/correlation lengths ξ remain the same, the spectrum gets sharper and more intense at low energies (see Figure 5.10). The excitations are still more intense in the branches heading inwards towards (0.5, 0.5) but with increasing J/J', other *weaker* branches heading outwards towards (0, 0) appear – this is reminiscent of the checkerboard LSWT model Equation 5.5, which has branches of *equal* intensity heading towards (0.5, 0.5) and (0, 0).

Finally, the assumption that the strongest spin-spin interactions are confined to the *ab* plane were borne out of the slightly stripy spin glass model. The effects of out-of-plane spin components and interactions were probed in the computational study in reference [54], which showed that the contribution of out-of-plane spin canting to the observed spectra[2] was negligible.

[2] In the experimental geometry with the $(h,\ k)$ plane as the scattering plane in a time-of-flight spectrometer

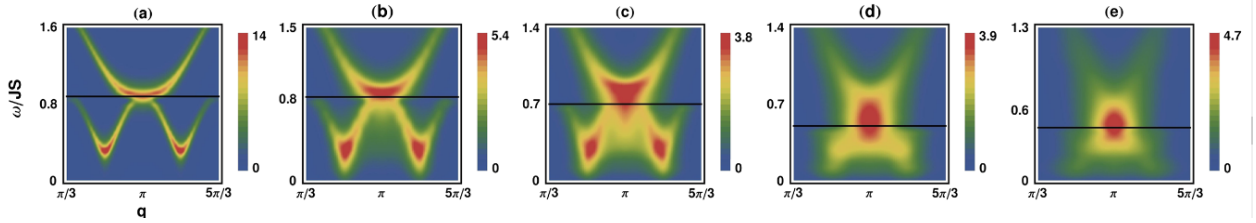

Figure 5.9: Simulation of magnetic excitations of disordered stripes in $La_{2-x}Sr_xCoO_4$, x =1/3. $J' = 0.05\ J$. From a) to e) the charge disorder increases. Each panel is divided at $\omega = \omega_S$, with the lower [upper] portion showing data along $\mathbf{q} = (q, q)$ $[(q, \pi)]$ in order to represent the high-intensity features. Figure from reference [18], reproduced with permission. Copyright American Physical Society (2012).

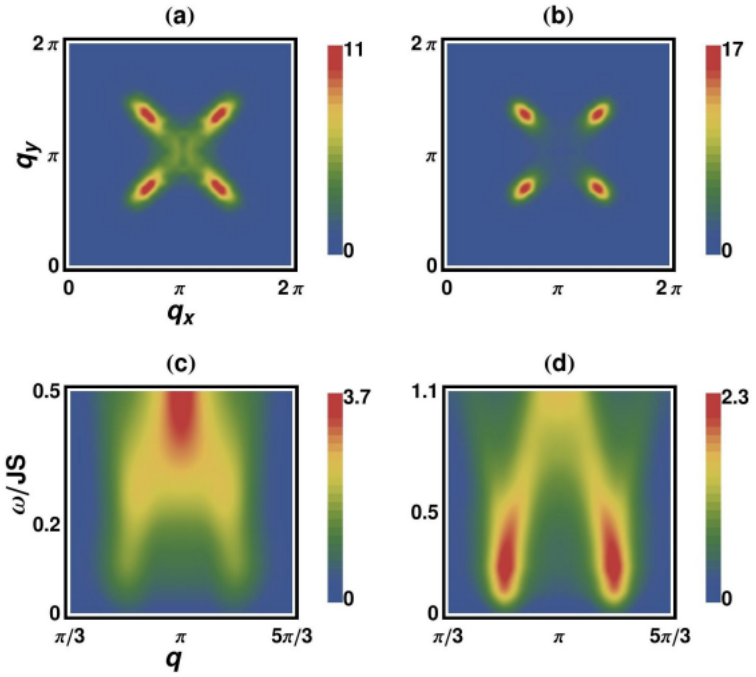

Figure 5.10: Influence of the exchange interaction parameter ratio J/J'. $\xi_C^{\parallel} \simeq 5$, $\xi_C^{\perp} \simeq 2$, $\omega_S = 0.50\ JS$. a), b): magnetic structure factor c), d): low energy part of the dynamic susceptibility along $\mathbf{q} = (h, h)$ for a), c) $J' = 0.05\ J$ and b), d) $J' = 0.15\ J$. Figure from reference [18], reproduced with permission. Copyright American Physical Society (2012).

5.2.4 An alternative model for intermediate doping concentrations: nanoscale phase separation of undoped and checkerboard regions

An alternative model presented for the hourglass spectrum lacks stripes, instead features a superposition of undoped x = 0 and checkerboard x = 1/2 phases [17]. The energy scales involved in the dispersion for x = 0 and x = 1/2 are sufficiently distinct that – roughly speaking – the x = 1/2

regions account for the excitations below the 'waist' of the hourglass ($\sim 15\,\text{meV}$) and the x = 0 regions account for the excitations above it, where the spectrum is isotropic. However, there are some inconsistencies in this picture.

Firstly, for the $La_{2-x}Sr_xCoO_4$ x = 1/3 samples in references [17, 57], the magnetic Bragg peaks are at $\sim (1/3, 1/3)$, and the spin wave branches heading outwards to (0, 0) are significantly weakened compared to those of the x = 1/2 branch, which is inconsistent with a simple superposition of x = 0 and x = 1/2 spectra that would be the standard interpretation of the coexistence of the x = 0 and x = 1/2 phases. The nanophase separation model suggests the spin wave modes are coupled as the x = 0 and x = 1/2 regions are of minimum $\sim$ nm size and very strongly intermingled [51, 58], with some resemblance to a fractal-like distribution of domain length scales akin to what was reported in reference [59]. However, no quantitative mechanism beyond proximity of the differently-doped regions is given for the coupling with Monte Carlo simulations only including two Heisenberg interactions and an effective spin of 1/2 for Co^{2+} [57].

Secondly, the magnetic Bragg peaks have an elliptical shape which is not well explained by the nanophase separation model. The elliptical shape implies that the magnetic order has different correlation lengths along the orthogonal $[1\,1\,0]$ and $[1\,-1\,0]$ directions, i.e. the magnetic order is shorter in range in one direction than the other. The nanophase model does not describe this anisotropy or the four-fold symmetry and positioning of the magnetic Bragg peaks for x = 1/3, which is in contrast to the stripe model and to the experimental data.

With a 'normal' coexistence of two phases, the expectation would be two magnetic ordering transitions at different temperatures (one for x = 0 and another for x = 1/2), although the data for $0.2 \geq x \geq 0.4$ do not show two obviously distinct transitions. The temperature dependence of the inelastic signal shows that the low energy excitations go from two peaks emerging from (0.25, 0.25) to a single peak from (0.5, 0.5) between 100 K and 200 K [58, 60], which persists weakly until $\sim 300\,\text{K}$. Finally, the spin wave spectrum presented in the nanophase separation model is isotropic about (1/2, 1/2) above $\sim 15\,\text{meV}$, which is in contrast to the stripe model. The size of the exchange parameters is also different: in reference [57] $J = 5.8\,\text{meV}$ and $J' = 0.85\,\text{meV}$, using the convention that AFM J_i are positive, with an effective spin $S = 1/2$.

5.2.5 Summary of different magnetic excitation models

In conclusion to this review, there have been multiple investigations into the spin waves of the $La_{2-x}Sr_xCoO_4$ series across the range $0 \leq x \leq 1/2$ and a variety of theoretical models accompany the data in references [13, 17, 43, 49–52, 54, 55, 57]. To summarise the differences between these

models, I have created an illustration (Figure 5.11), which shows a cartoon depiction of constant energy slices in the (h, k) plane. Neutron scatterers love a colourmap and tend to favour the ones with non-uniform colour perception so I have tried to put the key results from the different models on a more level playing field! Note the similar form, but different periodicity, in reciprocal space of the excitations for x = 0 and x = 1/2 (§ 5.2.1). These two examples have quite different energy scales too: the anisotropy gap shrinking from ~ 10 meV to ~ 3 meV, and the energy maximum of the dispersion dropping from ~ 61 meV to ~ 13 meV for x = 0 compared to x = 1/2. This makes sense when you consider the length of the nearest-neighbour exchange along x and y directions doubles from x = 0 to x = 1/2, and the strength of the exchange diminishes accordingly.

The doping concentrations of x = 0 and x = 1/2 have (nearly) commensurate magnetic order. Away from these doping concentrations, the evidence is for incommensurate magnetic order with magnetic Bragg peaks shifting quasi-linearly with x [51]. The inelastic spectra look quite different from x = 0 and x = 1/2 too: x = 1/3 is the case in point here. The differences between the charge stripe model (§ 5.2.2) and the nanoscale phase separation model (§ 5.2.4) are also made more obvious: the 'four-leaf clover' dispersion along $(h, 0.5)$ and $(0.5, h)$ above ~ 15 meV for the former contrasting with the isotropic, outwards dispersion above ~ 15 meV for the latter. The nanoscale phase separation model also has less 'elliptical' magnetic Bragg peaks than the stripe model. This is because the stripe model has different correlation lengths parallel to and along the stripe directions (and the stripes have a preferred direction in the *ab* plane, due to strong magnetocrystalline planar anisotropy), whereas the nanophase separation model has a more or less isotropic distribution of *nn* AFM regions and checkerboard-ordered regions, and no source of in-plane anisotropy for the Co^{2+} moments.

For x = 1/3, there is also the matter of the higher energy (~ 40 meV), out-of-plane mode observed in reference [57] and attributed to the nanophase separation model, which was not seen in the experiments of reference [49].

The sharpest magnetic Bragg peak is for the undoped parent compound La_2CoO_4, which exhibits long range magnetic order. The x = 1/2 doping also has long range order but x = 1/3 has much more diffuse magnetic Bragg peaks. The peaks themselves are broad, rather than there being a diffuse background with a sharp peak on top. This also translates to the inelastic signal being less distinct/less sharp/fuzzy/a hot mess for x = 1/3 compared to x = 0 and x = 1/2. This diffuse scattering is suggested by broadening the signals depicted in Figure 5.11.

In summary, the hourglass spectra can be interpreted either as the minimum of spin waves

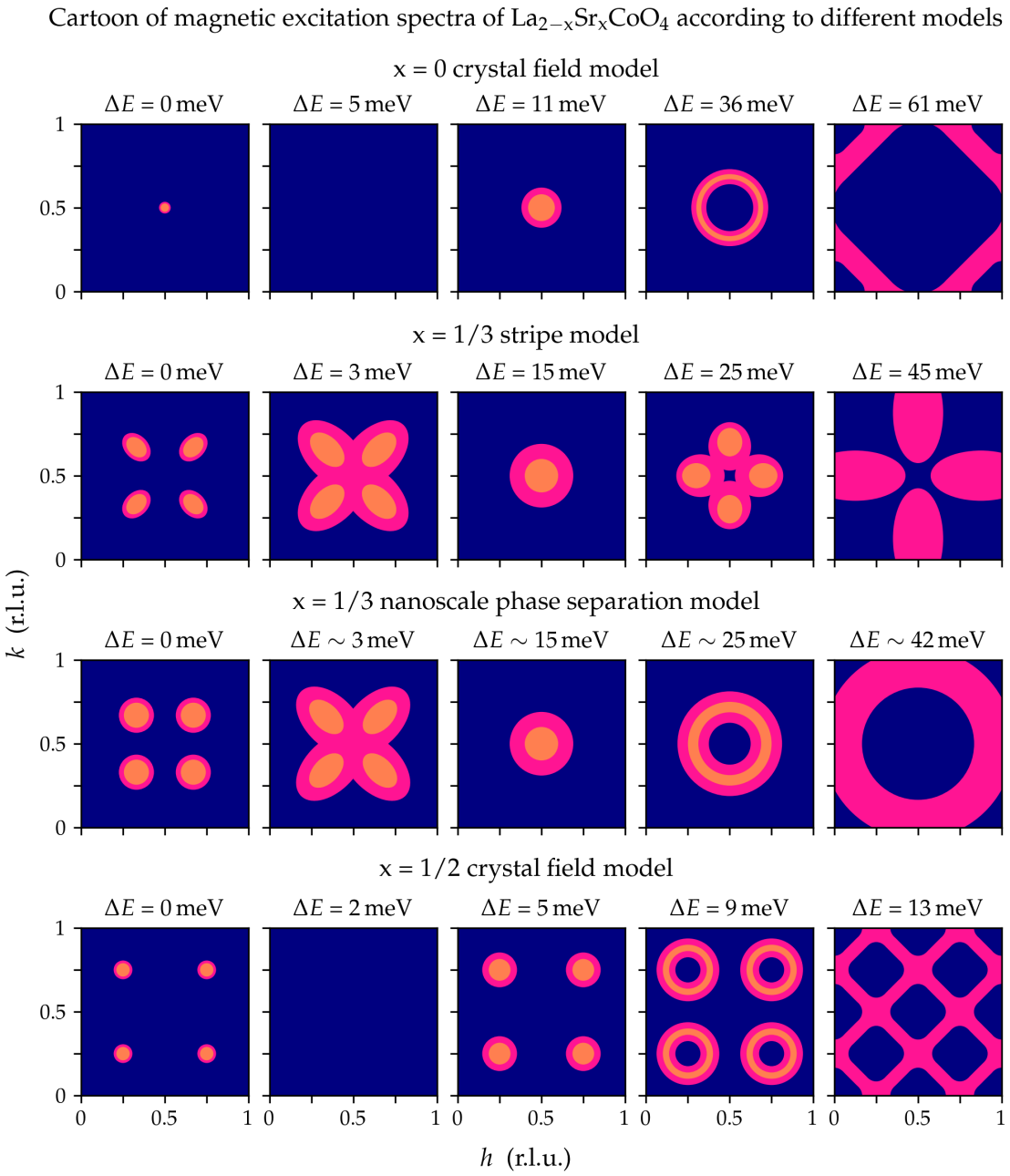

Figure 5.11: This cartoon highlights the different features (attributed to magnetic excitations) appearing in constant energy slices of (h, k) plane for various models and doping concentrations of $La_{2-x}Sr_xCoO_4$. This figure is intended only as a qualitative comparison between the models and the intensity colourmap is not consistent. For a full quantitative description, as well as the data/simulations these illustrations are based on, see the following references: x = 0 crystal field model [55], x = 1/3 stripe model [49, 50], x = 1/3 nanoscale phase separation model [17, 51, 57, 58], x = 1/2 crystal field model [13, 43]. Not represented in this figure are the flatter, less dispersive excitations at $\sim$ 190 meV for x = 0, $\sim$ 40 meV for x = 1/3 with the nanophase separation model, and $\sim$ 28 meV for x = 1/2 (c.f. Figure 4 of reference [60]). Due to the variation in the spectra of the slight stripy spin glass model [18], that model is not represented in this figure.

along a stripe meeting the maximum of spin waves propagating between stripes (charge stripe with exchange and crystal field anisotropy), or the minimum of an undoped region meeting the maximum of a hole-doped region (nanophase separation). Heisenberg interactions drive collinear alignment of spins, while the strong anisotropy of the system and higher energy excitations are the effects of the Co^{2+} crystal field. Disorder may be accounted for via phenomenological broadening of the spectra or Ising-like interactions between electrons and holes associated with different oxidation states of Co (slightly stripy spin glass).

5.3 $La_{2-x}Ba_xCoO_4$ samples and initial characterisation

Two large single crystals of $La_{2-x}Ba_xCoO_4$ were grown by the floating zone method by Dharmalingham Prabhakaran. The synthesis procedure was as follows:

1. Polycrystalline $La_{2-x}Ba_xCoO_4$ samples with x = 0.33 and x = 0.5 were prepared by a standard solid-state reaction method using La_2O_3, BaO_3, and Co_3O_4 powders with a purity $>$ 99.99 % as starting materials. Dried powders were mixed in stoichiometric compositions.
2. Sintering was carried out at 1150°C for 48 hours in air with intermediate grinding.
3. Polycrystalline powders were pressed into cylindrical rods with a diameter of 8 mm and length 10 cm and sintered at 1250°C for 12 hours.
4. Finally single crystals were grown using optical floating zone furnace (Crystal Systems Corp. Japan) at a growth rate of 2–5 mm/h in an oxygen atmosphere.

5.3.1 X-ray diffraction

Both samples of $La_{2-x}Ba_xCoO_4$, x = 1/2 and x = 1/3, had low mosaicity confirmed by x-ray Laue diffraction (Figure 5.12).

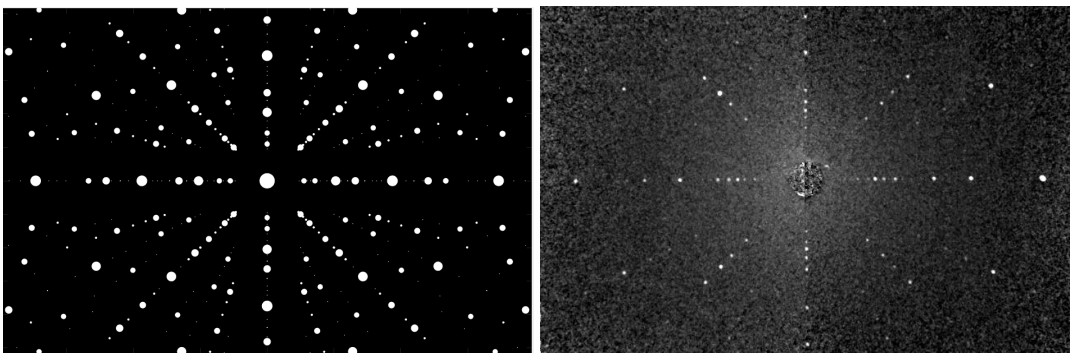

Figure 5.12: X-ray Laue diffraction pattern from $La_{2-x}Ba_xCoO_4$, x = 1/2 sample with *c* axis parallel to beam and *b* axis vertical, left = simulated pattern assuming space group $I4/mmm$, right = data.

5.3.2 Magnetometry

A Quantum Design PPMS system was used to measure the magnetisation of smaller pieces cut from the main crystals of x = 1/2 (mass ≈ 53 mg) and x = 1/3 (mass ≈ 18 mg). The *ab* plane was parallel to the applied magnetic field **H**. Magnetisation measurements showed a magnetic transition at temperature $T_N \approx 12$ K indicated by the bifurcation of field-cooled and zero field-cooled susceptibility curves (Figure 5.13). The susceptibility curves for x = 1/2 and x = 1/3 look mostly similar, although there is a slight difference in T_N. At T_N, there is a smooth peak in the ZFC data, rather than a sharp cusp that is the stereotypical indication of an AFM with long-range order arising from a Landau-style second-order phase transition. Unlike the magnetisation data for $La_{2-x}Sr_xCoO_4$ x = 1/2 [43], there is no broad peak (centre ∼ 60 K) before the bifurcation of FC and ZFC curves at a small cusp (≈ 31 K). The FC data is nearly temperature-independent below T_N, especially for the x = 1/3 sample (similar to $La_{2-x}Sr_xCoO_4$ x = 1/3 [49]). This is a feature which is associated with spin glasses. These two observations are consistent with short-range AFM order. A broad peak (as opposed to a cusp) can result from lower-dimension magnetic ordering or a mixture of valence states on the same crystallographic site [61]. Both explanations are relevant in our case for short-range charge order of Co^{2+} and Co^{3+}, with the spins of Co^{2+} ions suspected to lie in the *ab* plane, due to 2D magnetic interactions.

The inverse susceptibility data were fitted according to the modified Curie-Weiss law [61]

$$\chi^{-1} = \frac{T - \theta_{CW}}{\chi_0 \cdot (T - \theta_{CW}) + C} \tag{5.6}$$

in the temperature range 15 K to 50 K. The fitted parameters are given in Table 5.2, with μ_{eff} calculated according to Equation 2.40. The additional temperature-independent paramagnetic susceptibility χ_0 is sizeable (larger than typical background) and may be caused by a build-up of short-range magnetic correlations, which do not follow the Curie-Weiss law. The negative value of θ_{CW} indicates predominantly antiferromagnetic interactions. The magnitude of θ_{CW} is of the same order as T_N.

The μ_{eff} per Co ion can be converted to a nominal μ_{eff} per Co^{2+} ion by dividing by x. This yields a moment of 2.10 μ_B assuming x = 1/3 and 2.62 μ_B assuming x = 1/2. These values can be compared to the simple calculation for the magnetic moment of a spin-only (no crystal field or spin-orbit coupling) 3*d* transition metal ion:

$$\mu_{cal} = 2\sqrt{S(S+1)}\,\mu_B. \tag{5.7}$$

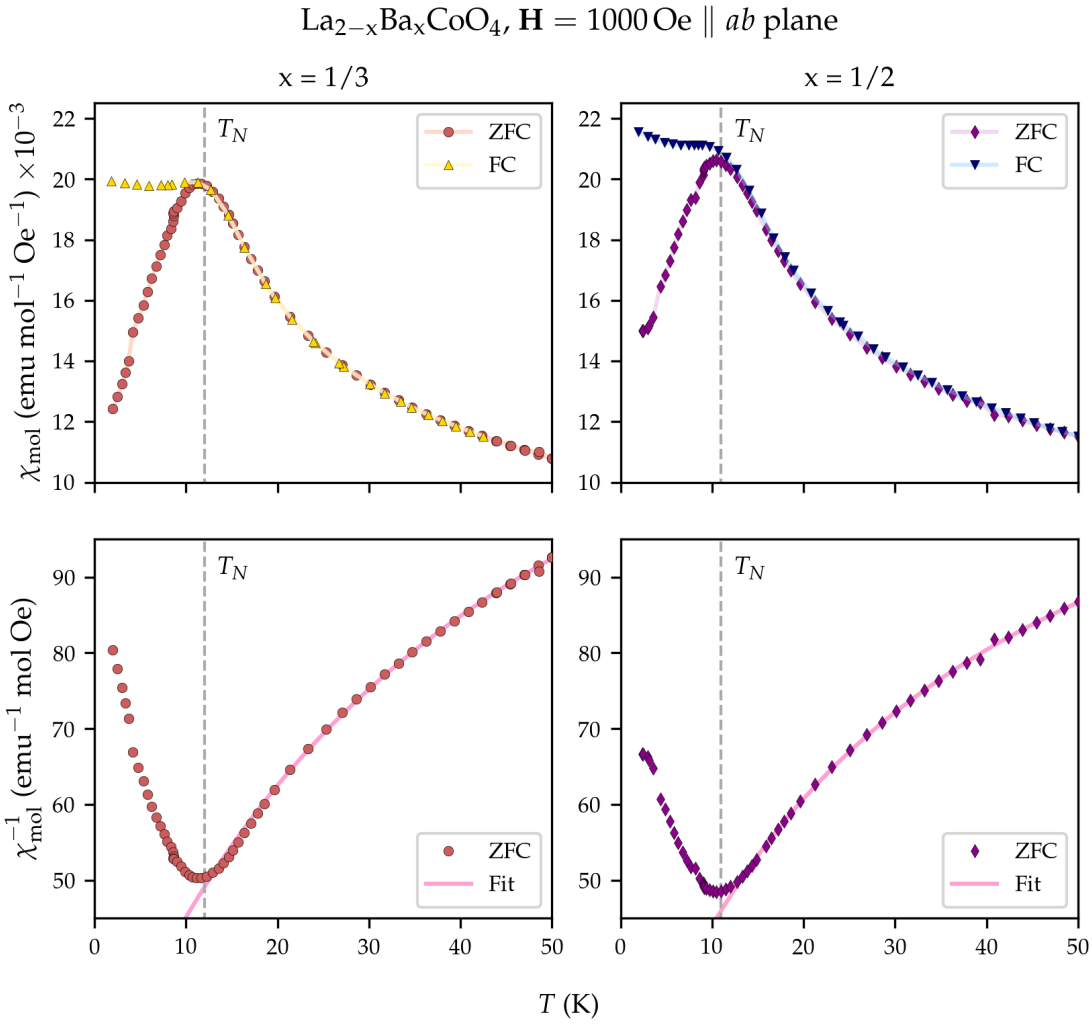

Figure 5.13: Magnetisation data (FC = field cooled, ZFC = zero field cooled) for $La_{2-x}Ba_xCoO_4$. $T_N \approx 12\,K$ for x = 1/3 and $T_N \approx 11\,K$ for x = 1/2. The fitted equation is a modified Curie-Weiss law (Equation 5.6).

Table 5.2: Fitted parameters of a modified Curie-Weiss law (Equation 5.6) for $La_{2-x}Ba_xCoO_4$ magnetisation data.

$La_{2-x}Ba_xCoO_4$	χ_0 (emu mol^{-1} Oe^{-1})	θ_{CW} (K)	C (K^{-1} emu mol^{-1} Oe^{-1})	$\mu_{eff.}$[1] (μ_B)
x = 1/2	7.57×10^{-3}	-4.33 ± 0.02	2.15	1.31
x = 1/3	6.41×10^{-3}	-5.52 ± 0.01	2.44	1.40

[1] This is the effective magnetic moment per Co ion, μ_{eff}, which in the case of $La_{2-x}Ba_xCoO_4$ is the same as the effective magnetic moment per formula unit.

Equation 5.7 yield $\mu_{cal} = 1.73\,\mu_B$ with $S = 1/2$, and $\mu_{cal} = 3.87\,\mu_B$ with $S = 3/2$. The estimated moments per Co^{2+} ion lie between these two values, possibly explained by partial occupancy of crystal field levels. The fact that neither the estimated moments per Co^{2+} ion nor the μ_{eff} per Co

ion are larger than μ_{cal} for $S = 3/2$ means that it is very unlikely the Co^{3+} ions are magnetic.

5.4 Single crystal neutron diffraction of $La_{2-x}Ba_xCoO_4$ on ILL D10

5.4.1 Method

Two samples of $La_{2-x}Ba_xCoO_4$, of nominal doping concentrations x = 1/2 (mass $\sim$ 25 mg) and x = 1/3 (mass $\sim$ 80 mg) were measured on the four-circle diffractometer D10 at the ILL using an area detector. The sample environment was a closed-cycle LHe cryostat mounted on a Eulerian cradle. The experiment consisted of two main parts: the measurement of nuclear Bragg peaks to determine the crystal structure at low temperature, and a temperature-dependent sweep of the (h, k) plane in order to detect likely diffuse signatures of magnetic order for the x = 1/3 sample. Unless otherwise stated, the $I4/mmm$ space group (in the standard setting) applies to all (h, k, l) indices in this section.

5.4.2 Analysis and results

The structures were refined in MAG2POL [62]. Refinements were performed using the tetragonal space group $I4/mmm$ ($a = b = 3.83$ Å, c = 12.5 Å) and then also the orthorhombic space group $Cmce$ (a = 5.37 Å, b = 12.5 Å, c = 5.4 Å) for both x = 1/2 and x = 1/3. The variation among symmetry-equivalent peaks was $R_{int} = 13.4$ % for x = 1/2 in the $I4/mmm$ space group and $R_{int} = 10.12$ % in the $Cmce$ space group; $R_{int} \approx 10.6$ % for x = 1/3 in both the $I4/mmm$ and $Cmce$ space groups. Unit cells for each space group are pictured in Figure 5.14. The twinned appearance of the peaks motivated the choice of the orthorhombic space group, which is common to other $La_{2-x}A_xCoO_4$ materials, especially at low temperatures where octahedral tilting takes place (shown in Figure 5.16). The split between the twin domains was around 90% to 10%; however, this may not reflect the proportion of each twin domain in the original large crystals from the floating zone furnace, bearing in mind the small size of the samples used for the D10 experiment.

The observed integrated Bragg peak intensities I_{obs} are plotted against the calculated intensities I_{calc} in Figure 5.15. Although the intensity units are arbitrary, the intensity of the x = 1/2 data is correct relative to the x = 1/3 data. The large error bars reflect the weak measured intensities, especially for the x = 1/2 crystal. For both doping concentrations, the $Cmce$ structure was a better fit judging by R_F. The results of the refinements in this space group are given in Table 5.3 and Table 5.4 for x = 1/2 and x = 1/3 respectively. The stoichiometry was not fixed during the refinement. The results show a slight oxygen deficiency in both samples and a Ba doping of x = 0.504 for the nominally x = 1/2

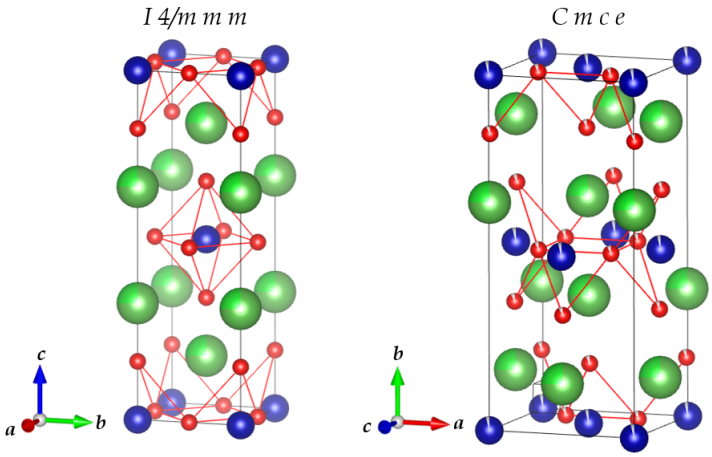

Figure 5.14: The unit cells of the structures proposed for $La_{2-x}Ba_xCoO_4$: left, $I4/mmm$ (space group #139); and right, $Cmce$ (space group #64). Note that the longest axis of the unit cell is the c axis in $I4/mmm$ and the b axis in $Cmce$ using the standard convention for these space groups. Figure produced using VESTA [12].

sample, and x = 0.59 for the nominally x = 1/3 sample. The latter is a significant deviation. A possible explanation for the oxygen deficiency may be attributed to the degradation of samples in air during handling and transport. Aside from the oxygen occupancies and extinction parameters, the refinements yielded largely similar structural parameters.

Although the orthorhombic $Cmce$ structure proved a better fit than the $I4/mmm$ structure, I will continue to use the $I4/mmm$ unit cell and peak indexing for the remainder of this chapter. The differences in the spacing of the Co ions is not significantly changed by the choice of space group, and it is simpler to discuss the magnetic structure and excitations in terms of a (pseudo)tetragonal unit cell given the existing literature for $La_{2-x}Sr_xCoO_4$.

On the larger x = 1/3 sample, the scans along the (h, h) direction (using the $I4/mmm$ space group) revealed a weak broad peak centred on (0.27, 0.27), which decreased in intensity with increasing temperature. The peak disappeared altogether by 30 K as seen in Figure 5.17.

5.4.3 Discussion

The rough temperature dependence of the peak at (h, h) = (0.27, 0.27) shown in Figure 5.17 suggests it is indeed magnetic in origin, consistent with the magnetisation data showing $T_N \approx 12$ K, although the nature of the phase transition cannot be ascertained from our data. Previous studies on similar Sr-doped compounds have shown a more gradual onset of magnetic order with temperature (as opposed to a sharp Landau-like transition), and fits of critical exponents to those data are consistent with strongly 2D, rather than 3D, magnetic order [31, 50]. The phase transition may

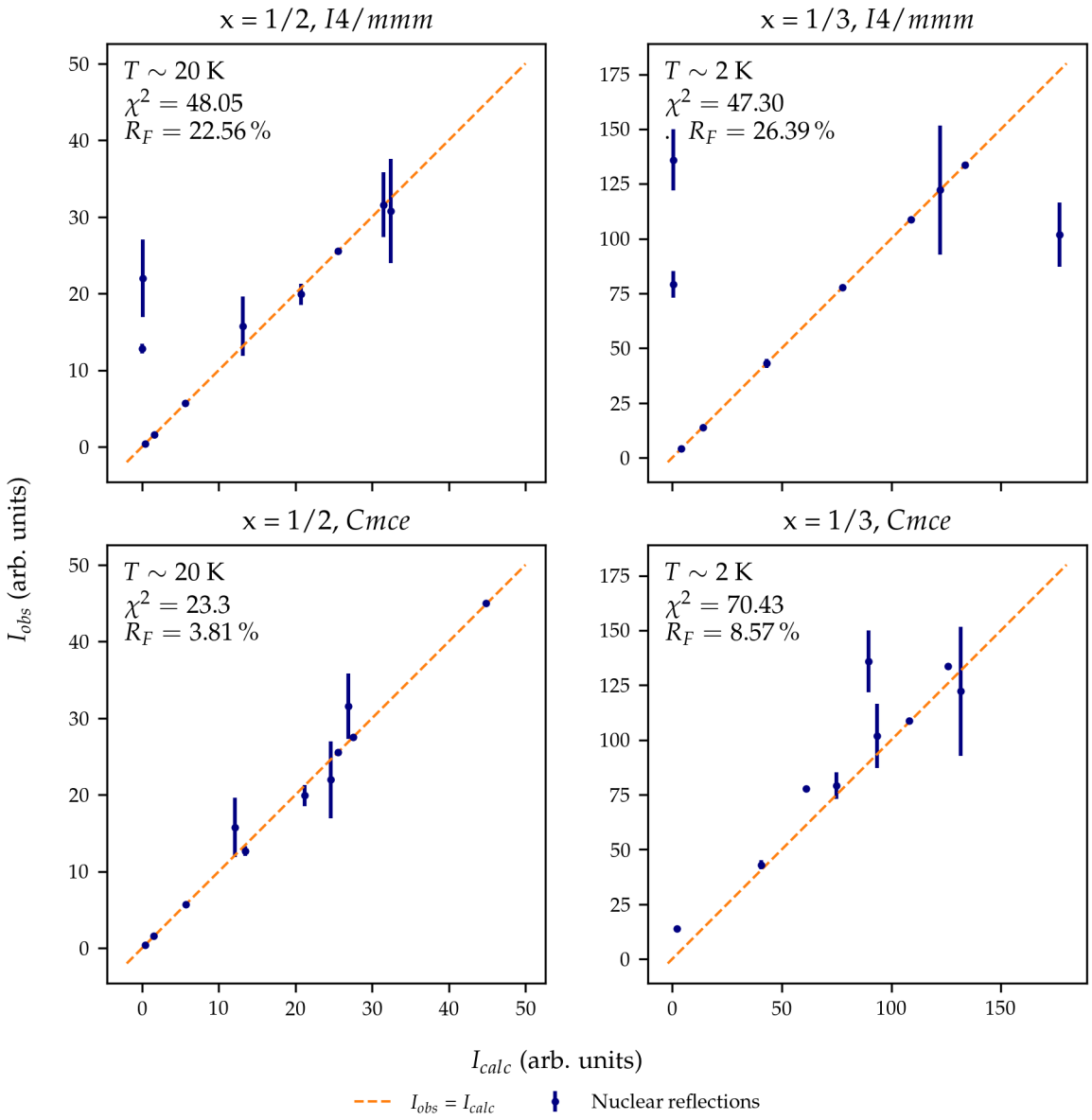

Figure 5.15: Plots showing calculated vs observed intensities of reflections from D10 experiment on $La_{2-x}Ba_xCoO_4$, x = 1/3 and x = 1/2.

instead be akin to a percolation-type growth of spin stripes or cluster AFM domains. The data shown in Figure 5.17 are not inconsistent with this reasoning, although the magnetic order is more short-range in $La_{2-x}Ba_xCoO_4$ than $La_{2-x}Sr_xCoO_4$.

5.5 Single crystal time-of-flight spectroscopy of $La_{2-x}Ba_xCoO_4$ on ISIS MERLIN

Inelastic neutron scattering was performed on larger samples of both crystals at the ISIS MERLIN time-of-flight spectrometer [63] at $T = 7$ K, with incident energies E_i of up to 70.80 meV and the

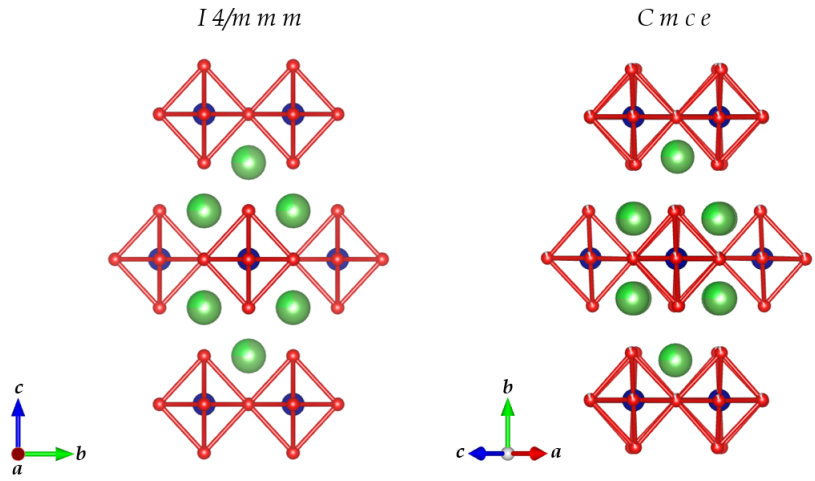

Figure 5.16: Equivalent views of the structures proposed for $La_{2-x}Ba_xCoO_4$: left, $I4/mmm$ (space group #139); and right, $Cmce$ (space group #64). This angle clearly shows the tilting of the octahedra. Figure produced using VESTA [12].

Table 5.3: Structural and extinction parameters x_{ij} for $La_{2-x}Ba_xCoO_4$, x = 1/2 determined by refinement in the space group $Cmce$ (#64) against integrated intensities collected at ~ 20 K. $\chi^2 = 23.3$ and $R_F = 3.81$ for this refinement.

Atom	Wyckoff position	x	y	z	B_{iso}	Occupancy
La	$8f$	0	0.359	0.013	0.014	0.748
Ba	$8f$	0	0.359	0.013	0.010	0.252
O	$8e$	0.25	0.002	0.25	0.040	0.972
O	$8f$	0	0.167	0.022	0.037	0.980
Co	$4a$	0	0	0 0	0.08	0.966

Extinction parameter	Value
x_{11}	0.25439
x_{22}	0.01926
x_{33}	0.001
x_{12}	0
x_{23}	0
x_{13}	0

Twin matrix	Twin 1 proportion	Twin 2 proportion
$\begin{bmatrix} 0 & 0 & 1 \\ 0 & -1 & 0 \\ 1 & 0 & 0 \end{bmatrix}$	0.897	0.10

c axis parallel to the beam. This sample orientation allowed Q_x and Q_y to be independent of ΔE. The layered nature of the material means that the magnetic structure is effectively 2D, and so any dispersion should be independent of l. Hence we prioritised the energy-independence and coverage of Q_x and Q_y, over that of Q_z. The sample temperature was maintained in a top-loading closed-cycle LHe cryostat. Repetition rate multiplication meant that data were collected

Table 5.4: Structural and extinction parameters x_{ij} for $La_{2-x}Ba_xCoO_4$, x = 1/3 determined by refinement in the space group *Cmce* (#64) against integrated intensities collected at ∼ 2 K. $\chi^2 = 70.43$ and $R_F = 8.57$ for this refinement.

Atom	Wyckoff position	x	y	z	B_{iso}	Occupancy
La	$8f$	0	0.352	0.053	0.014	0.710
Ba	$8f$	0	0.352	0.053	0.010	0.290
O	$8e$	0.25	0.003	0.25	0.040	0.879
O	$8f$	0	0.167	0.020	0.037	1.002
Co	$4a$	0	0	0 0	0.08	1.000

Extinction parameter	Value
x_{11}	0.1
x_{22}	0.06396
x_{33}	0.25546
x_{12}	0.02570
x_{23}	0.09380
x_{13}	0.06733

Twin matrix	Twin 1 proportion	Twin 2 proportion
$\begin{bmatrix} 0 & 0 & 1 \\ 0 & -1 & 0 \\ 1 & 0 & 0 \end{bmatrix}$	0.905	0.095

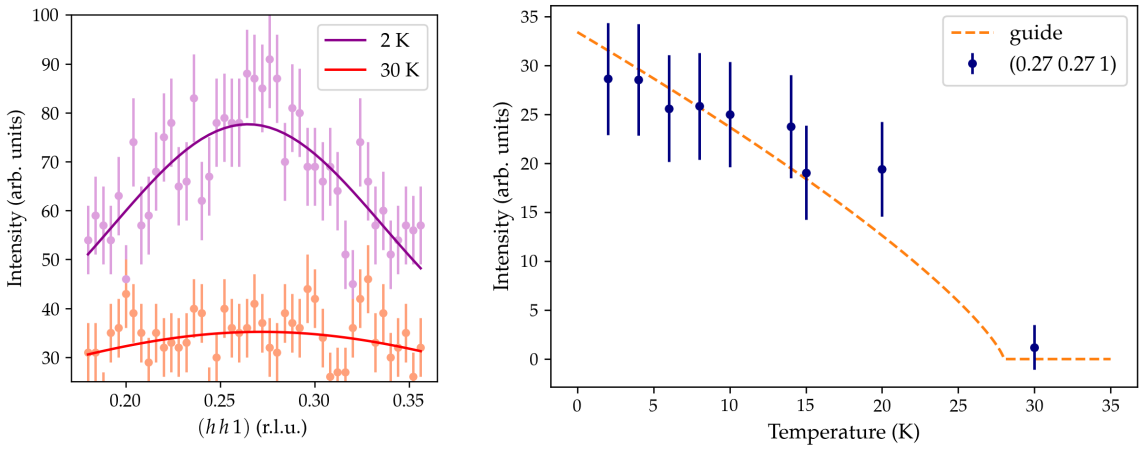

Figure 5.17: Single crystal diffraction of $La_{2-x}Ba_xCoO_4$, x = 1/3, measured on D10 at the ILL. *Left*, the broad magnetic peak at (0.27, 0.27, 1) seen on a scan along $(h, h, 1)$ at 2 K completely disappeared at 30 K. *Right*, the temperature dependence of the magnetic peak at (0.27, 0.27, 1). The dashed orange line is a guide to the eye.

simultaneously for E_i = 70.8 meV, 23.7 meV and 11 meV [64].

5.5.1 Analysis and results of MERLIN elastic line data

Although the MERLIN instrument is primarily used for inelastic neutron scattering, the elastic line data present a useful complement to the ILL D10 data, particularly as a snapshot across a large swathe of reciprocal space. Once again, the $I4/mmm$ space group (in the standard setting) applies to all (h, k, l) indices in this section. None of the peaks are Q-resolution limited and so the twinning observed on ILL D10 can be ignored for this analysis. Using this space group simplifies the analysis, as well as enabling the symmetrising of the data in the (h, k) plane to maximise the signal-to-noise ratio. The magnetic structure factor is greatest at low Q ($\sim e^{-Q^2}$), while nuclear scattering from small distortions of the lattice associated with charge order would show up at higher Q as the nuclear structure factor for a lattice distortion goes as $\sim Q^2$. Hence, the $E_i = 70.8$ meV data that covered the highest Q were searched for indications of charge order, while the $E_i = 23.7$ meV data with slightly better E resolution were used to examine the magnetic Bragg peaks. The data were processed in MANTID [65] before being symmetrised and reduced in HORACE [66].

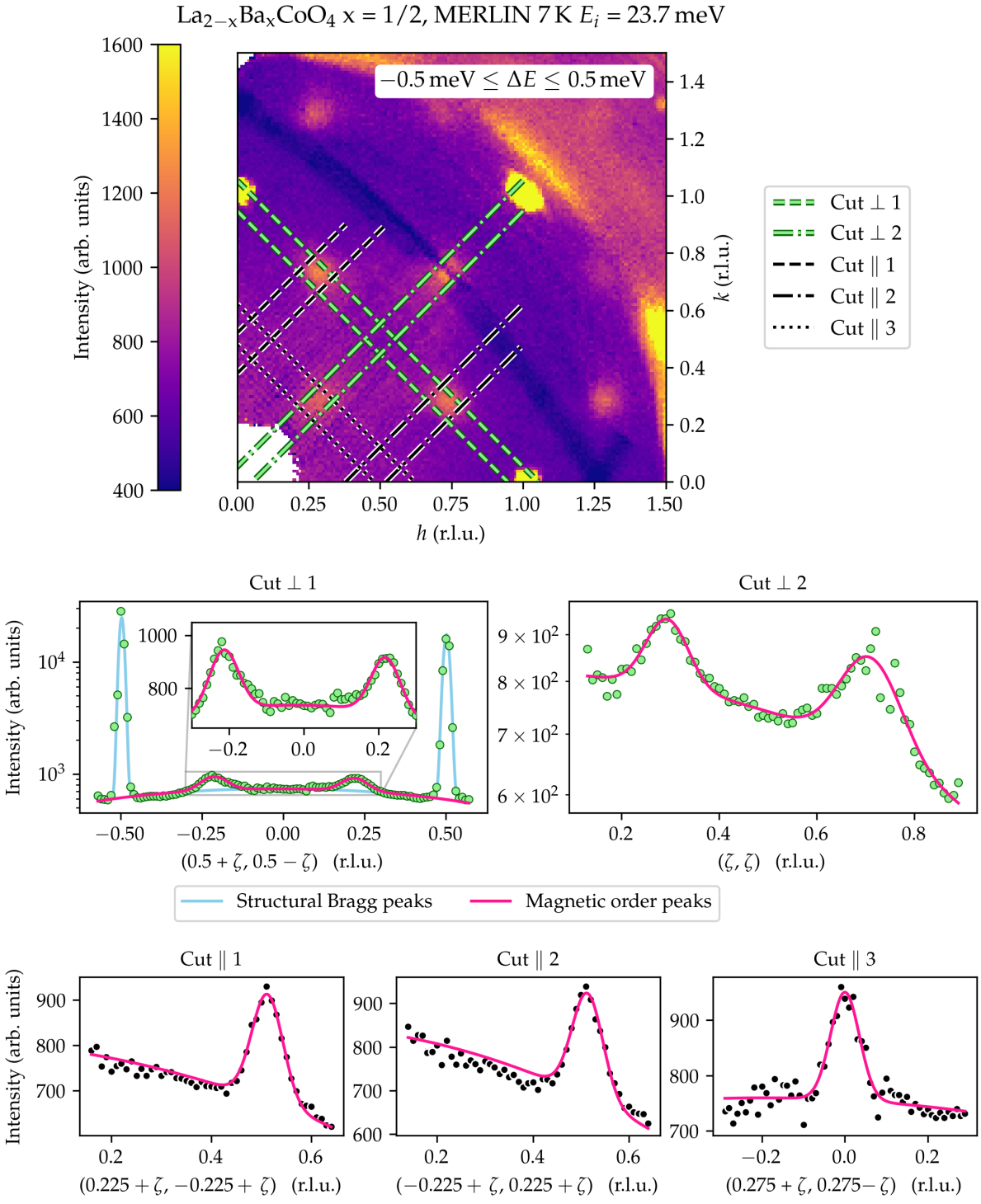

Figure 5.18: $La_{2-x}Ba_xCoO_4$, x = 1/2 MERLIN data taken at a temperature of 7 K. The colourmap shows the $hk0$ plane, integrated across the elastic line $\Delta E = [-0.5\,\text{meV},\ 0.5\,\text{meV}]$ and all l values. 1D cuts through the plane are fitted with multiple Gaussians to determine the locations of peaks attributed to structural reflections and magnetic superstructural reflections.

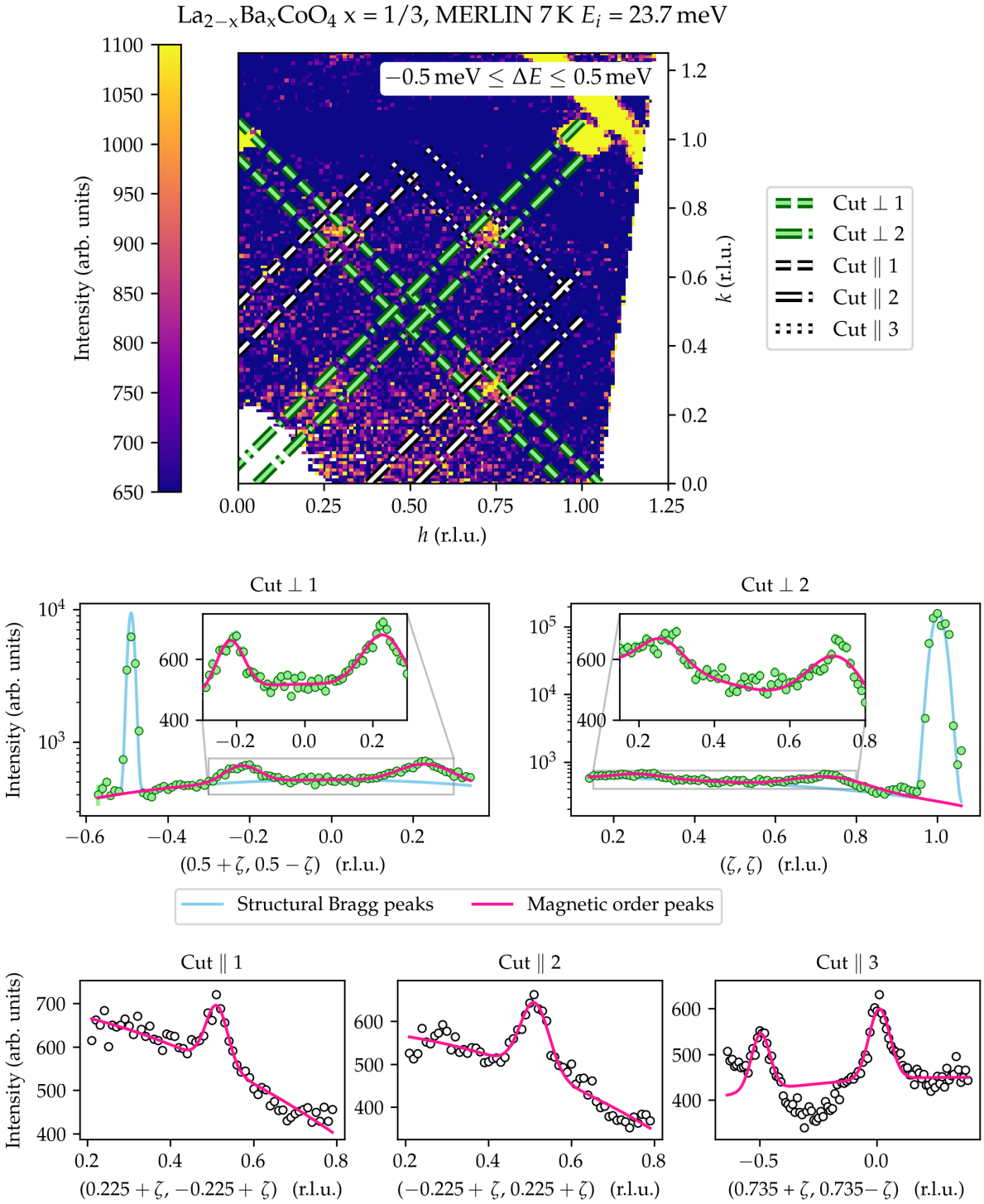

Figure 5.19: $La_{2-x}Ba_xCoO_4$, x = 1/3 MERLIN data taken at a temperature of 7 K. The colourmap shows the $hk0$ plane, integrated across the elastic line $\Delta E = [-0.5\,\text{meV},\ 0.5\,\text{meV}]$ and all l values. 1D cuts through the plane are fitted with multiple Gaussians to determine the locations of peaks attributed to structural reflections and magnetic superstructural reflections.

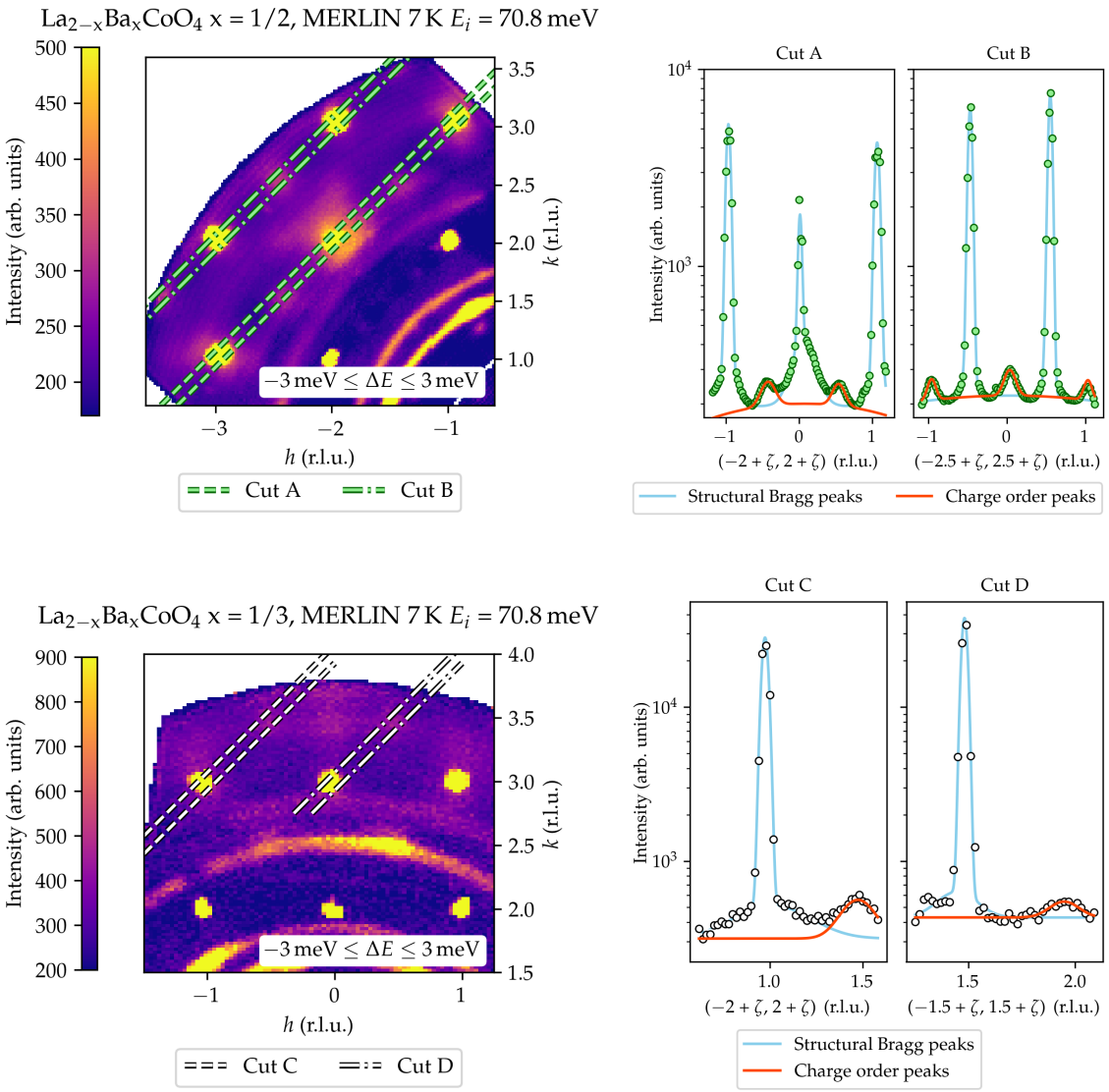

Figure 5.20: $La_{2-x}Ba_xCoO_4$, x = 1/2 and x = 1/3 MERLIN data taken at a temperature of 7 K. The colourmaps show the *hk* plane, integrated across the elastic line $\Delta E = [-3\,\text{meV},\ 3\,\text{meV}]$ and all *l* values. 1D cuts through the planes are fitted with multiple Gaussians to determine the locations of peaks attributed to structural reflections and charge order superstructural reflections.

5.5.2 Discussion of elastic scattering from MERLIN

Table 5.5 lists the fitted positions of the peaks observed in the line scans shown in Figures 5.18–5.20.

- The magnetic diffraction is weak in both the MERLIN and D10 data and slightly incommensurate with respect to both the period-3 stripe and checkerboard cases (commensurate period-3 stripe order would give $\eta = 1/6$ etc., checkerboard order $\eta = 1/4$).
- The charge order scattering is very weak, though admittedly the MERLIN experiment was not optimised to look for this. However, in the strontium doped cobaltate x = 1/2, the charge order was obvious at low Q too in the elastic line data from MAPS (a similar TOF spectrometer to MERLIN) [43].
- The Bragg peaks at higher Q are best described by a narrow Gaussian peak on top of a broad Gaussian base, which is possibly quasielastic in origin given the energy resolution of MERLIN. However, the difference in amplitude between these peaks is only an order of magnitude. The diffuse scattering at the Bragg peaks is not isotropic and can be seen extending out in lines (see Figure 5.20). This is likely a manifestation of the short-range (pretty disordered!) charge order, although I did not investigate this further.
- None of the features observed in the elastic line were Q-resolution limited, meaning that the calculated correlation lengths ξ are representative of the short-range of the electronic order.
- The correlation lengths for $La_{2-x}Ba_xCoO_4$ are larger and less anisotropic than those of $La_{1.67}Sr_{0.33}CoO_4$ and significantly smaller than those of $La_{1.5}Sr_{0.5}CoO_4$.

Table 5.5: Comparison of peaks seen in elastic line data for x = 1/2 and x = 1/3 $La_{2-x}Ba_xCoO_4$ crystals.

$La_{2-x}Ba_xCoO_4$	Instrument	Structural Bragg peak position (r.l.u.)	Magnetic order peak position η (r.l.u.)[1]	Charge order peak position (r.l.u.)
x = 1/2	MERLIN	1.000 ±0.007	0.23 ±0.01	0.54 ±0.01
x = 1/3	MERLIN	1.001 ±0.005	0.24 ±0.01	0.46 ±0.01
	D10	1.000 ±0.001	0.23 ±0.01	

[1] The magnetic order peak positions in the (h,k) plane are $(0.5 \pm \eta, 0.5 \pm \eta)$ and $(0.5 \pm \eta, 0.5 \mp \eta)$, accounting for two domains along (a,b) and $(a,-b)$ in the pseudotetragonal unit cell.

Table 5.6: Correlation lengths for $La_{2-x}A_xCoO_4$

$La_{2-x}A_xCoO_4$	$\xi_{\parallel_{C.O.}}$ (Å)	$\xi_{\perp_{C.O.}}$ (Å)	$\xi_{\parallel_M}$ (Å)	$\xi_{\perp_M}$ (Å)
A = Sr, x = 1/4 [54, 56]	≈ 19.3	≈ 13.5	≈ 7	≈ 3.5
A = Sr, x = 1/3 [18, 49]	≈ 5	≈ 2	≈ 5[1]	≈ 1[1]
A = Sr, x = 1/3 [57]	$\approx$ 7		$\approx$ 6[2]	
A = Sr, x = 1/2 [43]	23	8[3]	52	12[3]
A = Sr, x = 1/2 [40]	26	8.1[3]	79	10.7[3]
A = Ba, x = 1/3 (this work)	7.2 ± 0.9		15 ± 2	10 ± 2
A = Ba, x = 1/2 (this work)	7.4 ± 0.9		16 ± 0.6	13 ± 1

[1] Estimated from the results $\xi_{\parallel_M} \approx \xi_{\parallel_C}$ and $\xi_{\perp_M} \approx \xi_{\perp_C}/2$ in reference [18].
[2] This is the low-energy dynamic correlation length for the spin waves in [57].
[3] In [40, 43], $\xi_\perp$ refers to correlation lengths $\perp$ to the *ab* plane.

5.5.3 Analysis and results of inelastic scattering measurement

After reduction and symmetrisation as for the elastic line data, a series of 1D cuts were taken through constant ΔE and constant Q slices. Key directions in the 1D Q cuts through constant energy slices were along the diagonals (h, h), through the magnetic Bragg peaks $(h, 0.25)$, and through the magnetic zone centre $(h, 0.5)$. An example of 1D Q cuts through a constant energy slice is shown in Figure 5.21, with the distance between dashed lines of the same colour representing the integration width for that particular cut. Additionally, 1D energy cuts were taken through many Q positions, mostly to pin down the dispersion of the flatter mode at ~ 28 meV.

5.5.4 Discussion of inelastic scattering from MERLIN

Straightaway we can see that the excitations present in the inelastic spectrum of $La_{2-x}Ba_xCoO_4$ are less intense and more diffuse than those for $La_{2-x}Co_xCoO_4$, suggesting Ba-doping yields shorter-range excitations than Sr-doping. A closer inspection nevertheless reveals some interesting qualitative features among the fuzz for the x = 1/2 data (Figure 5.22):

- Low-energy spin waves emerge from $\sim(0.5 \pm 0.23, 0.5\pm 0.23)$, and converge inwards upon the zone centre (0.5, 0.5). Minimal, if any, intensity is present in outwards branches that meet at (0, 0) as in $La_{1.5}Sr_{0.5}CoO_4$. This is a large qualitative differences between dispersion of the

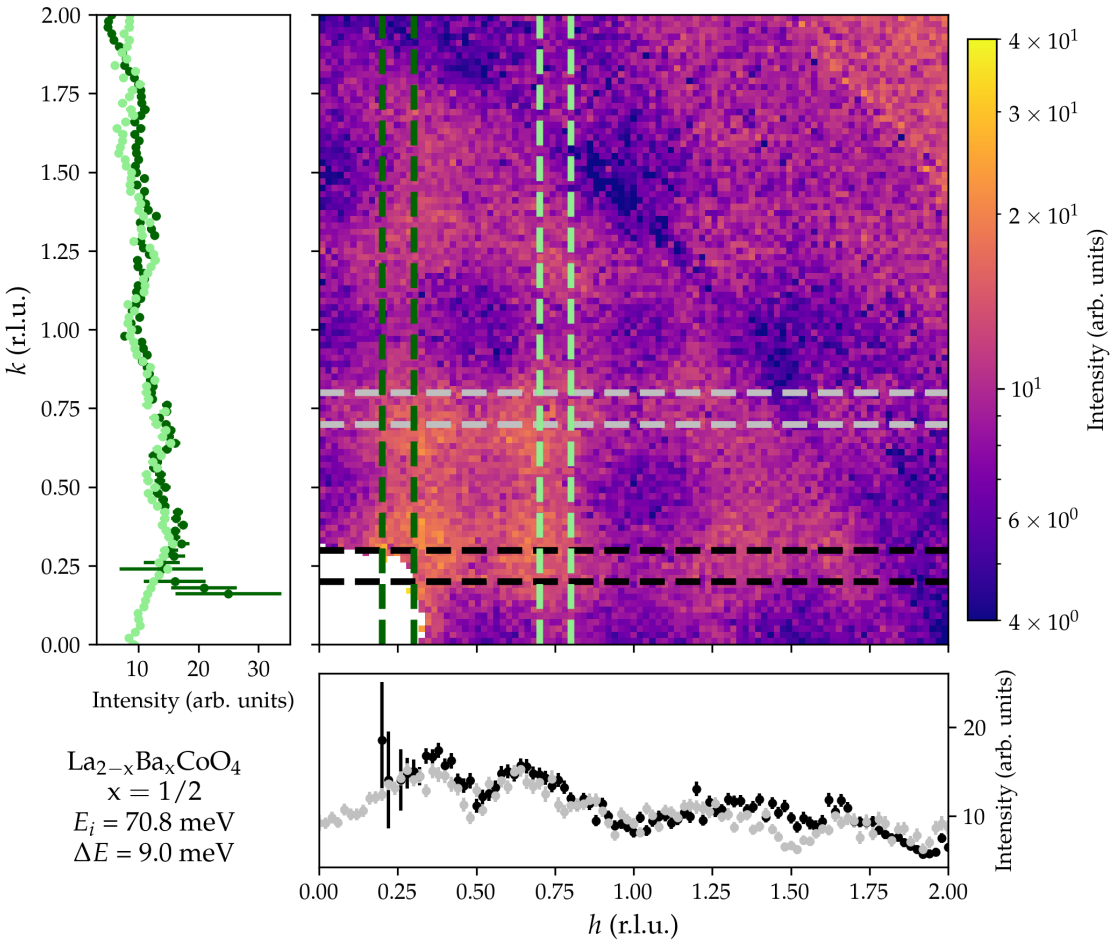

Figure 5.21: Constant energy slice in $(hk0)$ plane of $La_{2-x}Ba_xCoO_4$, $x = 1/2$, showing example constant energy **Q** cuts along (0.25, k, 0), (0.75, k, 0), $(h, 0.25, 0)$ and $(h, 0.75, 0)$ directions. The integration width for each cut was 2 meV in energy, all l values, and 0.1 r.l.u. in h or k as applicable.

Ba half-doped cobaltate and the Sr half-doped cobaltate for $\Delta E < 17$ meV.

- A second difference between the inelastic spectra for $La_{1.5}Ba_{0.5}CoO_4$ and $La_{1.5}Sr_{0.5}CoO_4$ is that there is a clear gap in the spectrum of the latter between 17 meV and ≈ 26 meV but no such gap in the former.
- The dispersion of $La_{1.5}Ba_{0.5}CoO_4$ pivots from being along (h, h) / $(h, -h)$ below 17 meV to being along $(0.5, h)$ / $(h, 0.5)$ above 17 meV.
- This means that the spin wave spectrum of $La_{1.5}Ba_{0.5}CoO_4$ can be viewed as a diffuse hourglass, a description more akin to the x = 1/3 or x = 1/4 Sr compounds than the x = 1/2 Sr compound.
- However, a common feature of $La_{1.5}Ba_{0.5}CoO_4$ and $La_{1.5}Sr_{0.5}CoO_4$ is a less dispersive, higher-energy mode at ~ 28 meV.

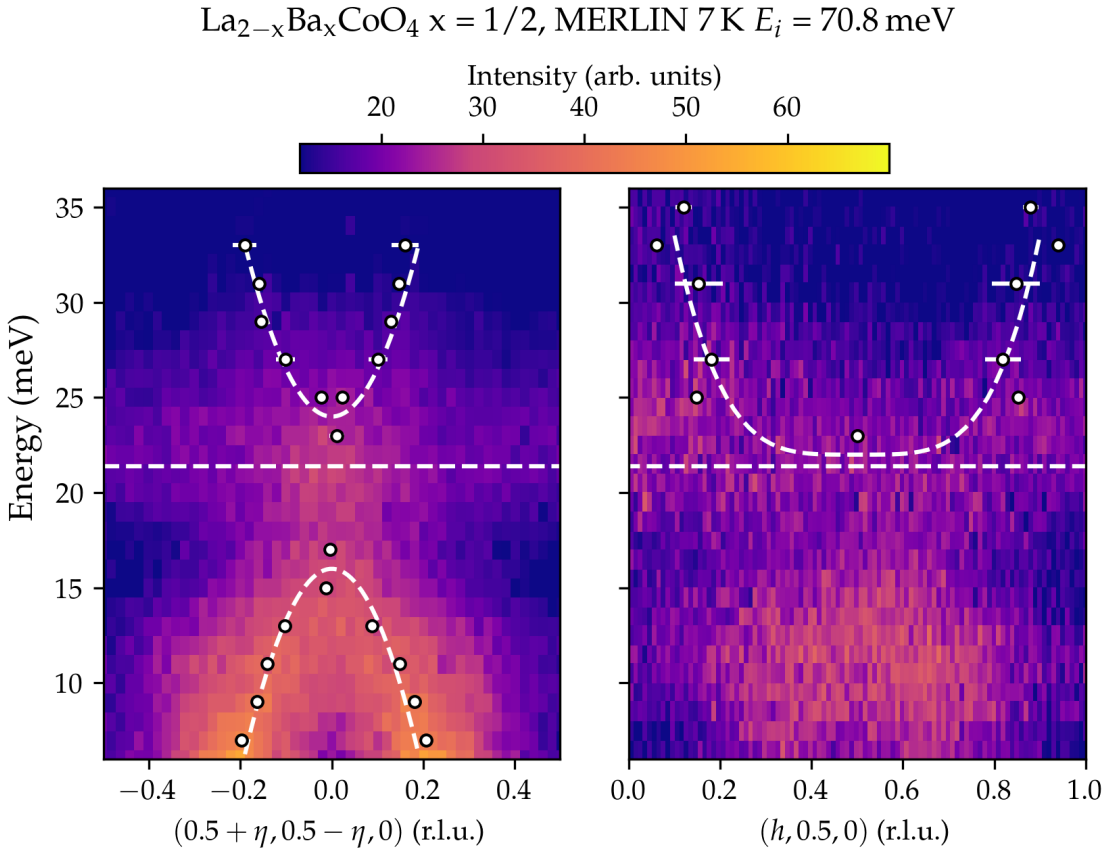

Figure 5.22: The (fuzzy) hourglass shape of the magnetic excitations of $La_{2-x}Ba_xCoO_4$, x = 1/2. Most of the intensity is concentrated at lower energies at $\approx (0.27, 0.27, 0)$ etc. before the 'waist' at ~ 17 meV. The weaker mode at ~ 28 meV is less dispersive along $\parallel (h, h, 0)$ than along $(h, 0.5, 0)$. This higher energy mode can be explained by the splitting of Co^{2+} $S = 3/2$ states by the spin-orbit interaction, combined with disordered stripes. White dashed lines are guides to the eye. Both subplots use the same colour scale for intensity.

- The spectra of $La_{2-x}Ba_xCoO_4$ x = 1/2 and x = 1/3 appear qualitatively similar, although the signal in the x = 1/3 data is weaker than in the x = 1/2 data (Figure 5.24).
- No features are present at low Q for $\Delta E > 40$ meV, although scattering intensity does appear at higher Q (Figure 5.25). This is likely to come from a phonon, a clear departure from the nanophase separation model.

The majority of these features are summarised visually in Figure 5.23.

A preliminary estimate of the exchange parameters J and J' was made by fitting the linear, low-energy spin wave branches to the LSWT Hamiltonian (Equation 5.5) using SPINW. A comparison of this model with the data for $La_{2-x}Ba_xCoO_4$, x = 1/2 and x = 1/3 is shown in Figure 5.24. This generated $J \approx 3.9$ meV and $J' \approx -0.8$ meV, using the δ, ϵ anisotropy parameters as in reference [13]. However, the LWST model is unsuitable for the excitation spectrum of $La_{2-x}Ba_xCoO_4$ as it does not

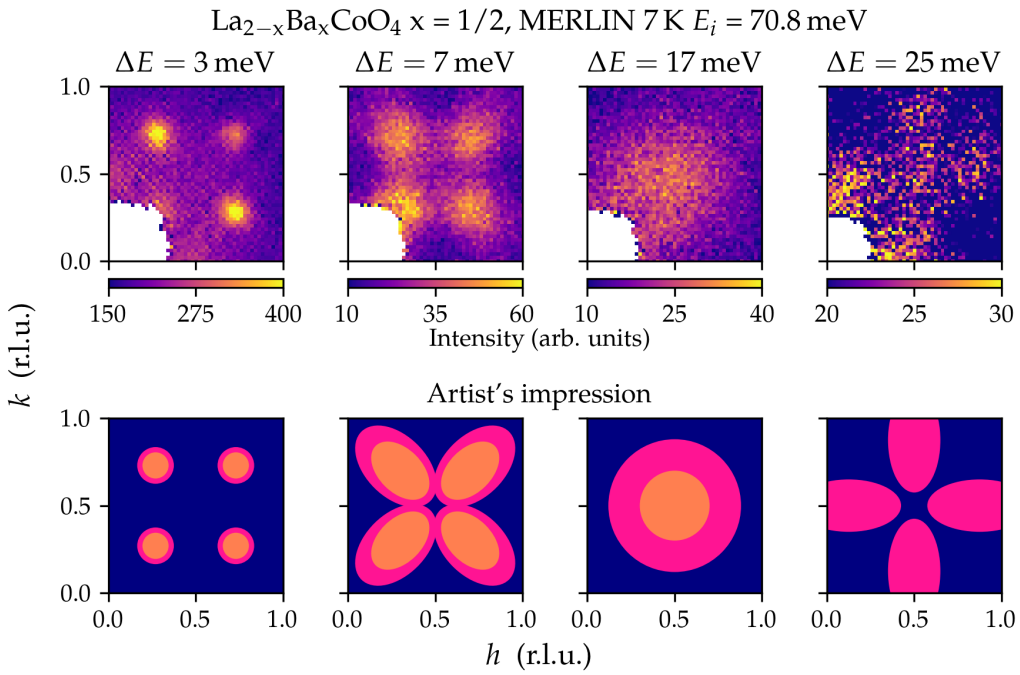

Figure 5.23: The upper panels show MERLIN data for $La_{2-x}Ba_xCoO_4$, x = 1/2 displayed as constant energy slices in the $(h, k, 0)$ plane. Integration width was 0.2 meV in energy and across all l values. Key features of the dispersion are highlighted in the lower "artist's impression" panels.

capture the anisotropic dispersion from the $(0.5 \pm \eta, 0.5 \pm \eta)$ magnetic Bragg peaks even at low energies.

Instead the key features of the measured spectrum are shared with the hourglass shape of the disordered spin glass model (§ 5.2.3). By linking the quantitative results of the slightly stripy spin glass model [18] to the qualitative features of the $La_{1.5}Ba_{0.5}CoO_4$ spectra and correlation lengths calculated earlier in this chapter, I was able to flesh out this rough interpretation:

- Hourglass waist energy $\omega_S \sim 0.60\ JS = 17$ meV (c.f. Figure 5.9 c) and d))
- J/J' ratio ~ 10 (c.f. Figure 5.10 b) and d)).

It looks like $J \sim 10\ J'$ for $La_{2-x}Ba_xCoO_4$, rather than $J \sim 20\ J'$ for $La_{2-x}Sr_xCoO_4$ (see Table 5.7), which has a more distinct hourglass spectrum. However, the estimated exchange parameter ratio for $La_{2-x}Ba_xCoO_4$ is larger than $J \sim 2\ J'$ seen in nickelates ([67, 68]).

5.6 Conclusions regarding the spin and charge order of $La_{2-x}Ba_xCoO_4$

In summary, the structure of $La_{2-x}Ba_xCoO_4$ is pseudotetragonal and twinned. No significant differences were observed between crystals of two different doping concentrations x in either

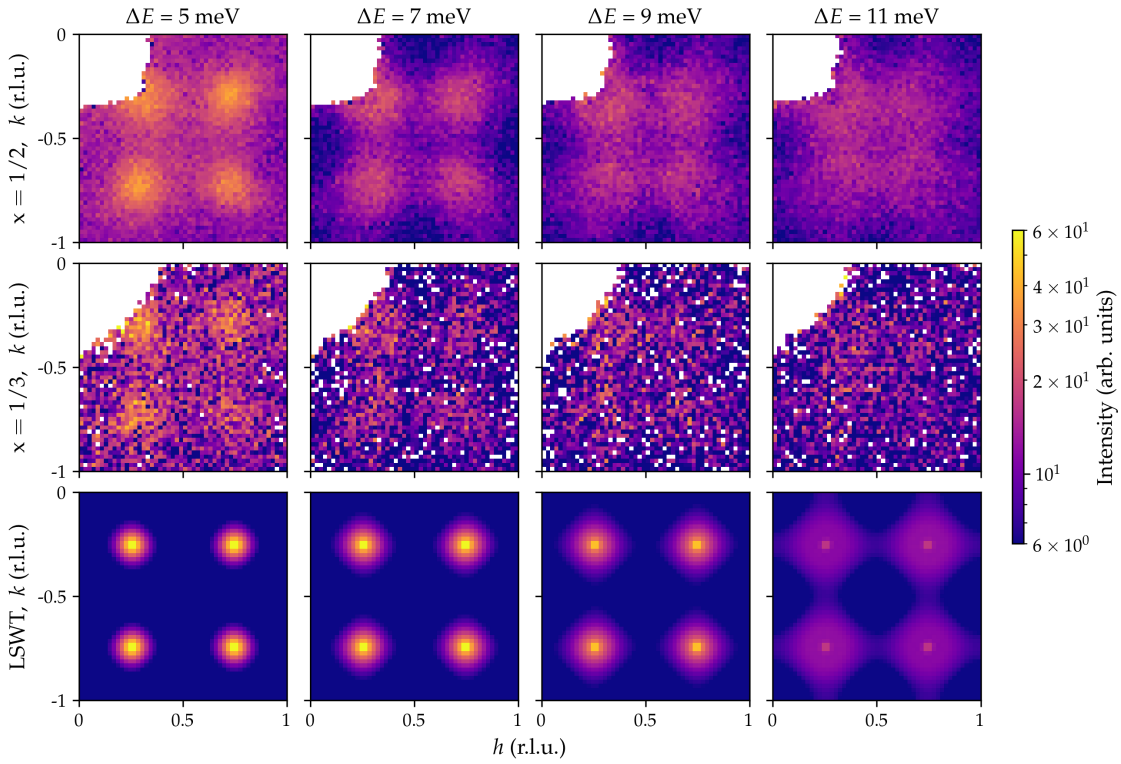

Figure 5.24: Constant energy slices of $La_{2-x}Ba_xCoO_4$, x = 1/2 (top row of panels) and x = 1/3 (middle row of panels) MERLIN data for low ΔE. Qualitatively, the x = 1/3 resembles the x = 1/2 data, although the signal is weaker (we also didn't count the x = 1/3 sample for as long as the x = 1/2 sample). The excitations are seen moving towards (0.5, 0.5, 0) as energy increases. This is not replicated by a fit of a LSWT model given by Equation 5.5 (bottom row of panels), which worked well for $La_{2-x}Sr_xCoO_4$, x = 1/2. Increasing δ in Equation 5.5 serves to move the dispersion maxima towards the magnetic zone centres (0, 0) and (0.5, 0.5) for the checkerboard model, but this is not what is seen for $La_{2-x}Ba_xCoO_4$, x = 1/2 and x = 1/3.

Table 5.7: Spin wave model parameters for $La_{2-x}Sr_xCoO_4$

$La_{2-x}Sr_xCoO_4$	J (meV)	J path	J' (meV)	J' path	B_2^0 (meV)	$\lvert \mathbf{H}_a \cdot \mathbf{S} \rvert$ (meV)
x = 0 [55]	9.69	a	$J_1 = 0.14$ $J_2 = 0.43$	$J_1 = 2a$ $J_2 = \sqrt{2}a$	14.6[1]	0.66
x = 1/4 [54]	≈ 11.25	a	≈ 0.56	$2a$		
x = 1/3 [49]	11.5	a	0.55	$2a$	13.0[1]	0
x = 1/3 [18]	≈ 12.5	a	≈ 0.625	$2a$		
x = 1/3 [57]	5.8	a	0.85	$2a$		
x = 1/2 [43]	1.4	$2a$	0	$\sqrt{2}a$	13.0[1]	0.22

[1] For these models using Equation 5.4, $\lambda = -18.7$ meV, $B_4^0 = -13.5$ meV, $B_4^4 = -8.0$ meV [43, 49, 55].

the neutron diffraction or magnetisation data. The magnetic structure is short-range AFM with $\mathbf{q} = (0.5 \pm 0.23, 0.5 \pm 0.23)$ in the *ab* plane. Correlation lengths are in the range of 7 Å for charge order and 15 Å for magnetic order. The hypothesis that Ba doping would stabilise the stripe order has not been borne out by our experimental data, which instead indicate more disorder than the equivalent Sr-doped compounds. The excitation spectrum, measured by inelastic neutron scattering, exhibits an hour glass shape, with a flat mode just above the hourglass waist. The spectrum is more diffuse and persists at a lower hole dopant concentration than for the strontium-doped cobaltates, which instead show long-range collinear AFM order for x = 1/2. The excitations cannot be described by linear spin wave theory. The spectrum is best described (qualitatively) by a cluster spin glass with stripe tendencies. The diffuse hourglass excitations are driven by a large difference in size between the nearest and next-nearest neighbour exchange interactions, with the former (which also introduces a degree of frustration) being around a tenth of the size of the latter.

Acknowledgements for this chapter

Affiliations are the University of Oxford unless otherwise stated.

The crystal synthesis and magnetisation measurements of $La_{2-x}Ba_xCoO_4$ were performed by Dharmalingam Prabhakaran.

The x-ray diffraction of $La_{2-x}Ba_xCoO_4$ was done by Siobhan Tobin.

The ILL D10 experiment was performed by Bachir Ouladdiaf (ILL), Siobhan Tobin, and Andrew Boothroyd. Data from this experiment are available via proposal number 5-41-1101 [69].

The ISIS MERLIN experiment was performed by Siobhan Tobin, Andrew Boothroyd and Helen Walker (ISIS). Data from this experiment are available via proposal number RB1920499 [70].

References

[1] J. M. Tranquada, B. J. Sternlieb, J. D. Axe, Y. Nakamura, and S. Uchida. "Evidence for stripe correlations of spins and holes in copper oxide superconductors". *Nature* 375.6532 (1995). DOI: 10.1038/375561a0 (cited on pages 121, 126).

[2] V. J. Emery, S. A. Kivelson, and J. M. Tranquada. "Stripe phases in high-temperature superconductors". *Proceedings of the National Academy of Sciences* 96.16 (1999). DOI: 10.1073/pnas.96.16.8814 (cited on pages 121, 125, 126).

[3] J. M. Tranquada. "Cuprate superconductors as viewed through a striped lens". *Advances in Physics* 69.4 (2020). DOI: 10.1080/00018732.2021.1935698 (cited on page 121).

[4] Y. Zhang, C. Lane, J. W. Furness, B. Barbiellini, J. P. Perdew, R. S. Markiewicz, A. Bansil, and J. Sun. "Competing stripe and magnetic phases in the cuprates from first principles". *Proceedings of the National Academy of Sciences* 117.1 (2020). DOI: 10.1073/pnas.1910411116 (cited on page 121).

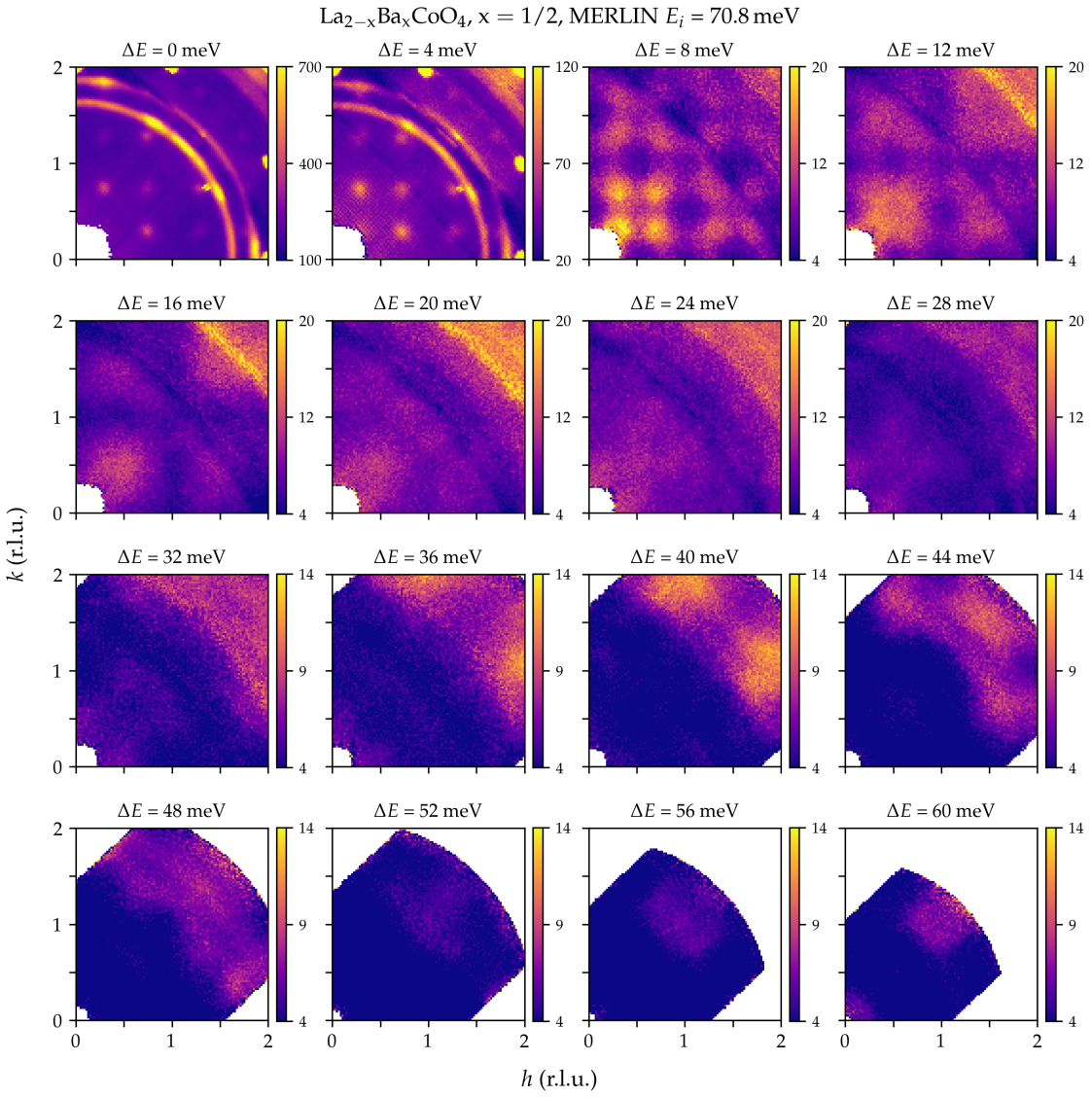

Figure 5.25: $La_{2-x}Ba_xCoO_4$, x = 1/2, energy slices all the way up to $\Delta E = 60$ meV, with $E_i = 70.80$ meV. The $\Delta E = 28$ meV slice clearly shows the four-leaf clover shape again. The integration width was $\Delta E = 4$ meV.

[5] H. Jacobsen et al. "Distinct Nature of Static and Dynamic Magnetic Stripes in Cuprate Superconductors". *Physical Review Letters* 120.3 (2018). DOI: 10.1103/PhysRevLett.120.037003 (cited on page 121).

[6] D. Sari, B. Yaşar, F. Pişkin, Y. E. Kalay, and T. Öztürk. "Segregation Resistant Nanocrystalline/Amorphous (La, Sr)CoO_3-(La,Sr)$_2CoO_4$ Composite Cathodes for IT-SOFCs". *Journal of The Electrochemical Society* 166.15 (2019). DOI: 10.1149/2.0201915jes (cited on page 122).

[7] G. Thornton, B. C. Tofield, and A. W. Hewat. "A neutron diffraction study of $LaCoO_3$ in the temperature range 4.2 < T < 1248 K". *Journal of Solid State Chemistry* 61.3 (1986). DOI: 10.1016/0022-4596(86)90035-6 (cited on pages 122, 129).

[8] E. Muhumuza, P. Wu, T. Nan, L. Zhao, P. Bai, S. Mintova, and Z. Yan. "Perovskite-Type $LaCoO_3$ as an Efficient and Green Catalyst for Sustainable Partial Oxidation of Cyclohexane". *Industrial & Engineering Chemistry Research* 59.49 (2020). DOI: 10.1021/acs.iecr.0c04095 (cited on page 122).

[9] Z. Shen et al. "Correlating the electronic structure of perovskite $La_{1-x}Sr_xCoO_3$ with activity for the oxygen evolution reaction: The critical role of Co 3*d* hole state". *Journal of Energy Chemistry* 65 (2022). DOI: 10.1016/j.jechem.2021.06.032 (cited on page 122).

[10] R. De Barros, M. Ceretti, W. Schmidt, V. Y. Pomjakushin, and W. Paulus. "Growth and Oxygen Stoichiometry Control of High-Quality $La_2CoO_{4+\delta}$ Single Crystals ($\delta = 0.25$)". *Crystal Growth & Design* 22.9 (2022). DOI: 10.1021/acs.cgd.2c00631 (cited on pages 122, 126, 129).

[11] H. Ulbrich and M. Braden. "Neutron scattering studies on stripe phases in non-cuprate materials". *Physica C: Superconductivity* 481 (2012). DOI: https://doi.org/10.1016/j.physc.2012.04.039 (cited on pages 122, 126–128, 130, 131, 140).

[12] K. Momma and F. Izumi. "VESTA 3 for three-dimensional visualization of crystal, volumetric and morphology data". *Journal of Applied Crystallography* 44.6 (2011). DOI: 10.1107/S0021889811038970 (cited on pages 123, 149, 151).

[13] L. M. Helme. "Neutron Scattering Studies of Correlated Electron Systems". PhD thesis. University of Oxford, 2006 (cited on pages 124, 126, 127, 133, 135, 136, 139, 142, 144, 160).

[14] S. A. Kivelson, I. P. Bindloss, E. Fradkin, V. Oganesyan, J. M. Tranquada, A. Kapitulnik, and C. Howald. "How to detect fluctuating stripes in the high-temperature superconductors". *Reviews of Modern Physics* 75.4 (2003). DOI: 10.1103/RevModPhys.75.1201 (cited on pages 123, 126).

[15] P. Abbamonte, A. Rusydi, S. Smadici, G. D. Gu, G. A. Sawatzky, and D. L. Feng. "Spatially modulated 'Mottness' in $La_{2-x}Ba_xCuO_4$". *Nature Physics* 1.3 (2005). DOI: 10.1038/nphys178 (cited on page 124).

[16] G. Campi et al. "Inhomogeneity of charge-density-wave order and quenched disorder in a high-Tc superconductor". *Nature* 525.7569 (2015). DOI: 10.1038/nature14987 (cited on page 124).

[17] Y. Drees, D. Lamago, A. Piovano, and A. C. Komarek. "Hour-glass magnetic spectrum in a stripeless insulating transition metal oxide". *Nature Communications* 4.1 (2013). DOI: 10.1038/ncomms3449 (cited on pages 124, 141, 142, 144).

[18] E. C. Andrade and M. Vojta. "Disorder, Cluster Spin Glass, and Hourglass Spectra in Striped Magnetic Insulators". *Physical Review Letters* 109.14 (2012). DOI: 10.1103/PhysRevLett.109.147201 (cited on pages 124, 133, 139–141, 144, 158, 161, 162).

[19] Y. Hu et al. "Real-space observation of incommensurate spin density wave and coexisting charge density wave on Cr (001) surface". *Nature Communications* 13.1 (2022). DOI: 10.1038/s41467-022-28104-2 (cited on page 125).

[20] B. H. Savitzky, I. El Baggari, A. S. Admasu, J. Kim, S.-W. Cheong, R. Hovden, and L. F. Kourkoutis. "Bending and breaking of stripes in a charge ordered manganite". *Nature Communications* 8.1 (2017). DOI: 10.1038/s41467-017-02156-1 (cited on page 125).

[21] N. Harrison. "Spin Density Waves and Magnons". *Encyclopedia of Condensed Matter Physics*. Ed. by F. Bassani, G. L. Liedl, and P. Wyder. Oxford: Elsevier, 2005. DOI: 10.1016/B0-12-369401-9/00667-7 (cited on page 125).

[22] A. M. Gabovich, A. I. Voitenko, J. F. Annett, and M. Ausloos. "Charge- and spin-density-wave superconductors". *Superconductor Science and Technology* 14.4 (2001). DOI: 10.1088/0953-2048/14/4/201 (cited on page 125).

[23] M. E. Kamminga, K. M. L. Krighaar, A. T. Rømer, L. Ø. Sandberg, P. P. Deen, M. Boehm, G. D. Gu, J. M. Tranquada, and K. Lefmann. "Evolution of magnetic stripes under uniaxial stress in $La_{1.885}Ba_{0.115}CuO_4$ studied by neutron scattering". *Physical Review B* 107.14 (2023). DOI: 10.1103/PhysRevB.107.144506 (cited on page 125).

[24] M. Jurkutat, C. Kattinger, S. Tsankov, R. Reznicek, A. Erb, and J. Haase. "How pressure enhances the critical temperature of superconductivity in $YBa_2Cu_3O_{6+y}$". *Proceedings of the National Academy of Sciences* 120.2 (2023). DOI: 10.1073/pnas.2215458120 (cited on page 125).

[25] A. C. Mark, J. C. Campuzano, and R. J. Hemley. "Progress and prospects for cuprate high temperature superconductors under pressure". *High Pressure Research* 42.2 (2022). DOI: 10.1080/08957959.2022.2059366 (cited on page 125).

[26] K. I. Kugel, A. L. Rakhmanov, A. O. Sboychakov, F. V. Kusmartsev, N. Poccia, and A. Bianconi. "A two-band model for the phase separation induced by the chemical mismatch pressure in different cuprate superconductors". *Superconductor Science and Technology* 22.1 (2008). DOI: 10.1088/0953-2048/22/1/014007 (cited on page 125).

[27] M. Marezio, F. Licci, and A. Gauzzi. "The Effect of Chemical Pressure on T_c of Layered Cuprate Superconductors". *Advances in Superconductivity XI*. Ed. by N. Koshizuka and S. Tajima. Tokyo: Springer Japan, 1999. DOI: 10.1007/978-4-431-66874-9_4 (cited on page 125).

[28] H. Ninomiya, K. Kawashima, A. Iyo, H. Fujihisa, S. Ishida, H. Ogino, Y. Yoshida, Y. Gotoh, and H. Eisaki. "Calcium-free double-layered cuprate superconductors with critical temperature above 100 K". *Communications Materials* 2.1 (2021). DOI: 10.1038/s43246-020-00116-9 (cited on page 125).

[29] S. J. Skinner and J. A. Kilner. "Oxygen diffusion and surface exchange in $La_{2-x}Sr_xNiO_{4+\delta}$". *Solid State Ionics*. Proceedings of the 12th International Conference on Solid State 135.1 (2000). DOI: 10.1016/S0167-2738(00)00388-X (cited on page 126).

[30] A. Aguadero, J. A. Alonso, and L. Daza. "Oxygen Excess in $La_2CoO_{4+\delta}$: A Neutron Diffraction Study". *Zeitschrift für Naturforschung B* 63.6 (2008). DOI: 10.1515/znb-2008-0604 (cited on pages 126, 129).

[31] K. Yamada, E. Kudo, Y. Endoh, Y. Hidaka, M. Oda, M. Suzuki, and T. Murakami. "The effect of the heat treatments on the antiferromagnetism in $La_2CuO_{4-\delta}$ single crystals". *Solid State Communications* 64.5 (1987). DOI: https://doi.org/10.1016/0038-1098(87)90693-4 (cited on pages 126, 149).

[32] S. Ohsugi, Y. Kitaoka, K. Ishida, G.-q. Zheng, and K. Asayama. "Cu NMR and NQR Studies of High-T_c Superconductor $La_{2-x}Sr_xCuO_4$". *Journal of the Physical Society of Japan* 63.2 (1994). DOI: 10.1143/JPSJ.63.700 (cited on page 126).

[33] M. Fujita, H. Goka, K. Yamada, J. M. Tranquada, and L. P. Regnault. "Stripe order, depinning, and fluctuations in $La_{1.875}Ba_{0.125}CuO_4$ and $La_{1.875}Ba_{0.075}Sr_{0.050}CuO_4$". *Physical Review B* 70.10 (2004). DOI: 10.1103/PhysRevB.70.104517 (cited on page 126).

[34] S. Wakimoto, J. M. Tranquada, T. Ono, K. M. Kojima, S. Uchida, S.-H. Lee, P. M. Gehring, and R. J. Birgeneau. "Diagonal static spin correlation in the low-temperature orthorhombic *Pccn* phase of $La_{1.55}Nd_{0.4}Sr_{0.05}CuO_4$". *Physical Review B* 64.17 (2001). DOI: 10.1103/PhysRevB.64.174505 (cited on page 126).

[35] G. M. Kaminsky, D. P. Belanger, F. Ye, J. A. Fernandez-Baca, J. Wang, M. Matsuda, and J.-Q. Yan. "Origin of the net magnetic moment in $LaCoO_3$". *Physical Review B* 97.2 (2018). DOI: 10.1103/PhysRevB.97.024418 (cited on pages 126, 129).

[36] N. Orlovskaya and D. Steinmetz. "Raman Diagnostics of $LaCoO_3$ Based Perovskites". *Mixed Ionic Electronic Conducting Perovskites for Advanced Energy Systems*. Ed. by N. Orlovskaya and N. Browning. Nato Science Series. Dordrecht: Springer Netherlands, 2004. DOI: 10.1007/978-1-4020-2349-1_4 (cited on pages 126, 129).

[37] K. Kleveland, N. Orlovskaya, T. Grande, A. M. M. Moe, M.-A. Einarsrud, K. Breder, and G. Gogotsi. "Ferroelastic Behavior of $LaCoO_3$-Based Ceramics". *Journal of the American Ceramic Society* 84.9 (2001). DOI: 10.1111/j.1151-2916.2001.tb00953.x (cited on pages 126, 129).

[38] J. Wu and C. Leighton. "Glassy ferromagnetism and magnetic phase separation in $La_{1-x}Sr_xCoO_3$". *Physical Review B* 67.17 (2003). DOI: 10.1103/PhysRevB.67.174408 (cited on pages 127, 129).

[39] B. Raveau and M. M. Seikh. "Crystal Chemistry of Cobalt Oxides". *Cobalt Oxides: From Crystal Chemistry to Physics*. Wiley-VCH Verlag GmbH & Co., 2012 (cited on pages 127, 128).

[40] I. A. Zaliznyak, J. P. Hill, J. M. Tranquada, R. Erwin, and Y. Moritomo. "Independent Freezing of Charge and Spin Dynamics in $La_{1.5}Sr_{0.5}CoO_4$". *Physical Review Letters* 85.20 (2000). DOI: 10.1103/PhysRevLett.85.4353 (cited on pages 127, 128, 130, 132, 158).

[41] R. Ang, Y. P. Sun, X. Luo, C. Y. Hao, and W. H. Song. "Studies of structural, magnetic, electrical and thermal properties in layered perovskite cobaltite $SrLnCoO_4$ (Ln = La, Ce, Pr, Nd, Eu, Gd and Tb)". *Journal of Physics D: Applied Physics* 41.4 (2008). DOI: 10.1088/0022-3727/41/4/045404 (cited on page 128).

[42] K. Horigane, H. Hiraka, T. Uchida, K. Yamada, and J. Akimitsu. "Spin and Charge Orders and Their Hole-Doping Dependence in Single Layered Cobaltate $La_{2-x}Ca_xCoO_4$ ($0.3 \leq x \leq 0.8$)". *Journal of the Physical Society of Japan* 76.11 (2007). DOI: 10.1143/JPSJ.76.114715 (cited on pages 128, 130, 131).

[43] L. M. Helme, A. T. Boothroyd, R. Coldea, D. Prabhakaran, C. D. Frost, D. A. Keen, L. P. Regnault, P. G. Freeman, M. Enderle, and J. Kulda. "Magnetic order and dynamics of the charge-ordered antiferromagnet $La_{1.5}Sr_{0.5}CoO_4$". *Physical Review B* 80.13 (2009). DOI: 10.1103/PhysRevB.80.134414 (cited on pages 128, 130, 132, 135, 136, 139, 142, 144, 146, 157, 158, 162).

[44] K. Yamada, M. Matsuda, Y. Endoh, B. Keimer, R. J. Birgeneau, S. Onodera, J. Mizusaki, T. Matsuura, and G. Shirane. "Successive antiferromagnetic phase transitions in single-crystal La_2CoO_4". *Physical Review B* 39.4 (1989). DOI: 10.1103/PhysRevB.39.2336 (cited on page 129).

[45] L. Le Dréau, C. Prestipino, O. Hernandez, J. Schefer, G. Vaughan, S. Paofai, J. M. Perez-Mato, S. Hosoya, and W.

Paulus. "Structural Modulation and Phase Transitions in $La_2CoO_{4.14}$ Investigated by Synchrotron X-ray and Neutron Single-Crystal Diffraction". *Inorganic Chemistry* 51.18 (2012). DOI: 10.1021/ic301165a (cited on page 129).

[46] R. A. Ewings, P. G. Freeman, M. Enderle, J. Kulda, D. Prabhakaran, and A. T. Boothroyd. "Ferromagnetic excitations in $La_{0.82}Sr_{0.18}CoO_3$ observed using neutron inelastic scattering". *Physical Review B* 82.14 (2010). DOI: 10.1103/PhysRevB.82.144401 (cited on page 129).

[47] A. T. Savici, I. A. Zaliznyak, G. D. Gu, and R. Erwin. "Stripeless incommensurate magnetism in strongly correlated oxide $La_{1.5}Sr_{0.5}CoO_4$". *Physical Review B* 75.18 (2007). DOI: 10.1103/PhysRevB.75.184443 (cited on page 130).

[48] M. Cwik, M. Benomar, T. Finger, Y. Sidis, D. Senff, M. Reuther, T. Lorenz, and M. Braden. "Magnetic Correlations in $La_{2-x}Sr_xCoO_4$ Studied by Neutron Scattering: Possible Evidence for Stripe Phases". *Physical Review Letters* 102.5 (2009). DOI: 10.1103/PhysRevLett.102.057201 (cited on page 130).

[49] A. T. Boothroyd, P. Babkevich, D. Prabhakaran, and P. G. Freeman. "An hour-glass magnetic spectrum in an insulating, hole-doped antiferromagnet". *Nature* 471.7338 (2011). DOI: 10.1038/nature09902 (cited on pages 130, 132, 133, 137–140, 142–144, 146, 158, 162).

[50] P. Babkevich, P. G. Freeman, M. Enderle, D. Prabhakaran, and A. T. Boothroyd. "Direct evidence for charge stripes in a layered cobalt oxide". *Nature Communications* 7.1 (2016). DOI: 10.1038/ncomms11632 (cited on pages 130, 137, 139, 140, 142, 144, 149).

[51] H. Guo, W. Schmidt, L. H. Tjeng, and A. C. Komarek. "Charge correlations in cobaltates $La_{2-x}Sr_xCoO_4$". *physica status solidi (RRL) – Rapid Research Letters* 9.10 (2015). DOI: 10.1002/pssr.201510290 (cited on pages 130, 133, 142–144).

[52] R. C. Williams et al. "Magnetic phase diagram of $La_{2-x}Sr_xCoO_4$ revised using muon-spin relaxation". *Physical Review B* 93.14 (2016). DOI: 10.1103/PhysRevB.93.140406 (cited on pages 131, 132, 142).

[53] N. Yamada, H. Sakai, H. Mori, and T. Ohoyama. "Magnetic properties of ε-Mn_3Ge". *Physica B+C* 149.1 (1988). DOI: 10.1016/0378-4363(88)90258-6 (cited on page 132).

[54] S. M. Gaw, E. C. Andrade, M. Vojta, C. D. Frost, D. T. Adroja, D. Prabhakaran, and A. T. Boothroyd. "Hour-glass magnetic spectrum arising from a striped cluster spin-glass ground state in $La_{1.75}Sr_{0.25}CoO_4$". *Physical Review B* 88.16 (2013). DOI: 10.1103/PhysRevB.88.165121 (cited on pages 132, 140, 142, 158, 162).

[55] P. Babkevich, D. Prabhakaran, C. D. Frost, and A. T. Boothroyd. "Magnetic spectrum of the two-dimensional antiferromagnet La_2CoO_4 studied by inelastic neutron scattering". *Physical Review B* 82.18 (2010). DOI: 10.1103/PhysRevB.82.184425 (cited on pages 133, 134, 142, 144, 162).

[56] S. M. Gaw. "Cooperative Spin Excitations in Quantum Materials Studied by Neutron Spectroscopy". PhD thesis. University of Oxford, 2014 (cited on pages 140, 158).

[57] Y. Drees et al. "Hour-glass magnetic excitations induced by nanoscopic phase separation in cobalt oxides". *Nature Communications* 5.1 (2014). DOI: 10.1038/ncomms6731 (cited on pages 142–144, 158, 162).

[58] H. Guo et al. "Suppression of the outwards-dispersing branches in hour-glass magnetic spectra induced by nanoscale phase separation in $La_{2-x}Sr_xCoO_4$". *Physical Review B* 100.1 (2019). DOI: 10.1103/PhysRevB.100.014411 (cited on pages 142, 144).

[59] M. Fratini, N. Poccia, A. Ricci, G. Campi, M. Burghammer, G. Aeppli, and A. Bianconi. "Scale-free structural organization of oxygen interstitials in La_2CuO_{4+y}". *Nature* 466.7308 (2010). DOI: 10.1038/nature09260 (cited on page 142).

[60] Z. W. Li et al. "Electronic and Magnetic Nano Phase Separation in Cobaltates $La_{2-x}Sr_xCoO_4$". *Journal of Superconductivity and Novel Magnetism* 29.3 (2016). DOI: 10.1007/s10948-015-3302-4 (cited on pages 142, 144).

[61] S. Mugiraneza and A. M. Hallas. "Tutorial: a beginner's guide to interpreting magnetic susceptibility data with the Curie-Weiss law". *Communications Physics* 5.1 (2022). DOI: 10.1038/s42005-022-00853-y (cited on page 146).

[62] N. Qureshi. "Mag2Pol: a program for the analysis of spherical neutron polarimetry, flipping ratio and integrated intensity data". *Journal of Applied Crystallography* 52.1 (2019). DOI: 10.1107/S1600576718016084 (cited on page 148).

[63] R. I. Bewley, R. S. Eccleston, K. A. McEwen, S. M. Hayden, M. T. Dove, S. M. Bennington, J. R. Treadgold, and R. L. S. Coleman. "MERLIN, a new high count rate spectrometer at ISIS". *Physica B: Condensed Matter* 385-386 (2006). DOI: 10.1016/j.physb.2006.05.328 (cited on page 150).

[64] M. Russina and F. Mezei. "First implementation of Repetition Rate Multiplication in neutron spectroscopy". *Nuclear Instruments and Methods in Physics Research Section A: Accelerators, Spectrometers, Detectors and Associated Equipment* 604.3 (2009). DOI: 10.1016/j.nima.2009.03.010 (cited on page 152).

[65] O. Arnold et al. "Mantid—Data analysis and visualization package for neutron scattering and μSR experiments". *Nuclear Instruments and Methods in Physics Research Section A: Accelerators, Spectrometers, Detectors and Associated Equipment* 764 (2014). DOI: 10.1016/j.nima.2014.07.029 (cited on page 153).

[66] R. A. Ewings, A. Buts, M. D. Le, J. van Duijn, I. Bustinduy, and T. G. Perring. "HORACE: Software for the analysis of data from single crystal spectroscopy experiments at time-of-flight neutron instruments". *Nuclear Instruments and Methods in Physics Research Section A: Accelerators, Spectrometers, Detectors and Associated Equipment* 834 (2016). DOI: 10.1016/j.nima.2016.07.036 (cited on page 153).

[67] A. T. Boothroyd, D. Prabhakaran, P. G. Freeman, S. J. S. Lister, M. Enderle, A. Hiess, and J. Kulda. "Spin dynamics in stripe-ordered $La_{5/3}Sr_{1/3}NiO_4$". *Physical Review B* 67.10 (2003). DOI: 10.1103/PhysRevB.67.100407 (cited on page 161).

[68] H. Woo, A. T. Boothroyd, K. Nakajima, T. G. Perring, C. D. Frost, P. G. Freeman, D. Prabhakaran, K. Yamada, and J. M. Tranquada. "Mapping spin-wave dispersions in stripe-ordered $La_{2-x}Sr_xNiO_4$ (x = 0.275, 0.333)". *Physical Review B* 72.6 (2005). DOI: 10.1103/PhysRevB.72.064437 (cited on page 161).

[69] S. M. Tobin, A. T. Boothroyd, and B. Ouladdiaf. "Magnetic and charge order of the cobalt oxide $La_{2-x}Ba_xCoO_4$". *Institut Laue Langevin* (2021). DOI: 10.5291/ILL-DATA.5-41-1101 (cited on page 163).

[70] A. T. Boothroyd, S. M. Tobin, and H. C. Walker. "Exploration of possible spin-charge ordered phases in $La_{2-x}Ba_xCoO_4$ (x = 1/3 and 1/2)". *STFC ISIS Neutron and Muon Source* (2019). DOI: 10.5286/ISIS.E.RB1920499-1 (cited on page 163).

6

The anisotropic magnetism of the cobalt-doped rare earth iron garnet $Lu_3Co_{0.5}Si_{0.5}Fe_4O_{12}$

6.1 Introduction

The rare earth iron garnets (REIGs, where *RE* is a rare earth element) have been a source of scientific interest for decades due to their ferrimagnetic properties [1, 2] and corresponding magnon dynamics [3]. The most famous member of the REIG family, YIG ($Y_3Fe_5O_{12}$), is the cornerstone of advances in spintronic and microwave technology, due to its exceptionally low magnon damping, microwave and magneto-optical properties [3–5]. However, less well known are the magnetic properties and magnetic excitations of other REIGs, such as LuIG. This chapter looks specifically at the doped LuIG, $Lu_3Fe_4Co_{0.5}Si_{0.5}O_{12}$ (abbreviated to LuCoSiIG), and the interactions between Fe and Co ions in this material. Co^{2+} doping is known to alter the magnetic properties of the REIGs, but the ramifications for the spin wave spectrum have not been experimentally investigated before now.

The work in this chapter includes:

- sample characterisation with X-ray diffraction and bulk magnetisation measurements (§ 6.2);
- spin wave dispersion mapped using inelastic neutron scattering data (§ 6.3);
- a linear spin wave theory model of the magnetic excitations of LuCoSiIG.

First I introduce the REIG family of materials (§ 6.1.1), highlighting the effects of doping the REIGs (§ 6.1.2), with $Lu_3Fe_4Co_{0.5}Si_{0.5}O_{12}$ given special attention (§ 6.1.2), as well as their spin wave properties (§ 6.1.3).

6.1.1 Rare earth iron garnets

The REIGs are described by space group $Ia\bar{3}d$ [1, 2]. The unit cell is large: the rare earth ions occupy the dodecahedral 24*c* Wyckoff positions, with eight oxygens providing an approximately cubic environment for each, and the Fe^{3+} ions are on the octahedral 16*a* and tetrahedral 24*d* sites (Figure 6.1). The Fe^{3+} ions magnetically order at $\sim$ 550 K for all undoped iron garnets. It is also possible to construct a rhombohedral unit cell: the body diagonal of the cube is parallel to the rhombohedral **c** axis (in the 'hexagonal' setting), while **a** and **b** are parallel to the face diagonals of the cube. The distribution of magnetic ions among different sites leads to ferrimagnetism with the moments oriented along $\langle 111 \rangle$: for every formula unit, three Fe^{3+} spins point one way and two spins point the other way. Under a magnetic field, the unit cell of the REIG can experience a slight trigonal distortion, e.g. the structure of a YIG sample in 0.1 T $\parallel$ to $[1\ 1\ 1]_{\text{cubic}}$ was refined in the $R\bar{3}$ space group with spins along the $[0\ 0\ 1]_{\text{rhombohedral}}$ direction (i.e. $\parallel$ to the applied magnetic field) [6]. Going forwards, I will stick to the cubic $Ia\bar{3}d$ description of the REIG structure unless otherwise specified.

The rare earth ion is in the 3+ oxidation state, so examples of iron garnets with either non-magnetic (e.g. Y, Lu) or magnetic (e.g. Yb, Tb) rare earth sublattices can be found. The rare earth moments can cant away from the $\langle 111 \rangle$ direction, leading to a magnetic structure described as an 'umbrella' for this sublattice [7, 8], but the Fe^{3+} ions are relatively unperturbed by the rare earth moments and remain oriented along [1 1 1] [1]. For REIG with a magnetic rare earth ion, this is signalled by a characteristic compensation temperature at which the overall bulk magnetisation is zero [1, 2]. For example, $T_{\text{comp}} \sim 8$ K for YbIG [9], $T_{\text{comp}} \sim 290$ K for GdIG [10]. For REIG with a non-magnetic rare earth ion, the temperature dependence of the magnetisation of the Fe sublattices is identical and so there will not be a compensation mechanism. There is strong coupling between the lattice and the magnetism: evidence for this in YIG includes magnetostriction (e.g. [11]) and a Debye frequency that depends on the direction of the applied magnetic field [12].

LuIG is not as well documented as its famous cousin YIG. Nevertheless, there are strong similarities: Y^{3+} has the electronic configuration [Kr] (i.e. an empty $4f$ shell) and Lu^{3+} has [Xe]$4f^{14}$ (i.e. a full $4f$ shell) and so both rare earth ions are non-magnetic with similar chemical properties. Lu is the smallest of the rare earths (the most lanthanide contracted). This has consequences including LuIG having the smallest lattice constant of the REIGs (e.g. reference [13] gives a = 12.283 Å for LuIG compared to a = 12.376 Å for YIG); a greater likelihood of rare earth antisite defects within the material [14], as well as a higher prevalence of oxygen vacancies as compared to YIG [15]. LuIG has $T_C = 530$ K [16], which is lower than $T_C = 560$ K [17], suggesting that the couplings between Fe

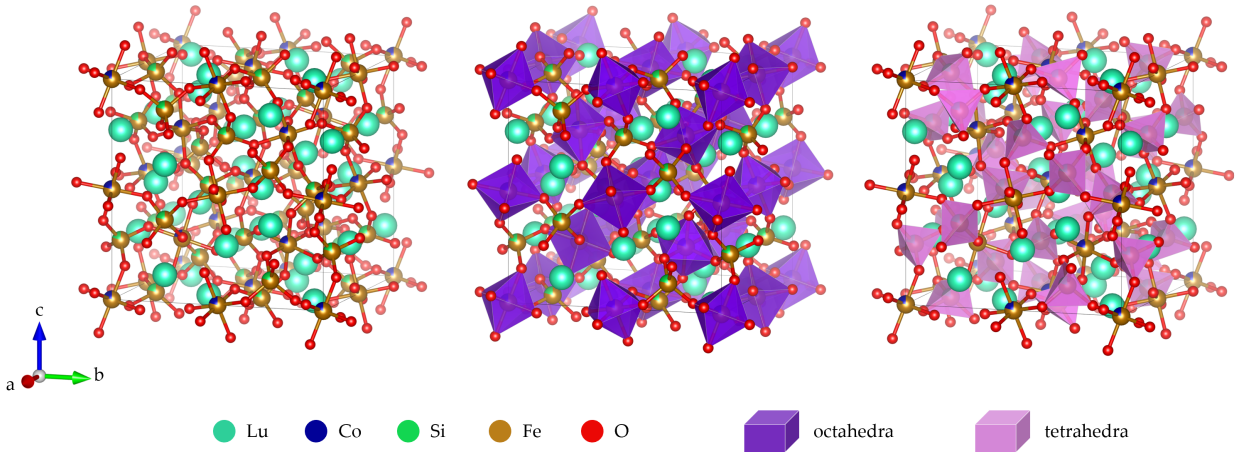

Figure 6.1: Crystal structure of the rare earth iron garnets, described by space group $Ia\bar{3}d$. Here the specific example pictured is $Lu_3Fe_4Co_{0.5}Si_{0.5}O_{12}$. The Fe^{3+} ions are located on both octahedral and tetrahedral sites. Figure prepared using VESTA [19].

ions are slightly weaker in LuIG than YIG. Most notably, LuIG possesses very long-lived magnons, like YIG. The magnon damping coefficent of a 5.3 nm thick LuIG film is $11.1(9)\times 10^{-4}$, which is certainly competitive with the coefficient of 38×10^{-4} that was measured in a 4 nm thick YIG film [18] (a lower damping coefficient means less damping and therefore longer-lived spin waves).

6.1.2 Doping of rare earth iron garnets

Early samples of REIG often contained impurities [1]. These days, deliberate doping of REIG is fairly common, especially with thin film samples grown epitaxially on substrates (e.g. [20–23]). The primary goal of doping the REIGs is to tune their magnetic properties, which can be achieved by doping on the a, d or c sites due to the differing ionic radii and local crystal field environments. Here I focus on REIG with Co^{2+} as the dopant, and examples of doped LuIG.

Doping with Co^{2+} ions

For Co^{2+} to be present, there must be a 4+ ion present in an equal amount for the charge of the REIG to be balanced, else non-magnetic Co^{3+} will be present as well. Co^{3+} has minimal impact on the anisotropy compared to Co^{2+} because $S = 0$ for Co^{3+}. For example, in reference [24], the Si^{4+} stabilises the Co^{2+} oxidation state, but the dopants occupy different sites, with Si^{4+} preferring the tetrahedral d sites and Co^{2+} the octahedral a sites. In this octahedral environment, Co^{2+} is in the high spin state $S = 3/2$ [25, 26]. Magnetic Co^{2+} will change the degree of ferrimagnetism present as the magnetic moment of Co^{2+} ($\approx 3.7\ \mu_B$) is less than that of Fe^{3+} ($\approx 5\ \mu_B$). Non-magnetic dopants on Fe sites can also have this effect. In general, Co^{2+} doping reduces T_C and saturisation

magnetisation, but coercivity increases with increased Co doping due to increased anisotropy [27–29]. While non-magnetic dopants such as Si^{4+} and Ge^{4+} replace Fe^{3+} on the tetrahedral *d* sites, an ion such as Ce^{4+} is large enough to substitute for the rare earth ion on the dodecahedral *c* site. This means that a Ce^{4+} and Co^{2+} doped REIG will have a higher T_C and saturisation magnetisation than a Ge^{4+} and Co^{2+} doped REIG, for example [28].

Undoped YIG and LuIG have very little magnetic anisotropy, as Fe^{3+} has $S = 5/2$ but no orbital angular momentum $L = 0$. The first experiments on Co-doped YIG (references [25, 30, 31][1]) focused on characterising the magnetocrystalline anisotropy. Intriguingly, the anisotropy in the Co-doped YIG showed great temperature dependence, much greater than the temperature dependence of the anisotropy in undoped YIG. Strongly temperature-dependent magnetic anisotropy is observed in other REIG where the RE itself is magnetic. This lead to the conclusion in reference [25] that Co^{2+} on the octahedral sites "looks like a rare earth". The anisotropy can also be seen in *M*–*H* curves at different temperatures, for example, in reference [32] the size of the hysteresis loop of polycrystalline $Sm_3Fe_{5-x}Co_xO_{12}$ is nearly independent of x at room temperature, but increases strongly with x at 5 K.

Of course, with all this anisotropy floating about, there is the possibility of spin canting as seen in REIG such as YbIG [9] (the so-called "double umbrella structure" involving both Fe^{3+} and Yb^{3+} moments canting away from $\langle 111 \rangle$). However, the mechanism behind the Co^{2+}-led anisotropy is different: it is the spin-orbit interaction, rather than the crystal field and anisotropic exchange[2] for REIG where the RE is magnetic. The theoretical work in reference [11] indicated that the canted structure affects the anisotropy constants K_i in the case of the latter, whereas canting does not impact the macroscopic anisotropy for Co-doped REIG and a collinear structure is sufficient.

Co^{2+} induces a tetragonal distortion in the oxygen octahedra [34]. This is the mechanism through which magnetocrystalline anisotropy is introduced. This leads to a number of interesting effects including a large increase in the magnetostriction constant for a field along the $\langle 100 \rangle$ direction for a Co-doped REIG compared to an undoped REIG [11]. The more Co^{2+}, the more anisotropy there is [11]. Eventually the combination of increased Co^{2+} on the octahedral *a* site and increased non-magnetic dopant on the tetrahedral *d* site is sufficient to ruin the ferrimagnetism of the Fe^{3+} ions [28].

However, an 'exchange isolation' affect has been proposed for Co^{2+} doped garnets and spinels,

[1] If a cobalt-doped REIG was good enough for Goodenough [30], then it's definitely good enough for me!

[2] The Heisenberg exchange interaction, even if it is anisotropic, only cares about the angles between neighbouring spins, not spins vs. the whole lattice [33].

where the charge-balancing 4+ cation clusters around Co^{2+} sites, effectively throttling the magnetocrystalline anisotropy [34–36]. This has been observed in doped YIGs $Y_3Fe_{5-2x}Co_xSi_xO_{12}$ [30] and
$(Y_{1.5-2v}Gd_{1.5}Ca_{2v})[Fe_{2-x}Co_x](Fe_{3-x-v}Si_xV_v)O_{12}$ for $x \approx 0.03$ and $0.01 < v < 1.2$ [36] i.e. for small dopant concentrations of Co^{2+} with or without a lot of extra non-magnetic dopants (Ca^{2+} and V^{5+}).

In thin film samples of $Y_{0.75}Ge_{0.25}Fe_{4.75}Co_{0.25}O_{12}$, the anisotropy introduced by Co^{2+} has been sufficient to change the easy axis of the magnetic moments from [1 1 1] to [1 0 0] upon cooling in a magnetic field oriented along [1 0 0] to favour one single [1 0 0] easy axis (rather than an equal distribution of [1 0 0], [0 1 0], and [0 0 1] easy axis anisotropy, which is symmetric about the prevailing [1 1 1] direction of the Fe^{3+} moments) [28]. When annealed, the easy axis shifts again to the [1 1 0] direction, with this being attributed to stress-induced anisotropy of the film as it is grown on a substrate of [1 1 0] $Gd_3Ga_5O_{12}$ [28]. A similar effect is the spin reorientation transition or phases as described in reference [37] for polycrystalline $Y_3Fe_{5-2x}Co_xGe_xO_{12}$ in zero field: some regions have a magnetic easy axis of $\langle 0\,0\,1 \rangle$, others have $\langle 1\,1\,1 \rangle$.

Finally, the properties contributing to the excitement around the REIGs for spintronic purposes can also be affected by Co^{2+} doping. Doping with Co^{2+} improves the magneto-optical properties of REIG, for example, enhancement of the Faraday effect in $Gd_3Fe_{5-2x}Co_xGe_xO_{12}$ attributed to the crystal field excitation of Co^{2+} [38]. Increasing anisotropy provides a mechanism to optically address Fe spins in $Y_2CaFe_{3.9}Co_{0.1}GeO_{12}$ [39] and $(YCa)_3(FeCoGe)_5O_{12}$ [40], whereby exciting Co ions with polarised light changes the local anisotropy and results in switching of the magnetisation between $\langle 1\,1\,1 \rangle$ directions. The spin wave stiffness[3] (a key parameter in micromagnetic simulations and spintronic development) and other dispersion characteristics are also influenced by the overall anisotropy, which in thin-film devices is a combination of shape and magnetocrystalline anisotropies [41, 42].

There is also evidence that the Debye frequency of YIG is dependent on the direction of the applied magnetic field [12] . This is important for the spin Seebeck effect, which relies on magnon-lattice coupling. Adding anisotropy through Co doping may also affect this.

Doping of LuIG

Several interesting examples of doped LuIGs have been studied. $Lu_2BiFe_4GaO_{12}$ features some Bi substituted onto the rare earth site and some Ga^{3+} on the Fe^{3+} sites. Note that the majority

[3] The spin wave stiffness D is defined by approximating the lowest energy magnon mode as a parabola $E = a + Dk^2$

($\sim$ 90 %) of the non-magnetic dopant Ga^{3+} occupies the tetrahedral *d* site, thereby increasing the compensation mechanism. This material exhibits the spin Seebeck effect[4] [22]. This effect is particularly enhanced in Ga-doped LuIG compared to YIG: the increased compensation mechanism affects the low energy magnon dispersion, which is most important for the spins mobilised thermally [22]. In a very similar material, $Lu_2BiFe_{3.4}Ga_{1.6}O_{12}$, investigating the coupling between magnetism and the lattice via an optical pump-probe method revealed coherent oscillations between magnons and phonons [43], as well as the magneto-optical Faraday effect.

In a film of LuIG with Y and Bi substituted onto some dodecahedral *c* sites it is possible to switch the spins via a photomagnetic effect [21]. This is very applicable to spintronic memory reading and writing. When this Lu-Y-Bi IG is combined with Ga doping on magnetic sites, this leads to dilution of the Fe sublattices and spin canting away from the [1 1 1] direction through the inverse Faraday effect[5] [44].

Doping of LuIG with Co^{2+} ions

LuCoSiIG (= $Lu_3Fe_4Co_{0.5}Si_{0.5}O_{12}$), the compound I investigated, is a specific example of a doped LuIG with increased anisotropy due to the Co^{2+} substitution [23]. The samples in reference [23] were thin films of $Lu_3Fe_{5-2x}Co_xSi_xO_{12}$ grown epitaxially on $Y_3Al_5O_{12}$ [1 1 1] substrate. LuCoSiIG has a higher coercivity ($H_C = 640$ Oe at 10 K) and lower saturisation magnetisation ($M_S = 27.4$ emu cm^{-2} at 10 K) than undoped LuIG ($H_C = 40$ Oe and $M_S = 84.6$ emu cm^{-2}) [23]. Inherent in this Co^{2+} doped LuIG is a degree of magnetic disorder (in addition to Lu antisite defects) and frustrated exchange interactions, leading to a magnetic transition at 200 K and an additional cluster spin glass phase below 190 K [23]. This gives a 'spin memory' effect when the material is exposed to an external magnetic field. At very low temperatures, the spins relax due to the temperature dependence of the spin wave damping, leading to excitations dominating over the freezing mechanism [23]. Whilst this study involved a thin film sample, the results are intriguing and may have implications for the spin wave dynamics.

6.1.3 Spin waves of rare earth iron garnets

The rare earth garnets are yet to be explored fully using neutron techniques. In particular, for this family of materials, few reports exist of magnon dispersion obtained using inelastic neutron

[4] The spin Seebeck effect, also known as the *inverse spin Hall effect*, refers to a spin current being driven (a 'spin voltage' of sorts) by a thermal gradient.

[5] The Faraday effect induces a circular polarisation in linearly-polarised light passing through a magnetic field, e.g. in a ferromagnetic semiconductor. The inverse Faraday effect uses polarised light to shift the direction of magnetisation in a material, $\mathbf{M} \propto |\mathbf{E}(\omega) \times \mathbf{E}^*(\omega)|$.

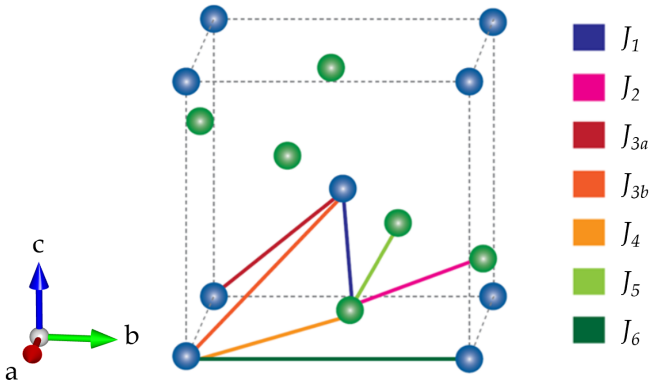

Figure 6.2: Exchange interactions in the REIG, with non-magnetic RE. Fe^{3+} octahedral *a* sites are in blue and tetrahedral *d* sites are in green. Here J_{3a} is along the [1 1 1] direction and J_{3b} is along the [-1 1 1] direction. Figure adapted from reference [4], under CC BY 4.0.

scattering. Knowledge of the spin waves of the REIGs is key as the magnons are involved in phenomena such as the spin Seebeck effect [45]. Of particular interest are the lowest energy magnon modes, which can be thermally populated at temperatures around room temperature.

The many spin wave modes of YIG have been mapped and are documented in references [4, 12] (see Figure 6.4). The magnetic interactions between effective spins $\mathbf{S}_i$ on the Fe ions were modelled with a Heisenberg Hamiltonian of the form

$$\mathcal{H} = \sum_{i,j} J_{ij} \mathbf{S}_i \cdot \mathbf{S}_j - \sum_i D \left(S_i^z\right)^2, \tag{6.1}$$

and the spin wave spectra calculated using linear spin-wave theory (LSWT) implemented with SpinW [46]. There is some variation in the number of exchange parameters required to model the spectrum up to 100 meV. In reference [4] a total of seven exchange parameters for the interactions between Fe^{3+} ions were fitted; on the other hand, reference [6] only fitted three. The additional parameters in [4] compared to [6] come from considering not just nearest neighbours on the various sublattices (J_1, J_2, J_3), but next-nearest neighbours as well (J_4, J_5, J_6), in addition to different exchange path symmetries (i.e. J_{3a} cf. J_{3b}) – see Figure 6.2. For ions located on octahedral sites, there are two exchange paths to consider for nearest-octahedral site neighbours, J_{3a} with 32 symmetry along the $\langle 1\ 1\ 1 \rangle$ diagonals of the unit cell, and J_{3b} with two-fold symmetry along the $\langle -1\ 1\ 1 \rangle$ diagonals. This difference in symmetry is shown in Figure 6.3.

For YIG, the linear spin wave theory fit was not improved by the addition of an anisotropy parameter D in reference [4] – any anisotropy gap in the spin wave spectrum was too small to be

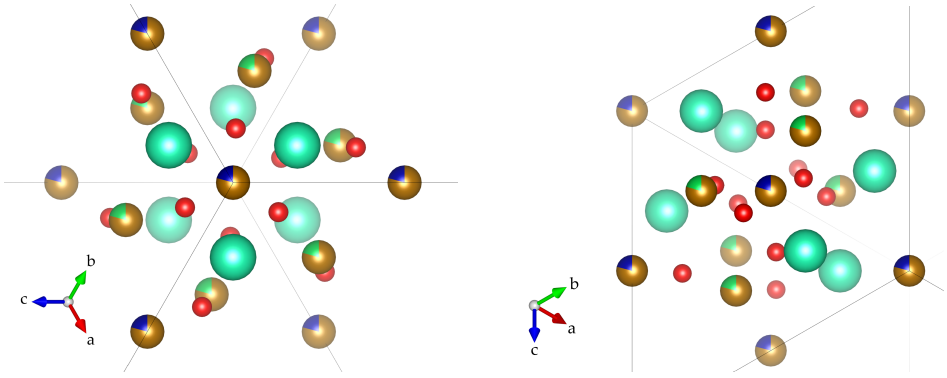

Figure 6.3: Different exchange path symmetries for nearest-octahedral-site neighbour interaction: a) 32 point group symmetry along the $\langle 1\ 1\ 1 \rangle$ diagonals, the direction of the exchange path for J_{3a}, b) two fold symmetry along the $\langle -1\ 1\ 1 \rangle$ diagonals, the direction of the exchange path for J_{3b}. LuCoSiIG is pictured. Figure prepared using VESTA [19]. The colour code for the atoms is the same as in Figure6.1.

resolved. In reference [6], the Zeeman energy gap[6] was estimated to be 0.9 $\pm$0.5 μeV. For another IG, the quantum gap (modelled as an easy axis anisotropy) due to magnetic Fe^{3+} alone was very small at 0.136 meV [47]. This is likely an upper bound for the anisotropy due to Fe^{3+}.

The chirality or polarisation of the spin waves is important for spin current generation in the REIG. Figure 6.5 illustrates the polarisation of spin wave modes for different types of magnetic order. In a ferromagnet, all spins are aligned and precess in the same direction, so there is only one polarisation. In an antiferromagnet, the spin wave mode is degenerate and both polarisations are present in equal measure, so there is no net spin current. In a ferrimagnet, the degeneracy is lifted, with the acoustic and optical modes having opposite polarisations. The spins in the optical mode are slightly tilted away from the [111] direction – the higher energy of the optical mode is a manifestation of the fact the spins aren't totally antiparallel [12, 48]. This is represented diagrammatically in Figure 6.5. Destructive interference between the two lowest energy magnons should be minimised for applications involving the spin Seebeck effect, for example. The spin Seebeck effect reduces in YIG at temperatures above 100 K, which is attributed to magnon-phonon interactions but also magnon broadening and the changing energy gap between the acoustic and optical spin waves, which is comparable to thermal energy scales [6, 12, 45, 48, 49]. In GdIG, the spin Seebeck voltage changes sign twice with temperature due to the varying strength of the magnetic sublattices and also the reduced gap between acoustic and optical modes [50]. The polarisation of the magnons may be affected by increasing magnetocrystalline anisotropy [12], as this would increase the canting of the spins away from the principal [111] direction in the optical

[6]The sample of YIG was in a magnetic field of 0.1 T $\parallel$ [111] in references [6, 12].

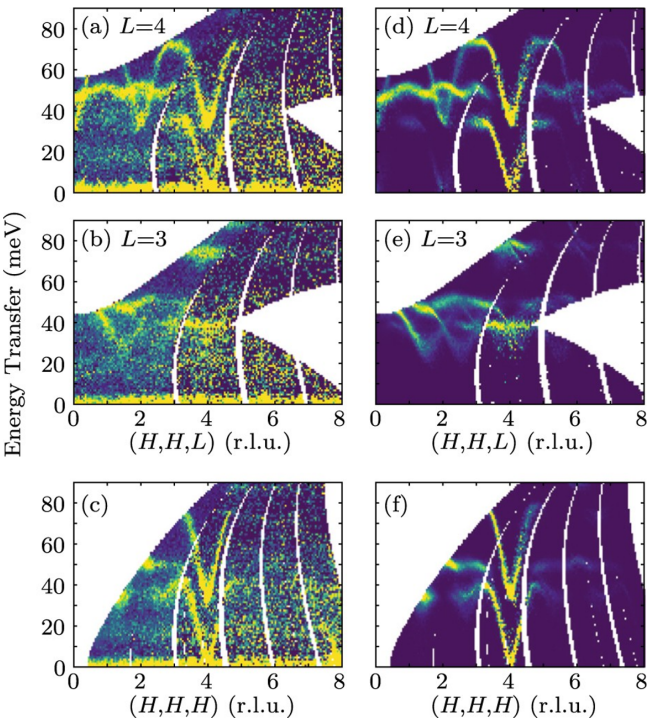

Figure 6.4: Spin waves of YIG measured with inelastic neutron scattering. Left panels: INS spectra measured on MAPS at ISIS. Right panels: fitted spin wave spectra (SpinW). Figure reproduced from reference [4], under CC BY 4.0.

mode, for example. Hence characterising the low energy magnons at different temperatures is important for evaluating a REIG's suitability for spintronic and magnonic purposes.

YbIG is another example of a REIG studied by inelastic neutron scattering [9]. While the spin waves are broadly similar to those of YIG, there is hybridisation between the crystal field excitations of Yb^{3+} and the magnons. A small energy gap $\sim$ 0.2 meV is seen in the spin wave spectrum. This originates from the anisotropic exchange coupling between the Yb $4f$ and Fe $3d$ electrons. This is much weaker than the Fe–Fe exchange coupling, with exchange parameters on the order of 0.2 meV. A different crystal field effect might be present in the spin wave spectrum of LuCoSiIG as the Co^{2+} resides in an octahedral crystal field. The ground state may be split by an axial distortion and then again by the smaller spin-orbit coupling (see the chapter on $La_{2-x}Ba_xCoO_4$ for more discussion on this).

At the present, no magnetic excitation dispersion data has been reported in the literature for a doped REIG such as LuCoSiIG. Key questions pertaining to the spin waves of LuCoSiIG:

- Is the Fe–Fe exchange perturbed by the presence of Co^{2+} (and non-magnetic Si^{4+})?
- Does the Co^{2+} ion introduce an anisotropy gap?

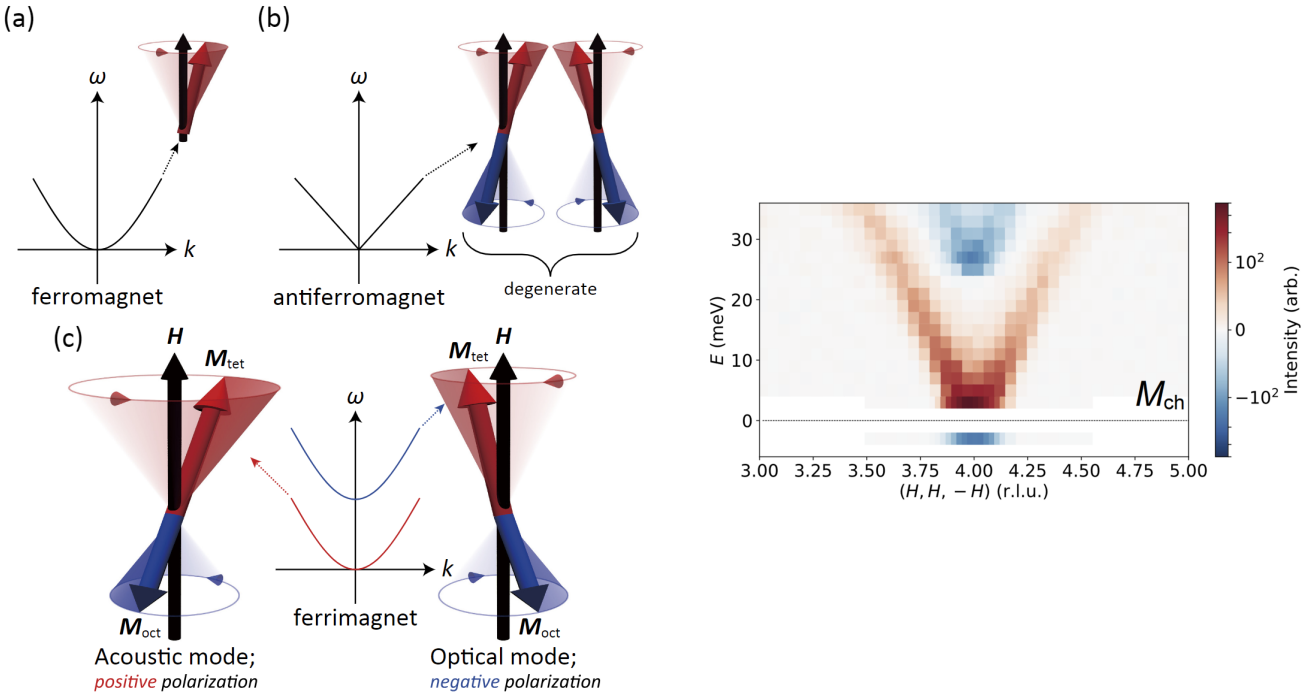

Figure 6.5: (Left) Spin polarised magnons in ferrimagnetic rare earth iron garnet. For the acoustic magnon mode, the spins on the octahedral and tetrahedral sublattices remain antiparallel. In the higher energy optical magnon mode, the spins have a finite cant away from [111]. The superposition of different amplitudes of acoustic and optical magnons is what generates a spin current. **(Right)** The chiral component of the lowest two spin wave modes of YIG has been measured using polarised neutron scattering. This figure is reproduced from reference [48] with permission. Copyright American Physical Society (2020).

- Is the linearity of the lowest acoustic dispersion affected by the change in magnetic compensation?
- What is the temperature dependence of magnon broadening, and the gap between the acoustic and optical modes?
- Are there signals of disorder/spin glass state of Co^{2+} moments?

6.2 $Lu_3Fe_4Co_{0.5}Si_{0.5}O_{12}$ sample and initial characterisation

A large single crystal of LuCoSiIG (= $Lu_3Fe_4Co_{0.5}Si_{0.5}O_{12}$) was grown by Dr Dharmalingam Prabhakaran via the optical floating zone method. The synthesis procedure was as follows:

1. A stoichiometric powder of $Lu_3Co_{0.5}Si_{0.5}Fe_4O_{12}$ was prepared by the solid-state reaction technique using high purity (>99.99%) starting chemicals of Lu_2O_3, Co_3O_4, SiO_2 and Fe_2O_3.
2. The mixed powder was sintered at 1200°C in air for 72 hours with intermediate grinding.

3. After confirming the single-phase purity of the sintered powder, a cylindrical rod of diameter 8 mm and 10 cm length was sintered at 1300°C for 12 hours.

4. A single crystal of $Lu_3Co_{0.5}Si_{0.5}Fe_4O_{12}$ was grown using the travelling solvent floating zone method. A cylindrical disc of 8 mm diameter and 2 mm thickness was used as solvent during growth. The feed and seed rods were rotated at 25 rpm in opposite directions to mix the melt and the crystal was grown at the rate of 0.25 mm/hour in oxygen atmosphere.

The sample is pictured in Figure 6.6. With a mass of 4.5 g, it was of a suitable size for inelastic neutron scattering.

Figure 6.6: The single crystal sample of LuCoSiIG used for inelastic neutron scattering measurements. The [1 -1 0] axis is approximately parallel to the ruler.

It is of excellent crystalline quality as evidenced by the XRD precession images (Figure 6.7) and the Laue diffraction patterns shown in Figure 6.8. The whole crystal was used for the x-ray Laue, while a smaller piece was used for neutron Laue on ILL's OrientExpress, and an even smaller piece for the lab XRD. The single crystal XRD was performed using a Bruker D8 Venture 4-circle κ diffractometer with a Ag source ($K_\alpha = 0.56$ Å). A preliminary refinement found that the symmetry of the crystal structure is indeed described by the $Ia\bar{3}d$ space group with $a = 12.279$ Å at $T \approx 300\,K$.

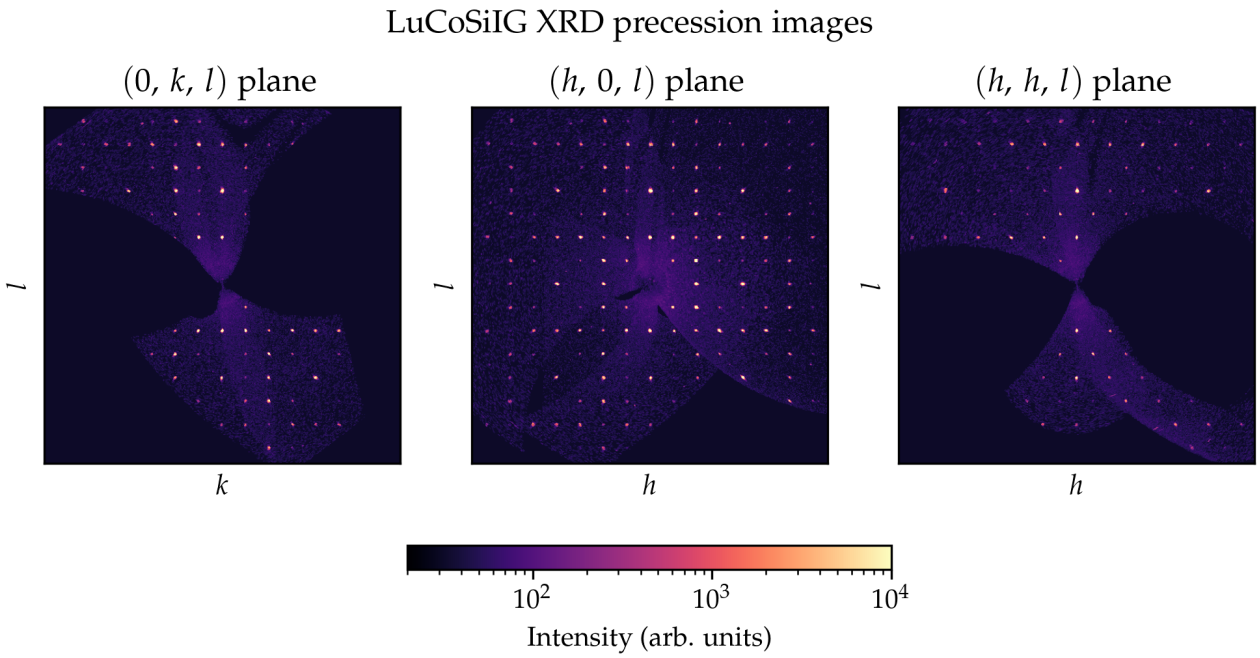

Figure 6.7: LuCoSiIG XRD precession images showing different planes in reciprocal space. Image data read using the FABIO Python package [51].

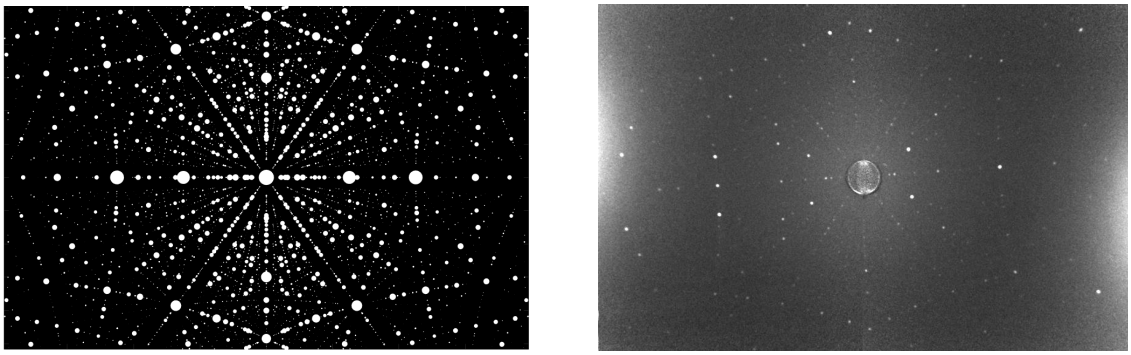

X-ray beam ∥ [1 -1 0], [0 0 1] vertical. Left: simulation, right: data.

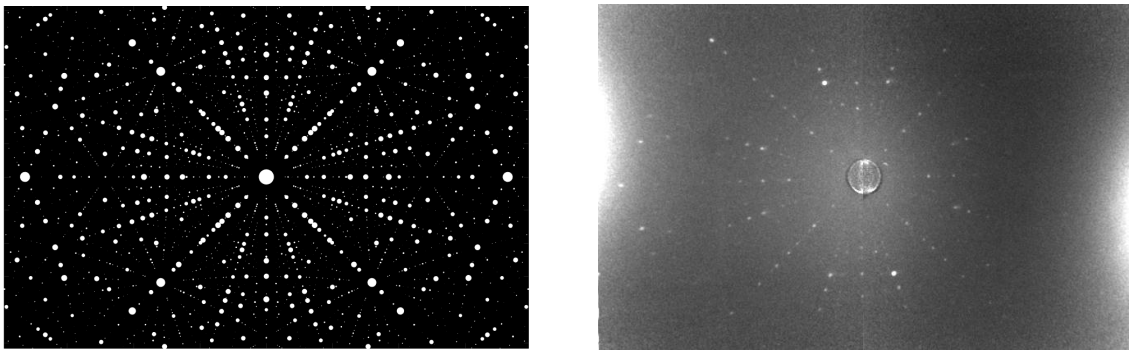

X-ray beam ∥ [0 0 1], [1 -1 0] vertical. Left: simulation, right: data.

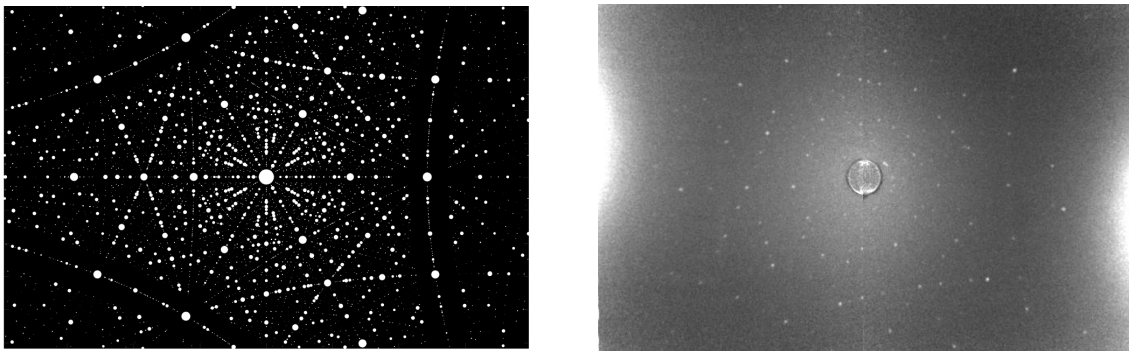

X-ray beam ∥ [1 1 -1], [1 -1 0] vertical. Left: simulation, right: data.

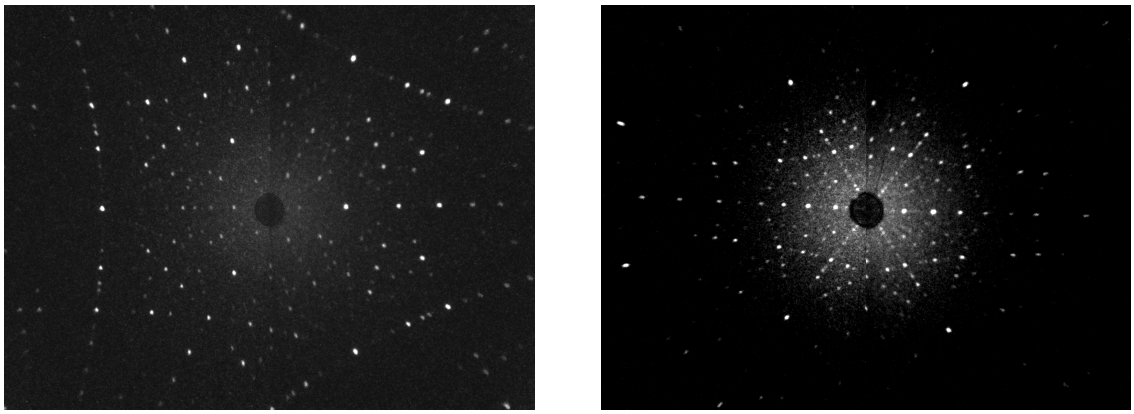

Left: neutron beam ∥ [1 1 1], [1 -1 0] vertical. Right: neutron beam ∥ [1 -1 0], [0 0 1] vertical.

Figure 6.8: X-ray and neutron Laue diffraction of LuCoSiIG. Neutron Laue diffraction performed on ILL OrientExpress.

6.2.1 Magnetisation measurements

Magnetisation measurements were performed on a small piece of the LuCoSiIG single crystal (Figure 6.6) using a SQUID (Quantum Design MPMS3) in VSM mode. Measurements were taken for two different orientations of the sample: with the applied field $H \parallel [110]$ in the temperature range 15 K – 350 K, and $H \parallel [001]$ in the temperature range 15 K – 600 K. For the low temperature measurements (15 K – 350 K) the sample was attached to a quartz paddle with GE varnish (and then placed inside a drinking straw for security). The high temperature measurements needed the oven insert, with the sample wrapped in copper foil.

Magnetisation as a function of temperature

The 'big picture' of magnetisation versus temperature is shown in Figure 6.9. As temperature decreases from 600 K, the magnetisation undergoes a step-change at $T_C \approx 480\,K$. This transition looks very ferro(i)magnetic and is due to the ordering of the Fe^{3+} moments. However, this T_C is low for a REIG (typical $T_C \approx 540\,\text{K} - 600\,\text{K}$). This is likely explained by the lower density of Fe^{3+} moments in LuCoSiIG compared to LuIG/YIG. The T_C in my data is considerably higher than the transition temperature (≈ 320 K) measured for thin film LuCoSiIG with $H \parallel [111]$ [23]; however, the thin film sample also showed a more gradual transition (M vs. T not as steep) and evidence of glassy/short-range order. A REIG with the same level of Co^{2+} doping, polycrystalline $Y_3Fe_4Co_{0.5}Ge_{0.5}O_{12}$, has a very similar $T_C \approx 450$ K [37].

Due to the necessary change in sample holder, a complete continuous sweep from 15 K to 600 K was not possible. This means the datasets have different backgrounds and also slightly different sample orientations – while the data below are all from the same piece of crystal, a realistic estimate of the uncertainty in the orientation (placing the small crystal in a slightly-less-small puddle of goop with tweezers) is 10°. Furthermore, the sample was not cooled down from the paramagnetic phase for each measurement, as that required a temperature of 550 K to be reached (not possible with the sample mounted on the quartz probe).

Previously published data for powder samples of YIG [52, 53] and LuIG [2] showed a smoothly increasing magnetisation as the temperature decreased: the magnetisation follows an approximately Landau order parameter type curve, and by 5 K has approached the theoretical value of $M_S = 5\ \mu_B$ f.u.$^{-1}$ for ferrimagnetic order of Fe^{3+} moments distributed among octahedral and tetrahedral sites [2, 53]. In contrast, the magnetisation of single crystal LuCoSiIG seems to plateau in the region $\sim$ 350 K – 450 K (the lower bound estimation is from the low temperature 'quartz'

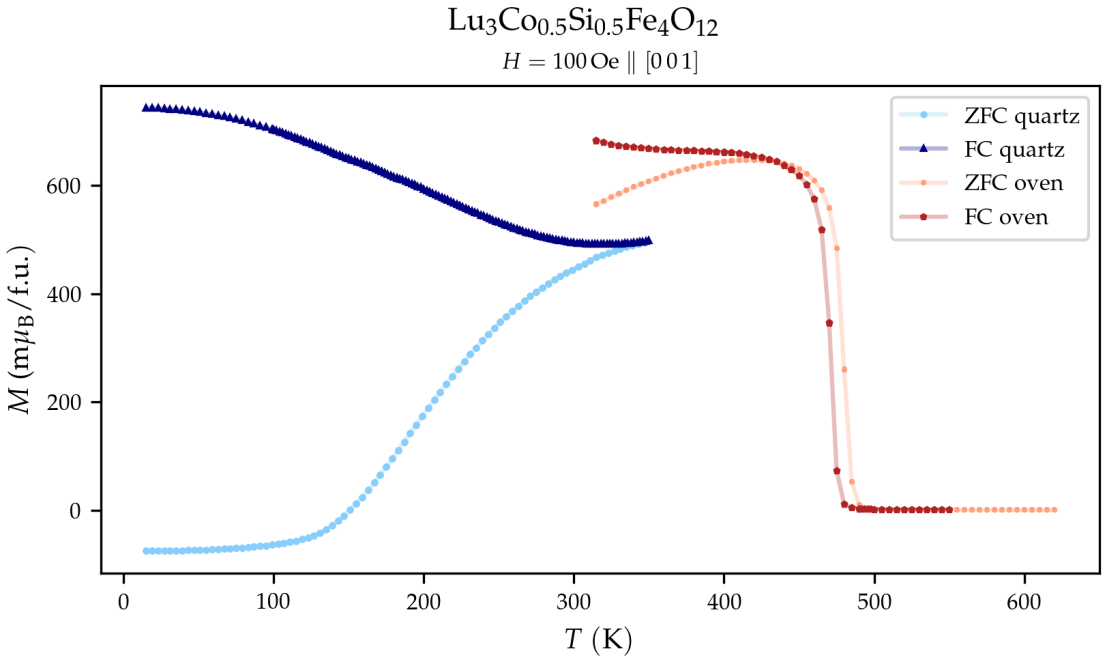

Figure 6.9: Temperature-dependent magnetisation of $Lu_3Fe_4Co_{0.5}Si_{0.5}O_{12}$ with $H = 100\,\mathrm{Oe} \parallel [0\,0\,1]$ from 15 K to 600 K. The low temperature data ($15\,\mathrm{K} < T < 350\,\mathrm{K}$) were taken with the sample mounted on a quartz paddle, while the high temperature data ($315\,\mathrm{K} < T < 600\,\mathrm{K}$) were taken using the 'oven' insert with the sample wrapped in copper foil.

data and the upper bound estimation is from the high temperature 'oven' data), before a splitting occurs between the ZFC and FC curves. No magnetic compensation (magnetisation decreasing to zero before increasing again) was seen, nor did we expect one, as LuCoSiIG is a less compensated ferrimagnet than either LuIG (no compensation but has more Fe^{3+} and so more 'balanced' sublattices) or a REIG with magnetic RE (the Fe^{3+} moments are compensated by the RE moments at a $T_{\mathrm{comp}} < T_C$).

Only a small bifurcation between the ZFC-FC curves was observed for YIG at low temperatures: the ZFC magnetisation was around 62% of the FC magnetisation at 10 K [52], with both measurements taken in a field of 200 Oe. In LuCoSiIG, the split at 15 K is larger, and anisotropic: the ZFC magnetisation is about 20 % of the FC magnetisation for $H \parallel [110]$, the ZFC magnetisation is close to zero and the gap between ZFC and FC is larger still for $H \parallel [001]$ (Figure 6.10). This low temperature section of the curve is more akin to the behaviour of a REIG with magnetic RE below T_{comp} (e.g. TbIG [52, 53]) and is direct evidence of the magnetocrystalline anisotropy originating from the Co doping. However, previous measurements on powder samples would have lost some information on the anisotropy due to directional averaging.

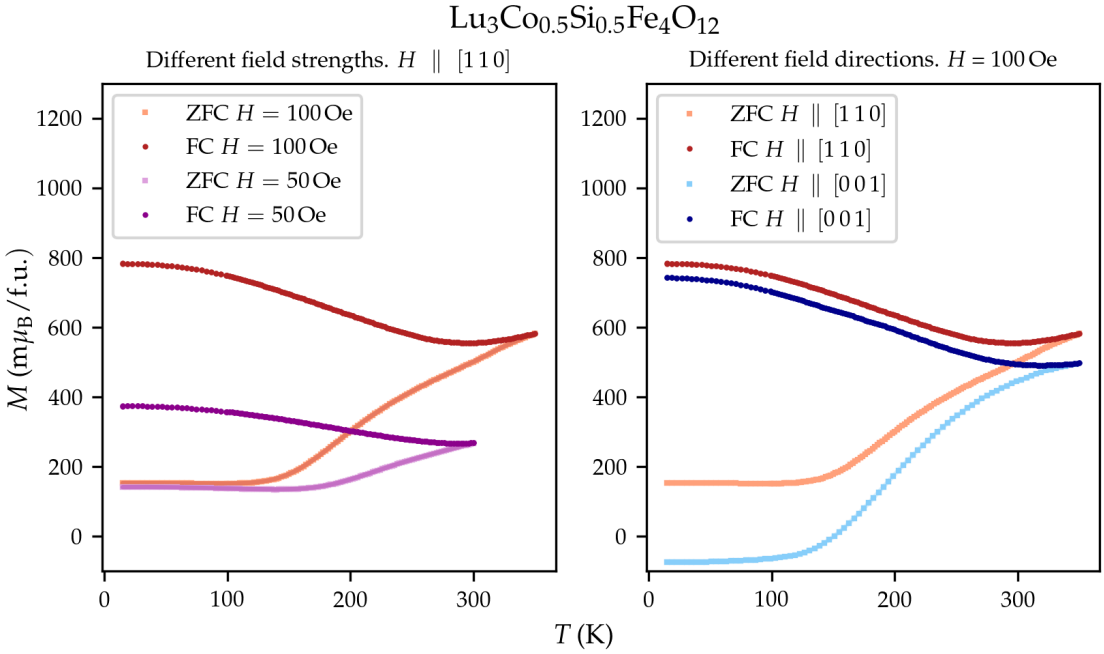

Figure 6.10: Temperature dependence of magnetisation of $Lu_3Fe_4Co_{0.5}Si_{0.5}O_{12}$ for different field strengths and directions. Left: a lower applied field strength lowers the temperature at which the ZFC and FC magnetisation curves split. Right: the size of the split between ZFC–FC curves at low temperatures depends strongly on the direction of the applied field. This indicates the magnetism is anisotropic. NB: the sample was slightly off-centre for the $H \parallel [001]$, $H = 100$ Oe data.

A fit of the inverse susceptibility data according to the modified Curie-Weiss law [54]

$$\chi^{-1} = \frac{T - \theta_{CW}}{\chi_0 \cdot (T - \theta_{CW}) + C} \tag{6.2}$$

was made in the temperature range 495 K to 550 K and is shown in Figure 6.11. The fitted parameters are given in Table 6.1, with μ_{eff} calculated according to Equation 2.40.

Table 6.1: Fitted parameters of a modified Curie-Weiss law (Equation 6.2) for $Lu_3Fe_4Co_{0.5}Si_{0.5}O_{12}$ magnetisation data.

χ_0 (emu mol^{-1} Oe^{-1})	θ_{CW} (K)	C (K^{-1} emu mol^{-1} Oe^{-1})	$\mu_{eff.}$ (μ_B/f.u.)
1.115×10^{-2}	490	1.164	3.05

The saturated magnetic moment per formula unit can be estimated from the saturated moments of the Fe^{3+} and Co^{2+} ions, and the nominal occupancies on the octahedral and tetrahedral sites ($N_{Co^{2+}\ oct} = 4$, $N_{Fe^{3+}\ oct} = 12$, $N_{Fe^{3+}\ tet} = 20$). There are eight formula units per unit cell in the $Ia\bar{3}d$

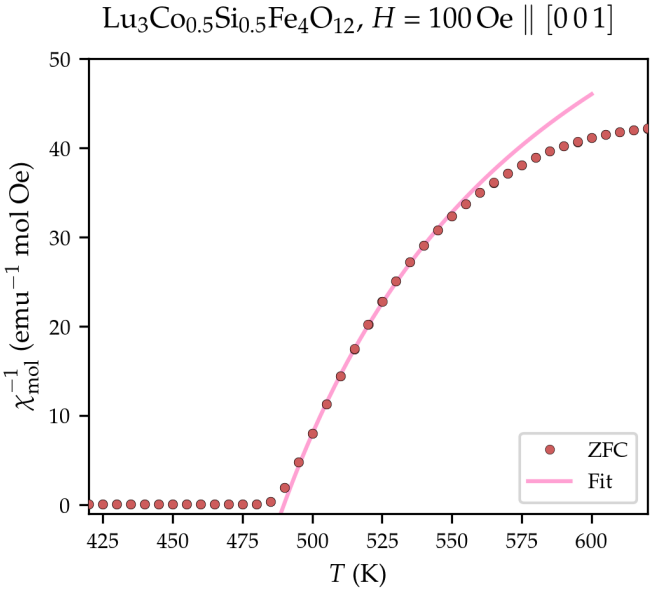

Figure 6.11: Modified Curie-Weiss law fit of $Lu_3Fe_4Co_{0.5}Si_{0.5}O_{12}$ magnetisation data.

space group.

$$\mu_{M_S} = \left[-\left(N_{\mathrm{Co}^{2+}\ \mathrm{oct}} \times 3.7\,\mu_\mathrm{B} + N_{\mathrm{Fe}^{3+}\ \mathrm{oct}} \times 5\,\mu_\mathrm{B}\right) + N_{\mathrm{Fe}^{3+}\ \mathrm{tet}} \times 5\,\mu_\mathrm{B} \right] \times \frac{1}{8} = 3.15\,\mu_\mathrm{B}\ \mathrm{/f.u.} \tag{6.3}$$

The theoretical $\mu_{M_S} = 3.15\,\mu_\mathrm{B}$/f.u. agrees well with $\mu_\mathrm{eff} = 3.05\,\mu_\mathrm{B}$/f.u. from the inverse susceptibility fit. θ_CW = 490 K is within 15 K of the observed ferrimagnetic transition temperature. As LuCoSiIG is a ferrimagnet, rather than an (anti)ferromagnet, the application of the Curie-Weiss law is not so clear cut, especially when there are different magnetic species on each sublattice. In this case, the model provides a good fit as most (90 %) of the magnetic ions in the unit cell are Fe^{3+}, which order at $T_C \approx 480$ K.

Magnetisation as a function of field

Measurements of magnetisation as a function of field were taken at two different temperatures (15 K and 350 K) and two different crystal orientations ($H \parallel [110]$ and $H \parallel [001]$). From zero field, the field was increased to $+H$, before being swept down to $-H$ and then back up to $+H$ again. The M vs. H curves again show clear evidence of temperature-dependent anisotropy (Figure 6.12). At 350 K, the differences between the different crystal orientations are small. The 350 K data displays no hysteresis in either field direction and the saturated magnetisation M_S is nearly identical for both field directions. A large hysteresis loop opens up at low temperatures, with a larger saturated magnetisation for the field along [0 0 1] compared to the field along [1 1 0]. Naturally, it would be

great to have done these measurements for $H \parallel [111]$ too, as this is the easy axis for the iron garnet family.

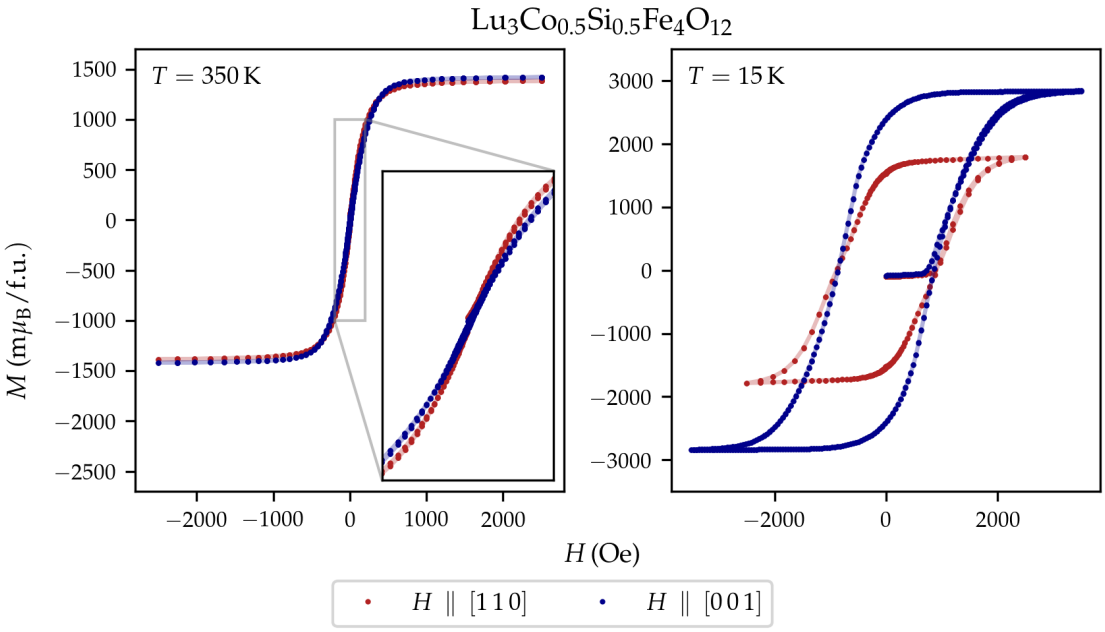

Figure 6.12: Field-dependent magnetisation of $Lu_3Fe_4Co_{0.5}Si_{0.5}O_{12}$. The 350 K data displays no hysteresis in either field direction and the saturated magnetisation is nearly identical for both field directions. A large hysteresis loop opens up at low temperatures, with a larger saturated magnetisation for the field along [0 0 1] compared to the field along [1 1 0].

The M vs. H data for this bulk measurement of LuCoSiIG are qualitatively consistent with the thin film measurement in reference [23], which showed that the size of the hysteresis loop increases with Co doping. Key quantities such as coercivity H_C, saturated magnetisation M_S and remanent magnetisation M_R are given in Table 6.2 for comparison. The poster crystal for the REIG, YIG, has a larger $M_S = 2.313\,\mu_B$ f.u.$^{-1}$ at room temperature than TbIG $M_S = 0.424\,\mu_B$ f.u.$^{-1}$. My crystal of LuCoSiIG (although measured at the slightly higher temperature of 350 K) lies in between with $M_S \approx 1.39\,\mu_B$ f.u.$^{-1}$. I suspect the Co^{2+} moments are more disordered at this temperature, as the M vs. H curves appear nearly isotropic and free from hysteresis. If the Co^{2+} is essentially not magnetically ordered at 350 K, then according to Equation 6.3, LuCoSiIG should have the same M_S as LuIG or YIG at this temperature. In reality, the additional "vacancies" in the magnetic unit cell will weaken the ordering of Fe^{3+} moments, hence the lower saturated magnetisation for LuCoSiIG compared to LuIG at $T \sim 300$ K.

The situation is reversed at low temperatures, where the large moment ($\approx 9.8\,\mu_B$) of the Tb^{3+} ions really kicks in (TbIG has the highest T_{comp} of all REIG). The variation of M_S with field direction in LuCoSiIG at 15 K may be qualitatively explained by the orientation of the octahedra along the

Table 6.2: Magnetic hysteresis parameters for some REIG

Material	Sample type and field direction	Temperature (K)	H_c (Oe)	M_S (μ_B/f.u.)	M_r (μ_B/f.u.)
YIG [52]	powder	300	13	2.313	0.132
YIG [52]	powder	10	64	3.304	0.489
YIG [12]	Bulk $H \parallel [111]$	300		2.247†	
YIG [12]	Bulk $H \parallel [111]$	5		3.131†	
YIG [12]	Bulk $H \parallel [001]$	300		3.568†	
YIG [12]	Bulk $H \parallel [001]$	5		5.052†	
TbIG [52]	powder	300	25	0.424	0.134
TbIG [52]	powder	10	1125	13.41	7.809
LuIG [23]	Thin film $H \parallel [111]$	10	40		
LuCoSiIG [23]	Thin film $H \parallel [111]$	10	640		
LuCoSiIG (this work)	Bulk $H \parallel [110]$	350	≈ 3	1.365(1)	< 0.01
LuCoSiIG (this work)	Bulk $H \parallel [110]$	15	874(1)	1.764(1)	1.509(1)
LuCoSiIG (this work)	Bulk $H \parallel [001]$	350	≈ 2	1.398(1)	< 0.01
LuCoSiIG (this work)	Bulk $H \parallel [001]$	15	869(1)	2.798(1)	2.338(1)

† From M vs T data with $B = 0.5$ T

[1 1 1] direction. The [1 1 1] direction is the easy axis, along which the Fe^{3+} moments lie, but the oxygen octahedra (some of which contain Co^{2+}) are three-fold symmetric about the [1 1 1] direction. The $\langle 0\,0\,1 \rangle$ directions are also three-fold symmetric about [1 1 1], so $H \parallel [0\ 0\ 1]$ likely gets all Co^{2+} spins pointing the same way, increasing the magnetisation. There may also be some domain walls (re)moved by the net octahedral distortion from the magnetocrystalline anisotropy, increasing the contribution from the Fe^{3+} moments as well. This could explain the observed $M_S = 2.798\ \mu_B$ f.u.$^{-1}$ for $H \parallel [0\ 0\ 1]$ at 15 K being closer to the predicted $\mu_{M_S} = 3.15\ \mu_B$ f.u.$^{-1}$ (Equation 6.3) than the equivalent M_S for $H \parallel [1\ 1\ 0]$, despite [0 0 1] not being a traditional "easier" axis for the REIG. As explained earlier, the sample was not cooled from the paramagnetic phase for these low temperature measurements: fewer domains would result in a higher measured value of M_S. Furthermore M_S is expected to be higher with $H \parallel [1\ 1\ 1]$, which is the easy axis for the REIG.

In terms of coercivity, all of the REIG in Table 6.2 are quite 'soft' at room temperature with $H_C \sim 15$ Oe. At low temperatures, TbIG is much harder ($H_C = 1125$ Oe) than YIG ($H_C = 64$ Oe). Impressively, LuCoSiIG manages to hold its own against TbIG with $H_C \approx 870$ Oe at 15 K. The LuCoSiIG thin film $H_C = 640$ Oe is of the same order of magnitude, though is along a different axis and is subject to shape anisotropy effects.

AC susceptibility

In the previous thin film work (reference [23]), the Co^{2+} moments undergo a more gradual transition to a frozen spin glass state. AC susceptibility of my LuCoSiIG sample provided a good opportunity to compare the slow spin dynamics of the thin film with a bulk single crystal. The sample was cooled in zero field then the AC field H_{AC} = 5 Oe was applied along the [001] direction, while H_{DC} = 5 Oe throughout warming from 315 K. The AC frequency was kept below 100 Hz, as I used the oven insert for the SQUID – at higher frequencies, the eddy currents from the copper foil (which provides thermal contact between the heater and the sample) swamp the signal from the sample itself. The AC susceptibility measurements (see Figure 6.13) revealed a cusp in χ' that was independent of frequency, but did depend on the thermal history of the sample (revealed by several successive temperature sweeps at different frequencies[7]), with T_C shifting by 10 K or so across five temperature sweeps. It is possible that the magnetisation dynamics are practically static on the timescales probed by an applied field oscillating at 1 Hz – 100 Hz, and that higher frequencies may give a different result. Also, the behaviour at lower temperatures should be explored as that is when the anisotropy from the Co^{2+} ions manifests, potentially as a re-entrant spin glass as in thin-film LuCoSiIG ([23]) and YIG ([52]).

χ' in the temperature range 315 K – 450 K decreases linearly, rather than a having steep non-linear drop as seen in the glassy thin film of LuCoSiIG [23]. LuCoSiIG χ' also behaves differently to that of YIG, where an increase in χ' is seen below T_C. Again, the closest match in the literature is a magnetic rare earth REIG such as TbIG: χ' decreases below T_C and only increases below T_{comp} [52, 53]. In these previous studies, ZFC vs FC was found to have little effect on the AC data (both χ' and χ'').

For completeness, I also present the imaginary component of the AC susceptibility χ'' in Figure 6.14. χ'' is about 10% of the size of χ'. The eddy current effects in the copper foil wrapped around the sample are responsible for the offset of the 100 Hz data above T_C compared to the other frequencies. T_C shows up as a cusp in the χ'' vs T plot, which is more distinct compared to the χ' vs T data. At temperatures above T_C, χ'' is nearly zero. χ'' is seen to increase until 315 K, the lowest temperature measured. In other REIG, frequency-dependent χ'' indicates two spin-freezing transitions well below T_C, and this appears to be solely due to the Fe^{3+} moments [52]. Hence it would be worthwhile repeating these measurements at low temperatures, since the Co^{2+} resides on the same sublattice as Fe^{3+}.

[7] I didn't get the loop in the MPMS sequence file right.

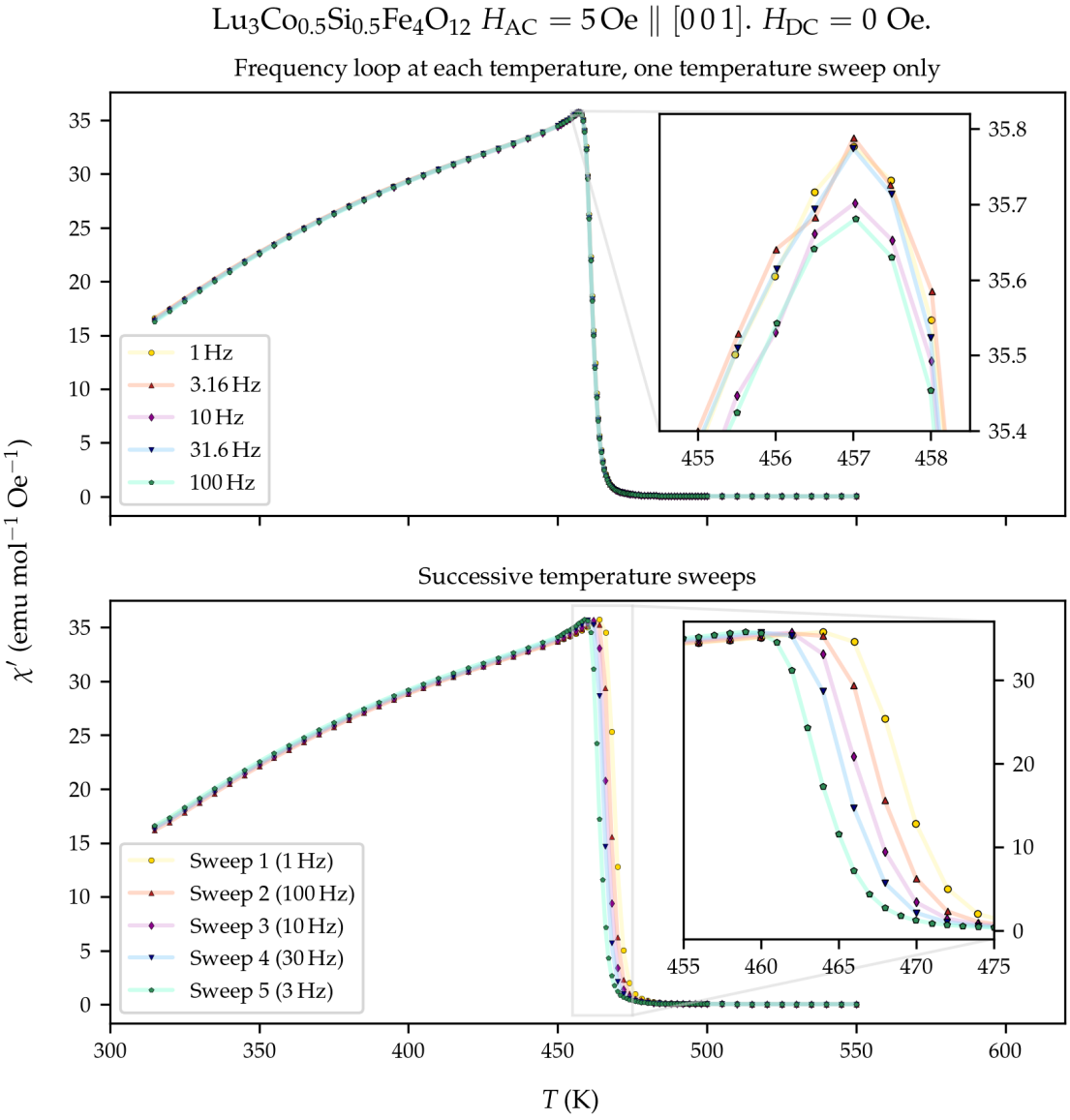

Figure 6.13: The real part of the AC susceptibility χ' of $Lu_3Fe_4Co_{0.5}Si_{0.5}O_{12}$ showing that the ferrimagnetic ordering transition temperature has little frequency dependence, but is affected by the thermal history of the sample, as evidenced by successive temperature sweeps.

6.3 Inelastic neutron scattering of $Lu_3Fe_4Co_{0.5}Si_{0.5}O_{12}$

With a large single crystal full of large Fe^{3+} moments, LuCoSiIG was ripe for an inelastic neutron scattering study!

6.3.1 Method

The crystal of LuCoSiIG was first measured on ANSTO's PELICAN cold time-of-flight neutron spectrometer [55], mounted in an Oxford Instruments closed-cycle LHe cryomagnet with the magnetic

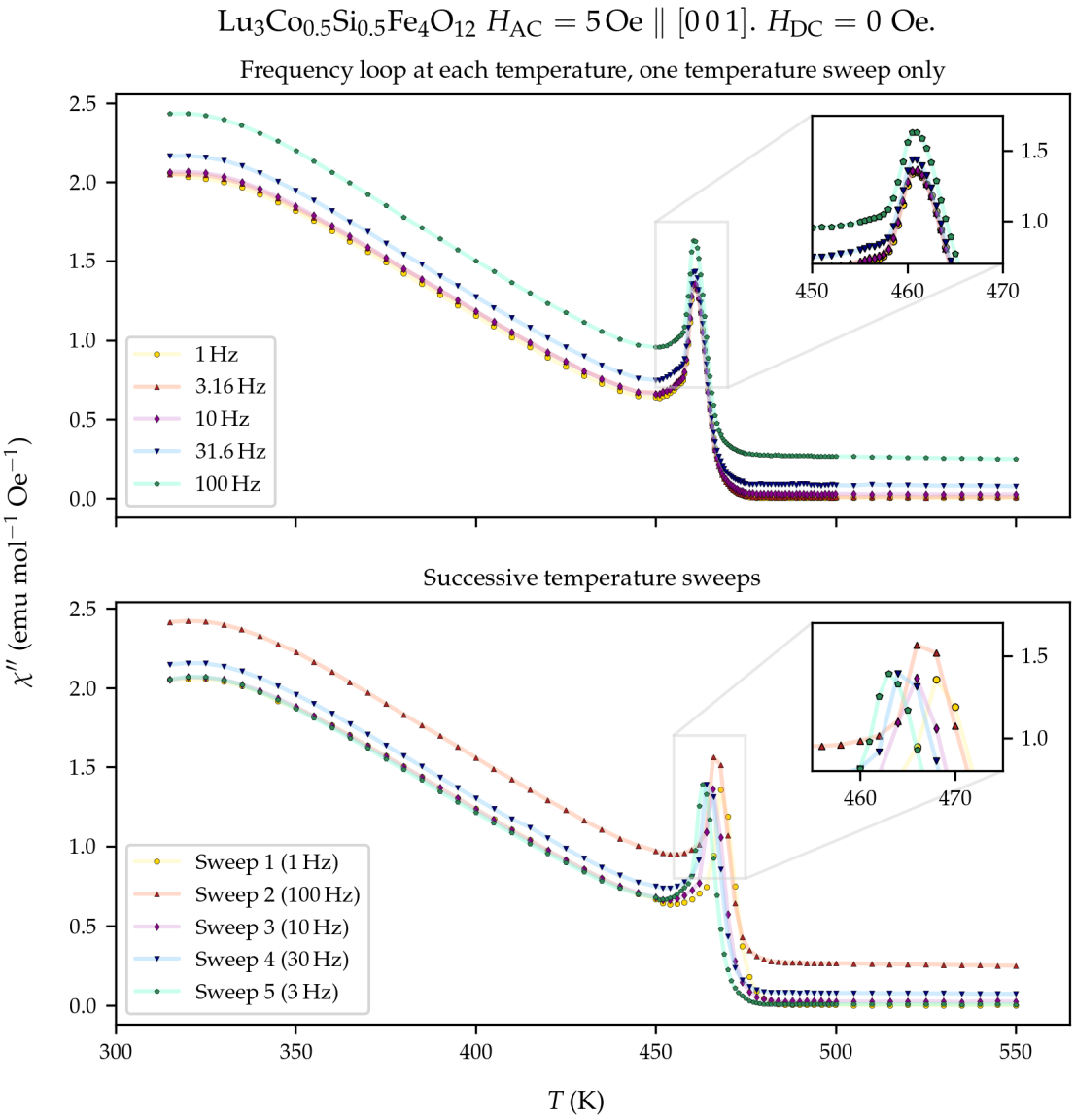

Figure 6.14: The imaginary part of the AC susceptibility χ'' of $Lu_3Fe_4Co_{0.5}Si_{0.5}O_{12}$. The ferrimagnetic ordering transition is marked by the cusp. Above this temperature, χ'' is nearly zero, except for the 100 Hz data. At 100 Hz and higher frequencies, the signal-to-noise ratio worsens due to eddy currents induced in the copper foil around the sample.

field set to 0 T for the entire experiment. A highly-oriented pyrolytic graphite monochromator with vertical focusing was set such that E_i =3.7 meV (λ = 4.69 Å mode) or E_i =14.9 meV ($\lambda/2$ mode). The maximum ΔE with these E_i were $\sim$ 9 meV and $\sim$ 2.5 meV respectively. The frequency of the Fermi choppers was set to minimise contamination from higher harmonics. With the [1 -1 0] axis of the crystal vertical, the [0 0 1], [1 1 1] and [1 1 0] directions were all accessible in the horizontal scattering plane by rotating the crystal about the vertical axis (angle ψ). At a temperature of 1.9 K, the measurement covered the range $\psi = 50°$ to $\psi = 179°$ in 2° steps, and $\psi = -30°$ to $\psi = 50°$ in 1° steps. At this low temperature, data was processed in 'frame overlap' mode, assuming

that counts on the energy gain side were in fact energy loss neutrons from the previous frame. The latter measurement from $\psi = -30^\circ$ to $\psi = 50^\circ$ in 1° steps was also repeated at 250 K but without the 'frame overlap' assumption, since the energy gain side was thermally populated at this higher temperature. Background measurements without the sample in the cryomagnet were also performed at both temperatures.

The LuCoSiIG crystal was then measured on ANSTO's TAIPAN thermal triple-axis spectrometer [56] mounted in a closed-cycle LHe cryostat (AS Scientific) in the same orientation, [1 −1 0] axis vertical. The vertically focusing pyrolytic graphite monochromator fixed $E_i = 14.87$ meV by the (0 0 2) reflection and E_f was adjusted so that ΔE varied between 5 meV and 45 meV. The low ΔE data ensured a viable comparison could be made with the data collected on PELICAN. Constant energy, **Q** scans were performed along the $(h\,h\,0)$ and $(h\,h\,h)$ directions at the base temperature of 6 K. Energy scans at fixed **Q** = (4 4 0) and (4 4 4) were also performed at 6 K. Additionally, constant energy scans along $\mathbf{Q} = (h\,h\,h)$ and energy scans at the zone centre (4 4 4) were performed at higher temperatures of 150 K, 200 K and 250 K.

6.3.2 Data analysis

The data from PELICAN was processed first using the Mantid software [57] and then background subtraction, normalisation and data reduction was performed using the Horace software [58]. By folding the data over Brillouin zone boundaries, the statistics were improved as counts from symmetrically-equivalent **Q** were added together. This generated 2D reciprocal space maps and energy vs **Q** plots, as well as 1D cuts of intensity vs **Q** or energy. The raw data from TAIPAN was already 1D and normalised to the beam monitor intensity. For each 1D cut, a number of peaks with Gaussian lineshape and a linear background were fitted. This was done using a suite of custom PYTHON programs (built using packages including those described in [59–62]).

6.3.3 Results

Low temperature data

Constant energy slices of the elastic line in the $Q_x = (h, h, 0)$, $Q_y = (0, 0, l)$ plane from the PELICAN data collected at 1.9 K were produced by integrating across [−0.1 meV, 0.1 meV] and $(-0.1, 0.1, 0) \leq Q_z \leq (0.1, -0.1, 0)$. The elastic line data with E_i = 14.9 meV and E_i = 3.7 meV are shown in Figure 6.15 and Figure 6.16 respectively, to show the region of the $h\,h\,l$ scattering plane that was measured.

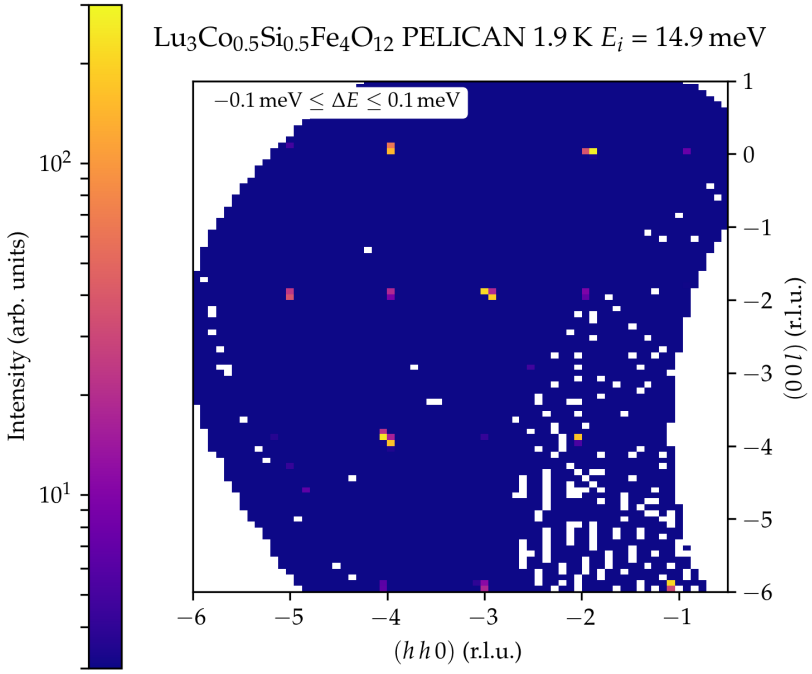

Figure 6.15: Elastic line data from inelastic neutron scattering of LuCoSiIG at 1.9 K on ANSTO PELICAN, $h\,h\,l$ plane with E_i = 14.9 meV. Here the background has been subtracted, but the data have not been folded.

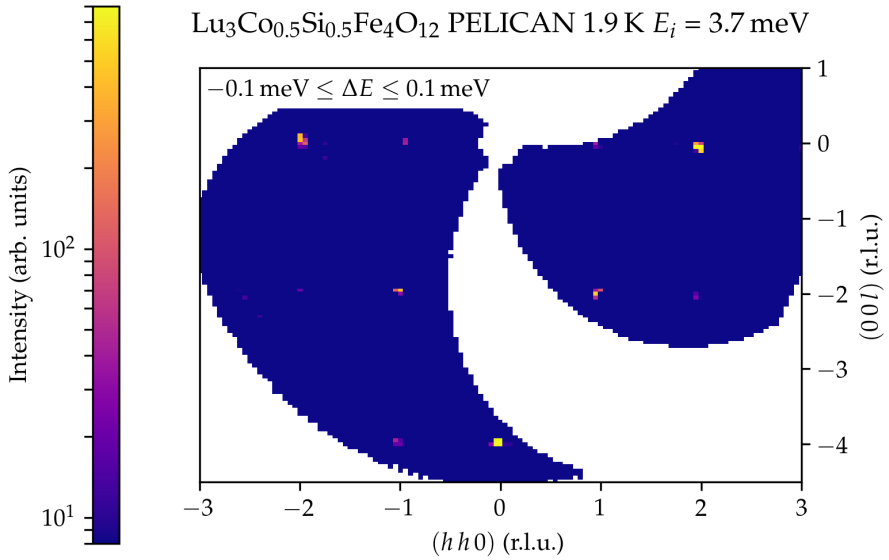

Figure 6.16: Elastic line data from inelastic neutron scattering of LuCoSiIG at 1.9 K on ANSTO PELICAN, $h\,h\,l$ plane with E_i = 3.7 meV. Here the background has been subtracted, but the data have not been folded.

The inelastic data from PELICAN collected at a temperature of 1.9 K with $E_i = 14.9$ meV and $E_i = 3.7$ meV are presented as plots of energy vs **Q** in Figure 6.17. The integration range for these plots was $(0, 0, -0.1) \leq Q_y \leq (0, 0, 0.1)$ and $(-0.1, 0.1, 0) \leq Q_z \leq (0.1, -0.1, 0)$. Sharp excitations are emanating from $(-4\ -4\ 0)$ and $(-2\ -2\ 0)$, with a clear energy gap observed in the $E_i = 3.7$ meV

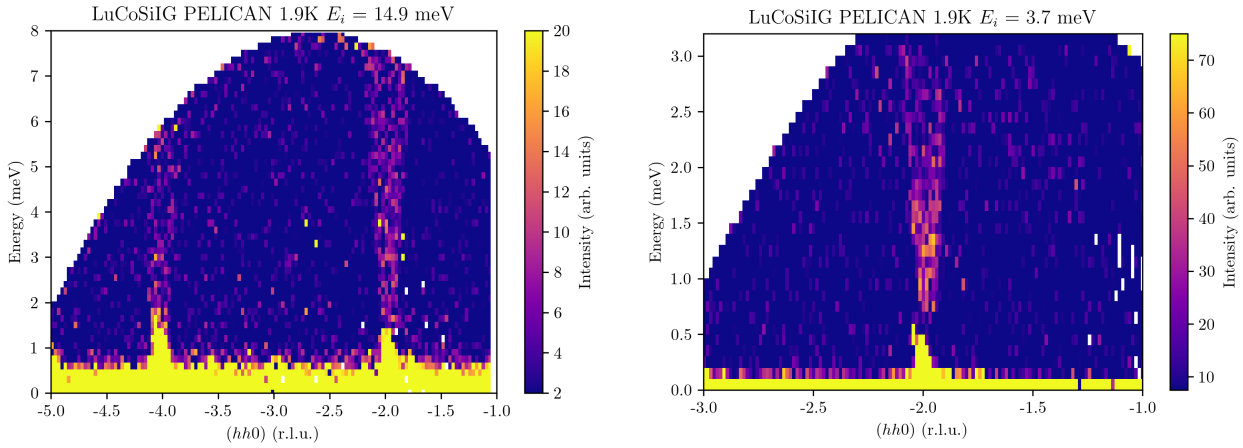

Figure 6.17: PELICAN data showing spin wave dispersion of LuCoSiIG at a temperature of 1.9 K along $(h\,h\,0)$ direction with $E_i = 14.9$ meV and $E_i = 3.7$ meV. The anisotropy gap of ~ 0.7 meV is clearly resolved in the $E_i = 3.7$ meV data. The bright spots at integer Q extending upwards in energy to 0.5 meV – 1 meV are from magnetic Bragg peaks; the signals manifested in the inelastic channels due to resolution broadening.

data, which has a higher energy resolution. The constant energy data from TAIPAN collected at a temperature of 6 K (the base temperature of the cryostat used) along the $(hh0)$ and (hhh) directions are shown in Figure 6.18. The dispersion of the first acoustic mode reaches a maximum energy of ~ 35 meV, with the optical mode appearing at ~ 20 meV and extending up to at least 55 meV (the maximum ΔE attainable on TAIPAN).

To determine the exchange parameters for LuCoSiIG, I modelled the data with the LSWT package SpinW [46]. My first approached was what I call the 'averaged spin' spin set-up: sites on the a and d sublattices were assigned an average spin based on relative occupation of Fe^{3+}, Co^{2+} and Si^{4+} (see Figure 6.19).

'Averaged spin' model

To begin with, the exchange parameters for LuCoSiIG in the 'averaged spin' model were estimated using the seven parameter model for YIG [4], defined in Figure 6.2. The isotropic Heisenberg exchange parameters were scaled down according to the occupancies and spins for LuCoSiIG/YIG to provide an initial estimate for the fitting routine. For example, an exchange interaction between an octahedral and tetrahedral site SJ_1 is scaled by the reduced occupancy of Fe^{3+} on the tetrahedral sites (20/24) and the combined Fe^{3+} (12/16) and Co^{2+} (4/16) on the octahedral site:

$$SJ_1(\text{LuCoSiIG}) = SJ_1(\text{YIG}) \times \frac{20}{24} \cdot \frac{5}{2} \times \left(\frac{12}{16} \cdot \frac{5}{2} + \frac{4}{16} \cdot \frac{3}{2}\right). \tag{6.4}$$

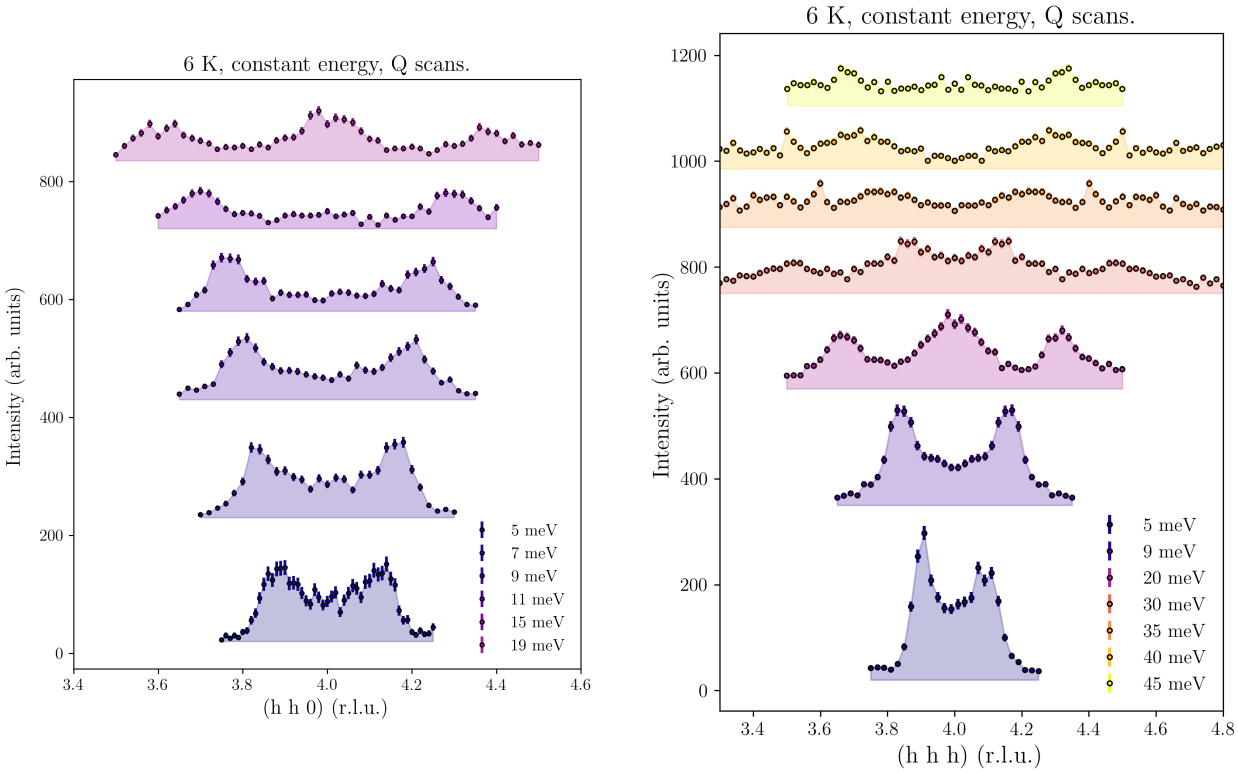

Figure 6.18: TAIPAN constant energy, **Q** cut data showing spin wave dispersion of LuCoSiIG at a temperature of 6 K along the $(hh0)$ and (hhh) directions. To aid the visual interpretation of the data, the (hhh) **Q** cuts at $\Delta E \geq 35$ meV have been mirrored about the high symmetry point (4 4 4).

The parameters SJ_1, SJ_2, SJ_{3a}, SJ_{3b} were then fit to the TAS and TOF data for LuCoSiIG assuming cubic $Ia\bar{3}d$ symmetry (the other parameters SJ_4, SJ_5 and SJ_6 were fixed at the scaled LuCoSiIG values as fits of all seven parameters to my data did not converge). Although the data do not cover the full extent of the calculated dispersion in energy or **Q**, overall the 'averaged spin' model is a good fit at higher energies (Figure 6.20).

However, the shortfalls of this approach become apparent at low energies $\Delta E < 6$ meV. The dispersion is steeper than predicted by the 'averaged spin' model, and also there is a clear minimum in the dispersion around 1 meV. So I added an easy-axis anisotropy term $-\sum_i D(S_i^z)^2$ along the [1 1 1] direction to Equation 6.1; however, this was not possible using the cubic $Ia\bar{3}d$ symmetry setting in SpinW, which interprets that as "isotropic" anisotropy. It was time to swap to the rhombohedral unit cell (Figure 6.21)...

The rhombohedral unit cell I used was not primitive. The lattice vectors for the rhombohedral unit

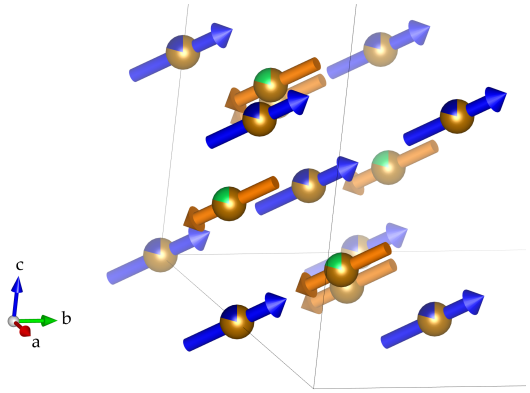

Figure 6.19: 'Averaged spin' magnetic structure used for spin wave modelling of LuCoSiIG. In the 'averaged spin' set-up, sites on the a and d sublattices were assigned an average spin (blue spin = average tetrahedral site spin, orange arrow = average octahedral site spin) based on relative occupation of Fe^{3+} (brown), Co^{2+} (blue) and Si^{4+} (green).

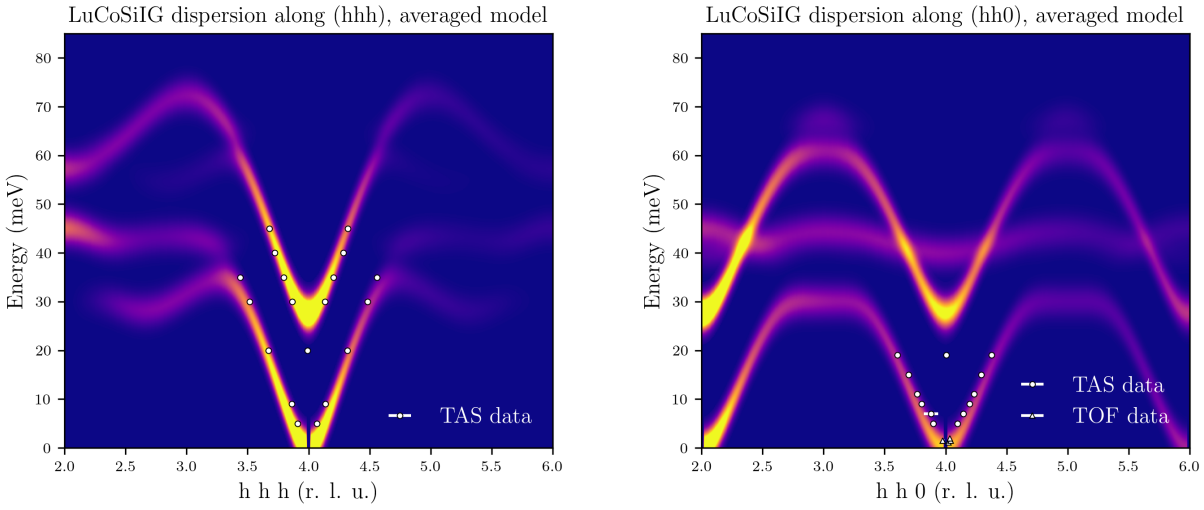

Figure 6.20: Spin wave dispersion for LuCoSiIG 'averaged spin' model along (hhh) and $(hh0)$. The initial parameters for the fit were scaled from those for YIG described in [4].

cell $\mathbf{a}'$, $\mathbf{b}'$, $\mathbf{c}'$ are defined in terms of the lattice vectors of the cubic unit cell $\mathbf{a}$, $\mathbf{b}$ and $\mathbf{c}$:

$$\begin{aligned} \mathbf{a}' &= \mathbf{a} - \mathbf{b} \\ \mathbf{b}' &= \mathbf{b} - \mathbf{c} \\ \mathbf{c}' &= \frac{1}{2}(\mathbf{a} + \mathbf{b} + \mathbf{c}). \end{aligned} \tag{6.5}$$

Hence in reciprocal space $(h, h, h)_{\text{cubic}} \parallel (0, 0, h)_{\text{rhombo}}$ and $(h, h, 0)_{\text{cubic}} \parallel (h, -2h, 0)_{\text{rhombo}}$ etc. The parameters SJ_1, SJ_2 and D (the easy axis anisotropy along $[0\,0\,1]_{\text{rhombo}}$) were then fit based on the low energy TOF data starting with the parameters obtained by fitting the higher energy TAS data. The fit, together with the data, is shown in Figure 6.23 but the **Q** axis has been converted back

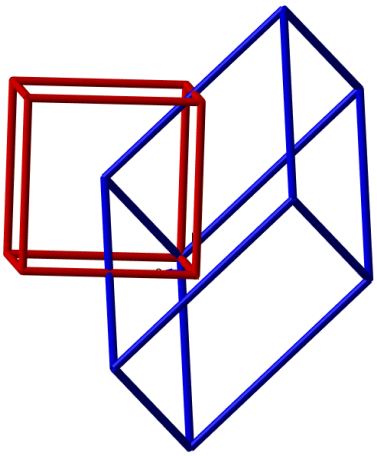

Figure 6.21: Cubic (red) and rhombohedral (blue) unit cells. $[1\ 1\ 1]_{\text{cubic}} \parallel [0\ 0\ 1]_{\text{rhombo}}$ for the hexagonal setting of the rhombohedral unit cell (shown).

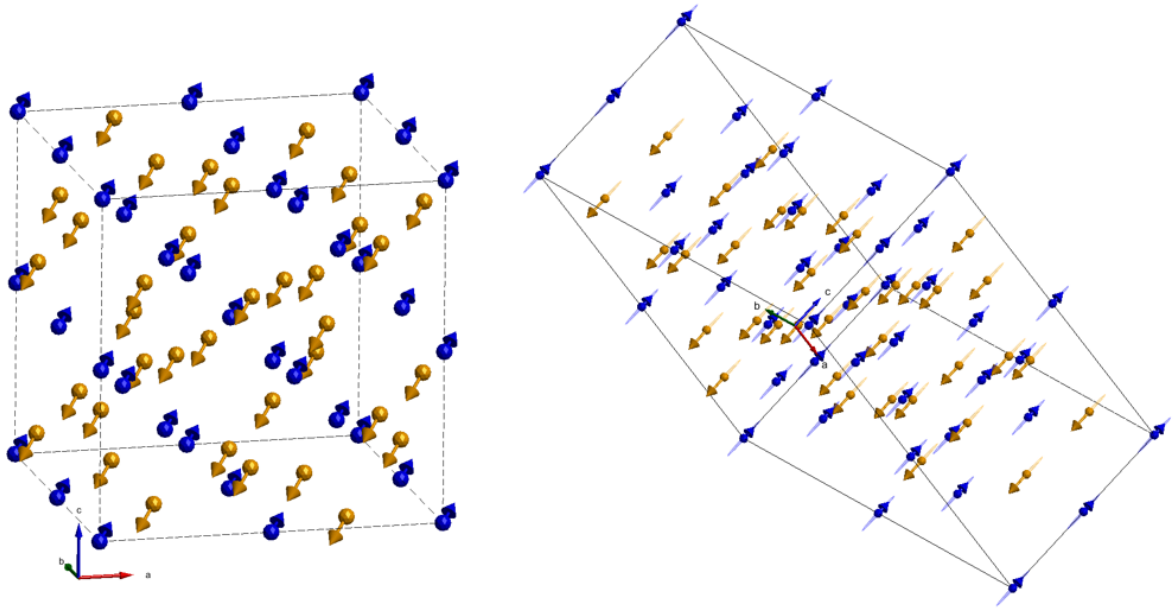

Figure 6.22: Left: 'averaged spin' model in the cubic unit cell. Right: 'averaged spin' model in the rhombohedral unit cell. For both 'averaged spin' models, all octahedral sites have the same spin (blue arrows), which is slightly smaller than the spin on all tetrahedral sites (orange arrows). The easy axis anisotropy in the rhombohedral cell is along $[0\ 0\ 1]_{\text{rhombo}} \parallel [111]_{\text{cubic}}$.

into cubic coordinates as these are more easily interpreted.

'Randomised spin' model

I also explored a second approach, which was less successful overall. In the 'randomised spin' set-up, sites were randomly populated with different ions but the overall stoichiometry of the unit

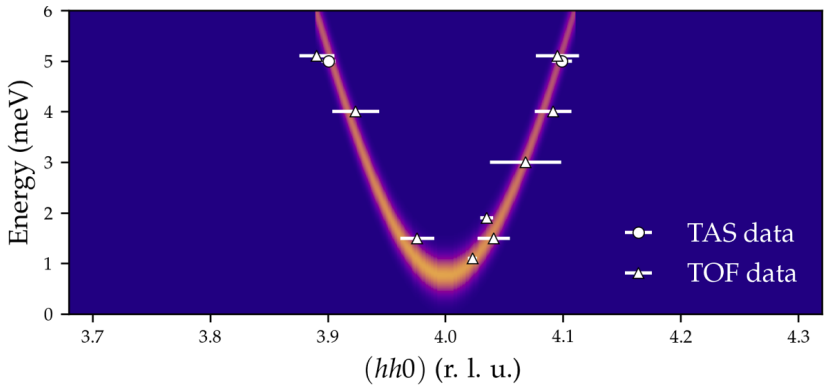

Figure 6.23: Low energy spin wave dispersion of LuCoSiIG, showing LSWT model with easy-axis anisotropy along $[0\ 0\ 1]_{\text{rhombo}}$. The **Q** axis is in cubic reciprocal lattice coordinates.

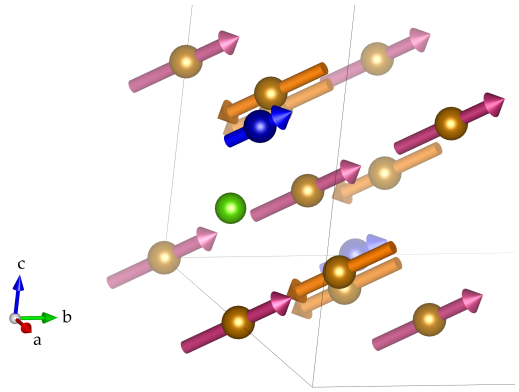

Figure 6.24: 'Randomised' structure used for spin wave modelling of LuCoSiIG. In the 'randomised spin' set-up, sites were randomly populated with different ions (same colour scheme for atoms, but different for spins. Blue arrows = Co^{2+} spins, orange arrows = Fe^{3+} octahedral spins and pink arrows = Fe^{3+} tetrahedral spins) but the overall stoichiometry of the unit cell remained the same.

cell remained the same (Figure 6.24). A similar approach was utilised for a different magnetic material in reference [63]. The key implications for the exchange parameters in the 'randomised' model were that Fe-Fe and Fe-Co exchange parameters were not necessarily the same, and that by lifting the $Ia\bar{3}d$ space group symmetry constraints of the 'averaged' model, a net easy-axis anisotropy could be attributed to the Co^{2+} ions wherever they appeared in the unit cell.

To do this in SpinW, it was necessary to set the symmetry of the model to $P1$, which vastly increased the number of parameters. By re-imposing the relevant symmetries on specific exchange paths, the parameter space reduced. I calculated the spin waves for an ensemble of randomised unit cells, and averaged these to deduce the effective exchange parameters. Although this approach worked ok at lower energies, discontinuities in the spectra were present at higher energies, which was not great. In the end, this 'randomised spin' approach was overkill as the sample was of very high crystalline quality and did not show signs of disorder. However, it was useful to unpack the proverbial black box and explore SpinW in more depth.

High temperature data

As per the treatment of the low temperature inelastic neutron scattering data, constant energy slices of the elastic line in the $Q_x = (h, h, 0)$, $Q_y = (0, 0, l)$ plane from the PELICAN data collected at 250 K were produced by integrating across [−0.1 meV, 0.1 meV] and $(-0.1, 0.1, 0) \leq Q_z \leq (0.1, -0.1, 0)$. The elastic line data in the $h\,h\,l$ plane are shown in Figure 6.25 for E_i = 3.7 meV. The inelastic data are presented as plots of energy vs **Q** in Figure 6.26. The integration range for these plots was $(0, 0, -0.1) \leq Q_y \leq (0, 0, 0.1)$ and $(-0.1, 0.1, 0) \leq Q_z \leq (0.1, -0.1, 0)$. This high temperature data differs from the low temperature data in several ways:

- The anisotropy gap has completely disappeared.
- The intensity of the low energy magnon is higher due to the acoustic spin wave mode being thermally (de)populated $E = k_B T \approx 20$ meV. Accordingly the spin wave on the energy gain side (negative E in Figure 6.26) is much stronger than it was for the low temperature measurement.
- The magnons are much broader due to a shorter magnon lifetime from constant thermal excitation and increased disorder of the Co^{2+} spins in particular.

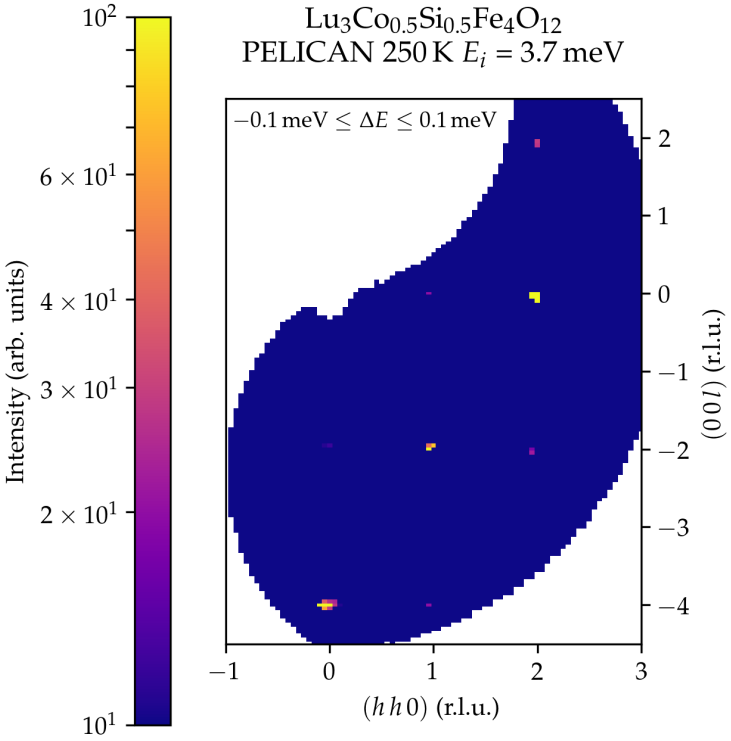

Figure 6.25: Elastic line data from inelastic neutron scattering of LuCoSiIG at 250 K on ANSTO PELICAN, $h\,h\,l$ plane with E_i = 3.7 meV. Here the background has been subtracted, but the data have not been folded.

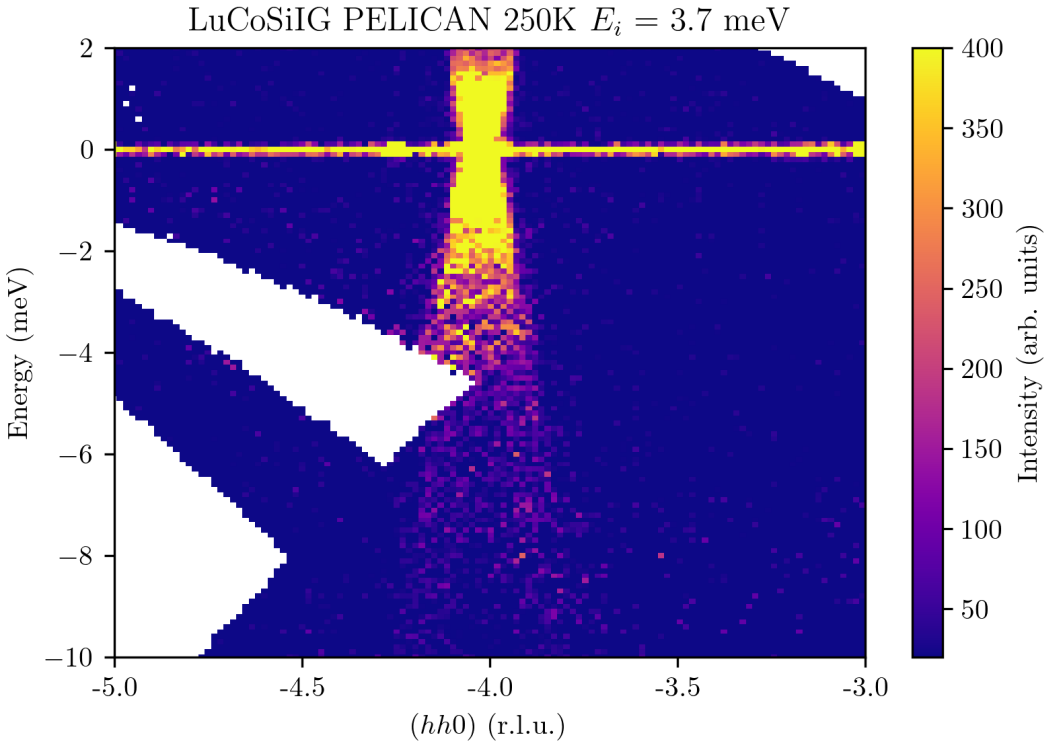

Figure 6.26: PELICAN data showing spin wave dispersion of LuCoSiIG at a temperature of 250 K along $(h\ h\ 0)$ direction with $E_i = 3.7$ meV. The anisotropy gap has closed and the energy gain side is well populated.

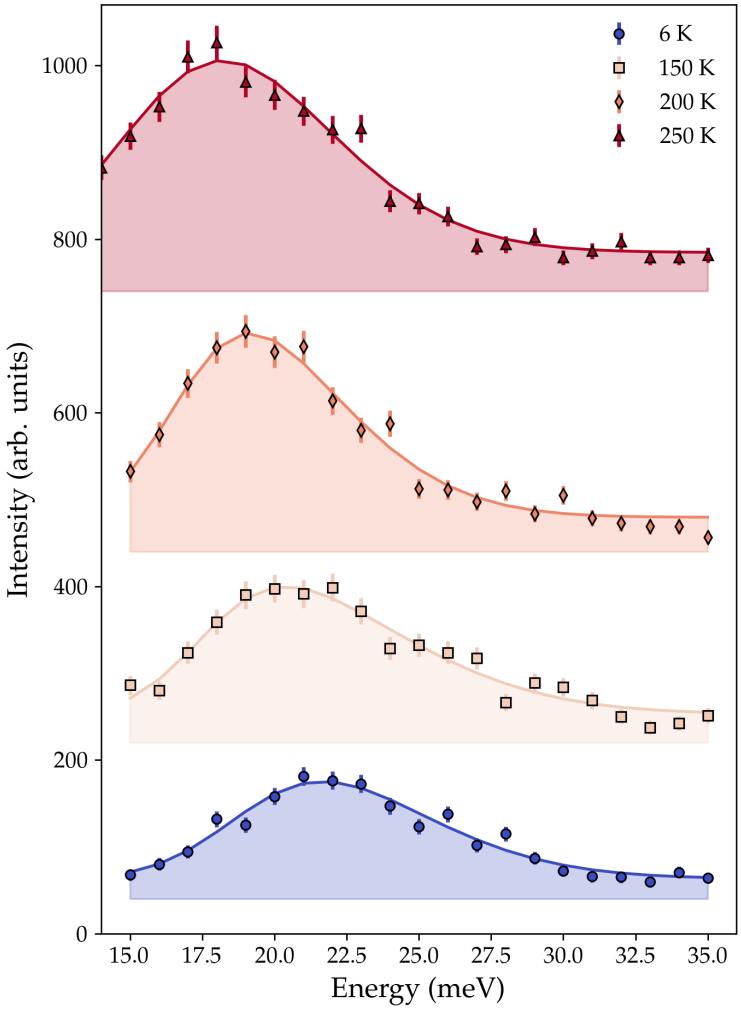

Figure 6.27: TAIPAN data showing the decrease in the energy between the first acoustic and optical magnons of LuCoSiIG with temperature. Data are shown with arbitrary offset along the intensity axis. Fits are skewed Gaussians.

With increasing temperature, the energy gap to the next spin wave – the optical mode – decreased. This is shown in Figure 6.27. This trend is plotted in Figure 6.28. The intensity of the optical mode seemed to remain relatively constant with temperature, judging by the peak heights in Figure 6.27. Note that no background subtraction was done for the TAIPAN data (unlike the PELICAN data).

6.3.4 Discussion

The magnetocrystalline anisotropy of LuCoSiIG means that describing the vipers nest of spin waves is at least as complicated as it is for YIG, though not as complicated as for YbIG or TbIG! The PELICAN elastic line data shows no intensity at non-integer positions in the (hhl) plane, consistent with the magnetic unit cell being the same size as the structural unit cell, and ferrimagnetic ordering along the [1 1 1] axis. The inclusion of Co^{2+} as a dopant has a demonstrable effect on the lowest energy magnon mode, especially at low temperatures by introducing an energy gap of ≈ 0.7 meV.

The nearest neighbour antiferromagnetic exchange interaction between the octahedral and tetrahedral lattices SJ_1 is slightly smaller than for YIG. In fact, this is true for all the fitted exchange parameters shown in Table 6.3, which were SJ_1, SJ_2, SJ_{3a} and SJ_{3b} (remember SJ_4, SJ_5, SJ_6 were 'scaled down' from the YIG model in reference [4]). The difference is largest for SJ_2, which is affected by the lower occupancy by Fe^{3+} of the 24*d* sites in LuCoSiIG (due to doping with non-magnetic Si^{4+}) as compared to YIG. The easy-axis anisotropy SD is small but mighty: in TbIG, $SD = 0.271$ meV is enough to gap the magnon spectrum by ≈ 12 meV, and in LuCoSiIG $SD = 0.04$ meV results in a gap of 0.7 meV. Admittedly, the TbIG easy-axis anisotropy is driven by the massive moments of the Tb^{3+} ions at low temperature (Fe^{3+} having basically no anisotropy ever). To put a more positive spin on it, LuCoSiIG has infinitely more anisotropy than YIG.

My LSWT model considers the average exchange interaction between sites; however, it is worth pointing out that this is driven by the interactions between individual ions. In an early paper on Co doped YIG, the Fe^{3+}–Co^{2+} exchange was estimated to be only 45 % of the Fe^{3+}–Fe^{3+} exchange [30]. Obtaining exchange parameters larger than those of YIG would have been unlikely for LuCoSiIG.

Regarding the variation in the spin wave spectrum with temperature, the most significant observations are the closing of the anisotropy gap and the decrease in the energy gap between the acoustic and optical magnons. Firstly, the anisotropy originates from the Co^{2+} moments and as temperature increases, the ordering of these would become shorter in range. By 250 K (and certainly by 350 K according to the magnetisation data) the Co^{2+} spins are likely disordered, thus having no influence on the spin wave spectrum of LuCoSiIG other than making the spectrum more diffuse. Compare this to the temperature dependence of the (tiny) energy gap in the spin wave spectrum of YIG induced by an external magnetic field of 0.1 T – the excitation spectrum was gapless by ~ 10 K [12]. This drives home the relative fragility of any influence canting the spins away from [111] compared to the robust ferrimagnetic order of the Fe^{3+} ions. Admittedly the Zeeman energy gap measured for YIG [6, 12] is much smaller than the gap we have measured for LuCoSiIG. There

Table 6.3: Experimentally determined exchange parameters for some REIG. Positive values denote antiferromagnetic coupling, negative values denote ferromagnetic coupling. Exchange constants J_i are defined in Figure 6.2, with J_{3a} along the $\langle 1\,1\,1\rangle$ directions and J_{3b} along the $\langle -1\,1\,1\rangle$ directions. D is defined such that a positive value indicates an easy-axis anisotropy and a negative value, an easy-plane anisotropy. All values are per pair of spins.

Exchange interaction	SJ_1 (meV)	SJ_2 (meV)	SJ_{3a} (meV)	SJ_{3b} (meV)	SJ_4 (meV)	SJ_5 (meV)	SJ_6 (meV)	SD (meV)
Between sites	*a d*	*d d*	*a a*	*a a*	*a d*	*d d*	*a a*	-
YIG [4]	6.8(2)	0.52(4)	0.0(1)	1.1(3)	−0.07(2)	0.47(8)	−0.09(5)	
YIG [6]	5.80(14)	0.70(16)	0.0(1)	0.01(1)				
TbIG† [64]	6.579(5)	0.688(5)	0.00(3)	0.998(8)	−0.065(2)	0.031(5)	−0.103(5)	0.271
LuCoSiIG (this work)	4.8(1)	0.03(1)	0.0(1)	0.68(2)	−0.05(1)	0.33(4)	−0.07(3)	0.04(1)

† The model in reference [64] also included exchange terms for the interactions between Tb^{3+} and Fe^{3+} moments, although these were small (< 0.5 meV).

are no comparable inelastic neutron scattering data available for a Co^{2+} doped YIG; however, the smaller lattice parameter of LuCoSiIG likely favours a stronger anisotropy contribution from the Co^{2+}.

The polarisation of the spin waves would also be affected by a canted ferrimagnetic ground state if there was one (as compared to the assumed ferrimagnetic ground state with moments along [1 1 1]), although no satellite/non-integer reflections were seen in the elastic line data to suggest this. However, increasing the cobalt concentration may make this more likely. At the extreme of a garnet where the only magnetic ion is Co^{2+}, the ordering temperature is much lower (~ 8 K) [37]. Factors such as clustering of Co^{2+} and Si^{4+} ions and possible Lu site disorder would affect the superexchange paths. In this case, the Laue diffraction patterns show no signs of short-range/diffuse order for LuCoSiIG.

Secondly, the decrease in the energy gap to the optical magnon mode of LuCoSiIG with temperature can be interpreted as thermal motion enhancing the canting of the spins away from the [111] direction in this oscillatory mode. The reduction in the energy gap follows the same temperature dependence trend as YIG and TbIG (see Figure 6.28). Overall the energy of the optical magnon is lower due to the lower exchange interaction strength between Fe^{3+} and Fe^{3+}/Co^{2+} sites. The energy is comparable with thermal energy scales at a temperature of ≈ 200 K (Figure 6.28). Accordingly, I would expect the spin Seebeck effect to be much diminished in LuCoSiIG at this temperature.

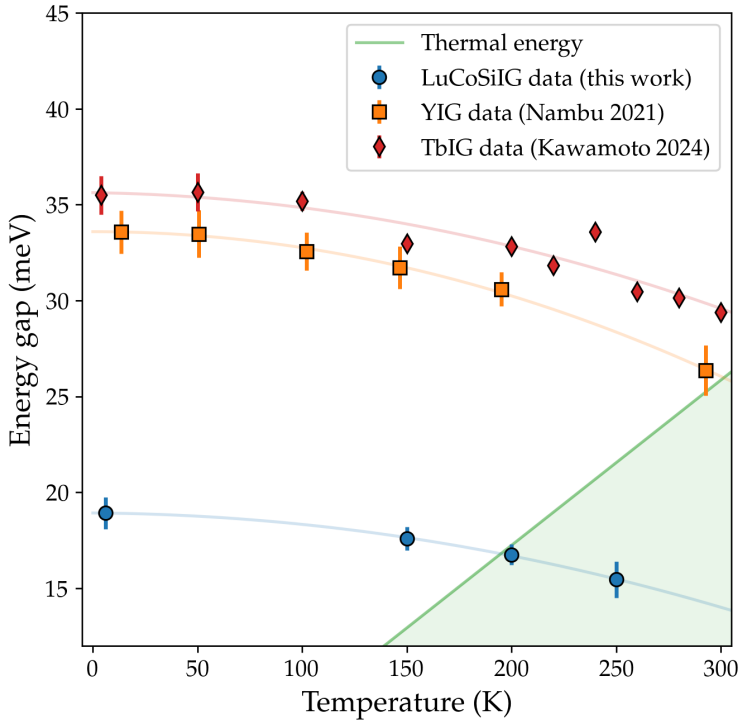

Figure 6.28: Temperature dependence of the energy gap between the first acoustic and optical magnons for LuCoSiIG, YIG (data from Nambu *et al.* [12]), and TbIG (data from Kawamoto *et al.* [64]). Solid lines are a guide to the eye. Thermal energy $E \leq k_B T$ is shown in green.

6.4 Conclusion

In summary, this chapter examined the anisotropic magnetism and spin waves of the Co^{2+} doped REIG $Lu_3Co_{0.5}Si_{0.5}Fe_4O_{12}$. In non-magnetic REIG systems, there is very little magnetocrystalline anisotropy observed in either magnetisation or inelastic neutron scattering data. Introducing Co^{2+} (charge balanced with Si^{4+}) to LuIG has bucked this trend. The magnetisation of LuCoSiIG showing large hysteresis and bifurcation of ZFC–FC curves at low temperatures, comparable to the magnetic REIG such as TbIG. However, LuCoSiIG (like the non-magnetic REIG) does not display temperature-dependent magnetic compensation. The magnetisation of bulk single crystal LuCoSiIG is consistent with straight up-and-down ferrimagnetic order of Fe^{3+} and Co^{2+} moments along the body diagonal of the cubic unit cell ([1 1 1] direction) and I did not find any signs of a spin glass phase in the AC susceptibility data, which was previously seen in a thin film of LuCoSiIG.

The results of inelastic neutron scattering experiments on LuCoSiIG presented here showed that the two lowest energy spin wave modes about the magnetic zone centres are similar to those of other REIG. The exchange interactions in LuCoSiIG are weaker overall. This can be qualitatively explained by two contributions. Firstly, the Fe^{3+}–Co^{2+} exchange is not as strong as the Fe^{3+}–

Fe^{3+} exchange (this plays out on exchange paths involving the octahedral sites). Secondly, the Fe^{3+}–Fe^{3+} exchange is also not as strong due to the "magnetic vacancies" introduced by Si^{4+} (this affects exchange paths involving the tetrahedral sites). Overall, the average exchange parameters quantified by my LSWT model are lower than those previously reported for e.g. YIG or TbIG. A small anisotropy gap was observed in the cold neutron time-of-flight experiment with the sample at 1.9 K, which is not a feature of the spectra of non-doped non-magnetic REIG such as YIG. This is attributed to an effective easy-axis single ion anisotropy along the $[1\ 1\ 1]_{\text{cubic}}$ or $[0\ 0\ 1]_{\text{rhombohedral}}$ direction from the Co^{2+} moments on octahedral sites. The anisotropy did not appreciably affect the stiffness of the acoustic mode – similar to TbIG, which has a larger anisotropy. At the higher temperature of 250 K, the spin wave spectrum of LuCoSiIG showed that the anisotropy gap had closed and the lowest energy acoustic mode was thermally populated as well as being much broader.

As far as LuCoSiIG's prospects as a material for spintronic applications go, I would suggest that YIG is probably better for anything requiring polarised spin currents: the energy gap between the lowest energy magnons of different polarisations is smaller in LuCoSiIG than YIG. This energy gap reduces with increasing temperature in all REIG, but thermal population of both modes occurs at a lower temperature in LuCoSiIG than for TbIG or YIG, meaning there would be a reduction in the net spin current. However, LuCoSiIG's significantly larger anisotropy and hardness (as compared to YIG) may suit spin memories or devices where domain structure is important, especially if optical control of the anisotropy can be demonstrated as for Co^{2+} doped YIG.

LuCoSiIG is a curious material that seems to act like a non-magnetic REIG ($\sim$ YIG) at room temperature and a bit more like a magnetic REIG ($\sim$ TbIG) at low temperature. Future investigations could probe the details of the phase diagram of LuCoSiIG through neutron diffraction, including the field dependence of the Co^{2+} anisotropy. In fact I actually went to the ILL in March 2024 to perform a single crystal diffraction experiment on LuCoSiIG using the D10 four-circle diffractometer[8]. This included field-dependence measurements of some magnetic Bragg peaks. Another extension to the material in this chapter would be to add more magnetisation measurements, e.g. DC susceptibility for $H \parallel [1\ 1\ 1]$, and low temperature AC susceptibility.

[8] Analysis of the data will happen as a follow-on to this DPhil thesis!

Acknowledgements for this chapter

Affiliations are the University of Oxford unless otherwise stated.

The synthesis of the LuCoSiIG single crystal was the work of Dharmalingam Prabhakaran.

The XRD was performed by Siobhan Tobin, Oscar Ramon Fabelo Rosa (ILL) and Vivianne Peçanha-Antonio.

The ANSTO PELICAN experiment was performed by Siobhan Tobin and Richard Mole (ANSTO). The ANSTO TAIPAN experiment was performed by Siobhan Tobin and Kirrily Rule (ANSTO). The proposal number for both ANSTO experiments is P13938 and data are available on request.

The ILL OrientExpress experiment was performed by Siobhan Tobin, Iurii Kibalin (ILL) and Andrew Wildes (ILL). The ILL D10 experiment (data not presented or analysed in this chapter) was performed by Siobhan Tobin, Vivianne Peçanha-Antonio, Iurii Kibalin (ILL) and Bachir Ouladdiaf (ILL). Data from these experiments will be available via proposal number 5-41-1255.

References

[1] R. Pauthenet. "Magnetic Properties of the Rare Earth Garnets". *Journal of Applied Physics* 30.4 (1959). DOI: 10.1063/1.2185937 (cited on pages 169–171).

[2] L. Néel, R. Pauthenet, and B. Dreyfus. "Chapter VII The Rare Earth Garnets". *Progress in Low Temperature Physics*. Ed. by C. J. Gorter. Vol. 4. Elsevier, 1964 (cited on pages 169, 170, 182).

[3] A. A. Serga, A. V. Chumak, and B. Hillebrands. "YIG magnonics". *Journal of Physics D: Applied Physics* 43.26 (2010). DOI: 10.1088/0022-3727/43/26/264002 (cited on page 169).

[4] A. J. Princep, R. A. Ewings, S. Ward, S. Tóth, C. Dubs, D. Prabhakaran, and A. T. Boothroyd. "The full magnon spectrum of yttrium iron garnet". *npj Quantum Materials* 2.1 (2017). DOI: 10.1038/s41535-017-0067-y (cited on pages 169, 175, 177, 193, 195, 201, 202).

[5] B. L. Giles, Z. Yang, J. S. Jamison, and R. C. Myers. "Long-range pure magnon spin diffusion observed in a nonlocal spin-Seebeck geometry". *Physical Review B* 92.22 (2015). DOI: 10.1103/PhysRevB.92.224415 (cited on page 169).

[6] S.-i. Shamoto et al. "Neutron scattering study of yttrium iron garnet". *Physical Review B* 97.5 (2018). DOI: 10.1103/PhysRevB.97.054429 (cited on pages 170, 175, 176, 201, 202).

[7] R. Hock, H. Fuess, T. Vogt, and M. Bonnet. "Crystallographic distortion and magnetic structure of terbium iron garnet at low temperatures". *Journal of Solid State Chemistry* 84.1 (1990). DOI: 10.1016/0022-4596(90)90182-W (cited on page 170).

[8] B. Tomasello, D. Mannix, S. Geprägs, and T. Ziman. "Origin and dynamics of umbrella states in rare-earth iron garnets". *Annals of Physics* 447 (2022). DOI: 10.1016/j.aop.2022.169117 (cited on page 170).

[9] V. Peçanha-Antonio, D. Prabhakaran, C. Balz, A. Krajewska, and A. T. Boothroyd. "Model for coupled $4f-3d$ magnetic spectra: A neutron scattering study of the Yb-Fe hybridization in $Yb_3Fe_5O_{12}$". *Physical Review B* 105.10 (2022). DOI: 10.1103/PhysRevB.105.104422 (cited on pages 170, 172, 177).

[10] L.-W. Wang, L.-S. Xie, P.-X. Xu, and K. Xia. "First-principles study of magnon-phonon interactions in gadolinium iron garnet". *Physical Review B* 101.16 (2020). DOI: 10.1103/PhysRevB.101.165137 (cited on page 170).

[11] P. Hansen, W. Tolksdorf, and R. Krishnan. "Anisotropy and magnetostriction of cobalt-substituted yttrium iron

garnet". *Physical Review B* 16.9 (1977). DOI: 10.1103/PhysRevB.16.3973 (cited on pages 170, 172).

[12] Y. Nambu and S.-i. Shamoto. "Neutron Scattering Study on Yttrium Iron Garnet for Spintronics". *Journal of the Physical Society of Japan* 90.8 (2021). DOI: 10.7566/JPSJ.90.081002 (cited on pages 170, 173, 175, 176, 187, 201, 203).

[13] G. P. Espinosa. "Crystal Chemical Study of the Rare-Earth Iron Garnets". *The Journal of Chemical Physics* 37.10 (1962). DOI: 10.1063/1.1733008 (cited on page 170).

[14] V. Chlan, P. Novák, H. Štěpánková, J. Englich, J. Kuriplach, and D. Nižňanský. "Hyperfine interactions in lutetium iron garnet". *Journal of Applied Physics* 99.8 (2006). DOI: 10.1063/1.2158687 (cited on page 170).

[15] C. Milanese, V. Buscaglia, F. Maglia, and U. Anselmi-Tamburini. "Disorder and Nonstoichiometry in Synthetic Garnets $A_3B_5O_{12}$ (A = Y, Lu-La, B = Al, Fe, Ga). A Simulation Study". *Chemistry of Materials* 16.7 (2004). DOI: 10.1021/cm031138u (cited on page 170).

[16] A. A. Stelmach, E. E. Anderson, and S. Arajs. "Magnetization of lutetium iron garnet near the critical point". *Journal of Physics and Chemistry of Solids* 34.8 (1973). DOI: 10.1016/S0022-3697(73)80031-9 (cited on page 170).

[17] U. Köbler and A. Hoser. "First order spin flop transition in yttrium iron garnet (YIG)". *Solid State Communications* 142.6 (2007). DOI: 10.1016/j.ssc.2007.02.041 (cited on page 170).

[18] C. L. Jermain, H. Paik, S. V. Aradhya, R. A. Buhrman, D. G. Schlom, and D. C. Ralph. "Low-damping sub-10-nm thin films of lutetium iron garnet grown by molecular-beam epitaxy". *Applied Physics Letters* 109.19 (2016). DOI: 10.1063/1.4967695 (cited on page 171).

[19] K. Momma and F. Izumi. "VESTA 3 for three-dimensional visualization of crystal, volumetric and morphology data". *Journal of Applied Crystallography* 44.6 (2011). DOI: 10.1107/S0021889811038970 (cited on pages 171, 176).

[20] M. Malathi, G. Venkat, A. Arora, I. I. Syvorotka, V. Sivasubramanian, and A. Prabhakar. "Magnetization spin dynamics in a $(LuBi)_3Fe_5O_{12}$ (BLIG) epitaxial film". *Journal of Magnetism and Magnetic Materials*. International Conference on Magnetic Materials and Applications – ICMAGMA2017 448 (2018). DOI: 10.1016/j.jmmm.2017.06.011 (cited on page 171).

[21] F. Hansteen, A. Kimel, A. Kirilyuk, and T. Rasing. "Femtosecond Photomagnetic Switching of Spins in Ferrimagnetic Garnet Films". *Physical Review Letters* 95.4 (2005). DOI: 10.1103/PhysRevLett.95.047402 (cited on pages 171, 174).

[22] R. Ramos, T. Hioki, Y. Hashimoto, T. Kikkawa, P. Frey, A. J. E. Kreil, V. I. Vasyuchka, A. A. Serga, B. Hillebrands, and E. Saitoh. "Room temperature and low-field resonant enhancement of spin Seebeck effect in partially compensated magnets". *Nature Communications* 10.1 (2019). DOI: 10.1038/s41467-019-13121-5 (cited on pages 171, 174).

[23] H. Yamahara, M. Seki, and H. Tabata. "High temperature spin cluster glass behavior in Co- and Si-substituted garnet ferrite thin films". *Journal of Magnetism and Magnetic Materials* 501 (2020). DOI: 10.1016/j.jmmm.2020.166437 (cited on pages 171, 174, 182, 186–188).

[24] S. Geller. "Crystal chemistry of the garnets". *Zeitschrift fur Kristallographie - New Crystal Structures* 125.125 (1967). DOI: 10.1524/zkri.1967.125.125.1 (cited on page 171).

[25] M. D. Sturge, E. M. Gyorgy, R. C. LeCraw, and J. P. Remeika. "Magnetic Behavior of Cobalt in Garnets. II. Magnetocrystalline Anisotropy and Ferrimagnetic Resonance of Cobalt-Doped Yttrium Iron Garnet". *Physical Review* 180.2 (1969). DOI: 10.1103/PhysRev.180.413 (cited on pages 171, 172).

[26] D. Piwowarska, P. Gnutek, and C. Rudowicz. "Origin of the Ground Kramers Doublets for $Co^{2+}(3d^7)$ Ions with the Effective Spin 3/2 Versus the Fictitious 'Spin' 1/2". *Applied Magnetic Resonance* 50.6 (2019). DOI: 10.1007/s00723-018-1080-4 (cited on page 171).

[27] R. Peña-Garcia, Y. Guerra, D. M. Buitrago, L. R. F. Leal, F. E. P. Santos, and E. Padrón-Hernández. "Synthesis and characterization of yttrium iron garnet nanoparticles doped with cobalt". *Ceramics International* 44.10 (2018). DOI: 10.1016/j.ceramint.2018.03.179 (cited on page 172).

[28] D. Dale, G. Hu, V. Balbarin, and Y. Suzuki. "In-plane uniaxial magnetic anisotropy of cobalt-doped $Y_3Fe_5O_{12}$ epitaxial films". *Applied Physics Letters* 74.20 (1999). DOI: 10.1063/1.124053 (cited on pages 172, 173).

[29] R. Tholkappiyan and K. Vishista. "Tuning the composition and magnetostructure of dysprosium iron garnets by Co-substitution: An XRD, FT-IR, XPS and VSM study". *Applied Surface Science* 351 (2015). DOI: 10.1016/j.apsusc.2015.05.193 (cited on page 172).

[30] G. F. Dionne and J. B. Goodenough. "Effects of Co^{2+} and Mn^{3+} ion substitutions on the anisotropy and mag-

netostriction constants of $Y_3Fe_5O_{12}$". *Materials Research Bulletin* 7.8 (1972). DOI: 10.1016/0025-5408(72)90123-7 (cited on pages 172, 173, 201).

[31] T. Okada, H. Sekizawa, and S. Iida. "Ferromagnetic Resonance in Garnet $Y_3Fe_{5-x}Co_{x/2}Ge_{x/2}O_{12}$". *Journal of the Physical Society of Japan* 18.7 (1963). DOI: 10.1143/JPSJ.18.981 (cited on page 172).

[32] K. Rohith Vinod, N. K. Mathew, G. Theertharaman, R. Radha, K. Sethupathi, P. Saravanan, and S. Balakumar. "Coexistence of ferri and ferromagnetism in cobalt substituted samarium iron garnet". *Materials Science and Engineering: B* 276 (2022). DOI: 10.1016/j.mseb.2021.115521 (cited on page 172).

[33] R. Skomski. "Models of magnetic anisotropy". *Simple Models of Magnetism*. Ed. by R. Skomski. Oxford University Press, 2008. DOI: 10.1093/acprof:oso/9780198570752.003.0003 (cited on page 172).

[34] G. F. Dionne. "Origin of the magnetostriction effects from Mn^{3+}, Co^{2+}, and Fe^{2+} ions in ferrimagnetic spinels and garnets". *Journal of Applied Physics* 50.6 (1979). DOI: 10.1063/1.326459 (cited on pages 172, 173).

[35] G. F. Dionne. *Anisotropy and Relaxation Effects of Co^{2+} Ions in LiTi Ferrite.*: tech. rep. Fort Belvoir, VA: Defense Technical Information Center, 1984. DOI: 10.21236/ADA146550 (cited on page 173).

[36] G. F. Dionne. "Theory of Co^{2+} exchange isolation in ferrimagnetic spinels and garnets". *Journal of Applied Physics* 64.3 (1988). DOI: 10.1063/1.341854 (cited on page 173).

[37] S. Geller, G. Balestrino, A. K. Ray, and A. Tucciarone. "Broad magnetic transitions in cobalt-substituted yttrium iron garnet". *Physical Review B* 27.1 (1983). DOI: 10.1103/PhysRevB.27.326 (cited on pages 173, 182, 202).

[38] K. Egashira, T. Manabe, and H. Katsuraki. "Effects of Foreign Co^{2+} and Fe^{2+} Ions on the Magneto-Optical Properties of Gadolinium Iron Garnet". *Journal of Applied Physics* 42.11 (1971). DOI: 10.1063/1.1659776 (cited on page 173).

[39] A. Stupakiewicz, K. Szerenos, M. D. Davydova, K. A. Zvezdin, A. K. Zvezdin, A. Kirilyuk, and A. V. Kimel. "Selection rules for all-optical magnetic recording in iron garnet". *Nature Communications* 10.1 (2019). DOI: 10.1038/s41467-019-08458-w (cited on page 173).

[40] A. B. Chizhik, I. I. Davidenko, A. Maziewski, and A. Stupakiewicz. "High-temperature photomagnetism in Co-doped yttrium iron garnet films". *Physical Review B* 57.22 (1998). DOI: 10.1103/PhysRevB.57.14366 (cited on page 173).

[41] C. M. Srivastava and R. Aiyar. "Spin wave stiffness constants in some ferrimagnetics". *Journal of Physics C: Solid State Physics* 20.8 (1987). DOI: 10.1088/0022-3719/20/8/013 (cited on page 173).

[42] K. Sekiguchi, S.-W. Lee, H. Sukegawa, N. Sato, S.-H. Oh, R. D. McMichael, and K.-J. Lee. "Spin-wave propagation in cubic anisotropic materials". *NPG Asia Materials* 9.6 (2017). DOI: 10.1038/am.2017.87 (cited on page 173).

[43] T. Hioki, Y. Hashimoto, and E. Saitoh. "Coherent oscillation between phonons and magnons". *Communications Physics* 5.1 (2022). DOI: 10.1038/s42005-022-00888-1 (cited on page 174).

[44] A. H. M. Reid, A. V. Kimel, A. Kirilyuk, J. F. Gregg, and T. Rasing. "Optical Excitation of a Forbidden Magnetic Resonance Mode in a Doped Lutetium-Iron-Garnet Film via the Inverse Faraday Effect". *Physical Review Letters* 105.10 (2010). DOI: 10.1103/PhysRevLett.105.107402 (cited on page 174).

[45] J. Barker and G. E. W. Bauer. "Thermal Spin Dynamics of Yttrium Iron Garnet". *Physical Review Letters* 117.21 (2016). DOI: 10.1103/PhysRevLett.117.217201 (cited on pages 175, 176).

[46] S. Toth and B. Lake. "Linear spin wave theory for single-Q incommensurate magnetic structures". *Journal of Physics: Condensed Matter* 27.16 (2015). DOI: 10.1088/0953-8984/27/16/166002 (cited on pages 175, 193).

[47] T. Brueckel, B. Dorner, A. G. Gukasov, V. P. Plakhty, W. Prandl, E. F. Shender, and O. P. Smirnow. "Dynamical interaction of antiferromagnetic subsystems: a neutron scattering study of the spinwave spectrum of the garnet $Fe_2Ca_3(GeO_4)_3$". *Zeitschrift für Physik B Condensed Matter* 72.4 (1988). DOI: 10.1007/BF01314529 (cited on page 176).

[48] Y. Nambu et al. "Observation of Magnon Polarization". *Phys. Rev. Lett.* 125.2 (2020). DOI: 10.1103/PhysRevLett.125.027201 (cited on pages 176, 178).

[49] S.-i. Shamoto, Y. Yasui, M. Matsuura, M. Akatsu, Y. Kobayashi, Y. Nemoto, and J. Ieda. "Ultralow-energy magnon anomaly in yttrium iron garnet". *Physical Review Research* 2.3 (2020). DOI: 10.1103/PhysRevResearch.2.033235 (cited on page 176).

[50] S. Geprägs et al. "Origin of the spin Seebeck effect in compensated ferrimagnets". *Nature Communications* 7.1 (2016). DOI: 10.1038/ncomms10452 (cited on page 176).

[51] E. B. Knudsen, H. O. Sørensen, J. P. Wright, G. Goret, and J. Kieffer. "FabIO: easy access to two-dimensional X-ray detector images in Python". *Journal of Applied Crystallography* 46.2 (2013). DOI: 10.1107/S0021889813000150 (cited on page 180).

[52] J. S. McCloy and B. Walsh. "Sublattice Magnetic Relaxation in Rare Earth Iron Garnets". *IEEE Transactions on Magnetics* 49.7 (2013). DOI: 10.1109/TMAG.2013.2238510 (cited on pages 182, 183, 187, 188).

[53] M. Uemura, T. Yamagishi, S. Ebisu, S. Chikazawa, and S. Nagata. "A double peak of the coercive force near the compensation temperature in the rare earth iron garnets". *Philosophical Magazine* 88.2 (2008). DOI: 10.1080/14786430701805582 (cited on pages 182, 183, 188).

[54] S. Mugiraneza and A. M. Hallas. "Tutorial: a beginner's guide to interpreting magnetic susceptibility data with the Curie-Weiss law". *Communications Physics* 5.1 (2022). DOI: 10.1038/s42005-022-00853-y (cited on page 184).

[55] D. Yu, R. Mole, T. Noakes, S. Kennedy, and R. Robinson. "Pelican - a Time of Flight Cold Neutron Polarization Analysis Spectrometer at OPAL". *Journal of the Physical Society of Japan* 82.Suppl.A (2013). DOI: 10.7566/JPSJS.82SA.SA027 (cited on page 189).

[56] S. A. Danilkin, G. Horton, R. Moore, G. Braoudakis, and M. Hagen. "The TAIPAN thermal triple-axis spectrometer at the OPAL reactor". *Journal of Neutron Research* 15.1 (2007). DOI: 10.1080/10238160601045755 (cited on page 191).

[57] O. Arnold et al. "Mantid—Data analysis and visualization package for neutron scattering and μSR experiments". *Nuclear Instruments and Methods in Physics Research Section A: Accelerators, Spectrometers, Detectors and Associated Equipment* 764 (2014). DOI: 10.1016/j.nima.2014.07.029 (cited on page 191).

[58] R. A. Ewings, A. Buts, M. D. Le, J. van Duijn, I. Bustinduy, and T. G. Perring. "HORACE: Software for the analysis of data from single crystal spectroscopy experiments at time-of-flight neutron instruments". *Nuclear Instruments and Methods in Physics Research Section A: Accelerators, Spectrometers, Detectors and Associated Equipment* 834 (2016). DOI: 10.1016/j.nima.2016.07.036 (cited on page 191).

[59] J. D. Hunter. "Matplotlib: A 2D Graphics Environment". *Computing in Science & Engineering* 9.3 (2007). DOI: 10.1109/MCSE.2007.55 (cited on page 191).

[60] C. R. Harris et al. "Array programming with NumPy". *Nature* 585.7825 (2020). DOI: 10.1038/s41586-020-2649-2 (cited on page 191).

[61] P. Virtanen et al. "SciPy 1.0: fundamental algorithms for scientific computing in Python". *Nature Methods* 17.3 (2020). DOI: 10.1038/s41592-019-0686-2 (cited on page 191).

[62] M. Newville, T. Stensitzki, D. B. Allen, and A. Ingargiola. *LMFIT: Non-Linear Least-Square Minimization and Curve-Fitting for Python*. 2014. DOI: 10.5281/zenodo.11813 (cited on page 191).

[63] E. Fogh, O. Mustonen, P. Babkevich, V. M. Katukuri, H. C. Walker, L. Mangin-Thro, M. Karppinen, S. Ward, B. Normand, and H. M. Rønnow. "Randomness and frustration in a S = 1/2 square-lattice Heisenberg antiferromagnet". *Physical Review B* 105.18 (2022). DOI: 10.1103/PhysRevB.105.184410 (cited on page 197).

[64] Y. Kawamoto et al. "Understanding spin currents from magnon dispersion and polarization: Spin-Seebeck effect and neutron scattering study on $Tb_3Fe_5O_{12}$". *Applied Physics Letters* 124.13 (2024). DOI: 10.1063/5.0197831 (cited on pages 202, 203).

Conclusion

In this thesis I described the magnetism of four different quantum materials. The cornerstone of this work was the neutron scattering data collected on seven different instruments across three different central facilities (ILL, ISIS, ANSTO). The bedrock is really the advances in neutron instrumentation: neutron supermirrors delivering increased flux to the sample, large position sensitive detectors to chart reciprocal space and amass big data for spin wave studies, and sample environments that make extreme experimental conditions possible. It has been an enormous privilege to benefit as much as I have from these amazing facilities, and to learn from their dedicated staff. On top of this, the open source software developments within the scattering community have made increasingly complex data analysis reproducible and accessible to many more scientists. The magic of magnetism really shines through with neutron scattering!

The first two materials featured in this thesis were the topological materials $YbMnSb_2$ and $MnSb_4Te_7$. Both feature Mn^{2+} as the magnetic main character and both possess distinctly layered crystal structures, with Sb ions driving the topological characteristics of these materials. However, this is is where the 'bulk' similarities end.

$YbMnSb_2$ has a high magnetic ordering temperature of $T_N \approx 345\,\mathrm{K}$. The magnetic structure is coupled to the (topological) electronic band structure; however, previous *ab initio* calculations had yielded different magnetic ground states. Single crystal neutron diffraction revealed that $YbMnSb_2$ exhibits C-type antiferromagnetism with the moments oriented along the c axis and propagation vector $\mathbf{q} = (0, 0, 0)$. Half-polarised neutron diffraction constrained the in-plane FM moment canted away from the c axis to less than $0.01\,\mu_\mathrm{B}$. The magnetic moments are well localised on the Mn sites based on a maximum entropy reconstruction of the magnetisation density within the unit cell. This experimental evidence supports the hypothesis that $YbMnSb_2$ is a gapped Dirac semimetal. The spin waves spectrum in two different scattering planes was mapped using the FLATCONE detector array. With the experimentally determined magnetic structure as a starting point, I modelled the triple-axis spectroscopy data using linear spin wave theory. Notably, the exchange interaction along the c axis was much larger than for similar materials such as $YbMnBi_2$, which is consistent

with the higher T_N. This points to a possible enhancement of interactions between the electrons involved in topological transport phenomena and the electrons responsible for the magnetism in this material.

The van der Waals crystal $MnSb_4Te_7$ has much weaker interactions overall with $T_N \approx 14\,\mathrm{K}$. While the original magnetic topological insulator $MnBi_2Te_4$ has been extensively studied, the equivalent $(MnSb_2Te_4)(Sb_2Te_3)_m$ materials are not as well known. I studied the first single crystals synthesised of $MnSb_4Te_7$ with single crystal neutron diffraction. The results from this experiment demonstrated that this compound has more site mixing between Mn and Sb ions than the equivalent Bi compound. Although the magnetic interactions are predominantly 2D, there is strong antiferromagnetic coupling between the Mn on different sites and weaker antiferromagnetic coupling between the different septuple Mn layers separated by the topological quintuple Sb_2Te_3 layer along the c axis. I found that the propagation vector for the magnetic order was $\mathbf{q} = (0, 0, 1/2)$. The interlayer coupling is sufficiently weak that a field of 0.2 T induces a spin-flip transition. This may hinder the the realisation of the axion insulator state in $MnSb_4Te_7$ as compared to similar Bi compounds.

I researched the charge-doped antiferromagnetic Mott insulator $La_{2-x}Ba_xCoO_4$, an entirely different strongly correlated electron system to the topological materials. This cobalt oxide is isostructural to some of the high temperature cuprate superconductors. The similarities between these materials may extend to some electronic and magnetic degrees of freedom, such as charge stripe order. However, I found that $La_{2-x}Ba_xCoO_4$ possesses short-range charge and magnetic order, with correlation lengths of ≈ 7 Å and ≈ 15 Å respectively. Single crystal diffraction indicated that there was a slight tetragonal distortion at low temperatures, involving tilting of the oxygen octahedra. The magnetic order has the incommensurate propagation vector $\mathbf{q} = (0.5 \pm 0.23, 0.5 \pm 0.23)$ in the (h, h) plane for x = 0.5. The hypothesis that Ba doping would stabilise the stripe order in the ab plane was disproven. Nevertheless, the distinctive, yet diffuse, hour-glass shaped spin wave spectrum persisted. The magnetism of $La_{1.5}Ba_{0.5}CoO_4$ can be qualitatively described by the disordered cluster spin glass model, which is quite different to the long-range collinear AFM seen in $La_{1.5}Sr_{0.5}CoO_4$.

While the spin wave characteristics of the rare earth iron garnets such as YIG have been thoroughly probed, the effects of cobalt doping on the excitation spectrum have not. In this thesis, I reported the first inelastic neutron scattering measurements of the cobalt-doped rare earth iron garnet $Lu_3Co_{0.5}Si_{0.5}Fe_4O_{12}$. As in other REIG, the exchange interactions are strong leading to ferrimagnetic order, but the material has a slightly lower ordering temperature of $T_C \approx 480$K. At $T = 2\,\mathrm{K}$, I found that the Co^{2+} moments introduced an anisotropy gap to the spin wave spectrum. This was

observed with cold neutron time-of-flight spectroscopy. This data was combined with data from a thermal triple-axis spectrometer and then I modelled the excitation spectrum using linear spin wave theory. Magnetometry measurements revealed the extent of the magnetocrystalline anisotropy at low temperatures. $Lu_3Co_{0.5}Si_{0.5}Fe_4O_{12}$ is a much harder magnet than undoped, non-magnetic REIG such as YIG and LuIG at low temperatures. In fact, the degree of anisotropy in the system at low temperatures is similar to magnetic REIG. At $T \sim 250\,\mathrm{K}$, $Lu_3Co_{0.5}Si_{0.5}Fe_4O_{12}$ is a soft magnet and the spin wave spectrum is no longer gapped. As temperature increases, there is also a reduction in the energy gap between the two lowest energy spin wave modes, which becomes comparable to the available thermal energy at room temperature. Previous studies have shown these magnons have different polarisations in the REIG materials. Hence the increased thermal population of the optical mode in $Lu_3Co_{0.5}Si_{0.5}Fe_4O_{12}$ will likely reduce the net polarisation and overall spin current in spintronic devices.